AD NUMBER
AD848608
LIMITATION CHANGES

TO:

Approved for public release; distribution is unlimited. Document partially illegible.

FROM:

Distribution authorized to U.S. Gov't. agencies and their contractors; Critical Technology; JAN 1968. Other requests shall be referred to Defense Advanced Research Projects Agency, 675 North Randolph Street, Arlington, VA 22203-2114. This document contains export-controlled technical data.
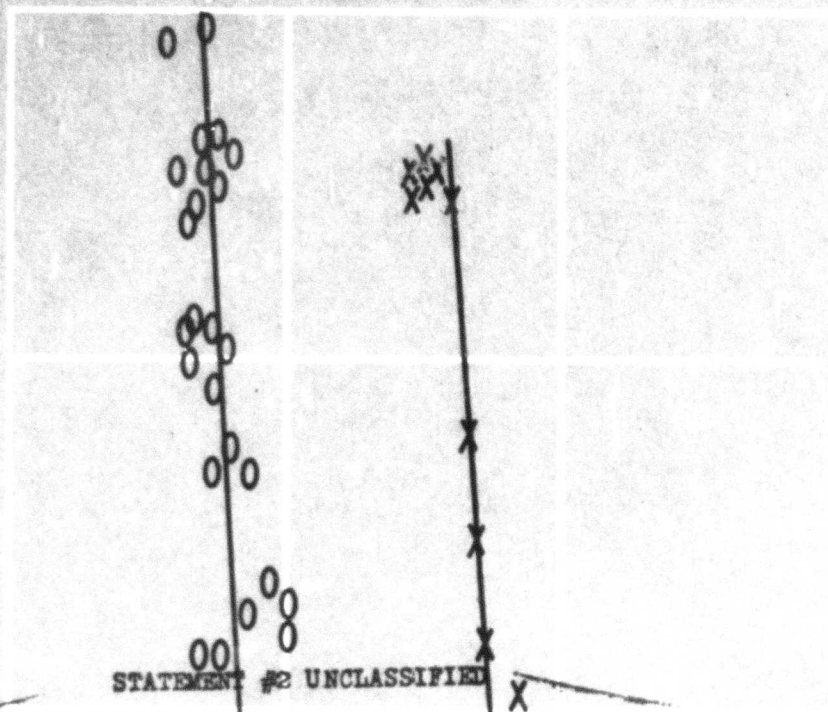
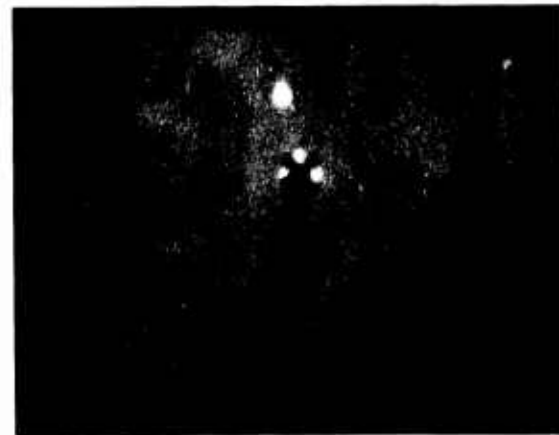| AUTHORITY |
|---|
| ARPA ltr, 22 Apr 1971 |

AD848608

SEISMIC
COUPLING

January 1968

344

CLOSE IN OBSERVATION OF THE EXPLOSIVE GENERATION OF SEISMIC WAVES. Explosion source: 48" of 5 grain/ft PETN in a 1/16" hole in 1/8" Plexiglas. Optics: Argon bomb illumination source, plane polarized light Ektachrome film, B.&W. 189 framing camera, and inter-frame time 4.158 microseconds. Tensile prestress in model: 114 p.s.i. See paper by Thomson, Ahrens and Toksoz for a more detailed analysis.

SEISMIC COUPLING

Gene Simmons, editor

Proceedings of a Meeting Sponsored by the Advanced Research
Projects Agency, held at the Stanford Research Institute
on 15 and 16 January 1968.

PREFACE

As Chairman of this symposium, and later editor of the proceedings, I wish to take this opportunity to thank the participants for an excellent series of papers and presentations; the Stanford Research Institute for providing us with facilities, the Advanced Research Projects Agency for sponsoring the meeting, and Dr. R. K. Linde who made all of the local arrangements.

Gene Simmons
Cambridge, March 1968

CONTENTS

vi

1
COUPLING OF SEISMIC WAVES

J. M. DeNoyer
U. S. Geological Survey
Washington, D. C.

The objective of obtaining seismic source functions was considered of utmost importance during the early phases of the VELA Program. This aim was hopefully to be accomplished through the use of seismograms, a knowledge of propagation characteristics, and appropriate deconvolutions to compute source functions from distant seismic signals. Such a procedure, while very desirable in concept, became difficult and in most cases impossible to implement. A high degree of activity on this problem was prompted by pointing out its desirability in the Berkner Panel Report and by the desire of many participants in the VELA Program to contribute to the one most significant problem in the area. Stephen Simpson was able to show that he could design filters which would transform a number of the seismograms obtained from the HARD-TACK II recordings into upward directed impulses. All of these seismograms, however, were obtained from the near and regional seismic zones. His work was significant in the statistical theory of time series. It was, however, not conclusive when considered in the light of geophysics and the complicated multi-path phenomena which produced his initial data. The objective of Simpson's work was to determine first motion radiation patterns and not to determine the time history of the ground motion near the source.

James Brune made an interesting contribution by equalizing surface waves from underground explosions and earthquakes in a way that made it possible to determine radiation patterns. His technique made use of the longer period portion of the spectrum. He was indeed able to obtain "source functions" which could be related to radiation patterns. His analysis required good signal-to-noise ratios and a detailed knowledge of the dispersion characteristics of the propagation path to each station. This technique has definite application for stations where surface wave signals can be expected to be high and where the paths can be calibrated. Additional research in surface wave generation has indicated that explosions generate surface waves one to two orders of magnitude smaller than shallow earthquakes of equivalent body wave magnitude. This reduction in surface wave amplitude limits the utility of the use of source functions and radiation patterns obtained by surface wave phase equalization. Also, details of the source function (reduced displacement potential) can not be obtained from the long-period information carried by the surface waves or from the shorter period body wave

information since inadequate higher frequency components are propagated to large distances to describe the reduced displacement potential.

Knopoff recognized that source functions showing more detail than radiation patterns could probably not be obtained from seismograms at any large distance. He suggested that instead of computing the source function from the seismogram, a more rational approach would be to start with the source function, pass this function through a filter corresponding to the best model of the earth available, and compute the resulting seismogram at the desired station. He pointed out that attempts to obtain source functions from distant seismograms would result in elaborate descriptions of the earth filter and would not necessarily have anything to do with the source function as it existed near an explosion or an earthquake. Herbst, Springer, and Werth demonstrated that this could indeed be done for distance ranges of several hundred kilometers. Carpenter and Marshal have also obtained reasonable agreement with observational data for teleseismic distances.

Since these early attempts to compute seismic source functions, much empirical data has been accumulated on the coupling characteristics of various rock materials. The range of seismic magnitudes that can be expected for a given yield is large and depends on the properties of the media in which the explosion was detonated. With the large number of underground nuclear explosions now available, it is possible to see order emerging from what appeared to be a hopeless scatter of data points a few years ago. This order has come about through a more careful documentation of the media in which the explosions were detonated and from improvements in determining seismic body wave magnitude. We are still limited in our prediction capability for new materials. Some empirical relations between the properties of the materials and seismic coupling appear to establish at least some of the significant parameters. Tests of these relations are being implemented in experiments such as the planned SCROLL explosion. It would, however, be desirable to realistically investigate the magnitude-yield relationships for many materials without actually conducting a nuclear explosion. The reasons for the desirability of the computational approach are economics, time, impracticality of conducting tests at many of the locations of interest to test detection.

Fortunately, a lot of progress has been made in developing our ability to predict what seismic source functions should be for real geologic materials. The Lawrence Radiation Laboratory has been a leader in developing these complicated codes. Other groups have also been making significant progress in this direction. The ability of computational codes to predict reduced displacement potentials is now quite acceptable provided the proper input parameters are available. Many of these input parameters must be obtained from laboratory investigations leading to the equations of state of rock materials. Failure criteria and time

2

dependence of rock properties under dynamic loading are also very important. Additional problems arise when large bodies of rock and the properties of these large bodies are compared with experimental data obtained from small experiments in the laboratory. The recognition of the rock mechanics problems has prompted renewed interest in this area within the VELA Program during recent months. The particular problems being emphasized in rock mechanics are intended to improve the input parameters for code calculations and to better define stability problems if full decoupling in large cavities is considered.

"There appears to be an upper limit to the yield which can be achieved under the restrictions of full decoupling. Extension of the yield range to higher values would entail techniques designed to facilitate larger yield detonations in holes which are engineeringly feasible." Seismic source functions for explosions in such cavities can be obtained by using the computational codes available provided proper failure criteria and non-elastic behavioral properties are used. Such techniques are probably more sensitive to adequate rock mechanics information than the fully decoupled or even the fully tamped explosions. The stability of large cavities is also critically dependent on problems in rock mechanics that are not adequately solved. Laboratory and theoretical investigations of these rock mechanics problems are under investigation and will hopefully be yielding significant results in the near future.

The ability to compute the amplitudes of seismic signals at distant stations has been progressing steadily for a number of years. This capability has been developed for use in systems studies for real and hypothetical networks of seismic stations. At the present time it is possible to use seismic magnitude as an input (this assumes the yield-magnitude relations are known). Account can also be taken of the noise conditions and the statistical distribution of the noise at the station and of expected variations in signal amplitudes. Results of comparing these systems studies with the performance of real networks is indeed encouraging. It is not a large additional step to compute magnitude-yield relations from reduced displacement potentials if the reduced displacement potentials can be produced with reasonable accuracy for any selected geologic medium. It should also be possible to use reduced displacement potentials instead of magnitudes as the initial input into estimates of the signal amplitude that would be recorded at any given distant station. An additional feature that should be attainable is a reasonable estimate of the waveform that would be recorded at a distant station provided sufficient information on the crustal and upper mantle structure and propagation characteristics near the source and near the station are known. Once either amplitudes or waveforms at individual stations are determined it is then possible to evaluate the performance of a system of any group of real or hypothetical seismograph stations. Such studies allow existing systems with individual station differences to be compared with planned or future systems provided the differences in propagation characteristics and noise statistics can be adequately estimated. Evasion threats and maximum undetectable yields can also be evaluated.

The purpose of this meeting is to look at the individual pieces that can contribute to the estimation of a seismic signal provided the yield of the bomb, the media, and the location are specified. Hopefully, we are nearing the point when it will be possible to specify a probable material at any point on the earth; calculate the maximum yield that could be detonated in this material without being detected; or, given a detectable yield within the specified material, compute the probability of detection and possibly an estimate of the waveform at each station of the network. The ability to accomplish this objective will make it possible to include the effects of local geology in the USSR and China in our estimates of seismic capability. As more is learned about the geology and the physical properties of the rock materials in the USSR and China it will be possible to include the seismic coupling characteristics of these earth materials.

GEOLOGIC STUDIES OF USSR AND CHINA FOR NUCLEAR TEST DETECTION

L. D. Bonham
U. S. Geological Survey
Washington, D. C.

ABSTRACT

Since 1962, the U. S. Geological Survey on behalf of the Advanced Research Projects Agency has been interpreting the environment of the Sino-Soviet area in relation to underground nuclear test detection. Small-scale and medium-scale atlases of geology, seismicity, and other environmental topics are being prepared to aid in identification of potential test areas, analysis of seismic signals, planning and operation of on-site inspection, and study of test techniques. Special studies are being conducted on distribution of low-coupling media and for inspection training.

DYNAMIC PROPERTIES OF GEOLOGIC MEDIA

G. D. Anderson and R. K. Linde
Stanford Research Institute

ABSTRACT

In order to perform computations to predict how a given energy source distur-
bance in the earth will couple to the surrounding medium and how the subsequent
stress wave will propagate, it is necessary to know certain properties of the me-
dium. The properties which must be known depend upon the model that is being
used to describe the medium, e.g., elastic, elastic-plastic, or hydrodynamic. The
material properties are generally referred to as the constitutive relation or equa-
tion of state. In the case of nonreactive flow, knowledge of a complete equation of
state is not necessary. A stress-volume-energy (σ-v-e) equation of state is suffi-
cient to solve the equations of motion.

Shock wave techniques provide a powerful tool in studying a (σ-v-e) equation of
state of a solid. Most solids exhibit an elastic-plastic behavior. Plane shock waves
can be used to study the Hugoniot curve (locus of final states of normal stress, spe-
cific volume, and specific energy behind the shock), the Hugoniot elastic limit (yield
stress under uniaxial strain) and the path the material follows when it is released
to a lower stress by rarefaction waves. Optical and electronic stress gages can be
used to observe stress-time profiles as shock waves pass over an element of mate-
rial.

These techniques have been used to study the material properties of a variety
of solid rocks, porous rocks and dry and moist soil materials at room temperature
and at -10°C (to simulate permafrost). The results of these studies indicate that
the moisture present in the soil and the existence of polymorphic phase changes in
soils containing large amounts of silica affect the shock impedance (how the medium
will couple to adjacent media) and how finite duration shock pulses attenuate as the
wave propagates. The majority of the work performed at SRI has been in the high
stress regime, i.e., 50 to 500 kbar. Laboratory prepared samples rather than
naturally occurring samples have been used primarily since the latter frequently
contain inhomogeneities which are large on the size scale of the experiment.
Studies of porous metals indicate that simple models of material behavior in the
low stress region $\lesssim$ 30 kbar) may not be adequate for reliable prediction of wave
profiles and attenuation.

More experimental data on yield strengths, shock profiles, and attenuation
characteristics are needed. These low stress data are important because the major-
ity of the material affected by a sudden release of energy in the earth will experience
relatively low stress. The region of validity laboratory tests of scaled down or re-
constituted earth materials with large scale inhomogeneities should be seriously
considered. Finally, an evaluation and classification should be made of the large
amount of existing shock wave data on geologic materials to assure that it is
being most effectively and efficiently used in present computation programs.

DYNAMIC PROPERTIES OF GEOLOGIC MEDIA

Gordon D. Anderson and Ronald K. Linde
Poulter Laboratory for High Pressure Research
Stanford Research Institute
Menlo Park, California

INTRODUCTION

The partial differential equations of motion which express the conservation of mass and momentum in continuous media are independent of the material to which they are applied. In order to apply these equations of motion to a particular material and to solve them to predict the motion resulting from a particular disturbance, it is necessary to supplement the equations of motion with an equation or set of equations describing the material properties of the particular medium. This involves assigning an appropriate model (e.g., hydrodynamics, elastic-plastic, etc.) to describe the medium and then prescribing relationships between the material parameters necessary to describe the model. These relationships are commonly called equations-of-state or constitutive relations. Shock wave experiments are not only a powerful tool for investigating equations of state, but are essential for describing material response to impulsive loading such as that produced by natural or artificial seismic sources. We have studied a wide variety of materials to date, ranging from pure metals to heterogeneous soils. The purpose of this paper is to familiarize the audience with some of the techniques used, and types of laboratory measurements made, and to present some results and point out some problems that we feel are pertinent to the seismic coupling program.

SHOCK WAVE EXPERIMENTS

Plane shock waves are produced in materials in the laboratory either by placing the material in contact with a high explosive or by impact with a high velocity flat plate. Typically, pressures range between the order of one kilobar and ten megabars, compressions for solids range from less than 1 percent to more than 50 percent, and the time during which the material is subjected to these stresses and compressions in the laboratory ranges from 10^{-7} to 10^{-5} sec. For strong shocks in compressible materials (particularly in porous materials) extremely high temperatures are reached, so that the material may even vaporize after release of pressure. The states of the material on either side of the shock are related by the Rankine-Hugoniot jump conditions expressing conservation of mass, momentum, and energy:

$$\rho_o U = \rho_1 (U - u_1) \tag{1}$$

8

$$p \cdot p_o - \rho_o U u_1 \tag{2}$$

$$e_1 - e_o - \frac{1}{2}(p_1 + p_o)(v_o - v) \tag{3}$$

where ρ is density, U is shock velocity, u is particle velocity, p is pressure, v is specific volume, and e is specific internal energy. The subscripts o and 1 refer to states ahead of and behind the shock, respectively. The mass and momentum equations (equations 1 and 2) contain four variables associated with the shock. These variables are U, u_1, p_1, and ρ_1. Measurement of any two of these variables permits one to compute the remaining two. Equation-of-state data are obtained by measuring one of these variables as a function of one of the others. This functional relationship is called the Rankine-Hugoniot equation, or simply the Hugoniot of the material. Shock velocity is measured optically or electronically by recording the transit time of a shock through a known thickness of material, the particle velocity is usually inferred from a measurement of the velocity of a free surface, and the pressure or stress may be measured by a piezoelectric or piezoresistive stress gage. In studying porous media it is customary to use experimental samples that are large compared to the scale of the inhomogeneities in density. In this case the material is treated as a continuum and the Hugoniot jump conditions refer to the macroscopic stress-volume-energy states of the shocked material. If the sample under study is not large compared to the inhomogeneities, steady state conditions may not be achieved in times short compared to the duration of the experiment. In this case the validity of using the Rankine-Hugoniot jump conditions to determine equation-of-state data must be critically examined.

When studying solids, it is customary to loosely classify shock wave experiments as either high or low pressure. High pressure refers to the case in which the pressure greatly exceeds the yield strength of the material so that the stress configuration is nearly hydrostatic. Low pressure shocks are of the order of the dynamic yield strength of the material. In the case of most metals the dynamic yield strength is below about 10 kbar, while it may be as high as 50 kbar in some rocks and 50-200 kbar in some single-crystal minerals. The highest pressures reached at SRI have been obtained by impact with an explosively accelerated metal plate. The system is shown in figure 1. Pressures in excess of 1400 kbar in tungsten, 790 kbar in aluminum [1, 2] and 400 kbar in porous soils [3] are routinely achieved. Streak camera photography is most frequently used to record shock transit times and free surface motion. The lower pressure work at SRI is often performed on the light gas gun [4, 5] shown in figure 2. This gun is capable of accelerating a 200 gm, 2 1 2-inch diameter projectile to a velocity of about 1 mm/μsec. The head of the projectile which impacts the target is lapped flat and may be made from any solid material desired. The main body of the projectile is aluminum. The target to be studied is mounted on the muzzle end of the gun as shown in figure 3. A linear array of velocity pins measure projectile velocity and acceleration near the muzzle. A set of three

9

radial pins for the purpose of further velocity measurement and triggering of electronic equipment are placed very near the face of the target; the actual impact is recorded by four tilt pins in the target surface. Transducers may be placed in the projectile head, within the target or on the back surface of the target to monitor stress.

The manganin wire gage [6, 7] is one type of sensor that is frequently employed to record stress time profiles. Manganin (84% Cu, 12% Mn, 4% Ni) is a piezoresistive alloy for which the percentage change in resistance is proportional to the pressure, but essentially independent of the temperature. Manganin is used in the form of a wire or thin film through which a constant current is passed. The wire configuration is shown schematically in figure 4. The thin wire is embedded in the material under study and comes to stress equilibrium with the surrounding medium rapidly, so that a measurement of the voltage drop across a portion of the wire as a function of time yields a stress-time profile.

Quartz gages [8] are also used routine on gas gun shots to study wave profiles [4, 5]. They have the advantage of greater ser tivity at low stresses ($\cong 20$ kbar) but the disadvantage of perturbing the wave shape being studied due to the shock impedance mismatch between quartz and most samples.

EXPERIMENTAL RESULTS

Let us now look at some examples of material properties obtained from shock wave experiments and observe particularly the complicated behavior of porous materials at low stress levels. We have included examples of porous ("foam") metal specimens in order to illustrate the effect of porosity, present in most rocks, without the additional complicating factors such as phase transitions and solid inhomogeneities.

At very high stresses, when the yield strength is greatly exceeded, the stress configuration is nearly hydrostatic. In this regime the terms stress and pressure are frequently used interchangably and a hydrodynamic model is sufficient to describe the material for most purposes. (We shall see a major exception later.) An energy-pressure-volume (e-p-v) equation of state is then a sufficient description of the medium for the equations of motion to be solved. As an example of high pressure equation-of-state data let us consider aluminum. Using the explosive system shown in figure 1 to induce strong shock waves into specimens, an e-p-v equation of state was generated for pure aluminum over the pressure range between about 200 and 700 kbar. A high speed rotating mirror streak camera was used to record shock and free surface velocities. Porous aluminum samples were shocked to obtain e-p-v states to the right of the Hugoniot curve for solid aluminum. Hugoniot curves were obtained for aluminum with porosity ratios $\rho_o/\rho_{oo} = 1.0$, 1.4, 1.7, and 2.0, where ρ_o is the void-free density of solid aluminum at standard conditions and ρ_{oo} is the bulk density of the porous aluminum. In analyzing the data it was assumed that (1) the final shock state of the aluminum lies close to the equilibrium e-p-v

surface for aluminum, (2) the crushing strength of the porous aluminum is negligible, and (3) the initial internal energy of solid and porous aluminum at standard conditions is the same. Under these assumptions the data were fitted to an e-p-v equation of state of the form

$$p = be + f(v) \tag{4}$$

where b is a constant and $f(v)$ is a function of volume. The experimental data and Hugoniot curves generated by combining equation 3 and 4 are shown in Figure 5. Equation 4 is a Mie-Grüneisen equation of state in which Grüneisen's ratio, , is directly proportional to volume, i.e. $(\partial p / \partial e)_v$ is constant over the pressure-volume regime studied. The function $f(v)$ was evaluated using an analytical fit to the Hugoniot for solid aluminum, $p_S = p_S(v)$. Since equation 4 must hold along the Hugoniot of solid aluminum,

$$p_S(v) = be_S + f(v) \tag{5}$$

where e_S is the internal energy along the Hugoniot of solid aluminum. From equation 3 we know the energy, pressure, and volume along the Hugoniot are related by

$$e_S = e_{oS} + \frac{1}{2} p_S(v)(v_o - v) \tag{6}$$

where p_o has been set equal to zero and the subscript S signifies "solid." Substituting equation 6 into equation 5 we can solve for the function $f(v)$ in terms of the pressure-volume fit to the Hugoniot of solid aluminum, $p_S(v)$,

$$f(v) = p_S(v)\left[1 - \frac{b}{2}(v_o - v)\right] + be_o \tag{7}$$

The equation of state (5) can also be written in the form

$$p - p_S(v) = \frac{\gamma}{v}(e - e_S(v)) \tag{8}$$

where $p_S(v)$ and $e_S(v)$ are respectively the pressure and specific internal energy as functions of volume along the Hugoniot of solid aluminum. The constant b has been replaced by γ/v, which was found to be nearly constant in the case of aluminum, but about 10 percent higher than its zero pressure equilibrium value. Using equation 8, Hugoniots of porous aluminum can be generated. Along Hugoniots for porous aluminum

$$p_F - p_S = \frac{\gamma}{v}(e_F - e_S) \tag{9}$$

where the subscripts F and S signify (porous) foam and solid, respectively. Along the Hugoniot of the foam the energy relationship given by equation 6 holds, viz.,

$$e_F = e_{oF} + \frac{1}{2} p_F(v_{oo} - v) \tag{10}$$

11

where v_{oo} is the initial specific volume of the foam. Recall that in the analysis we have ignored the small difference in initial internal energy of the solid and foam so that $e_{oF} = e_{oS}$. Combining equations 9 and 10 we can generate the Hugoniots of foams of various porosities:

$$p_F(v) = p_S(v) \left[\frac{1 - \frac{\gamma}{2v}(v_o - v)}{1 - \frac{\gamma}{2v}(v_{oo} - v)} \right] \tag{11}$$

The Hugoniots of porous aluminum shown in figure 5 were computed in this way. An equivalent expression in terms of the function $f(v)$ can be obtained by combining equations 5 and 10. In this case the Hugoniot of the porous material is given by

$$p_F(v) = \frac{f(v) + \frac{\gamma e_o}{v}}{1 - \frac{\gamma}{2v}(v_{oo} - v)} \tag{12}$$

The Hugoniots of the porous materials (for which $\gamma/v > 0$) lie to the right of the Hugoniot of the solid in the pressure-specific volume plane. This is due to the large amount of heating caused by the irreversible conversion of mechanical work to heat in the shock compaction of the foam. For many metals the assumption that γ/v is constant over a wide pressure range is quite good, so that knowledge of γ/v at one point enables one to make predictions of the Hugoniot of a foam at high pressure if the Hugoniot of the solid is known. As we shall see later, this analysis breaks down at low pressures where the foam is not completely collapsed to solid.

When performing shock attenuation calculations, it is necessary to know the release path. In porous material the release path is generally quite different in shape from the Hugoniot, or loading curve. Release paths can be determined experimentally by techniques similar to those used for determining Hugoniots. Two examples of Hugoniot curves and release paths in the pressure-particle velocity plane for porous soils are shown in figures 6 and 7. Figure 6 shows a Hugoniot and release curve for dry Nevada Test Site (NTS) playa pressed to an initial density of 1.55 g/cm^3. Note the steep slope of the release curve from the highest pressure. Although release curves in porous media are generally much steeper than the Hugoniot (due to the irreversible compaction taking place in the shock process), the extraordinary steepness seen in figure 6 is believed to be a manifestation of a phase transition. The Hugoniot and release curves in figure 7 are for NTS playa containing about 19% water by weight. The bulk density of the water and soil combined is again 1.55 g/cm^3. The high pressure release curve is not so steep in this case; however, the free surface velocities (particle velocities upon release to zero pressure) are very high. This could be due to vaporization and expansion of the water upon release. The shape of these release curves determines the velocities of rarefaction

12

waves and governs how the compressive stress waves will attenuate when they are overtaken by rarefaction waves. It is therefore imperative that they be accurately known when attenuation calculations are performed.

Even though the stress may be nearly hydrostatic at very high pressures, the material may still retain considerable strength, and shock attenuation may be highly nonhydrodynamic. (See for example, refs. 9 and 10.) In fact, the relative strength of materials at high pressure is one of the major unknowns at present, and appears to be considerably different for different minerals [13].

At lower stress levels the behavior of materials under shock loading becomes more complex. A simple hydrodynamic model is not adequate to describe even compressive stress wave propagation. The effect of material rigidity (ability to support a shear stress) gives rise to a double wave structure and in some cases nonsteady-state stress wave profiles. The behavior of porous materials is further complicated at low stresses because the stress wave may not completely collapse or crush the porous structure. In cases such as this, knowledge of the e-p-v equation-of-state surface of solid material is inadequate to solve problems, because the macroscopic states for porous materials do not lie near that surface and cannot be predicted from a knowledge of that surface.

Some examples of stress-wave profiles in porous aluminum and graphite are shown in figure 8. These profiles were generated by impacting the samples with a gas gun projectiles (as in figure 3) and were recorded using quartz crystal stress gages. The stress magnitudes are those transmitted to the quartz, and are somewhat higher than exist in the initially porous material prior to interaction with the quartz. Note the low amplitude (generally less than 1 kbar) elastic* precursor wave preceding the higher amplitude plastic wave. In a porous material the amplitude and velocity of this precursor depend upon the porosity, the matrix structure of th porous material and upon any material, such as water, that may occupy the pores. This precursor wave does not collapse the porous structure but is transmitted as an essentially elastic wave. It must be emphasized, however, that the amplitude and velocity of this wave cannot, in general, be simply predicted from the yield strength and elastic moduli of the solid material. Figure 8(f) shows a double (elastic-plastic) wave profile in solid aluminum with about a 5 kbar elastic precursor. The precursor in foam aluminum shown in figures 8(a) and 8(b) is less than one kbar. The plastic wave following the precursor may still not completely crush or compact the porous structure, even though its amplitude is several kilobars. Hugoniots for solid and porous tungsten are shown in figure 9. The Hugoniot of porous tungsten shows

---

*In a porous material, high stress concentrations exist at contact points when a load is applied. Thus, even the "elastic" precursor will in general cause a small amount localized plastic flow which enlarges contact surfaces and relieves high stress concentrations.

13

that some porosity still persists even at stresses near 150 kbar. At first sight, one might think that the offset between the Hugoniots of solid and porous tungsten at 150 kbar would be due to thermal effects. Some of the offset is due to heating, but heating does not account for all of it. Using a Mie-Grüneisen equation of state, the expected offsets due to heating were estimated using the best value and two extreme values of γ_o,* with γ/v held constant in equation 7. As can be seen from figure 9, the offset of the data from the solid tungsten Hugoniot is greater than what heating would produce, thereby indicating some remaining porosity at 150 kbar. Examination of specimens recovered after shocking disclosed residual porosities comparable to the porosities indicated at high pressure. Similar behavior was observed in copper, as shown in figure 10. This figure also shows the significant effect of foreign material in the pores. The black points represent the Hugoniot of the copper foam containing some oil in the voids. The Hugoniot of the very same foam after the oil was removed is represented by the open points. Clearly, the oil, which partially saturates the pores, adds considerably to the effective strength of the foam.

The Hugoniot curve represents the locus of final states the material can achieve by a shock process, and the shock velocity is proportional to the square root of the slope of the chord connecting the initial and final shock states in the stress-volume plane. Upon release of the stress, a particle proceeds along some release path such as the release curves shown in figures 9 and 10. The velocity of a relief wave (relative to the shock front) is proportional to the square root of the slope of the release curve in the stress-volume plane. Therefore, a comparison of the slopes of the Hugoniot and release curves give an indication of how rapidly a rarefaction wave will overtake a shock wave and attenuate it.

Particularly at low stresses, the Hugoniot and release paths for foams can be very different, due to the fact that the shock wave compacts the foam (at least partially), and upon release of stress the foam may recover only a small fraction of its initial volume. Thus porous materials are generally highly attenuating media. Observe the Hugoniot data for the partially saturated copper foam (figure 10). The Hugoniot is represented by the heavy dashed line, and has a rather shallow slope up to about 20 kbar. After release of pressure, however, recovered samples were found to have a volume considerably less than the initial specific volume (points labeled "recovered volume" in figure 10). The release curves must then have slopes given approximately by the dash-dot line drawn between the points in figure 10. The difference between the slopes of the Hugoniot and release curve is quite evident. It may be seen that for this example, the slope of the release curve is similar to that for initially solid material. Similar behavior is noted in figure 9 for porous tungsten.

---

*$\gamma_o \equiv \gamma(v = v_o)$

The effect of release path on shock attenuation is illustrated in figure 11, which shows stress-time profiles for a (porous) ATJ graphite specimen which has been impacted by a thin aluminum plate. The input pulse has been allowed to propagate long enough to become severely attenuated. (The input stress was 19.5 kbar, which would have resulted in a stress of about 40 kbar transmitted to the quartz.) The solid curve of figure 11 is an experimental profile as transmitted to a quartz gage. The dashed curve represents a computed profile assuming the material compacts and subsequently releases down a steep curve such as in the example for copper shown in figure 10. The dotted curve represents a profile computed assuming the material releases down the Hugoniot curve. The large difference between peak stress and arrival time clearly show the importance of choosing the proper release curve in attenuation calculations. It is of interest to note that recovered samples of ATJ graphite were found to be just as porous as unshocked samples, but the expansion to original volume evidently occurs later, at essentially zero stress.

Examples of the complicated behavior of porous media have been discussed here for aluminum, copper, and tungsten. These are materials which are considered relatively pure and simple compared to geologic materials. They have simple crystal structures and do not experience polymorphic phase transitions. Yet wave propagation in even these materials is very complex. The description of wave propagation in geologic materials which, in addition to being porous, may be mixtures of many compounds, may undergo phase transitions, and may contain varying amounts of water is even more complex.

It would be very desirable to be able to predict the behavior of an inhomogeneous porous medium from a knowledge of the material properties of the pure constituents of the medium. At the present time there appears to be no simple way of doing this, except at high pressure. One of the simplest examples of a heterogeneous natural medium is provided by rock salt (NaCl). Figures 12 and 13 show profiles of waves propagating along the <100> and <110> crystallographic directions of pure synthetic NaCl single crystals, 7 mm thick. In both figures elastic precursors are easily resolved. The amplitudes of the elastic waves are 0.3 kbar and 0.7 kbar for the <100> and <110> orientations, respectively. The precursor is 1 kbar in the <111> direction. Figure 14 shows a wave profile in natural polycrystalline NaCl of the same thickness, taken from the Tatum Salt Dome in Mississippi. No clear definite elastic precursor is discernible, although an abrupt change in the slope of the rise of the wave occurs at about 0.7 kbar. The precursor amplitude all vary with propagation distance.

An even more dramatic example is provided by recent work on rutile (TiO_2), [11] where the Hugoniot elastic limit (HEL) is lowered by about 25% by introduction of less than 2% porosity, and by about 60% by introduction of 4% porosity. Even the pressures over which a phase transitions occur can be drastically affected by porosity [12].

15

SUMMARY AND SUGGESTIONS FOR FUTURE STUDY

Knowledge of material properties is necessary to solve the equations of motion to predict wave propagation. Shock-wave experiments may be used to study dynamic material properties at stresses ranging from less than one kilobar up to several megabars. In the shock experiments, the material is subjected to compressions varying from less than one percent to more than 50 percent. Strain rates vary from 10^6 to 10^8 sec^{-1} in the laboratory, and extremely high temperatures are sometimes achieved in compressible materials (such as porous media). At very high stress levels solids can, for many purposes, be treated as fluids. In this case the stress is approximated as hydrostatic and an energy-pressure-volume equation-of-state is sufficient.

At low stress levels the effect of material shear strength becomes important and a hydrodynamic model is almost never adequate. Elastoplastic behavior and phase transitions lead to multiple wave structures. At low stresses, wave propagation in porous media becomes complex. Foams made of relatively simple materials such as aluminum, copper, and tungsten propagate and attenuate waves in a quite dissimilar manner from the way that solids do; porous geologic materials are even more complicated. Experimentation and calculation clearly show that stress-wave propagation and attenuation in a porous material cannot be accurately predicted in the low stress region from the knowledge of how the solid material behaves in the same stress region. In perform'.ig calculations of wave propagation through large geologic formations, such as granite which may contain many cracks and voids, one would not expect accurate computational results if the properties measured in the laboratory for a normal void- and crack-free piece of granite were used. The influence of porosity, foreign material included in the pores, and the structure of a porous medium cannot be overemphasized.

At present there appears to be no simple way of deducing the material properties of a porous medium at low stresses from the material properties of the solid from which the porous structure is formed. Future work should emphasize study of the low stress region because most of the material affected by a sudden release of energy within the earth will experience relatively low stresses and the behavior of the material in this stress regime is most complex. Small scale shock-wave experiments are useful for studying which models to use to describe material behavior. However, serious consideration is needed to assess the validity of using the results of small scale experiments to describe large-scale wave propagation in the earth. The experimenter must take into consideration the fact that large-scale geologic formations have cracks and inhomogeneities, and he must attempt to scale these effects into experiments. The theorist who attempts to make computations must make sure that the experimentally determined material properties he is using come from samples that represent the medium he is trying to describe.

The effects of nonsteady-state behavior of materials must be critically evaluated to assess their importance in the field. While early-time wave propagation effects may be of secondary

16

importance to ultimate late-time results, they may be all that we are measuring in the laboratory. Thus, the input data to the computer codes (particularly Hugoniot elastic limit data) may be wrong. These data should be verified through experiments on "thick" specimens.

Finally, the dynamic strength of materials at high pressure (i.e., at stresses substantially above the Hugoniot elastic limit) appears to vary considerably from material to material and is perhaps one of the most important areas for further investigation.

REFERENCES

1. G. D. Anderson, D. G. Doran and A. L. Fahrenbruch, Equation of State of Solids: Aluminum and Teflon, AFWL-TR-65-147, Stanford Res. Inst., Menlo Park, Calif., December 1965.

2. G. D. Anderson and A. L. Fahrenbruch, Equation of State of Solids II: Aluminum and Teflon, AFWL-TR-67-43, Stanford Res. Inst., Menlo Park, Calif., September 1967.

3. G. D. Anderson, et al., Investigation of the Equation of State of Porous Earth Media, AFWL-TR-65-146, Stanford Res. Inst., Stanford, Calif., July 1965.

4. R. K. Linde and D. N. Schmidt, "Measuring the Submicrosecond Response of Shock Loaded Materials," Rev. Sci. Inst., Vol. 37, 1966.

5. R. K. Linde and D. N. Schmidt, "Shock Propagation in Nonreactive Porous Solids," J. Appl. Phys., Vol. 37, 1966, p. 3259.

6. D. Bernstein and D. D. Keough, "Piezoresistivity of Manganin," J. Appl. Phys., Vol. 35, 1964, p. 1471.

7. D. D. Keough and W. Wilkinson, Manganin-Wire Shock-Transducer Investigation, AFWL-TR-65-170, Stanford Res. Inst., Stanford, Calif., December 1965.

8. R. A. Graham, F. W. Nielson and W. B. Benedick, "Piezoelectric Current from Shock-Loaded Quartz-A Submicrosecond Stress Gauge," J. Appl. Phys., Vol. 36, 1965, p. 1775.

9. D. R. Curran, "Nonhydrodynamic Attenuation of Shock Waves in Aluminum," J. Appl. Phys., Vol. 34, 1963, p. 2677.

10. J. O. Erkman, A. B. Christensen and G. R. Fowles, "Attenuation of Shock Waves in Solids," J. Appl. Phys., Vol. 38, 1967, p. 5395.

11. R. K. Linde and P. S. DeCarli, "Polymorphic Behavior of Titania under Dynamic Loading," J. Chem. Phys. (in press).

12. D. G. Doran and R. K. Linde, "Shock Effects in Solids," Solid State Physics, Vol. 19, F. Seitz and D. Turnbull eds., Academic Press, Inc., New York, 1966, pp. 229-290.

13. T. J. Ahrens and R. K. Linde, "The Response of Brittle Solids to Shock Compressions," Proc. of Symposium on Behavior of Dense Media under High Dynamic Pressure, IUTAM International Symposium, Paris, Sept. 11-15, 1967, to be published.

14. D. D. Keough and W. Wilkinson, Piezoresistive Stress-Time Transducer Development and Granite Adiabat Measurements for Project PILEDRIVER, Final Report SRI Project GSU-4832, Contract DA-49-146-XZ-280, Stanford Res. Inst., Stanford, Calif., February 1967.
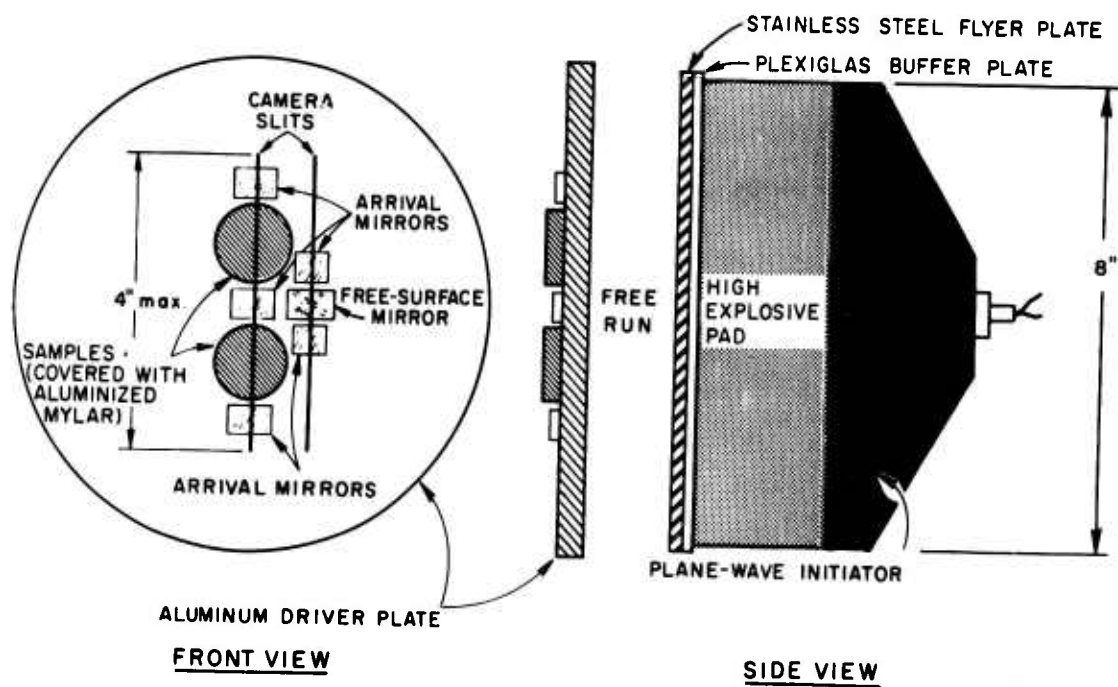
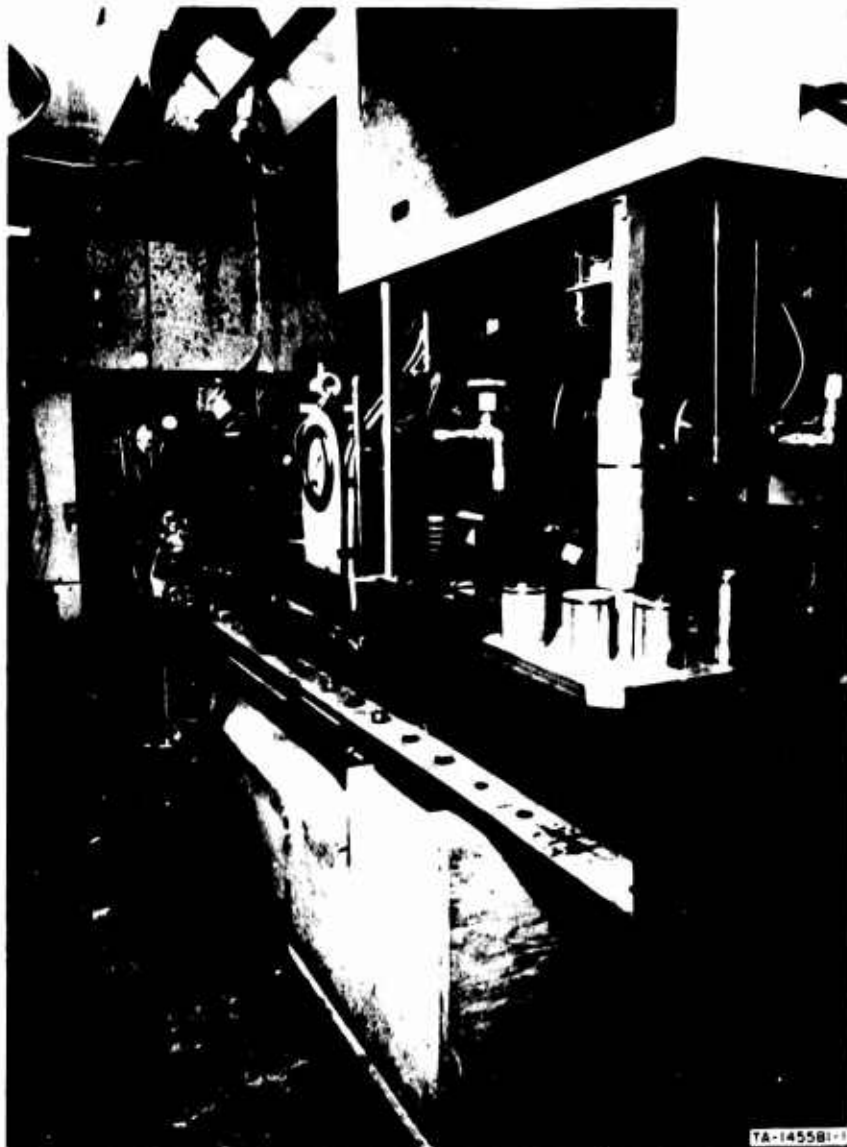FIGURE 1. PLANE WAVE EXPLOSIVE SYSTEM FOR ACHIEVING STRONG SHOCKS

FIGURE 2. SRI 2-1/2-INCH BORE LIGHT GAS GUN

20
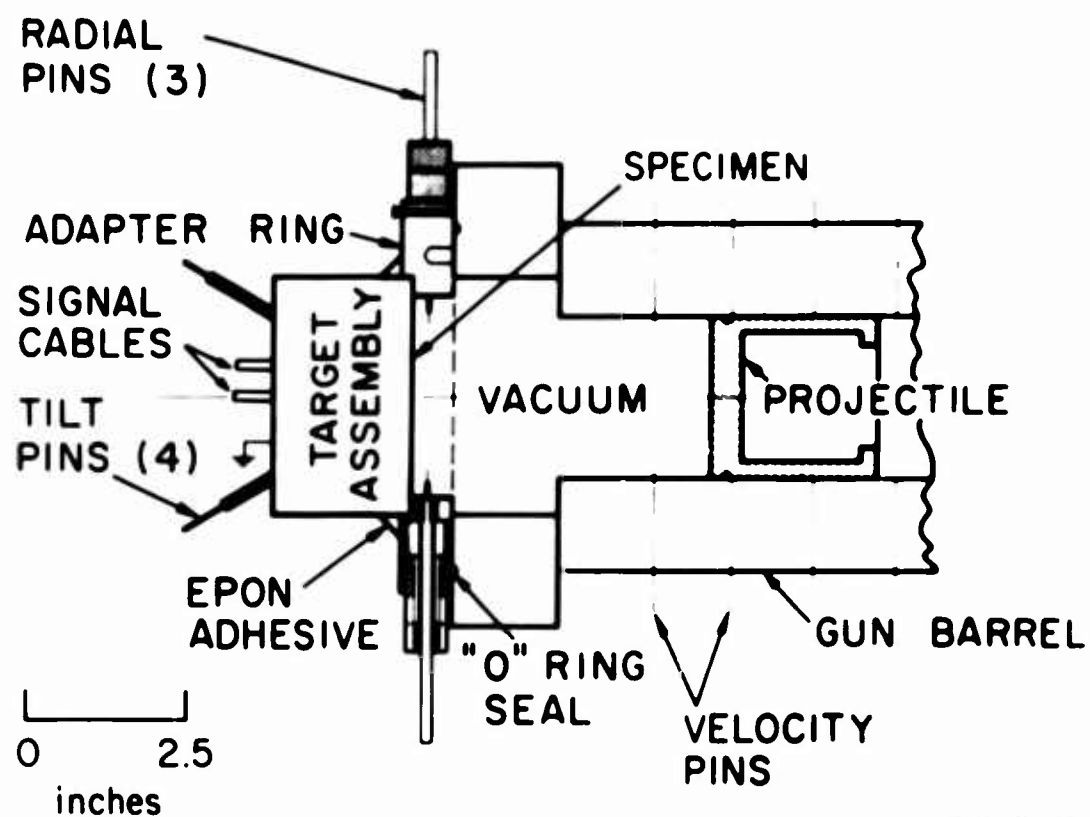
FIGURE 3. TARGET ASSEMBLY ON GAS GUN

21

INSULATOR

0.003" diam
MANGANIN WIRE

1/16" diam
MAGNESIUM LEADS

SPOT
WELDS

VOLTAGE
LEADS
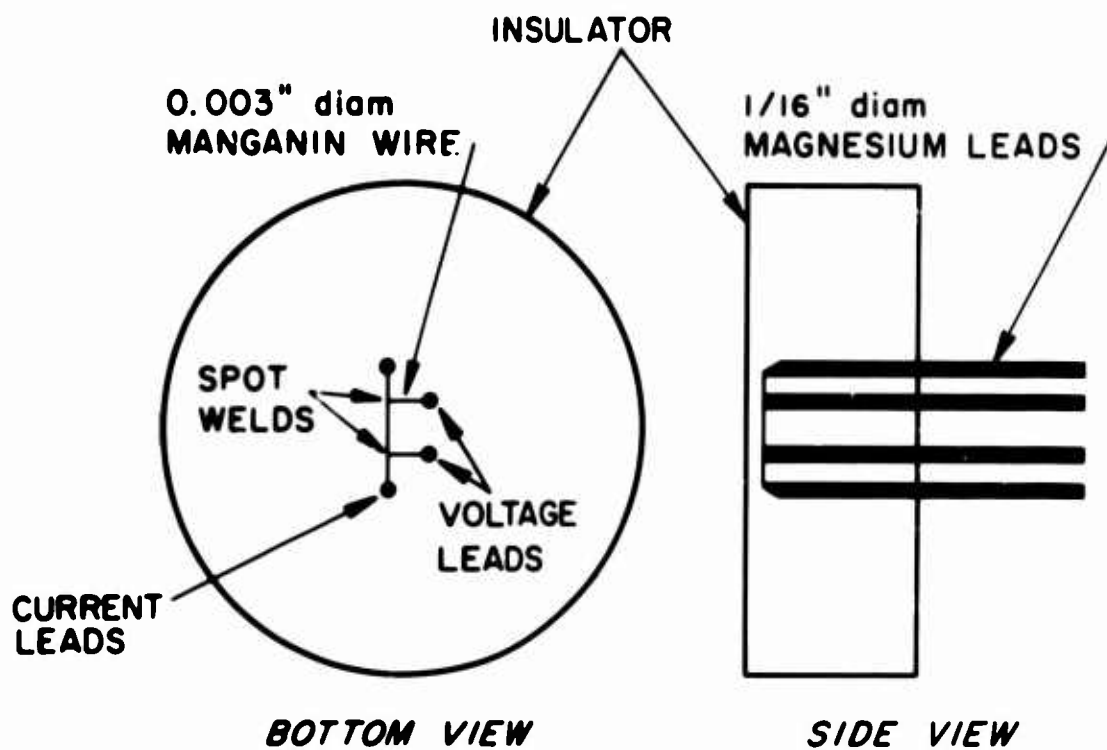
CURRENT
LEADS

BOTTOM VIEW
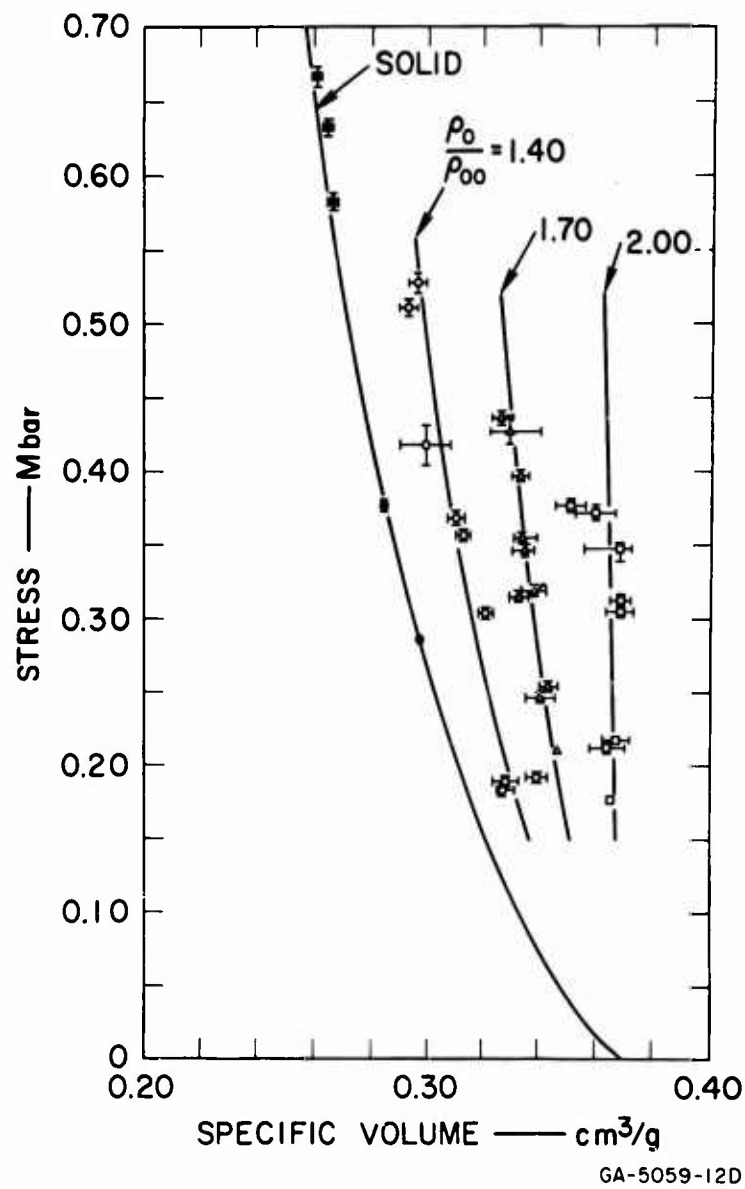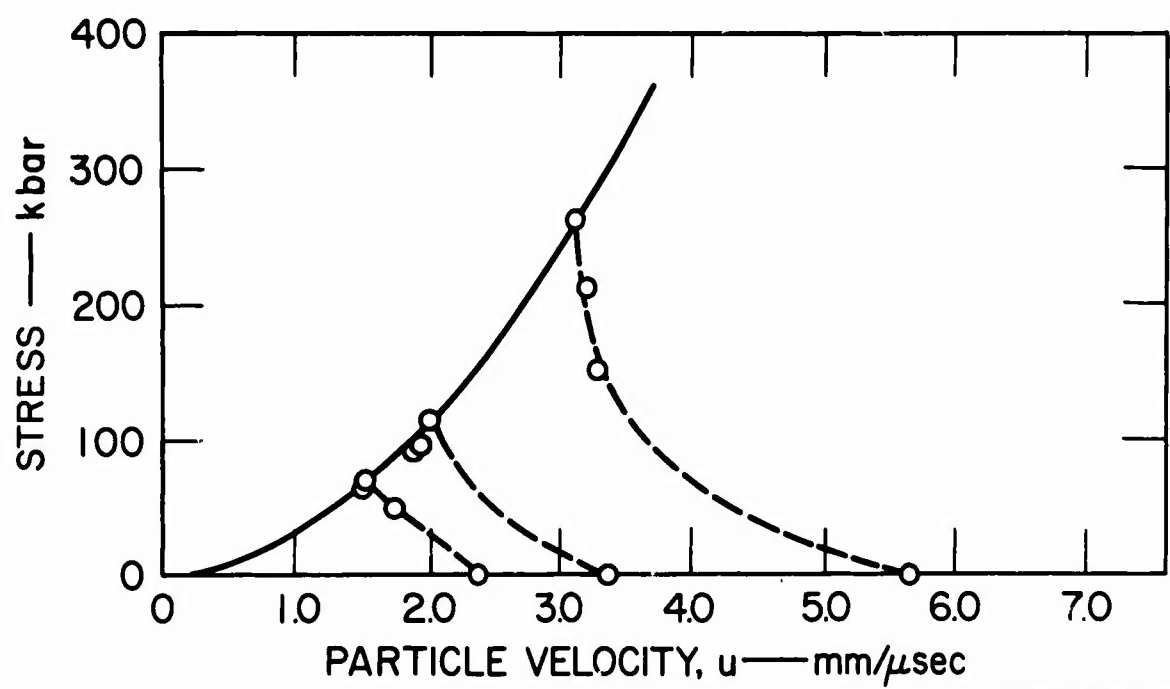
SIDE VIEW

FIGURE 4. MANGANIN WIRE STRESS GAGE CONFIGURATION

FIGURE 5. HUGONIOT CURVES FOR SOLID AND POROUS ALUMINUM

GA-5059-12D

GC-5059-21B

FIGURE 6. HUGONIOT AND RELEASE CURVES FOR DRY NTS PLAYA

GC-5059-22B
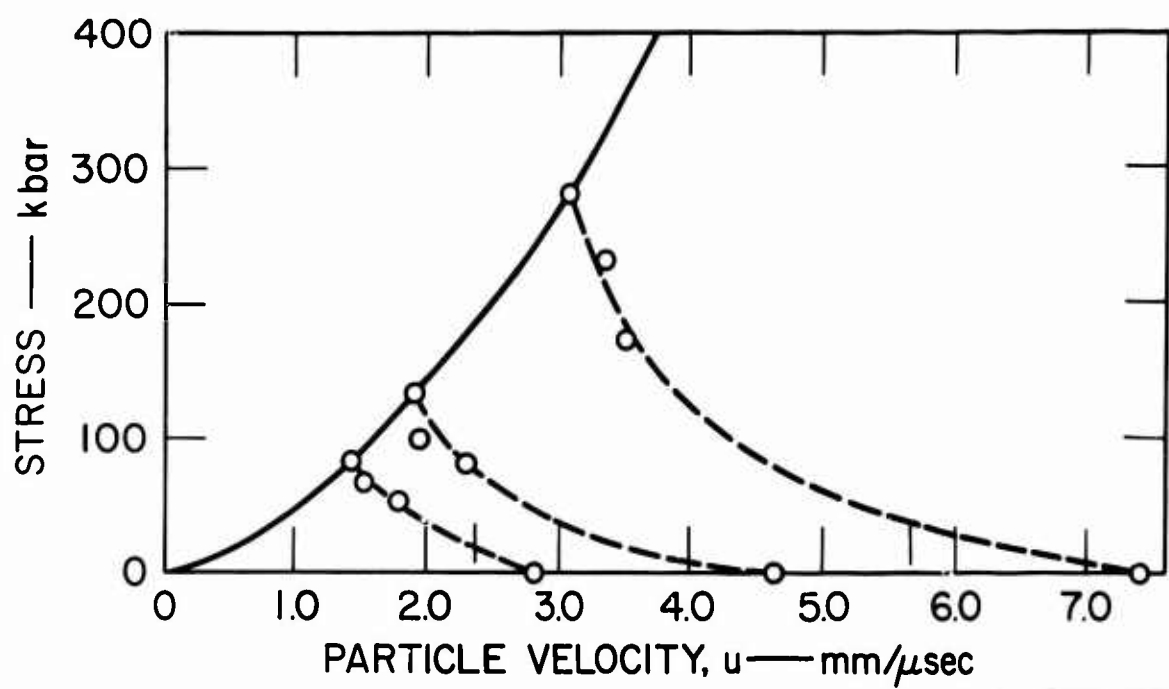
FIGURE 7.   HUGONIOT AND RELEASE CURVES FOR MOIST NTS PLAYA

(a) FORERUNNER DETAIL IN Al FOAM $\left(\frac{\rho_0}{\rho_{00}} = 1.28\right)$

(b) DOUBLE-WAVE PROFILE IN Al FOAM $\left(\frac{\rho_0}{\rho_{00}} = 1.28\right)$

(c) FORERUNNER DETAIL IN ATJ GRAPHITE $\left(\frac{\rho_0}{\rho_{00}} = 1.28\right)$

(d) DOUBLE-WAVE PROFILE IN ATJ GRAPHITE $\left(\frac{\rho_0}{\rho_{00}} = 1.28\right)$

(e) ATTENUATING DOUBLE-WAVE PROFILE IN ATJ GRAPHITE $\left(\frac{\rho_0}{\rho_{00}} = 1.28\right)$

(f) DOUBLE-WAVE PROFILE IN SOLID 2024-T351 Al

GP-5386-45C
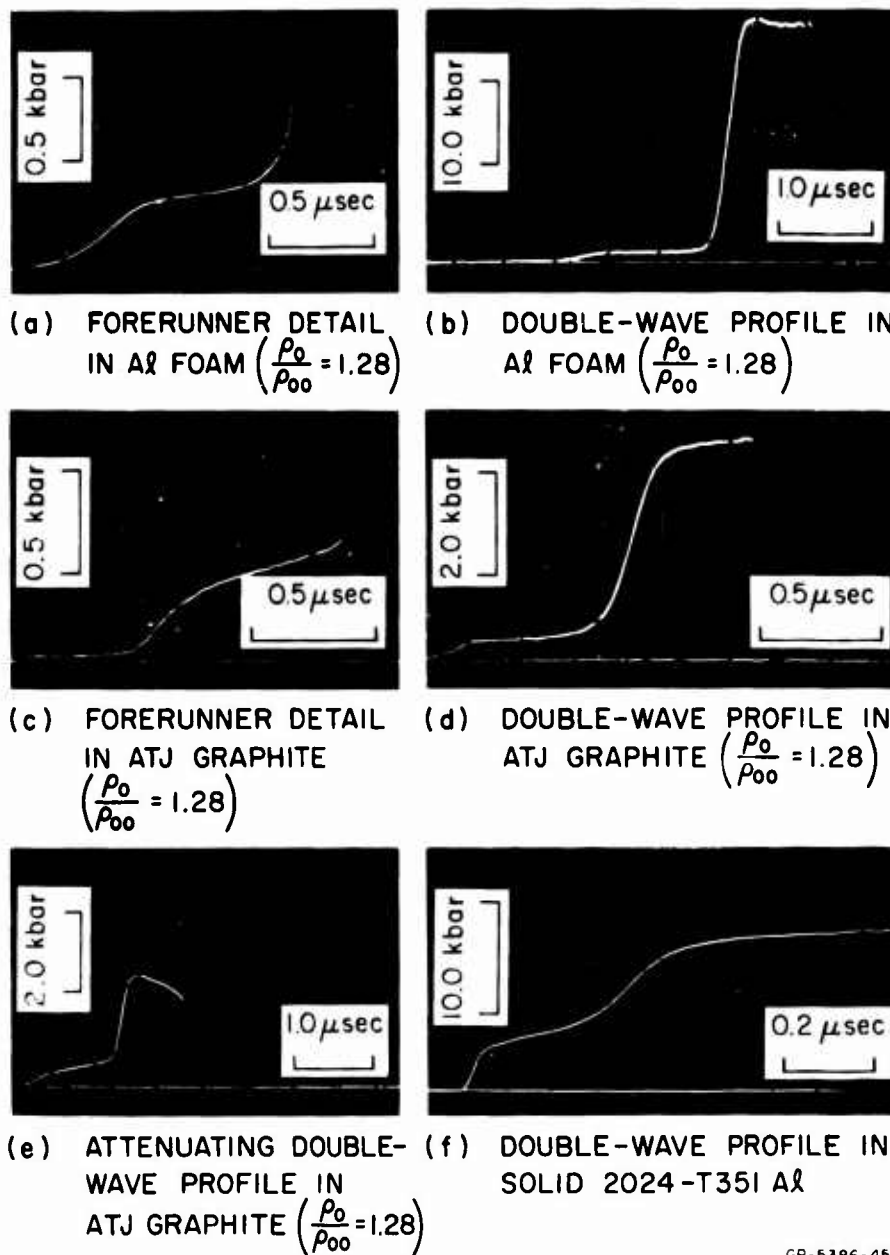
FIGURE 8. STRESS WAVE PROFILES IN POROUS ALUMINUM AND GRAPHITE
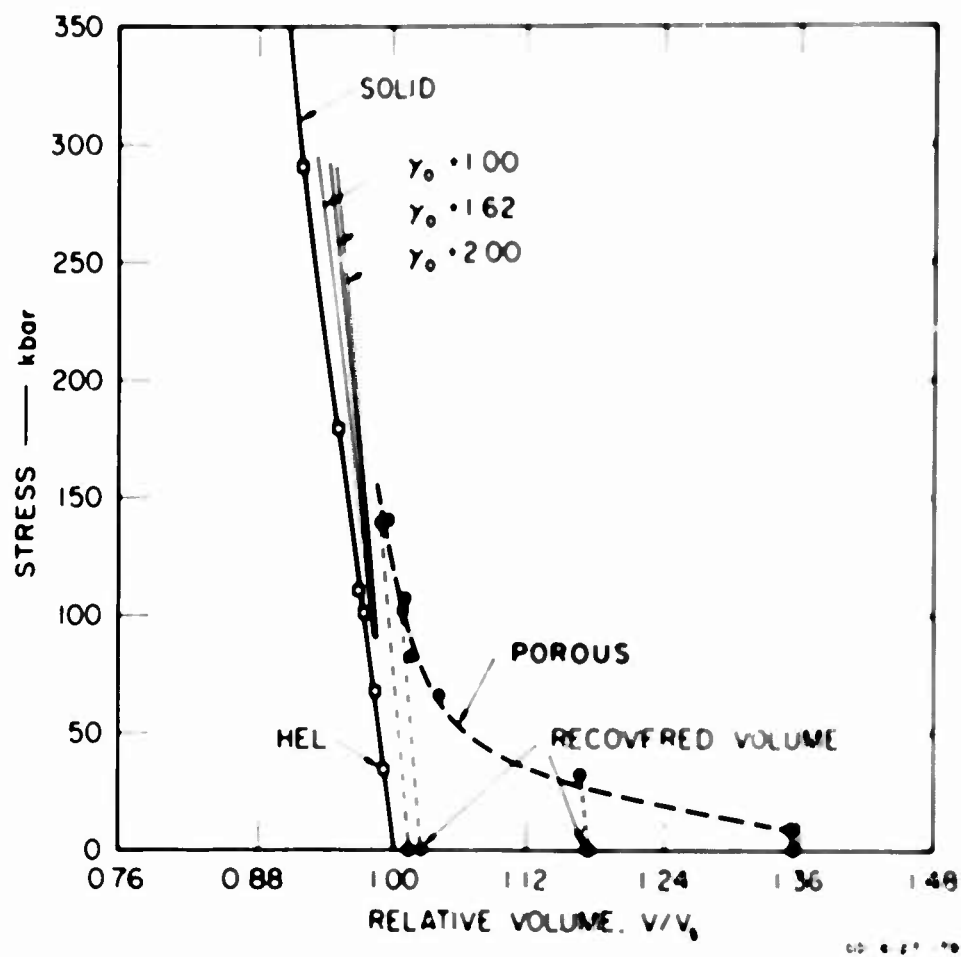
FIGURE 9. HUGONIOTS FOR SOLID AND POROUS TUNGSTEN
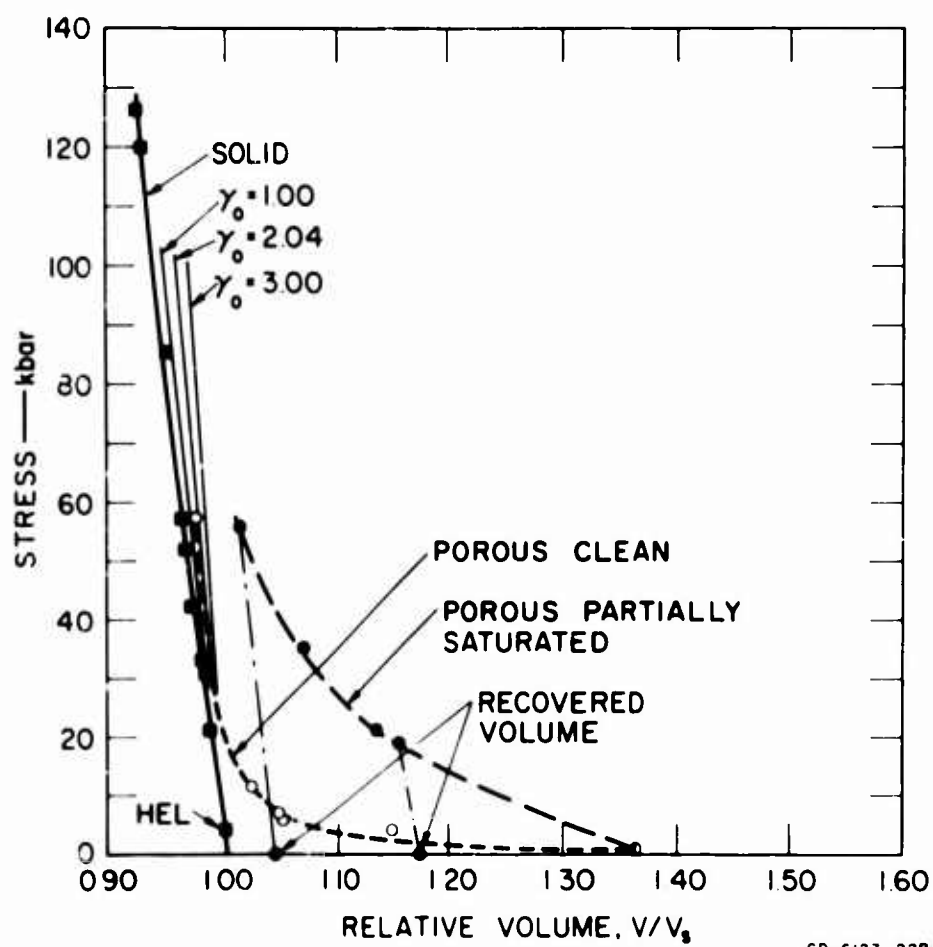
FIGURE 10. HUGONIOTS FOR SOLID AND POROUS COPPER
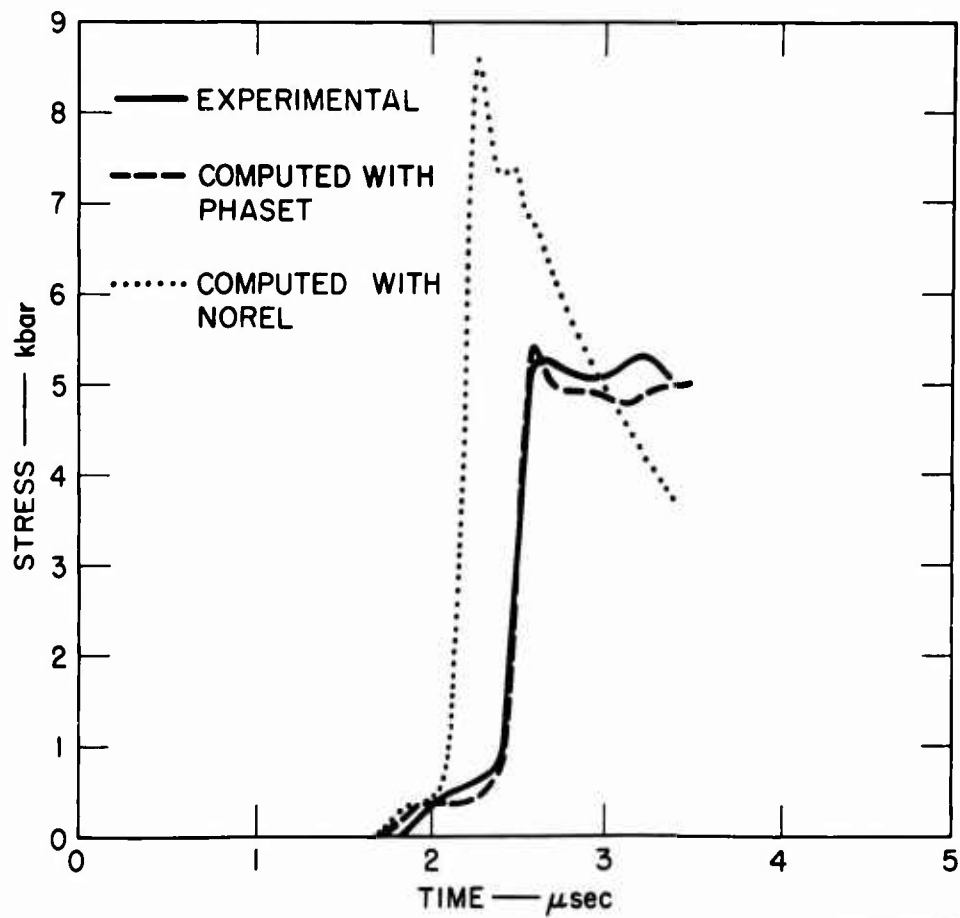
FIGURE 11. CALCULATED AND EXPERIMENTAL STRESS WAVE PROFILES IN (POROUS) ATJ GRAPHITE

29

FIGURE 12. STRESS WAVE PROFILE IN <100> SINGLE CRYSTAL SODIUM CHLORIDE

FIGURE 13. STRESS WAVE PROFILE IN <110> SINGLE CRYSTAL SODIUM CHLORIDE

31

FIGURE 14. STRESS WAVE PROFILE IN POLYCRYSTALLINE SODIUM CHLORIDE FROM
MISSISSIPPI TATUM SALT DOME

DYNAMIC PROPERTIES OF ROCKS

Thomas J. Ahrens
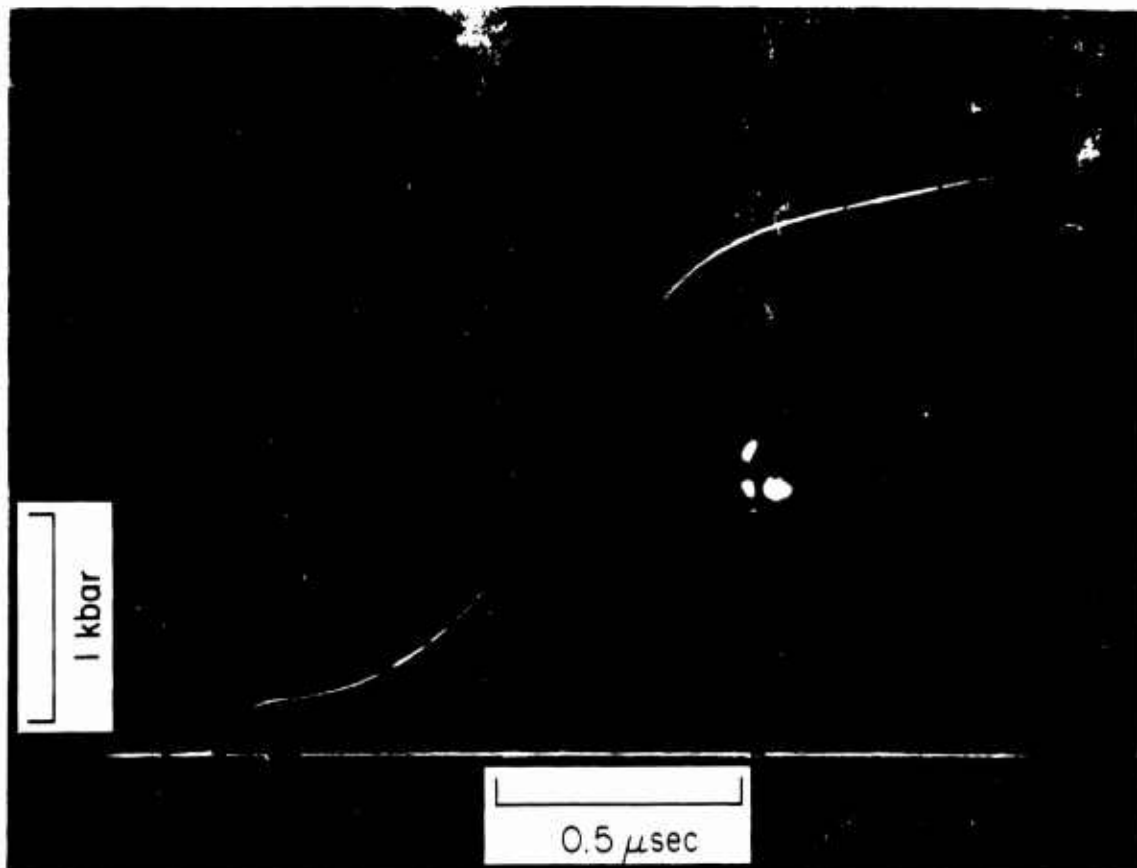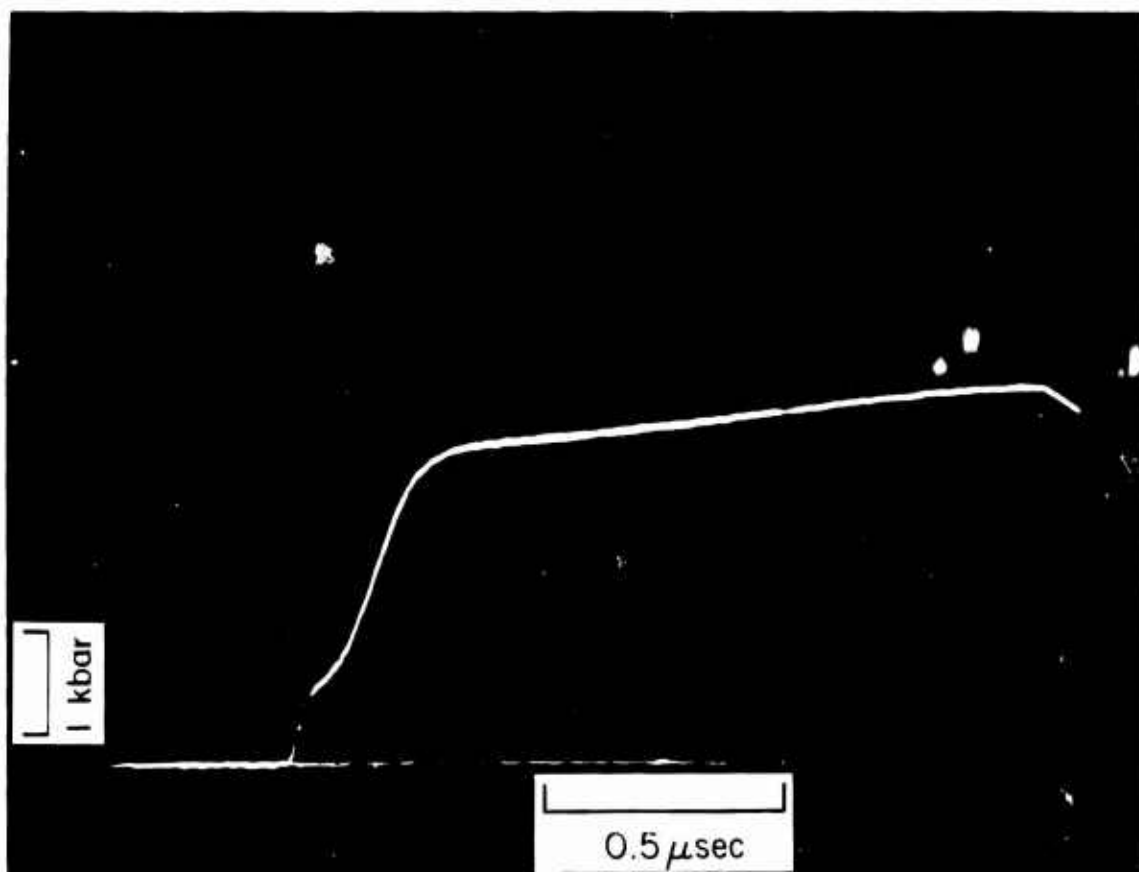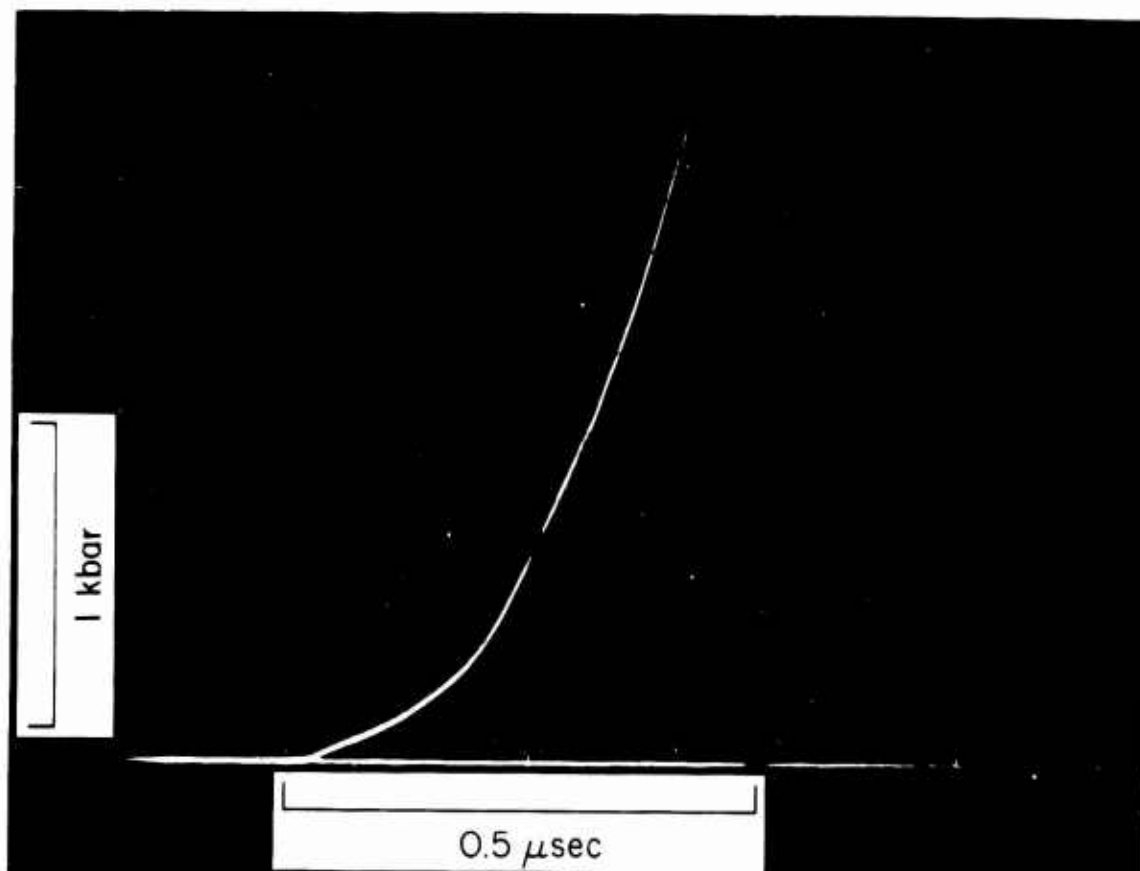California Institute of Technology
Seismological Laboratory
Pasadena, California

ABSTRACT

Rocks and rock-forming minerals exhibit dynamic yielding under one-dimensional shock stresses varying from several kbars to approximately 100 kbars. The dependence of the dynamic yield point, or the Hugoniot elastic limit, on mineralogy, porosity, and grain size in multimineralic rocks has not yet been studied. For shock stresses greater than the Hugoniot elastic limit, the achieved states lie along the deformational portion of the Hugoniot curve. Although non-porous rocks shocked to states along the deformational Hugoniot are often assumed to behave as fluids or elasto-plastic solids, few data as to their actual rheological behavior in this stress range are available.

In some materials, notably calcite and possibly carbonate bearing rocks and some silicates, the onset of dynamic yielding may be controlled by phase transitions. In virtually all the minerals which have been studied, including various forms of quartz, microcline, plagioclase, diopside, olivine, and calcite one or more phase transitions are indicated along the deformational Hugoniot either by anomalously high compression or the formation of multiple shock fronts. The crystallographic nature of these phase transitions are known in several cases from other high-pressure static or dynamic measurements. The available release adiabat data for quartz, fused quartz, and plagioclase all indicate that unloading from deformational shock states (at stresses as low as 150 kbars) takes place along steep pressure-volume curves. These release adiabats are thought to be characteristic of the high pressure phases, but elasto-plastic effects cannot be ruled out. Release curves from higher shock stresses (~300 kbar) indicate breakdown or melting of the high pressure products during pressure release.

DYNAMIC PROPERTIES OF ROCKS[*]

Thomas J. Ahrens
California Institute of Technology
Seismological Laboratory
Pasadena, California

INTRODUCTION

Equation-of-state data for rocks and minerals are needed for describing the intense stress-wave propagation and terminal response (cavity formation and cratering) in the vicinity of a nuclear or chemical explosion in an earth material. The constitutive equations (or in more general terms, equations of state) relate the dynamic stress, strain, and thermodynamic variables such as energy and temperature in a material. For purposes of predicting seismic coupling, shock wave equations of state and thermodynamic data are employed in calculations which are used to describe the wave propagation in the high pressure (hydrodynamic) and intermediate pressure (elasto-plastic) regime.

In the very high pressure, or hydrodynamic, regime which is in the immediate vicinity of the explosion, the magnitude of any one of the principal stresses (for example, the radial stress) will far exceed any possible stress difference which is supportable by the medium, and hence the medium is usually treated as a fluid. Experimental data for rocks and minerals indicate that phase transitions take place in nearly all of the common rock forming minerals and play an important role in determining the behavior of earth materials in this regime. In porous materials (e.g., soil) the initial density and moisture content is also known to be an important parameter in affecting the constitutive relations in this stress range. In terms of shock stress, the fluid or hydrodynamic regime is thought to extend from the multimegabar range down to hundreds and tens of kilobars for solids and porous materials, respectively. Equation-of-state data can presently be obtained by using explosive and hypervelocity impact techniques in only the lower portion of the hydrodynamic regime.

The transitional or elasto-plastic regime is thought to extend from a fraction of a kilobar to a few kilobars or hundreds of kilobars for porous and solid materials, respectively. It is within this stress regime that elastic and deformational shock fronts form and that dynamic yielding takes place. Materials after yielding may also exhibit finite strength effects in this pressure range. The latter behavior is often described in terms of an elasto-plastic model of the material. The porosity of an initially distended material is partially or completely irreversibly reduced as a result of propagation of stress waves in this pressure regime. The dynamic yielding properties of the medium determine both the stresses required to permanently

---

reduce material porosity, as well as the amplitude of the elastic precursor which forms over a certain range of shock stresses.

At a distance far enough from the source that the dynamic stress levels have decayed to the dynamic yield strength of the medium, an elastic type of behavior is usually assumed —as a first approximation —for the behavior of the material. In the elastic regime, the equation-of-state is usually obtained from laboratory low-amplitude shock, acoustic (ultrasonic), and quasi-static experiments. At the point at which the stress waves propagating from an explosion enter into the elastic regime, further description of propagation is usually obtained using seismological techniques (elastic ray and wave theory).

The measurement or calculation of the shock-wave propagation in vicinity of a nuclear explosion can thus be considered as a way of obtaining the source function input for the seismological problem of detection of clandestine underground nuclear explosions.

EQUATION-OF-STATE DATA FOR ROCKS AND MINERALS

A generalized Hugoniot curve, representative of several of the rocks and silicate minerals which have been studied to date, is shown in figure 1. Also indicated are the release adiabats which lead from states along the Hugoniot to states at zero pressure. While the Hugoniot curve represents the locus of shock states, the release adiabat represents the thermodynamic paths which material, that has been shocked to a high pressure state, follows upon being returned to zero pressure. Thus the unit mass in the vicinity of an explosion, upon being encompassed by a shock, achieves a thermodynamic state which corresponds to pressure and volume (P. V) along the Hugoniot. As this unit mass encounters the following rarefaction waves, the thermodynamic states which are followed lie along the release adiabat curve centered at P, V. Much of the shock wave research performed on rocks and minerals has been concerned with measuring Hugoniot and release adiabat curves of various earth materials. Experimental techniques used in measuring Hugoniot release adiabat states are given in general for solids by Doran [1], and with specific reference to rocks and minerals by Ahrens and Gregson [2]. Techniques for measuring release adiabats are discussed by Ahrens and Ruderman [3].

Hugoniot data for a wide variety of rocks and minerals, much of it to 1 megabar, have been tabulated in terms of the quantities usually measured, and shock particle velocity. Data reported to 1963 are tabulated by Rinehart [4], and a more recent tabulation which includes recent Soviet and Los Alamos results is given in the "Compendium of Shock Wave Data" (Van Thiel, [5]). A useful tabulation of Hugoniot data for basic rock forming minerals is given in the "Handbook of Physical Constants" (Clark, [6]). An extensive series of measurements of various rocks were recently reported by McQueen, Marsh and Fritz [7]. Hugoniot data for porous rocks and carbonates are given by Adadurov, et al. [8], Ahrens and Gregson [2], Flanigan [9] and Bass [10].

35

Hugoniot data for alluvium of various initial densities, moisture content, and in frozen and unfrozen states are available from 40 kbar to ~2 megabar from the work of Bass [10], Anderson, et al. [11], Anderson, [12], and Isbell [13]. Release adiabat data are available for only a few nonporous materials such as quartz, fused quartz and plagioclase. Because of their importance in the detection of underground testing and the prediction of response of protective construction, considerable release adiabat data are available for porous earth media such as dry and wet alluviums [11] and quartz sand in dry, wet and frozen form [12]. Some release adiabat data have been reported for wet and dry tuff by Weidermann and Curth [14], and Ahrens, et al. [15] in the 160 to 400 kbar range. At high pressure some data are also being obtained by Isbell [13].

The general shock behavior of rocks and minerals can be discussed in terms of the hypothetical Hugoniot and family of release adiabats sketched in figure 1. Shocks with amplitudes that lie between 0 and A, are associated with states lying along the elastic Hugoniot. The elastic Hugoniot represents the locus of shock states achieved by finite one-dimensional compression for which no internal rearrangement takes place at the shock front within the material. Elastic shock velocities for nonporous rocks and minerals are usually equal to or slightly greater than the corresponding longitudinal elastic wave velocity (table I). These data have been obtained mostly using the inclined mirror method for recording shock profiles in the sample [1]. In general, initial shock velocities which are equal to or slightly greater than corresponding longitudinal elastic wave velocities are observed in all of the silicates with the exception of diopside and augite, where the velocity of the initial shock is appreciably less than the longitudinal elastic wave velocity. In these cases, unless the elastic shock wave amplitudes are considerably lower than in other silicates, the failure to detect an elastic shock is not understood. In the case of material such as porous limestone, sandstone and halides, elastic shock amplitudes in the 0.5 to 10 kbar range have been measured. Virtually no data on the dynamic yielding of porous alluviums and tuff are yet available.

In general, the Hugoniot Elastic Limits (HEL) of 40 to 50 kbar observed in such solid rocks as HARDHAT granodiorite and Vacaville basalt are of the same magnitude as those of the constituent minerals of these rocks. The dependence of the elastic shock amplitude in porous rocks on porosity, mineralogy and grain size is largely unknown. Another effect, stress relaxation, in which the HEL is observed to vary with driving shock pressure, and shock propagation path length has been observed (Wackerle, [16]; Ahrens and Duvall, [17]) but has not yet been explored in most rock types and minerals. The relation of the normal stress in the direction of wave propagation (which, in general, is the only stress which is measured in shock experiments) to the other principal stresses for states along the deformational Hugoniot are needed in order to predict whether material which has been shocked to a deformational shock state will respond elastically or plastically to further compression or to pressure release. For shocks below the HEL, in the elastic regime, the longitudinal stress σ_x is related to the transverse stress σ_y, parallel to the wave front by

36

$$\sigma_y = \left(\frac{r}{1-r}\right)\sigma_x \qquad (1)$$

where r is the appropriate elastic Poisson's ratio. In contrast, in the very high pressure, hydrodynamic, regime where the stress differences reflecting material strength are small compared to σ_x, it is assumed that

$$\sigma_x \cong \sigma_y \qquad (2)$$

In the intermediate stress range the relation of σ_x to σ_y must be explicitly specified. To accomplish this, a rheological model of the material is often constructed. For example, it may be possible to describe the material as an elasto-plastic solid. In this case, at a given compression, the stress difference between the normal shock stress and the transverse stress is 2τ. It follows that material shocked to a state lying along the deformational Hugoniot will then support a shear stress of magnitude τ and the Hugoniot will be offset above the (isothermal) hydrostat by a stress

$$\Delta\sigma_x = \frac{4}{3}\tau \qquad (3)$$

Equation 3 neglects the effects of shock heating, which below several hundred kilobars are small for nonporous materials. In general, τ may be a function of such variables as stress, temperature and time. Sufficient low-pressure shock and hydrostatic compression data exist for a few geologic materials which allow meaningful examination of the magnitude of the stress offset between the Hugoniot and the hydrostat. Unfortunately in the few materials for which this stress offset can be examined it appears to vary widely, and seems to bear no simple re lation to the stress difference existing at the HEL. For example, the maximum shear stress in $CaCO_3$ in various directions, is at least as high along the deformation Hugoniot as it is at the HEL, and apparently increases with increasing shock stress (and hence with increasing mean stress), along the deformational Hugoniot (figure 2). This result is particularly striking in that generally calcite is thought to be a fairly weak mineral and that both the shock [2] and hydrostatic data [8] indicate that one or more phase transitions take place below 100 kbar. For SiO_2, below the onset of quartz-stishovite transition (McQueen, et al., [18]), the Hugoniot for both single crystal and polycrystalline materials appears to be offset slightly above the hydrostat (figure 3) while for polycrystalline Al_2O_3 (figure 4) the shock and hydrostatic results indicate that a shear stress comparable to that existing at the HEL is supported to perhaps 300 kbar. The results for MgO (figure 5) are striking; although this material has a fairly high Hugoniot elastic limit and under ordinary conditions appears to be a strong material, essentially no offset in stress of the deformational shock state is indicated by comparison with the shock data (McQueen and Marsh, [19]; Al'tshuler, et al., [20]; Ahrens, [21]) with hydrostatic data (Perez-Albuerne and Drickamer, [22]). *

*Recent analysis (22A) indicate that the shock data Fo MgO are consistent with a 15 kb offset of the Hugoniot curve above the hydrostat.

37

If elasto-plastic effects are ignored or, as in the case of MgO, appear to be absent, the adiabatic release paths from the final shock states A and B, AA' and BB'; indicate, that a zero-pressure volume that is greater than the initial volume is achieved upon pressure release. This effect is due to the shock heating arising from entropy gain of material encompassed by the shock front. The calculation of the pressure-volume-energy adiabats for materials which do not undergo phase transitions for minerals and rocks are similar to those for metals. Several calculational schemes are available for generating release adiabats when no phase transitions occur; for example one is described in Rice, et al., [23].

PHASE TRANSITIONS AND THEIR EFFECT ON THE HUGONIOT AND RELEASE ADIA-BATS. Virtually all the silicates, particularly rock forming minerals such as quartz, plagio-clase and olivine (forsterite and fayalite) as well as many of the oxides for example Fe_3O_4 and TiO_2, carbonates and halides which have been examined by shock-wave techniques, exhibit one or more phase transitions. In the silicates several of these phase transitions are related to the change in coordination of silicon from 4 oxygens to 6 oxygens in more closely packed structures. The zero pressure volumes for most of the silicates and many of the oxides in the high pressure, most highly coordinated state phases, are reduced by 20 to 50% ([7, 19]; Wang, [24]; Anderson and Kanamori, [25]). As a result of these phase changes, the Hugoniots of essentially all the rocks that contain the open structured silicates reflect phase changes taking place within their constituent minerals upon shock compression. For example the Hugoniot for Vacaville basalt containing olivine and augite (figure 6) or a granodiorite (fig-ure 7) containing predominately quartz and plagioclase will be affected by the phase changes in these minerals. In general the minerals within polymineralic rocks are not shocked to states along the Hugoniot of the component minerals when the rock itself undergoes shock compression. It appears from the results obtained by simply adding up Hugoniot volumes at a given pressure, on a mass fraction basis, for constituent minerals that the Hugoniot of an initially unknown nonporous rock may, however, be closely approximated. Calculations of the zero pressure densities of phases produced in various minerals and rocks [24, 25] shocked to high pressure [7, 19] indicate that at sufficiently high pressure, achieved densities are comparable, but in general not equal to, those which would be achieved by a mixture of oxides. Aside from the effect of phase transitions on the shape of the Hugoniot as indicated in figure 1, the release adiabats may be steeper than the Hugoniot. This generally indicates that some of the solid has transformed from, for example, Phase 1 to Phase 2 and that the Phase 2 material does not revert to Phase 1 upon release to zero pressure (figure 1). In a case of polycrystal-line quartz (figure 8), the Phase 2 material is believed to be stishovite ([18]; De Carli and Milton, [26]). In the case of plagioclase similar shaped release adiabats (Ahrens and Peter-son, [27]) indicate that this material is likely also to have a rutile-like modification similar to the high pressure form of $KAl_2Ge_3O_8$ (germinate orthoclase) prepared by Kume, et al. [28]). Recently Ringwood, et al. [29] reported that $KAl_2Ge_3O_8$ and $NaAl_2Ge_3O_8$ (analogous to ortho-clase and albite, respectively) transforms to the dense rutile-like hollandite structure.

Recovery experiments performed on some of the open structured silicates indicate that these high-pressure polymorphs are probably formed in only short range order ([26] Jamieson and De Carli, 1961).

Irreversible behavior is reflected also in the release adiabat data for polymineralic rocks containing the silicates such as granodiorite, tuff, playa, and quartz sand both dry, wet and in frozen condition. In the case of granodiorite the role of elasto-plastic behavior in determining the release adiabats is not clear.* For shock compression to high pressures (state D, figure 1) the Hugoniot of the mineral is shown as if it were transformed entirely to the denser phase, Phase 2. Upon pressure release (along DD') the denser high-pressure phase remains at zero pressure. For sufficiently high shock pressures, it is expected that upon release to zero pressure the shocked material will contain sufficient residual internal energy in the form of heat that the high-pressure phase is either entirely unstable, and becomes a melt, or perhaps turns into a gaseous phase. The melting behavior is indicated by the release adiabat curve EE'.

CONCLUSIONS

Although the dynamic yielding of single crystals of rock forming minerals is fairly well established, the dependence of the dynamic yield strength of polycrystalline and porous materials containing these minerals and their presumed dependence on porosity, mineralogy and grain size is poorly known. The rheologic properties of both porous and solid rocks which have been shocked above the HEL are also not well known. The shock pressures at which irreversible crushing of initially porous material as well as the extend to which solid rocks exhibit the elasto-plastic behavior is also not well established. The lack of knowledge of the elasto-plastic behavior for solid rocks probably has resulted from the fact that many of these materials also have phase transitions at very low shock pressures which tends to complicate their behavior. The nature of phase transitions in solids and porous rocks and particularly their effect on release adiabats of porous materials is not known sufficiently well so as to permit even approximate prediction.

RECOMMENDATIONS

With the goal of enhancing the national ability to predict the output signals from underground nuclear explosions, I think both the gathering of equation-of-state data and running code calculations should continue. The numerical description of stress-wave propagation should employ equations of state that take into account various models of dynamic yielding and rheological behavior, phase transitions, and various shaped release adiabats. Specifically the effect of varying the Hugoniot elastic limit, the magnitude of elasto-plastic effects and their dependence on porosity should be examined. The effects of reversible and irreversible phase changes and the effects of initially steep and then shallow release adiabats on shock propagation should be quantitatively investigated so as to ascertain which are the most important parameters for adequate prediction of seismic signals.

---

*Release adiabat data for granodiorite are reported in 26A.

ACKNOWLEDGMENTS

REFERENCES

1. D. G. Doran, "Measurements of Shock Pressures in Solids," in High Pressure Measurement, A. A. Giardini and E. C. Lloyd, eds., Butterworths, Washington, D. C., 1963.

2. T. J. Ahrens and V. G. Gregson, Jr., "Shock Compression of Crustal Rocks: Data for Quartz, Calcite, and Plagioclase Rocks," J. Geophys. Res., Vol. 69, 1964, pp. 4839-4874.

3. T. J. Ahrens and M. H. Ruderman, "Immersed-Foil Method for Measuring Shock Wave Profiles in Solids," J. Appl. Phys., Vol. 37, 1966, pp. 4758-4765.

4. J. S. Rinehart, Compilation of Dynamic Equation-of-State Data for Solids and Liquids, U. S. Naval Ordnance Test Station Report No. NOTS TP-3738, 1965.

5. M. Van Thiel, Compendium of Shock Wave Data, Report No. UCRL-50108, Vols. I and II, Lawrence Radiation Lab., Univ. of Calif., Livermore, Calif., 1966.

6. S. P. Clark, Jr., ed., Handbook of Physical Constants, Geol. Soc. Amer., New York, 1966.

7. R. G. McQueen, S. P. Marsh and J. N. Fritz, "Hugoniot Equation of State of Twelve Rocks," J. Geophys. Res., Vol. 72, 1967, pp. 4999-5036.

8. G. A. Adadurov, D. B. Balashov and A. N. Dremin, "A Study of the Volumetric Compressibility of Marble at High Pressures," Bull. Acad. Sci., USSR, Geophys. Ser., No. 5, 1961, pp. 463-466.

9. T. J. Flanagan, The Hugoniot Equation of State of Materials for the FERRIS WHEEL Program, Tech. Rept. SC-M-66-451, Sandia Corp., Albuquerque, N. M., 1966.

10. R. C. Bass, Additional Hugoniot Data for Geologic Materials, Rept. No. SC-RR-66-548, Sandia Corp., Albuquerque, N. M., 1966.

11. G. D. Anderson, et al., Investigation of the Equation of State of Porous Earth Media, AFWL TR65-146, Stanford Res. Inst., Stanford, Calif., 1965.

12. G. D. Anderson, The Equation of State of Ice and Composite Frozen Soil Material, Final Report on Proj. 6392, Stanford Res. Inst., Stanford, Calif., 1967.

13. W. Isbell, "Use of a Light Gas Gun in Studying Material Behavior at Megabar Pressures," in Symposium, High Dynamic Pressure, Paris, France, 1967, to be published.

14. A. H. Wiedermann and O. E. Curth, Shock Unloading Characteristics of Crushable Rocks, Rept. No. WL-TDR-64-52, IIT Res. Inst., Chicago, Ill., 1964.

15. T. J. Ahrens, T. J. Rosenberg and C. F. Petersen, Dynamic Properties of Rocks, Final Rept., Proj. 6273, Stanford Res. Inst., Stanford, Calif., 1968.

16. J. Wackerle, "Shock-Wave Compression of Quartz," J. Appl. Phys., Vol. 33, 1962, pp. 922-937.

17. T. J. Ahrens and G. E. Duvall, "Stress Relaxation Behind Elastic Shock Waves in Rocks," J. Geophys. Res., Vol. 71, 1966, pp. 4349-4360.

18. R. G. McQueen, J. N. Fritz and S. P. Marsh, "On the Equation of State of Stishovite," J. Geophys. Res., Vol. 68, 1963, pp. 2319-2322.

19. R. G. McQueen and S. P. Marsh, Reference No. 266 in F. Birch, "Compressibility; Elastic Constants," Handbook of Physical Constants, Rev. Ed., ed. by S. P. Clark, Jr., Geol. Soc. of Amer., New York, 1966.

20. L. V. Al'tshuler, R. F. Trunin and G. V. Simakov, "Shock Wave Compression of Periclase and Quartz and the Composition of the Earth's Lower Mantle," Acad. Sci., USSR, Phys. Solid Earth, No. 10, 1965, pp. 657-660.

21. T. J. Ahrens, "High-Pressure Electrical Behavior and Equation of State of Magnesium Oxide from Shock Wave Measurements," J. Appl. Phys., Vol. 37, 1966, pp. 2530-2541.

22. E. A. Perez-Albuerne and H. G. Drickamer, "Effect of High Pressures on the Compressibilities of Seven Crystals Having the NaCl or CsCl Structure," J. Chem. Phys., Vol. 43, 1965, pp. 1381-1387.

22A. T. J. Ahrens, D. L. Anderson and A. E. Ringwood, Equations of State and Crystal Structure of High Pressure Phases of Shocked Silicates and Oxides (to be published).

23. M. H. Rice, R. G. McQueen and J. M. Walsh, "Compression of Solids by Strong Shock Waves," in Solid State Physics, Vol. 6, F. Seitz and D. Turnbull, eds., Academic Press, New York, 1958, pp. 1-63.

24. C. Wang, "Phase Transitions in Rocks Under Shock Compression," Earth Plan. Sci. Letters, Vol. 3, 1967, pp. 107-113.

25. D. L. Anderson and H. Kanamori, Shock Wave Equations of State for Rocks and Minerals, 1968, Paper number 6 in this volume.

26. P. S. De Carli and D. J. Milton, "Stishovite: Synthesis by Shock Wave," Science, Vol. 147, 1965, pp. 144-145.

26A. C. F. Petersen, W. J. Murri, G. D. Anderson and C. F. Allen, Equation of State of Rocks, Stanford Research Institute, Interim Technical Report to Lawrence Radiation Laboratory, June 15, 1968.

27. T. J. Ahrens and C. F. Peterson, "Shock Compression and Adiabatic Release of Feldspar," Proc. Conf. on Shock Metamorphism, 1968, in press.

28. S. Kume, T. Matsumoto and M. Koizumi, "Dense Form of Germanate Orthoclase (KA1 Ge_3O_8)," J. Geophys. Res., Vol. 71, 1966, pp. 4999-5000.

29. A. E. Ringwood, A. F. Reid and A. D. Wadsley, "High Pressure Transformation of Alkali Aluminasilicates and Aluminogermanates," Earth Plan. Sci. Letters, Vol. 3, 1967, pp. 38-10.

30. T. J. Ahrens and R. K. Linde, "The Response of Brittle Solids to Shock Compression," Behavior of Dense Media Under High Dynamic Pressure, Int. Union Theoretical and Applied Mech., 1968, to be published.

31. R. K. Linde and P. S. De Carli, "Polymorphic Behavior of Titania Under Dynamic Loading," 1968, to be published

32. O. L. Anderson and R. C. Liebermann, Sound Velocities in Rocks and Minerals, VESIAC State-of-the-Art Rept. 7885-4-X, Willow Run Labs, Univ. of Mich., 1966.

33. G. R. Fowles, Shock Wave Compression of Quartz, Tech. Rept. 003-61, Stanford Res. Inst., Stanford, Calif., 1961.

34. L. Peselnick and R. A. Robie, "Elastic Constants of Calcite," J. Appl. Phys., Vol. 34, 1963, pp. 2494-2495.

35. T. J. Ahrens, W. H. Gust and E. B. Royce, "Material Strength Effect in the Shock Compression of Alumina," 1967, to be published.

36. O. L. Anderson and E. Schreiber, <u>Measurement of P and S Sound Velocities Under Pressure on Laboratory Models of the Earth's Mantle</u>, Final Report, Contract AF-AFOSR 49(638)-1355, Lamont Geol. Observ., Columbia Univ., Palisades, N. Y., 1965.

37. K. S. Alexandrov and T. V. Ryzhova, "Elastic Properties of Rock Forming Minerals: III, Feldspars," <u>Bull. Acad. Sci., USSR, Geophys. Ser.</u>, No. 2, 1962, pp. 129-131.

38. Birch, F., "Elastic Constants in Rutile—A Correction to a Paper by R. K. Verma, 'Elasticity of Some High-Density Crystals'," <u>J. Geophys. Res.</u>, Vol. 65, 1960, pp. 3855-3856.

39. Bridgman, P. W., "Rough Compres ons of 177 Substances to 40,000 KG/CM," <u>Proc. Am. Acad. Arts and Sciences</u>, Vol. 76, 1948, pp. 71-87.

40. Hart, M. V. and H. G. Drickamer, "Effect of High Pressure on the Lattice Parameters of Al_2O_3," <u>J. Chem. Phys.</u>, Vol. 43, 1965, pp. 2265-2266.

41. McWhan, D. B., "Linear Compression of α-Quartz to 150 kbar," <u>J. Appl. Phys.</u>, Vol. 38, 1967, pp. 347-352.

42. Bridgman, P. W., "The Compression of 39 Substances to 100,000 KG/CM^2," <u>Proc. Am. Acad. Arts and Sciences</u>, Vol. 76, 1948, pp. 55-70.

TABLE I. HUGONIOT ELASTIC LIMITS (HEL), ROCKS AND MINERALS

Material		Initial Density (g/cm^3)	Elastic Shock Velocity $(mm/\mu sec)$	Longitudinal Elastic Velocity $(mm/\mu sec)$	Hugoniot Elastic Limit $(kbar)$
TiO_2	[100]	4.25	~8.7[a]	8.00[b]	~70[c]
TiO_2	[001]	4.25	~10.7[a]	10.65[b]	~100[c]
MgO	[100]	3.576	8.91, 9.19[d]	8.83 - 9.13[e]	37.2[d]
MgO	[100]	3.576	10.07[d]	8.83 - 9.13[e]	89 ± 10[d]
SiO_2	[$\bar{1}2\bar{1}0$]	2.657	5.95[f]	5.74[f]	60[f]
SiO_2	[$10\bar{1}0$]	2.657	6.13[f]	5.99[f]	85[f]
SiO_2	[0001]	2.657	7.28[f]	6.37[f]	148[f]
$CaCO_3$	[$\bar{1}2\bar{1}0$]	2.71	7.32[g]	7.299[h]	22[g]
$CaCO_3$	[$10\bar{1}0$]	2.71	7.45[i]	7.346[h]	24[g]
$CaCO_3$	[0001]	2.71	5.55[g]	5.535[h]	19[g]
$CaCO_3$	[1011]	2.71	7.05[g]	7.237[h]	19[g]
Hot Pressed, TiO_2		4.24	9.3[a]	9.15 - 9.26[e]	75[c]
		4.18	8.9 - 9.3[a]	''	55[c]
		4.07	8.7 - 9.0[a]	''	33[c]
SiO_2					
Arkansas novaculite		2.628	6.15[j]	6.057 - 6.07[e]	70[j]
Eureka quartzite		2.629	5.96[j]	6.057 - 6.07[e]	70[j]
Sioux quartzite		2.626	5.95[j]	6.057 - 6.07[e]	48[j]
Al_2O_3, (Lucalox)		3.98	10.88 - 10.98[k]	10.845[l]	112[k]
Twin Sisters Dunite		3.289 - 3.315[l]	8.45 - 8.72[l]	8.32 - 8.42[m]	76 - 93[l]
Microcline [001]		2.55 - 2.56	~.09 - 7.56[l]	6.95[n]	79 - 85[l]
Muskwa Lake Oligoclase		3.63 - 3.64	6.8 - 7.6[o]	6.88[n]	37 - 56[o]
Polycrystalline Augite		3.47 - 3.48	7.3 - 8.0[l]	8.2 - 8.3[l]	33 - 71[l]
Polycrystalline Diopside		3.23 - 3.28	7.9 - 8.0[l]	7.3 - 10.0[l]	69 - 94[l]
Diopside [001]		3.2	6.6[l]	5.8[l]	42[l]

a. Ahrens and Linde [30].

b. Velocities and moduli from Birch, [38] Clark [6].

c. Linde and De Carli [31].
d. Ahrens [21].

e. From moduli compiled in Anderson and Liebermann [32].

f. Fowles [33].

g. Ahrens and Gregson [2].

h. Peselnick and Robie [34].

i. Ahrens, et al. [35].

j. Ahrens and Duvall [17].

k. Ahrens, et al. [15].

l. Anderson and Schreiber [36].

m. Clark [6], (Data by Birch, 4 - 10 kbar).

n. Alexsandrov and Rhyzova [37].
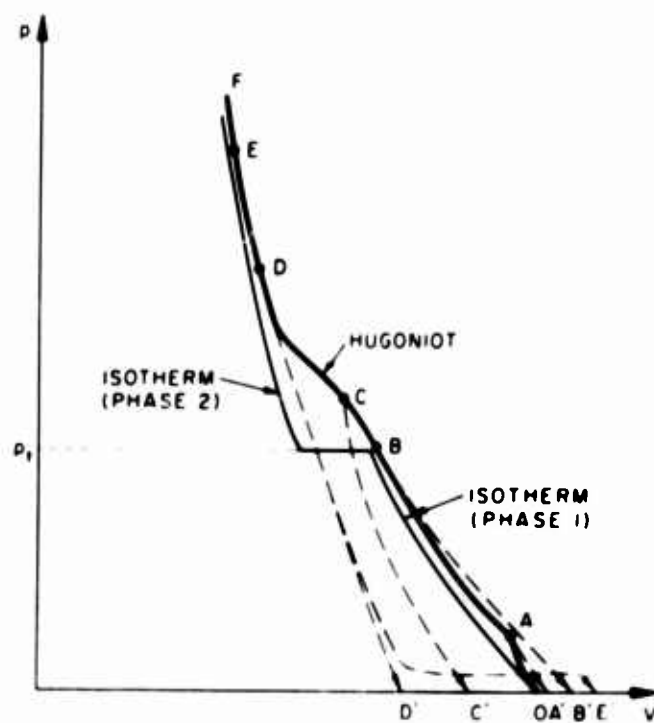
o. Ahrens and Peterson [27].

Figure 1. Hypothetical Hugoniot, isotherm, and release adiabat curves
for a silicate. Rarefaction from Hugoniot states A, B, C, D,
and E results in zero-pressure states A', B', C', D' and E'.
Isothermally compressed material will transform at pressure,
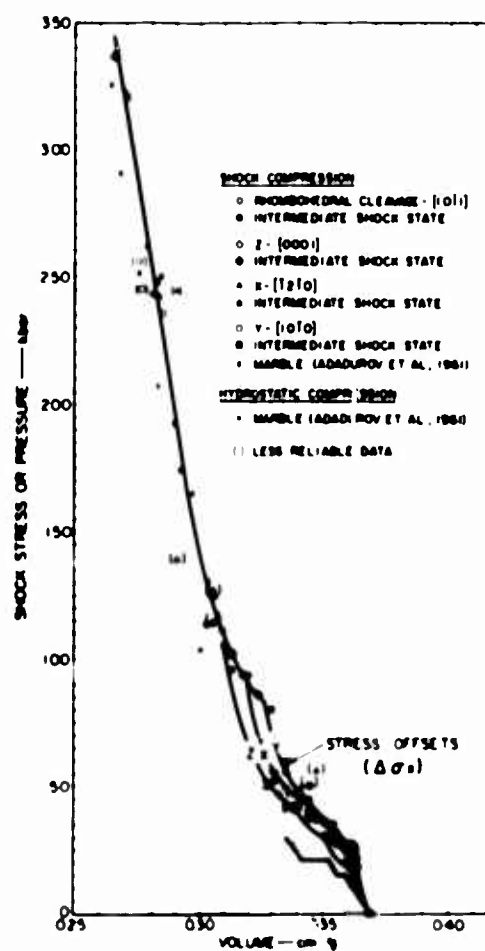p_t, from phase 1 to phase 2.

Figure 2. Shock Stress or Hydrostatic Pressure Versus Volume for Calcite (from Ahrens and Linde, 1968).
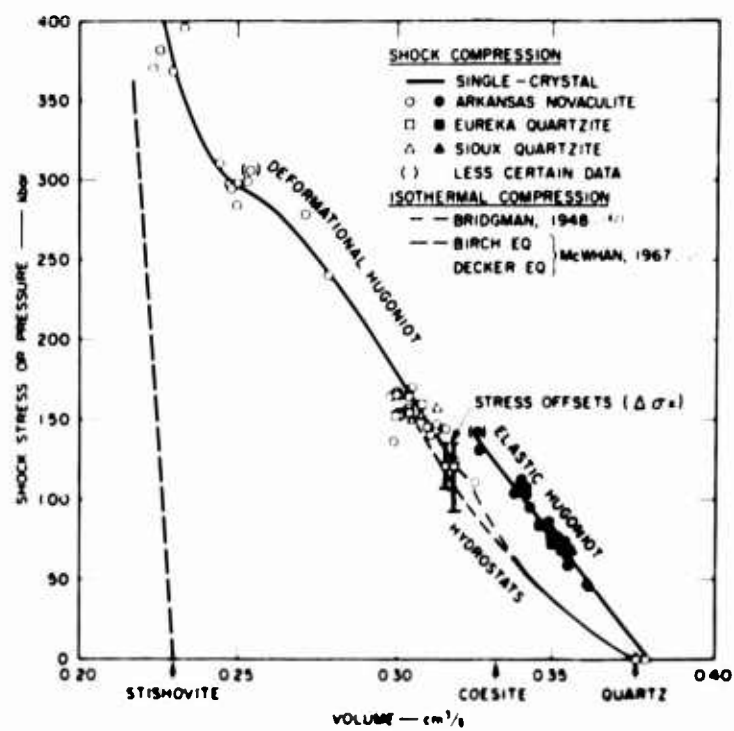
46

Figure 3. Shock stress or hydrostatic pressure versus volume for quartz (from Ahrens and Linde, 1968).
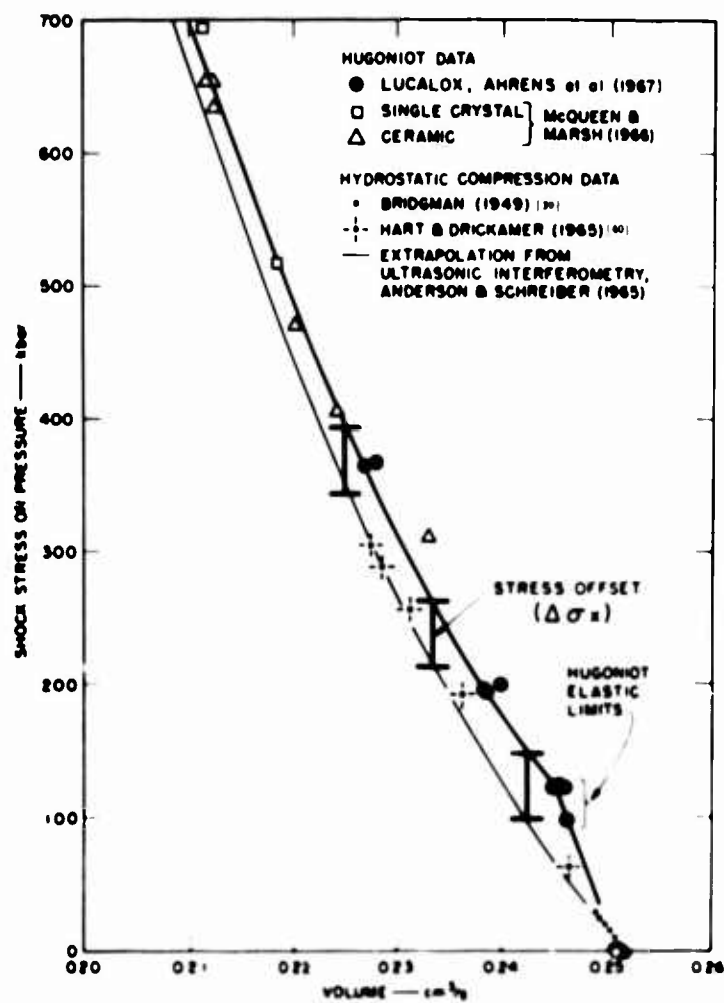
Figure 4. Shock stress or hydrostatic pressure versus volume for alumina
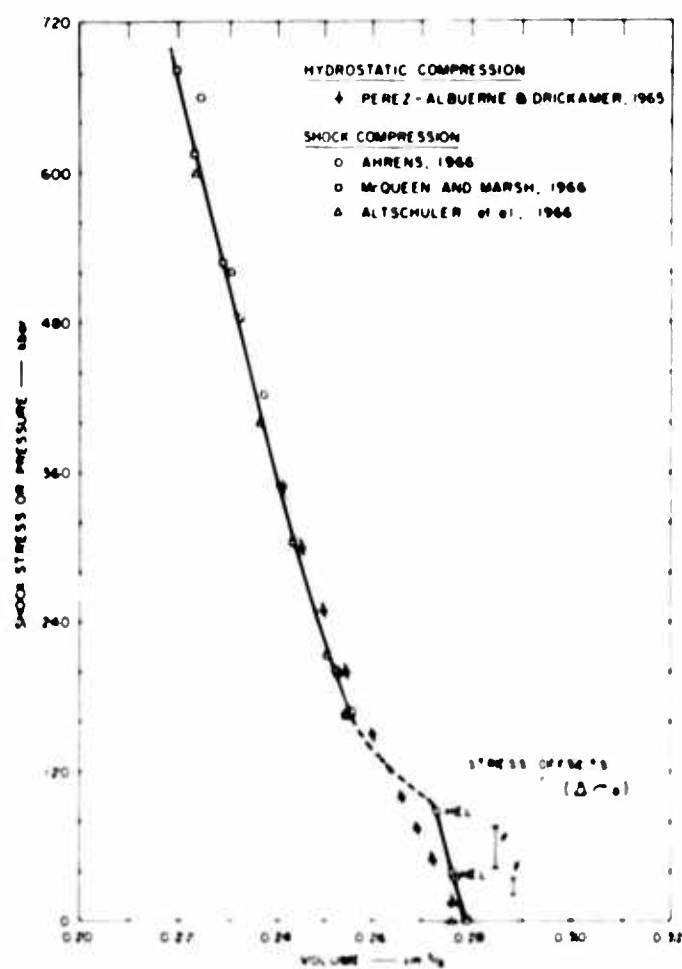(from Ahrens and Linde, 1968).

Figure 5. Shock stress or hydrostatic pressure versus volume for MgO (from Ahrens and Linde, 1968).

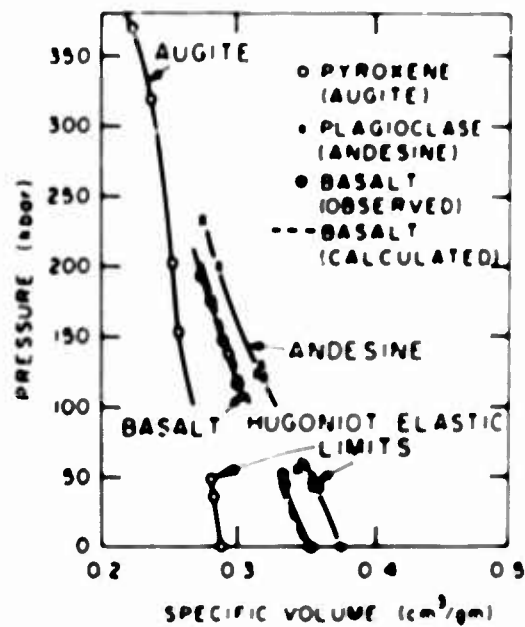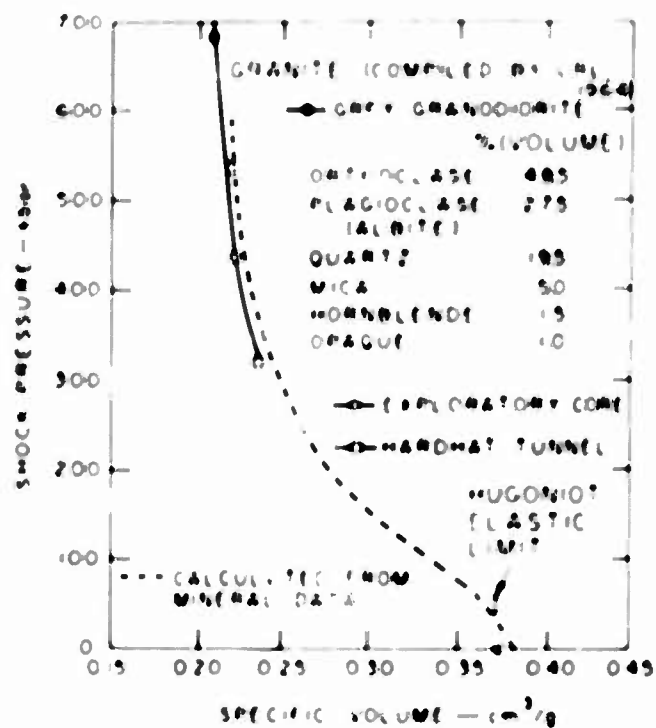Figure 6. Hugoniot curve for Vacaville basalt calculated from augite and anorthosite Hugoniots.

Figure 1. Suspended curve for Hardhat granodiorite calculated from constituent mineral data.
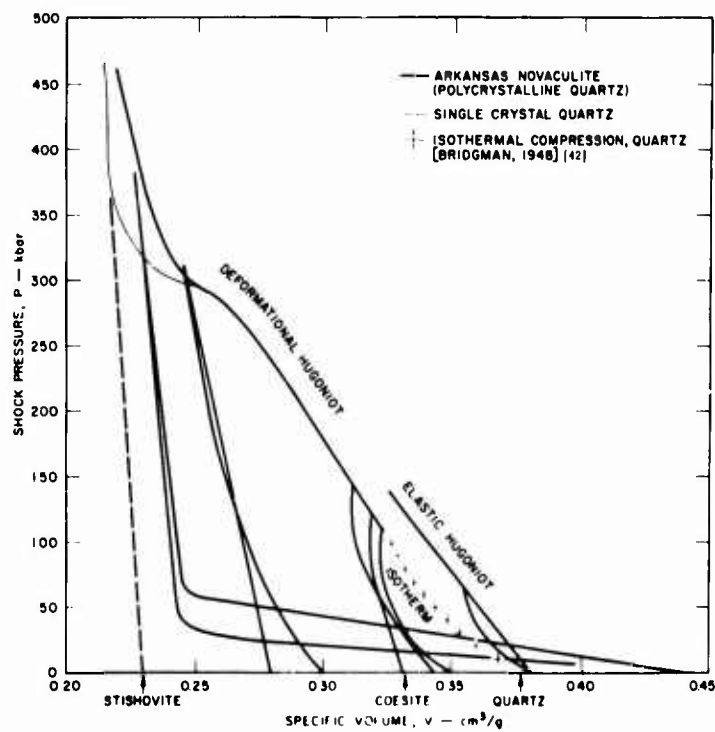
Figure 8. Release adiabats for polycrystalline quartz (from Ahrens et al, 1966).

5
SHOCK-WAVE DATA AND EQUATIONS OF STATE

R. McQueen
Los Alamos Scientific Laboratory
University of California
Los Alamos, New Mexico

INTRODUCTION

Since it is obviously impossible to measure the equation of state of all the materials of interest for various military and scientific applications, a study has been undertaken to measure the Hugoniots of a few selected materials and to compare these Hugoniots with ones computed from the known equation of state of their constituents. Such materials fall into two large categories: those in which there is no chemical interaction of the constituents, that is simple mixtures; and those in which there is a chemical reaction or bonding of the constituents on an atomic scale. In the case of simple mixtures probably the most common naturally occurring examples are rocks. Other simple mixtures are synthetic materials such as the various plastic bonded solids and the commonly available Elkonites (mixtures of good electrically conducting materials, copper and silver, with very hard materials, tungsten, molybdenum and tungsten carbide). For these materials there is no problem associated with the bonding and crystal structure. However, because these are heterogeneous materials the problem of how hydrodynamic and thermodynamic equilibrium behind the shock wave are obtained is more complicated. Since the shock wave not only sees particles of different shock impedance but travels through these particles at different velocities it is apparent that the specimens under investigation must be made of very small particles if equilibrium conditions are to be obtained in the short times available, particularly the thermal equilibrium.

We have included alloys as a separate class for two reasons. One is that a large number of so-called alloys are actually simple mixtures. The other reason is that metallic bonding produces a much smaller volume and energy change from ideal mixing than do ionic and covalent bonding. It then becomes of interest to see how well the theory of ideal mixtures can account for the Hugoniot curves of various alloys.

For a large class of compounds simple mixing models are obviously inadequate and it would be far better to attempt to derive a high-pressure equation of state by other means. For example if the equation of state of an ionic solid were desired it would probably be far better to use the known bonding energies and some assumed potential rather than to attempt to mix the two components. There are some types of compounds that are somewhat amenable to mixing calculations. For example, to a certain extent the silicates can be considered to

be made up of mixtures of their basic neutral oxide components. Hence, if the equation of state of the oxides are known, the similarities that exist in the bonding suggest that simple mixing models may be adequate for most purposes.

CALCULATIONAL MODEL

There are several models that could be used in an attempt to predict the Hugoniots of mixtures from the known equation of state of their components. One approach might be to consider the mixture as a laminated structure and to compute an average shock velocity based on the shock transit time through the various layers. Such a method is appealing in that one is attempting to compute the quantity that is subject to direct measurement. Another approach would be to interpolate pressure-volume Hugoniots at constant pressure on the basis of the volume occupied by the various components. This method appears to be a bit more straight-forward and is more or less the method being pursued here with minor modifications.

It is clear that for a pure mixture the isothermal equation of state measured in a high-pressure static device should be precisely that obtained by the addition of the volumes occupied by the various components at any pressure.

For a Hugoniot curve, this simple mixing is slightly complicated by the different temperature increases in different constituents resulting from pressure increases produced by a shock. However, this is a small effect compared to the compressional energy stored in each of the components by the shock. The change in pressure resulting from the redistribution of energy because of these temperature differences is less than the uncertainties in pressure changes produced by our limited knowledge of the behavior of the Grüneisen parameter at high pressures. Accordingly, a simplified method of calculating the shock pressure of a mixture is used. A "zero-Kelvin" curve is calculated for each component. For the present application we have used a constant specific heat, C_v, and a constant value for $(\partial E/\partial P)_V$. Once the $P = 0$ zero-Kelvin density is obtained the rest of the curve is calculated by simultaneously satisfying the thermodynamic law

$$dE = -PdV \qquad (dS = 0)$$

the experimental Hugoniot and the Grüneisen parameter. The specific heat, of course, vanishes as T goes to zero, but we only make a small error (small relative to the uncertainties in P in the Hugoniot data) in the low T range of this extrapolation. Since we go down and up in temperature in the same way, the "zero-Kelvin" curve may be regarded as an artifice of the calculation, although the resulting $P - \rho$ curves will actually be quite near the real zero-Kelvin curve. A zero-Kelvin curve may now be obtained from the mixture from the following equations:

$$1/\rho_k = V_k = \Sigma m_i V_i(P)$$

$$E_k = \Sigma m_i E_i(P)$$

54

where ρ, V and E are the density, specific volume and specific energy of the mixture on the zero-Kelvin curve; m_i are the mass fraction of the components in the mixture; and V_i and E_i are the volume and energy for the ith component as a function of pressure along the zero-Kelvin curve. To extend the energy function up in pressure at constant volume we need the Grüneisen parameter of the mixture, or equivalently, the quantity $(\partial E/\partial P)_v$ V/γ. To center the Hugoniot of the mixture at some temperature other than zero, we need the specific heat at constant volume of the mixture. For these two quantities we use the equations:

$$V/\gamma = \Sigma m_i (V/\gamma)_i$$

$$C_v = \Sigma m_i C_{vi}$$

We now have an E(P, V) relation for the mixture given by

$$E = E_k + (P - P_k) \cdot V/\gamma$$

This function is used in the Rankine-Hugoniot relationship to calculate the Hugoniot of the mixture. A slight error is introduced in this procedure because it is necessary to compute pressure offsets at a constant volume of the mixture while the γ's used in this calculation have been computed at constant pressure from constant volumes of the components. This is not considered to be a limiting defect since the values of γ at high pressure are not accurately known.

CALCULATION OF ELASTIC WAVE VELOCITIES OF MIXTURES

In addition to measuring and calculating the Hugoniots of mixtures there is another quantity that is subject to experimental investigation. This is the propagation of elastic waves in a heterogeneous substance. As before it is desired to sum the extensive quantities since these are additive for the mixture.

The purely extensive quantity most closely connected with the bulk sound speed, C_B, is $-\partial V/\partial P)_T$. It is this quantity which is additive for mixtures provided the intensive variables P and T have come to equilibrium. However, in a sound wave, whether or not temperature equilibrium is achieved between different components of the mixture depends on grain size. If no heat flow occurs, individual "grains" are compressed and released isentropically. Then the extensive quantity S, the entropy, is constant, and the expression $-\partial V/\partial P)_S = 1/\rho^2 C^2$ is linearly additive; that is, the function should be a linear function of the mass fractions m_i, and therefore a linear function of the specific volume $(1/\rho)$ of the mixture.

The same arguments apply with respect to the longitudinal wave velocity, C_L, which lead to the result that $-\partial L/\partial T)_S = 1/\rho^2 C_L^2$ should be a linear function of the mass fractions. Here L is the length/unit mass and T the appropriate tension. However, among the class of extensive functions some are more extensive than others. In contrast to the bulk compression we do not expect this function to be exactly linear. It would be if the phases were stacked up in series, but they can occur in parallel. If they are in parallel, the stiffer member of the system

55

can take up more of the tension and $\partial L/\partial T$ will decrease. This would be an interesting feature to check in some properly prepared specimens where one could vary the orientation of some laminated materials, or perhaps, some fiber imbedded materials.

Since shearing motions do not involve extensive quantities particularly, these arguments say nothing about the shear waves directly, but its variation is now specified by the isotropic relationship

$$C_B^2 = C_L^2 - 4/3 \, C_S^2$$

where C_S is the elastic shear wave velocity. Thus in principle it should be possible to estimate the value of the elastic moduli of an isotropic mixture from its constituents.

If these thermodynamic arguments are to be applicable to a material, it must be homogeneous for distances larger than a fraction of the wave length of the elastic wave and heterogeneous on an atomic scale (i.e., chemical reactions should not drastically change the component materials). A material can have voids, have a soft component in a hard matrix, or vice versa. It can be fibred, layered, have preferred orientations of highly anisotropic materials, or a host of other peculiarities that cause it to deviate from results predicted by the simple thermodynamic mixing we have used here. Strong shocks tend to get rid of voids and structure (at least make it less important) and tend to make materials more isotropic. We expect these difficulties to plague a zero-pressure sound speed measurement much more than the Hugoniot data.

As an alternative to the ideal mixing, we consider a layered model. The time for a wave to travel through many layers is simply the sum of the individual times for each layer. Hence the reciprocal average velocity is the sum of the reciprocal component velocities, weighted by the volume fraction of the component. For a two component system, with m the mass fraction of component 2, this leads to

$$\frac{1}{C} = \frac{1}{(1 - m)\rho_1 + m\rho_2} \left[\frac{(1 - m)\rho_1}{C_1} + \frac{m\rho_2}{C_2} \right]$$

Mixing generally tends to lower velocities. The layered structure permits each component to transmit the wave as fast as each component can. The above result usually serves as an upper bound for expected values of measured velocities.

EXPERIMENTAL RESULTS

The shock-wave experimental techniques used here have most recently been described in an article on shock wave compression of rocks [1]. Incidently the same calculational procedures described in that report are used here. The results of the experimental investigation are grouped into the large categories of mixtures, compounds and mixtures of compounds. No work on alloys, other than the Au-Ge alloys which actually are almost perfect simple mixtures, is presented here.

A. The Zero-Pressure Sound Velocities and Hugoniots of Some Elkonites

Elkonite is the name of a family of metal composites manufactured by P. R. Mallory and Co. Inc. They are composed of a sintered metal with a high melting point (W, WC, or Mo) into which has been infiltrated a metal having a lower melting point (Ag or Cu). The particular Elkonites (and their composition) which were used in this study are shown in table I.

TABLE I. ELKONITE COMPOSITIONS

| TRADE | $\rho_0(gm/cm^3)$ | | Weight per cent of | | | |
NAME	(meas.)	(calc.)	Ag	Cu	W	WC
20S	15.21	15.67	27.6	-	72.4	-
35S	14.68	15.16	32.5	-	67.5	-
50S	13.27	13.68	48.9	-	51.1	-
4050	13.14	13.85	46.9	-	53.1	-
2125C	9.69	10.35	-	74.5	25.5	-
1W3	12.40	12.68	-	45.0	55.0	-
3W3	13.80	14.70	-	32.0	68.0	-
10W3	14.85	15.09	-	24.0	76.0	-
TC-10	11.65	11.68	-	42.0	-	58.0

The composition was determined by wet analysis. On the basis of the measured composition we have calculated what the density should be and have compared it with the measured density. It can be seen that all samples have porosity, some worse than others. It was also found that for a given type of material the composition varied as well as the amount of porosity. This has caused considerable scatter in the Hugoniot data and in the sound speed measurements. The results of the sound speed measurements are compared with the calculated sound velocities in figures 1 and 2.

The solid curves in these two figures are the ideal mixing results. The dashed curves are the layer model results. The data favors ideal mixing and, as expected, the layer calculation serves as an upper bound to the measured sound speeds. One trend that can be observed in the data is the increase in sound speed over that predicted by the mixing model as we go toward larger weight percents of tungsten. One could suppose that the rigid material forms continuous paths at these higher densities, and in spite of voids or the lower density, lower sound speed filler material, the sound wave is transmitted by these "bridges" over a path length approximately equal to the thickness of the sample and at a velocity somewhere between that of the longitudinal velocity or the rod velocity (i.e., the one given by Young's modulus) of the tungsten. On the other hand, as we go toward the copper or silver rich regions, bridges of tungsten must become more tenuous and less well braced. There may be transmission along these weaker bridges, but it will attenuate more rapidly and let the copper or silver carry the bulk of the wave. Here, porosity can have a greater effect, in that it now creates copper or silver bridges loaded with high density tungsten. When the tungsten no longer forms bridges it effectively no longer transmits the signal at its higher longitudinal velocity and its high density now becomes a drag on the wave. These topological considerations indicate the complexity of the problem and also indicate that elaborate statistical considerations are necessary to even

solve the problem for an ensemble of samples. For large grain sizes one can still expect a considerable scatter of individual samples about an average solution even if it were obtained. We have not tried to handle the porosity we know to be in our samples in our calculations for the sound speed. We have taken it into account in our calculations for the shock wave experiments. Unfortunately we cannot simply extrapolate the shock model to zero compression to get the acoustic limit, for any voids in this model would lead to a zero limit for the sound speed. The hydrodynamic model does not take rigidity into account, and the rigidity, of course, keeps the voids from collapsing, especially in the very low pressure regime.

The Hugoniots of four Cu - W and one Cu - WC Elkonites have been measured. The equation of state used for the constituents is given in table II.

TABLE II. EQUATIONS OF STATE OF COPPER, TUNGSTEN AND TUNGSTEN CARBIDE

Material	Cu	W	WC
ρ_0 gm/cm^3	8.93	19.30	15.02
C_0 km/sec	3.940	4.029	4.920
S	1.489	1.237	1.339
γ_0	2.00	1.54	1.50
C_v 10^7 ergs/gm-$^\circ$K	0.386	0.135	0.128
M (moles/gm)	63.54	183.86	195.87

The Cu Hugoniot is one of Los Alamos Scientific Laboratory's shock-wave standards [2] for impedance-match solutions. The W and WC Hugoniots were partially determined using this standard. Hence the three materials should be compatible. The Elkonites were also measured with this standard. The data and calculations are compared in figures 3-12 in both the U_s - U_p plane and in the P - ρ plane. The agreement of the Cu - W data with the experiments is truly satisfying. In general the scatter in the data is due to variation in density in the samples. Since the composition of each sample was not measured these density variations could be due to non-uniform composition or a lack of uniformity in the porosity. One feature common to all the U_s - U_p shots is the falling off of the shock velocity at low pressure. This is due to the porosity and has been observed for many other materials. The calculations account for this in a satisfactory manner.

The data for the TC 10 material does not agree as well with the calculations as the Cu - W series. There are two possible explanations for this. One is that the material used for the determination of the WC Hugoniot is slightly different than used in the mixture. It is known that the WC for the former contained a Co binder. The other reason is that the WC Hugoniot is reflecting the residual shear stress due to the large rigidity in this material. The measured WC Hugoniot could very well be in a highly non-hydrostatic state, while in the mixture the Cu

58

will flow plastically and allow the rigid material to be compressed more hydrostatically. This is one of the reasons this study was initiated, that is to develop a technique for measuring the Hugoniots of very rigid materials by imbedding them in materials that deform easily by plastic flow in the shock front. The good results with Cu - W series indicate that this might indeed be a very useful technique. The U_s - U_p Hugoniot for WC measured here (figure 13) reflect the difficulties encountered in applying the usual techniques. The Hugoniot of SiC, also very rigid, shows this same effect.

B. The Hugoniot Equation of State of Au-Ge Alloys

The Hugoniots of two Au-Ge alloys have been measured using the standard GMX-6 impedance-match method with Cu used as the standard. Although these two alloys came from the same casting their compositions are different because Ge is not soluble in Au, and separation occurred in the casting.

The weight percents have been calculated from the densities. Samples have been sent for chemical analysis. The measured and calculated sound velocities are given in table III.

TABLE III. MEASURED SOUND VELOCITIES OF Au-Ge ALLOYS

ρ_0 g/cm^3	Wt % Ge	V_1 km/sec meas. (calc.)	V_s km/sec meas. (calc.)	V_b km/sec meas. (calc.)
15.49	9.3	3.388 (3.49)	1.465 (1.72)	2.94 (2.87)
16.88	5.8	3.326 (3.41)	1.329 (1.56)	2.95 (2.89)

The data (ρ_0's and C_{ij}'s) used to calculate the end members for Au and Ge were taken from Clark's [3] handbook.

The shock-velocity particle-velocity data of these two materials are given in figure 14. Two features of these Hugoniots should be noted. The most important is that the data do not extrapolate to the zero-pressure sound velocity. The fact that they fall below the sound velocity by over 10% is an indication that a transition has occurred. This transition is shown at a U_p of about 0.15 km/sec. The other feature is the nonlinear behavior of the two curves. As with some other materials these Hugoniots can be drawn with two straight lines with the break occurring near a particle velocity of 1.0 km/sec. To help explain these features we have reproduced the phase diagram (P = 0) of the Au-Ge system [3] in figure 15. It is well known that Ge contracts upon melting and apparently the Au-Ge alloy at the eutectic also contracts on melting. Shocked Ge undergoes a transition at a pressure near 125 kb possibly due to melting. The transition we have indicated for the Au-Ge alloy in the figure U_p = 0.15 km/sec also occurs at about this pressure. This seems to be about correct considering the probable effect that Au will have on the slope of the phase line and the pressure-temperature relationship along the Hugoniot of the alloy. Although the Au-Ge alloys start to melt at this pressure, melting will not be complete until a higher temperature is attained; this corresponds to a considerably

59

higher pressure. The break in the U_s - U_p Hugoniot curve occurs at a pressure near 700 kb. Although this seems a bit high it is certainly not an unreasonably high pressure for the completion of melting.

To check our ability to predict the Hugoniot of mixtures we have taken the linear Hugoniot of Au

$$U_s = 3.075 + 1.560 \ U_p \quad \text{(where units are km/sec)}$$

and mixed it with the Hugoniot of transformed Ge. The transformed Ge Hugoniot was obtained from our Ge shock-wave data with our code TRANS. This code assumes that the metastable Hugoniot of a transformed material will have a linear U_s - U_p Hugoniot. It then determines the new zero-pressure density and sound speed for selected slopes, S. This calculation has been described in detail in the rock paper. These calculations predict the following equations of state for high density Ge.

TABLE IV. ZERO-PRESSURE DENSITY AND SOUND
VELOCITY FOR TRANSFORMED Ge AS A FUNCTION
OF SLOPE OF THE LINEAR U_s - U_p HUGONIOT

Slope	C_o	ρ_o
1.00	6.25 km/sec	7.48 g/cm^3
1.25	5.43 "	7.27 "
1.50	4.57 "	7.03 "

The results of these fits are compared with the original Ge data in figure 16. It is apparent that all three slopes adequately fit the data giving little reason to choose one slope over the others. However, the calculated volume changes at the transition can be compared with values obtained from static measurements. The slope of 1.5 gives the best agreement.

The mix code then takes these equations of state and the Grüneisen ratio and transforms them to zero-Kelvin isentropes.

The shock-particle velocity and pressure-density results of the mix calculation are shown in figures 17 and 18.

C. The Hugoniots of Some Oxides

Of considerable interest is our ability to synthesize the equation of state of minerals from the equation of state of these basic oxide constituents. There is some hope that this can be done since it is felt that the oxygen in both the oxides and more complicated minerals is largely controlling the compressibility with metallic ions causing variations in density. This is admittedly a great over-simplification and it is hoped that the comparison of these calculations with the experimental data will give some clues as to the type of bonding occurring in the high-pressure polymorphs that so many minerals have. In the meantime there are some data available to check the model.

60

The Hugoniots of the major oxides have been measured here using a 2024 Al standard. These Hugoniots will be changed slightly in the near future because of small changes being made in the 2024 Al standard. The Hugoniots of the materials are presented graphically in figures 19-27. An attempt was made on MgO and Al_2O_3 to measure the Grüneisen parameter at high pressure by using porous materials (ceramics). Although extreme precision is required in order to make high quality determinations of γ, such data do allow a straight forward check on the Grüneisen gammas used in our calculations. To this end we have simply run the mix problem as a single component but with voids. The figures show that we indeed have an adequate high-pressure representation of these functions.

The equation-of-state parameters used in our calculations are presented in table V.

TABLE V. EQUATION-OF-STATE PARAMETERS OF THE MATERIALS USED IN THE MIXTURE CALCULATIONS

Mineral	(MgO)	(Al_2O_3)***	(SiO_2)***	(FeO)*	(TiO_2)
ΔE (10^{10} ergs/gm)**	0.0	0.0	1.8	0.48	1.7
ρ_0 (gm/cm^3)	3.585	3.987	4.287	5.61	5.76
C_0 (km/sec)	6.71	7.94	10.6	4.26	10.0
S	1.363	1.3	1.25	1.25	1.25
γ_0	1.324	1.4	0.78	1.45	0.9
C_V (10^7 ergs/gm-^{0}K)	0.95	0.752	1.0	0.72	0.94
M (gm/mole)	10.31	101.96	60.09	71.85	79.90

*This equation of state for iron oxide is to be regarded as a rough preliminary estimate for this compound. The numbers were obtained by extrapolating on m, the average mass per atom, the high-pressure data on hematite and magnetite.

**The last three minerals in the above table have a phase transition between their zero pressure state and the high-pressure range of interest here. The equation of state as given in the above table refers to the high-pressure phase, which is metastable at zero pressure. The ΔE is the extra energy this metastable phase has over the normal state of the mineral at zero pressure. Since the mixture is centered at the normal state, this energy difference must be taken into account in the Rankine-Hugoniot equation for the energy.

***The parameters for corundum and stishovite were obtained from forms of these minerals at a density lower than crystal density. For quartz the fused silica samples were used, primarily because of the more numerous data points available. For corundum, a lower density was used because the large and fast elastic wave in crystal density material prevented the measurement of a hydrodynamic Hugoniot.

D. The Hugoniots of some "Oxide Mixtures"

Three of the oxides in the last section; periclase (MgO), corundum (Al_2O_3) and iron oxide (FeO); are essentially close-packed oxygen lattices with the metal ions dispersed in the interstices of the oxygen lattice. In quartz, on the other hand, the silicon ion is tetrahedrally

bonded to four oxygen atoms, and the lattice is composed of a rather loose-packing of these tetrahedra. In rutile (TiO_2), the oxygens are octahedrally coordinated about the titanium ion. In the high-pressure phase of quartz, stishovite, the coordination about the silicon is the same as it is for titanium in rutile. In the minerals formed from these oxides, the coordination of oxygen about a given metal ion tends to remain the same. If this behavior persists into the high-pressure phases of those oxides that undergo phase transitions, we can hope to approximate the high-pressure Hugoniot of the mineral by mixing high-pressure oxide equations of state. Table VI lists the minerals and rocks considered here and their oxide molar composition.

TABLE VI. OXIDE MOLAR COMPOSITIONS OF SOME
MINERALS AND ROCKS

Mineral/Rock	MgO	Al_2O_3	SiO_2	FeO	TiO_2
	Mole percent of above oxide				
Enstatite ($MgSiO_3$)	0.50	----	0.50	----	----
Forsterite (Mg_2SiO_4)	0.67	----	0.33	----	----
Spinel ($MgAl_2O_4$)	0.50	0.50	----	----	----
Mullite ($Al_6Si_2O_{13}$)	----	0.60	0.40	----	----
Fayalite (Fe_2SiO_4)	----	----	0.33	0.67	----
Ilmenite ($FeTiO_3$)	----	----	----	0.50	0.50
Granite[*]	0.09	----	0.81	----	----
Twin Sisters Dunite[*]	0.57	----	0.35	0.08	----
Mooihoek Dunite[*]	0.30	----	0.35	0.35	----

[*]The compositions given for the rocks are nominal, and such minor constituents as the alkaline and alkaline-earth oxides and water have been ignored.

Enstatite and forsterite are (1/1) and (2/1) molar mixtures of MgO and SiO_2. The crystal structure of enstatite contains long chains of SiO_4 tetrahedra as does quartz, but without the complex cross-linking and intertwining that occurs in quartz. The cross-linking is done by the Mg ions. In forsterite, on the other hand, the oxygens are approximately in a close packed structure, with the Si ions still at the center of the tetrahedra. In forsterite the Mg ions form a matrix that tends to surround individual SiO_4 tetrahedra, while in enstatite the matrix of Mg ions links chains of SiO_4 tetrahedra. Thus enstatite might be expected to adhere more closely to the predictions of a pure mixing theory. Although these considerations are weakened by the existence of a high-pressure phase transition the data for enstatite (admittedly sparse in the high-pressure region of interest) and forsterite shown in figures 28, 29 and 30 indicate that enstatite seems to satisfy the mixing model better than does forsterite.

The spinel structure, although somewhat complicated, (with 56 atoms in the unit cell), does have the oxygen atoms in approximate cubic close packing. For the ideal spinels used here ($MgAl_2O_4$), the Mg ions have the diamond structure and are in fourfold coordination

62

between a group of oxygen atoms. The Al ions are in sixfold coordination between an octahedral group of oxygens. Conversely each oxygen is linked to one Mg ion and three Al ions. This structure is somewhat more open than either the periclase or corundum structure as can be seen from the zero-pressure densities (MgO - 3.58 g/cm^4, Al$_2$O$_3$ - 3.99 g/cm^3 and MgAl$_2$O$_4$ - 3.58 g cm^3). Spinel undergoes a transformation with a large density increase as can be recognized from the U$_s$ - U$_p$ data (figure 31). Magnetite, which also has the spinel structure, exhibits a similar Hugoniot. It is not obvious how this structure rearranges itself to the more dense configuration. However, the final state is even slightly more dense than that predicted by the simple mixing of close packed periclase and corundum. When powdered mixtures of periclase and corundum were cold pressed and shocked, the Hugoniot was stiffer than predicted by the simple mixing calculations (figure 33). However, the density of these samples was so low $\left(\rho_c \sim 2.1 \text{ g cm}^3 \right)$ that heating effects become extremely important. An effort to obtain higher density samples of unreacted mixtures is underway.

Data on ceramic mullite is an acceptable agreement with the calculated equation of state from corundum and stishovite (figures 34 and 35). We believe the scatter in the data is due to sample thickness in the high-pressure region and to an uncompleted phase change in the lower pressure region.

Shock-wave data for fayalite are compared with the mix calculation for 2(FeO) · SiO$_2$ (stishovite) in figures 36-37. This is the first mineral examined that has a significant amount of FeO present. We believe the agreement should be better, based on the MgO · SiO$_2$ studies, and that probably the FeO equation of state is too soft. Further evidence that FeO is too soft is given by the ilmenite comparison in figures 38 and 39. We do not have any additional checks for TiO$_2$, but at least its equation of state was derived from experimental data.

The last two figures (40 and 41) are exceedingly encouraging. Here we have attempted to predict the high-pressure equation of state of these rocks on the basis of their chemical composition and density. We note that a slight improvement could be made in the agreement with the densities if a slightly stiffer equation of state for FeO were used.

CONCLUSION

First efforts in this program have been very encouraging. It has been shown that heterogeneous materials can come sufficiently close to hydrodynamic and thermodynamic equilibrium so that their measured Hugoniots are experimentally indistinguishable from that calculated from the ideal mixing model. It has been shown also that mixing techniques offer a new way to study materials that are complicated by rigidity effects. More work needs to be done on the minerals and mineral synthesis. On the whole, though it is rather apparent that with a minor adjustment of the equation of state of the basic oxides all the high-pressure data could be fitted well enough to satisfy any current practical application. The mixture calculations for minerals should be made sufficiently precise so that disagreements between the calculations and data can be interpreted in a meaningful manner. There should be no reason that mixture calculations

could not be used in the low-pressure regions. However, the existence of phase change and rigidity effects has prevented an accurate determination of the equation of state in this region. The effect of phase changes can be handled in a completely straightforward manner but will require additional information. The effect of rigidity appears to be a major area of difficulty in "hydrodynamic" studies in rocks. It is not immediately apparent how simple mixing ideas will apply to such problems.

REFERENCES

1. R. G. McQueen, S. P. Marsh and J. N. Fritz, "Hugoniot Equation of State of Twelve Rocks," J. Geophys. Res., Vol. 72, 1967, pp. 4999-5000.

2. R. G. McQueen, S. P. Marsh and W. J. Carter, Symposium, High Dynamic Pressure, Paris, France, 1967, to be published.

3. S. P. Clark, Jr., ed., Handbook of Physical Constants, Geol. Soc. Amer., New York, 1966.

4. J. Wackerle, "Shock-Wave Compression of Quartz," J. Appl. Phys., Vol. 33, 1962, pp. 922-937.
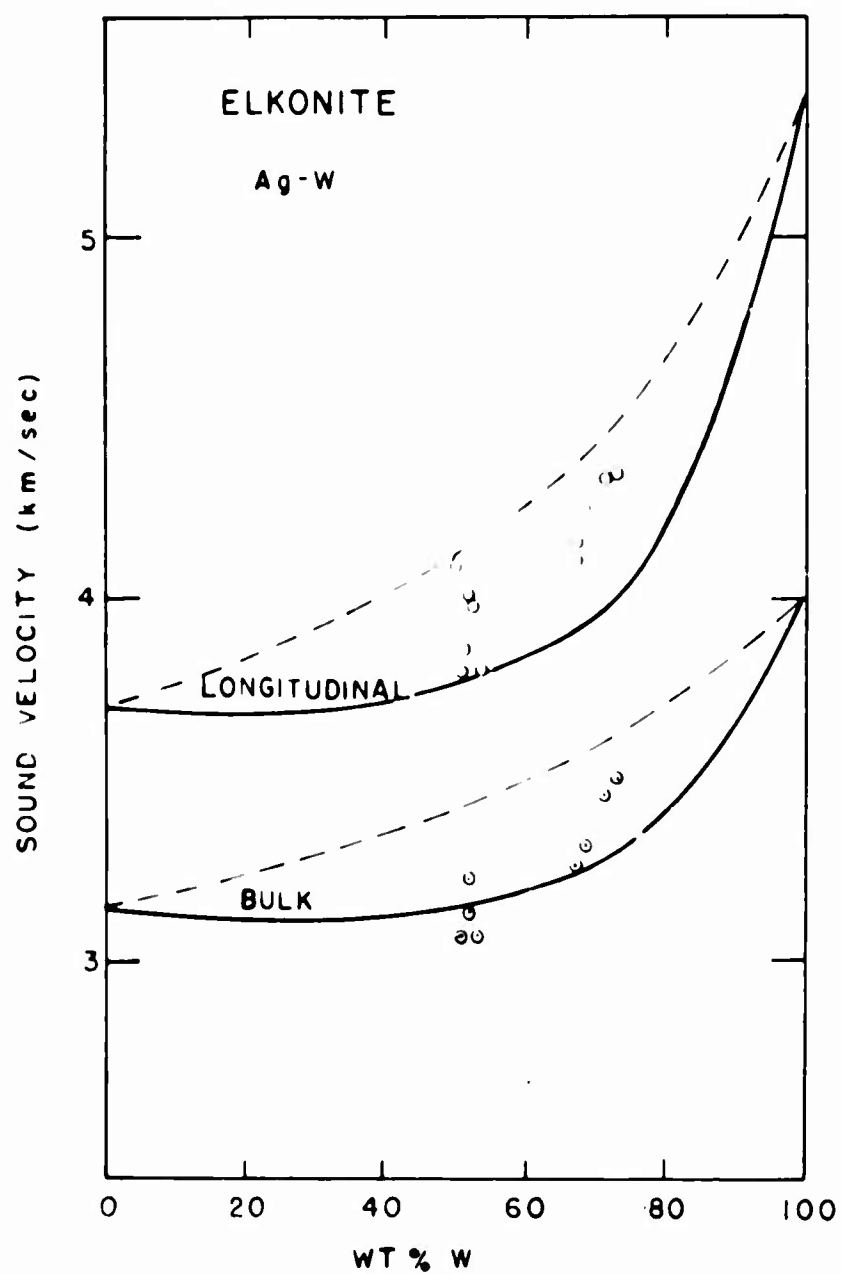
Figure 1. Longitudinal and Bulk Sound Velocities for the Ag-W Elkonites.
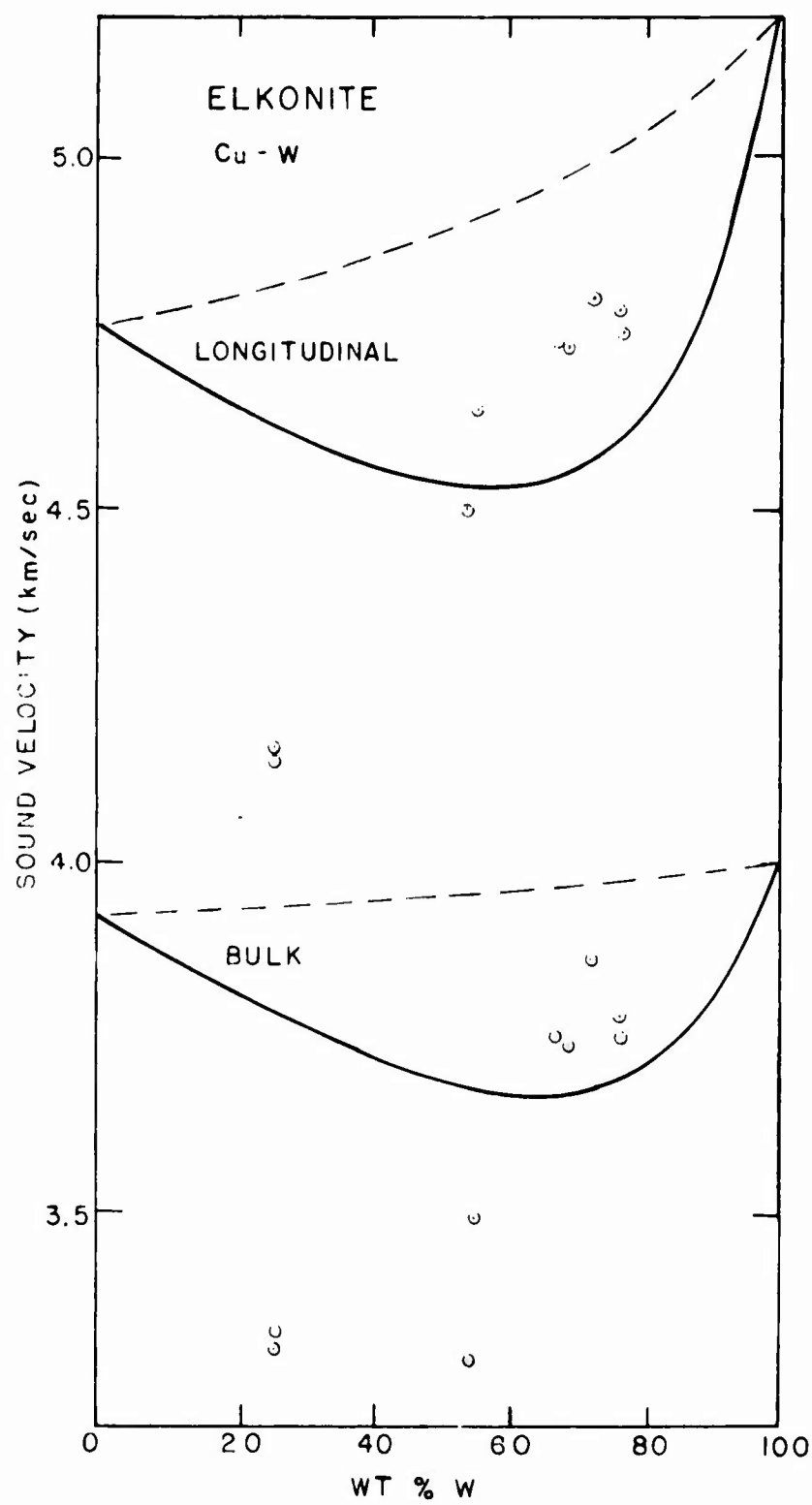
Figure 2. Longitudinal and Bulk Sound Velocities for the Cu-W Elkonites.
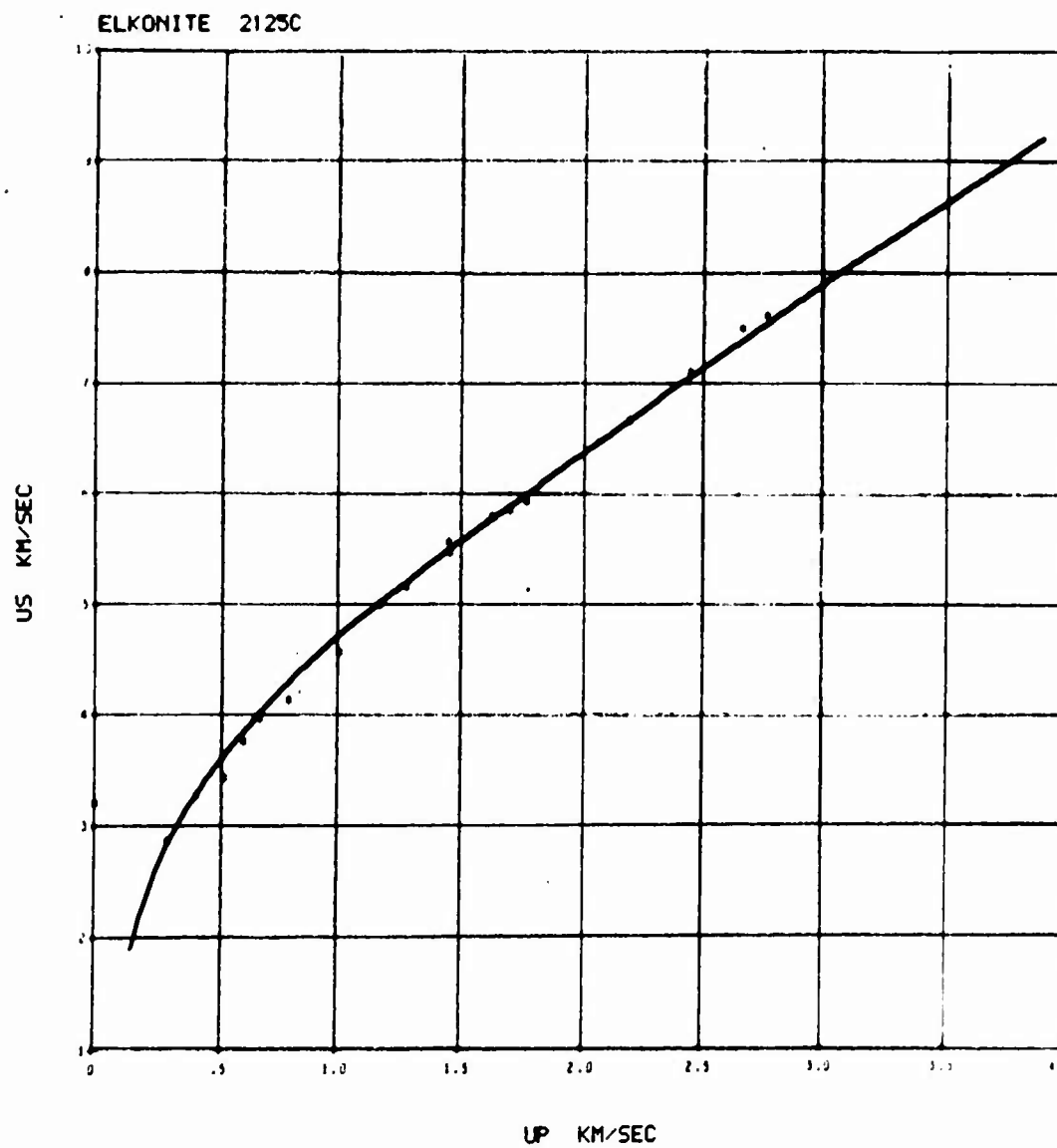
Figure 3. The Hugoniot of Elkonite 2125 C (74.5% Cu 25.5% W)
in the Shock-Velocity Particle-Velocity Plane.

ELKONITE 2125C

RHO G/CM**3

Figure 4. The Hugoniot of Elkonite 2125C (74.5% Cu 25.5% W) in the Pressure-Density Plane.

69

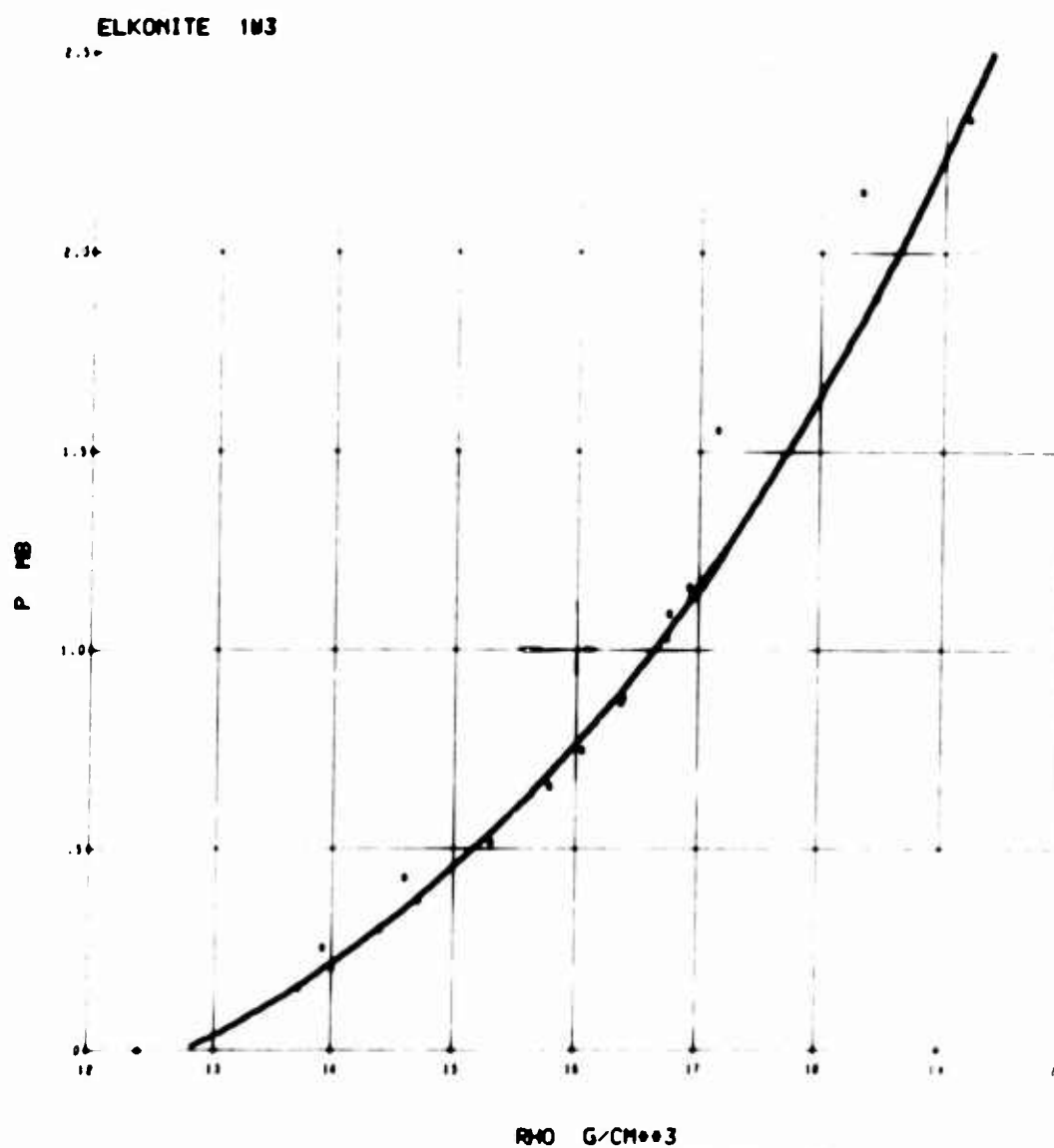Figure 5. The Hugoniot of Elkonite 1W3 (45.0% Cu 55.0% W) in the Shock-Velocity Particle-Velocity Plane.

Figure 6. The Hugoniot of Elkonite 1W3 (45.0% Cu 55.0% W) in
the Pressure-Density Plane. It is to be noted that the four data
points that lie far to the left of the calculated Hugoniot had initial
densities of 12.2, 13.0, 11.8 and 12.0 g/cm^3 from the bottom to
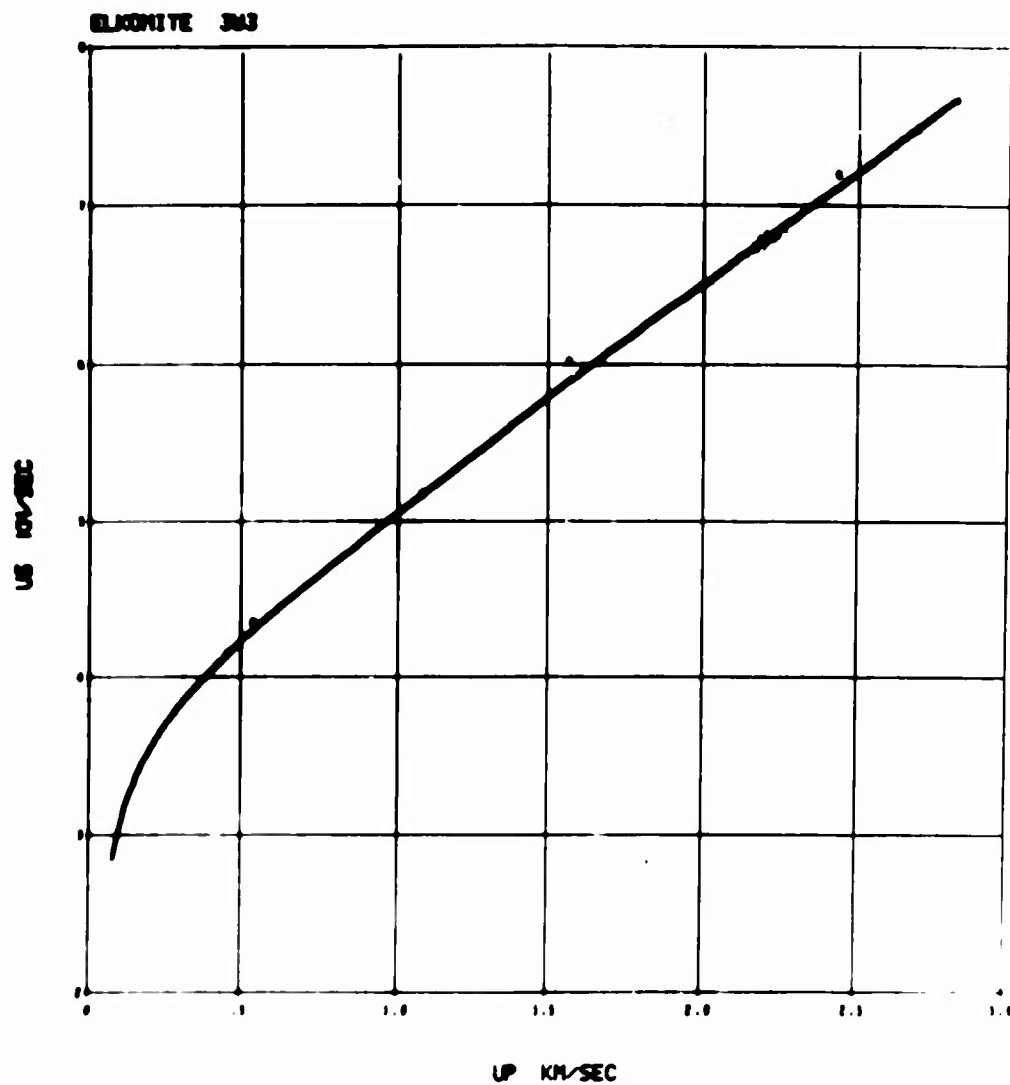top while the average density of the other samples was 12.4 g/cm^3.

71

ELKONITE 3W3

US KM/SEC (vertical axis)

UP KM/SEC

Figure 7. The Hugoniot of Elkonite 3W3 (32.0% Cu 68.0% W) in the Shock-Velocity Particle-Velocity Plane.
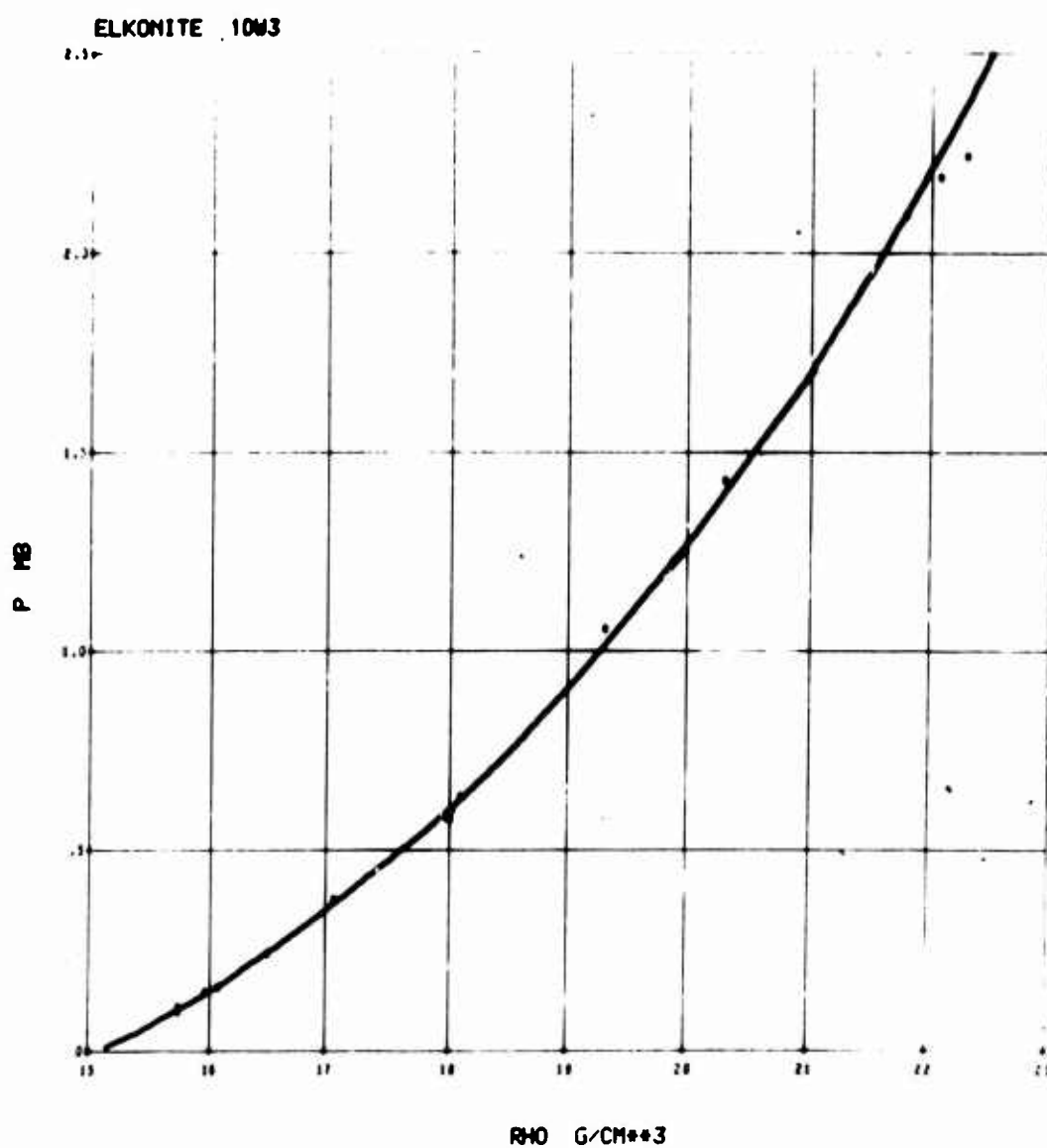
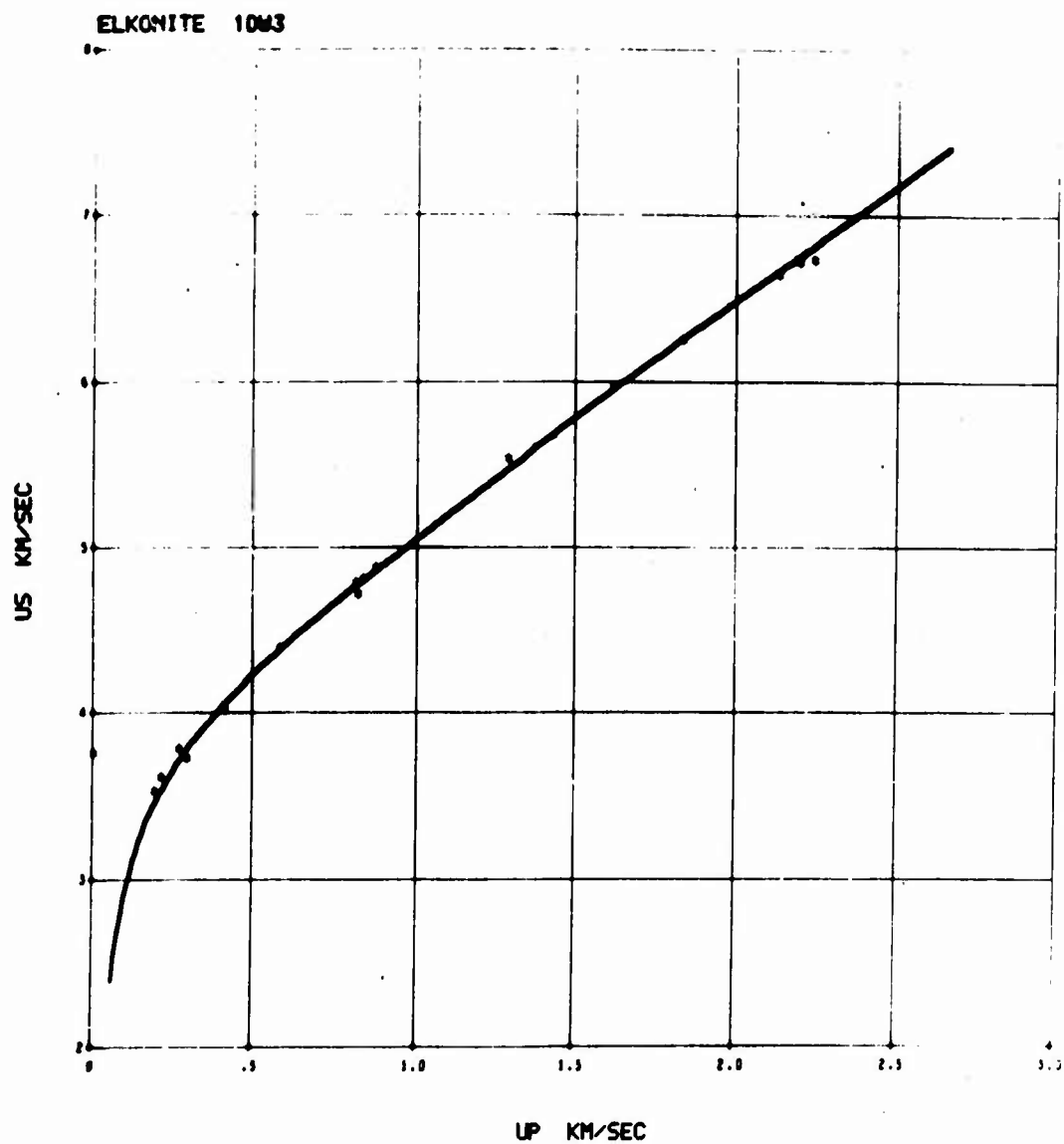Figure 8. The Hugoniot of the Elkonite 3W3 (32.0% Cu 68.0% W) in the Pressure-Density Plane.

Figure 9. The Hugoniot of the Elkonite 10W3 (24.0% Cu 76.0% W) in the Shock-Velocity Particle-Velocity Plane.
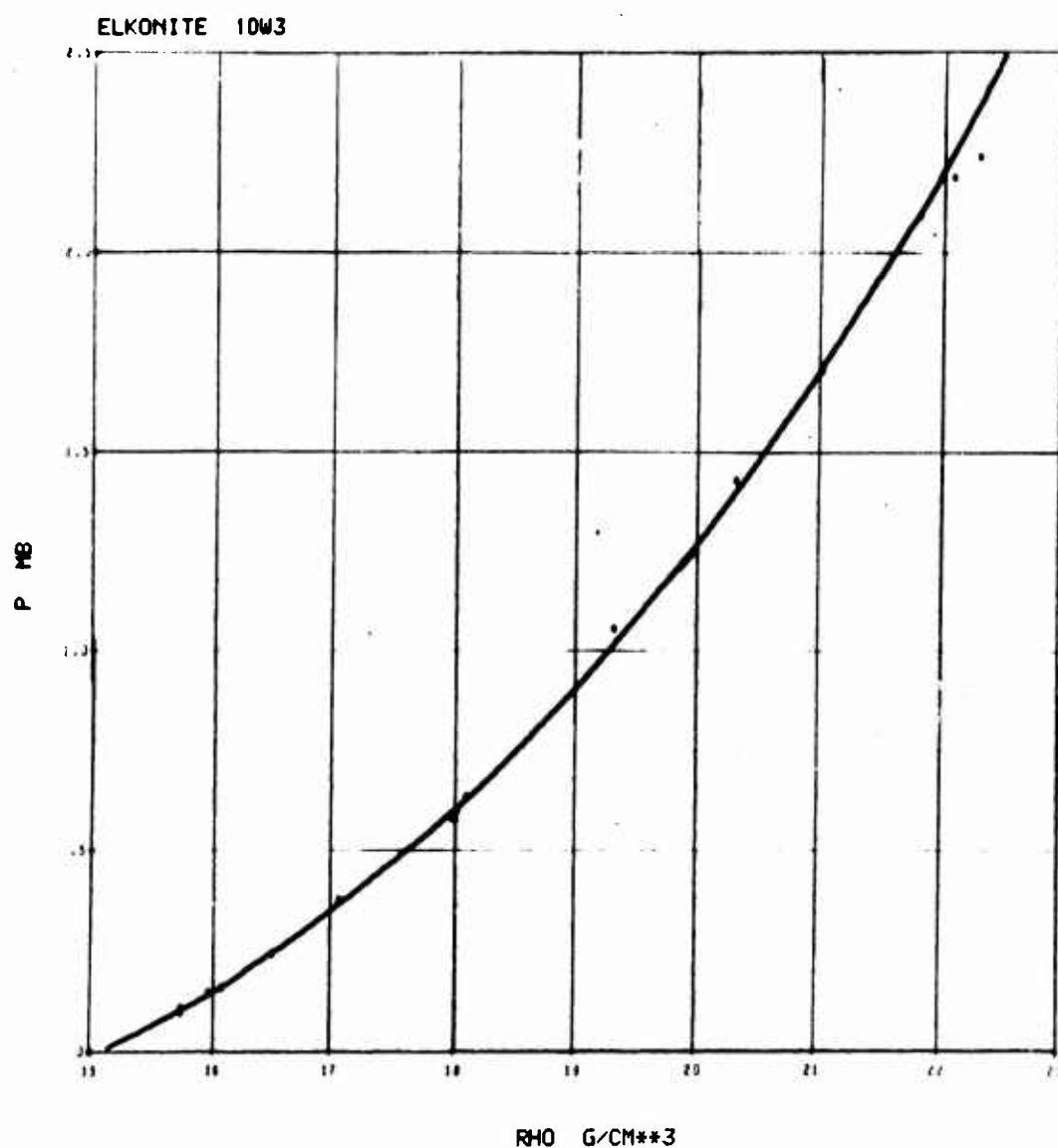
ELKONITE 10W3

RHO   G/CM**3

Figure 10. The Hugoniot of the Elkonite 10W3 (24.0% Cu 76.0% W)
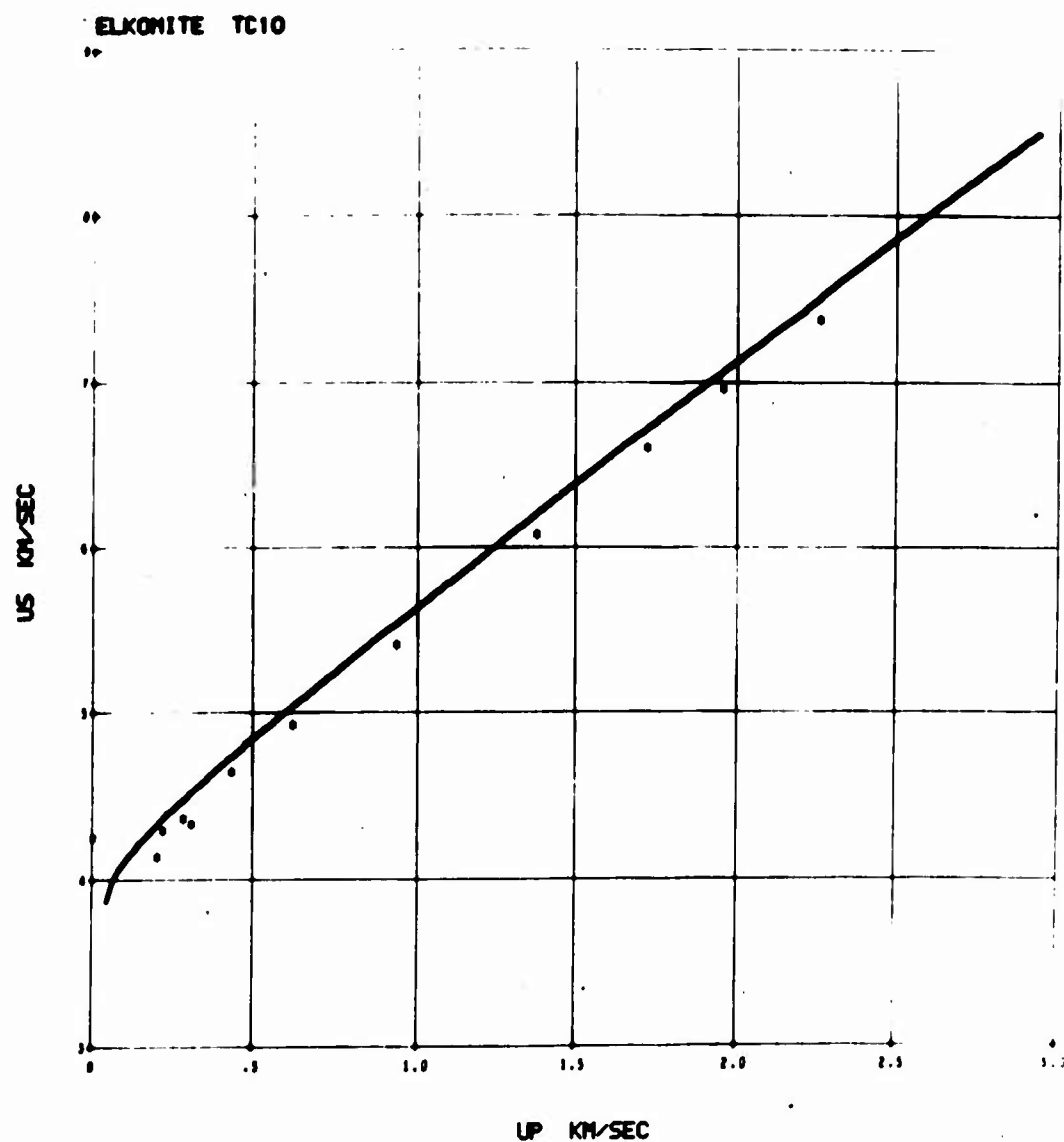in the Pressure-Density Plane.

Figure 11. The Hugoniot of the Elkonite TC-10 (42.0% Cu 58.0% WC)
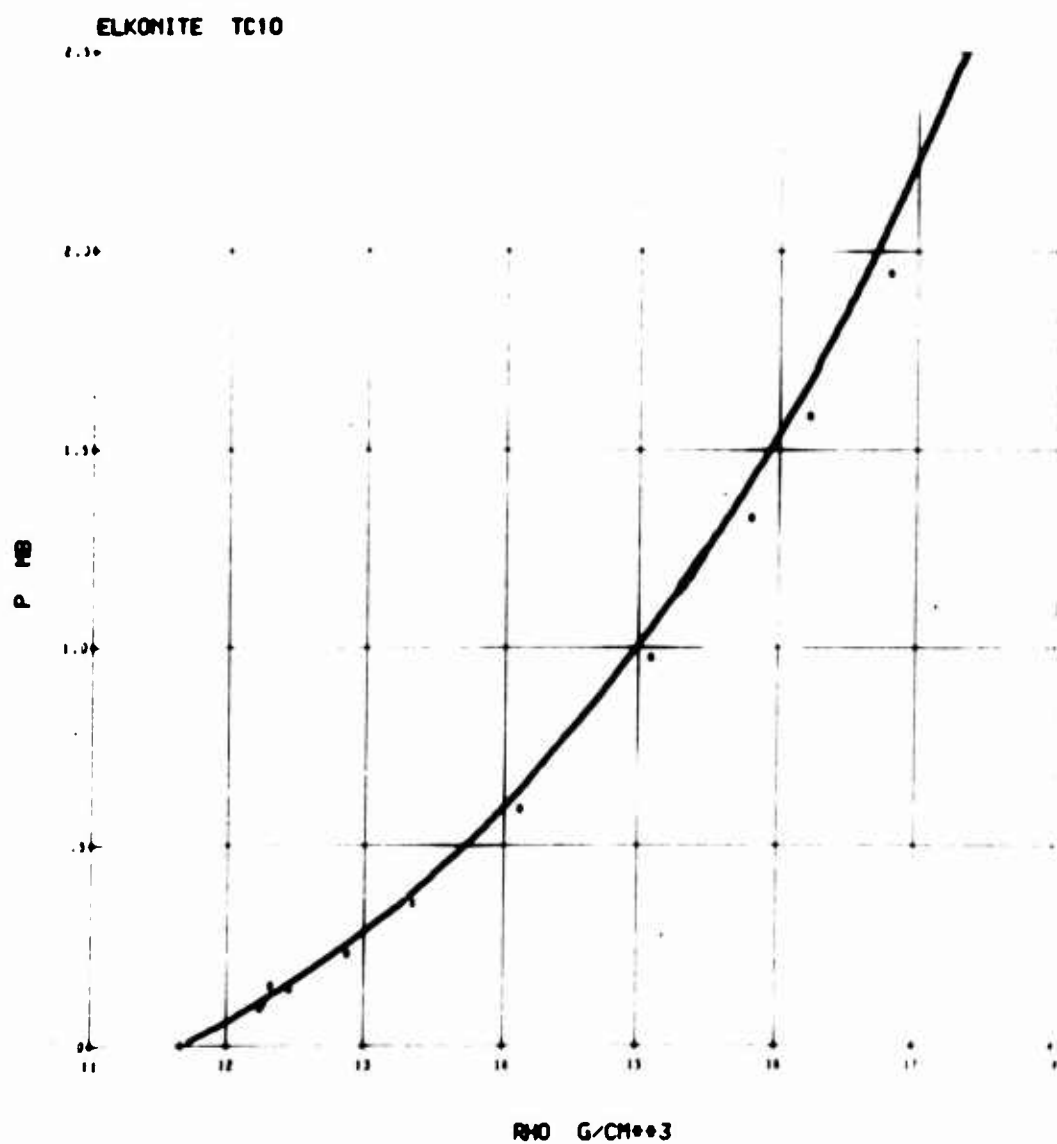in the Shock-Velocity Particle-Velocity Plane.

76

Figure 12. The Hugoniot of the Elkonite TC-10 (42.0% Cu 58.0% WC) in the Pressure-Density Plane.
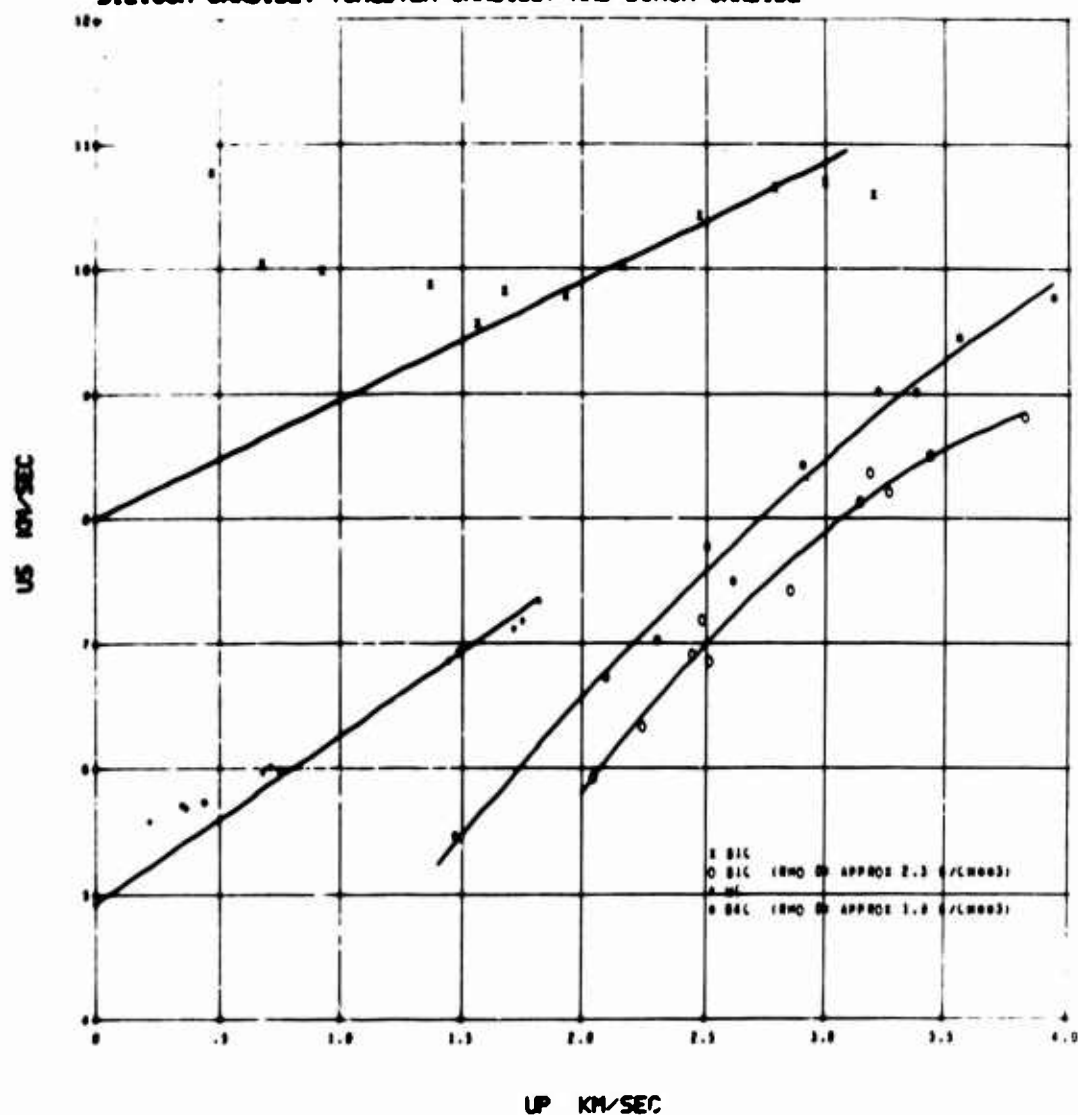
Figure 13. Shock-Velocity Particle-Velocity Data for Silicon Carbide, Tungsten Carbide and Boron Carbide. The low pressure data for both the SC and WC lie far above the Hugoniots that are arbitrarily drawn through the bulk sound velocities. The curve through the low density SiC was calculated from the crystal density linear U_s-U_p curve drawn on the figure.
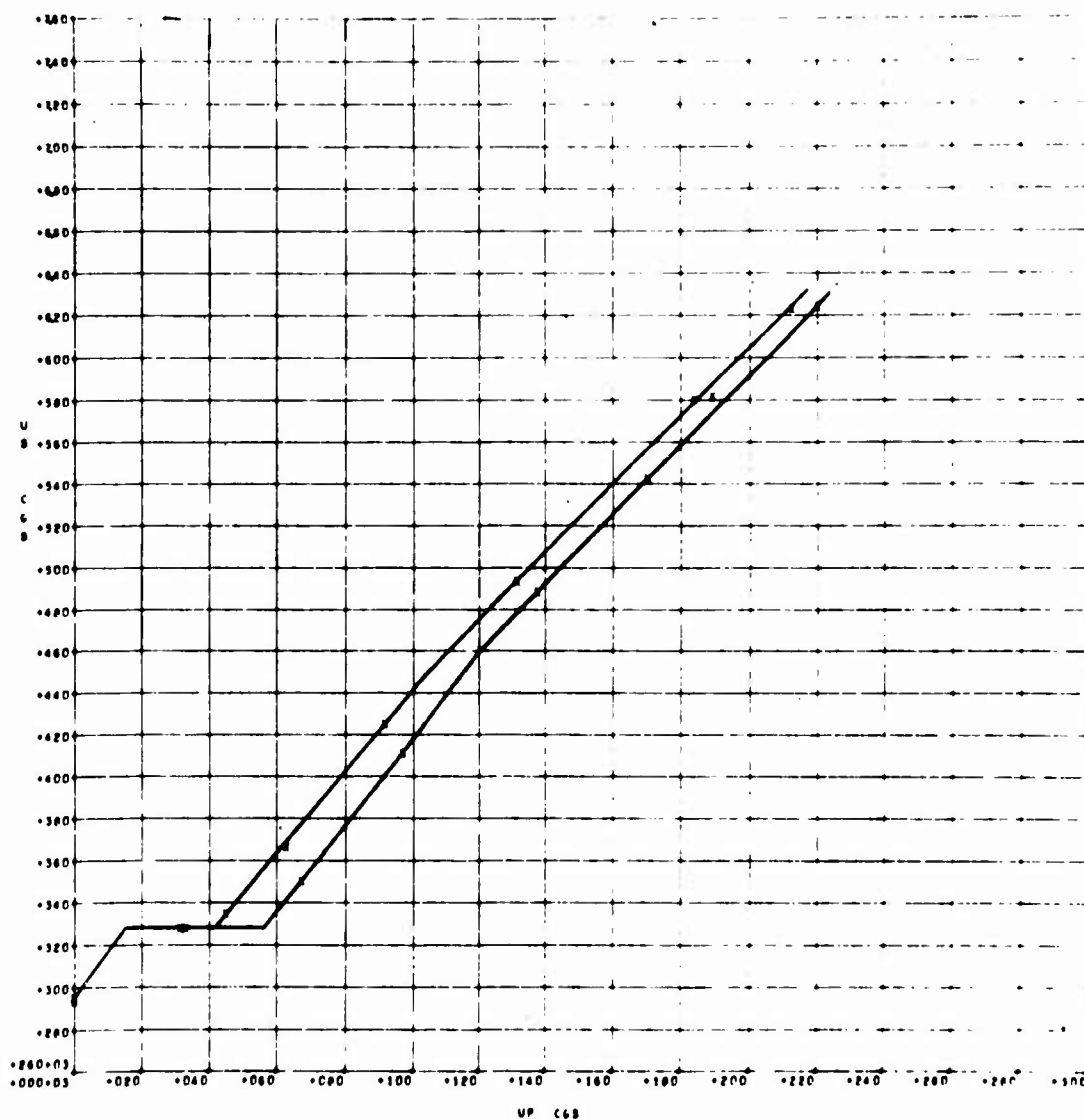
Figure 14. Shock-velocity particle-velocity Hugoniot data for Au-Ge alloys. The upper curve is the Hugoniot for 5.8 Wt % Ge alloy and the lower for 9.3 Wt % Ge alloy.
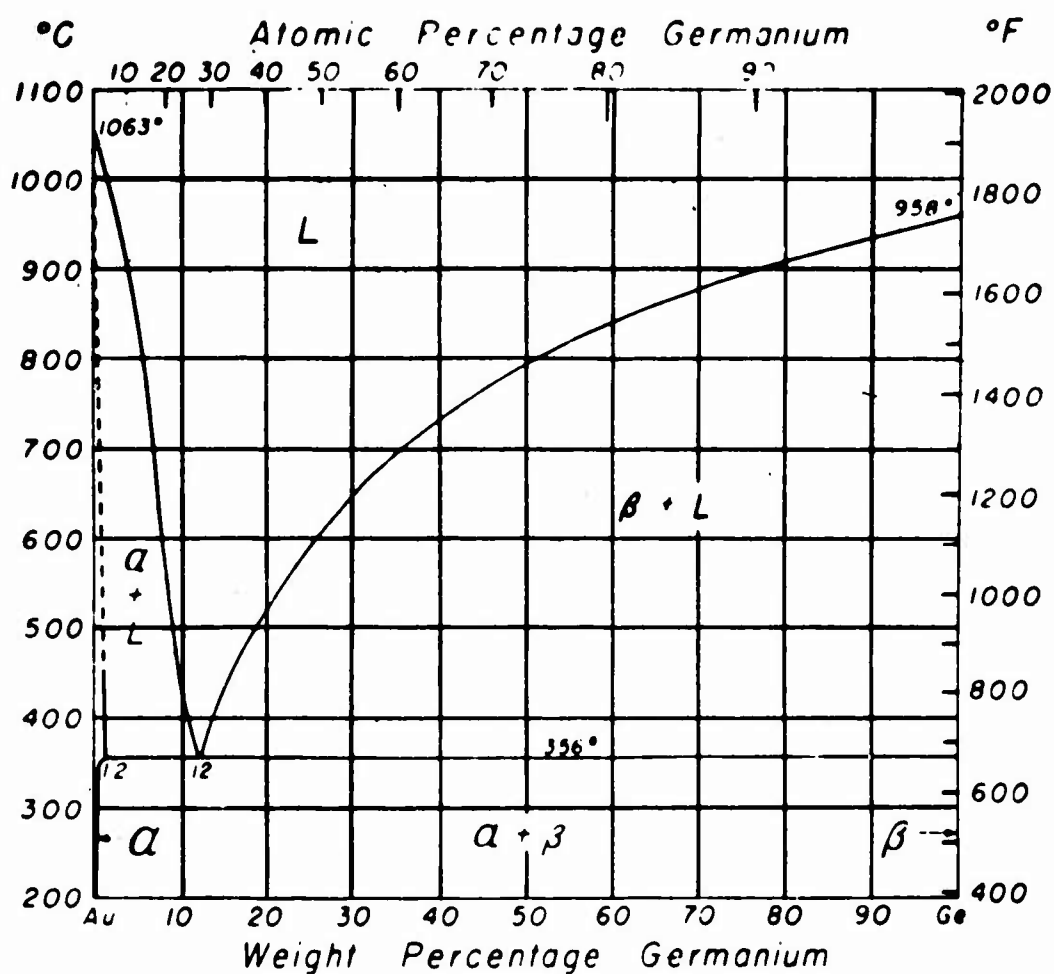
Figure 15. Phase diagram for the Au-Ge system. As can be seen all the alloys will begin to melt at 356°C. The completion of melting will depend on the composition.

Figure 16. Shock-velocity particle-velocity Hugoniot and calculations for Ge. The flat region at U_s = 4.2 km/sec is the manifestation of a two-wave structure in the shock front due to a transition. The data above U_s = 4.2 has been fitted from calculations using the three Hugoniots listed in Table 4. With so much scatter in the data one fit cannot be preferred to any other.

Figure 17. Calculated shock-velocity particle-velocity Hugoniots and the experimental data for two Au-Ge alloys.

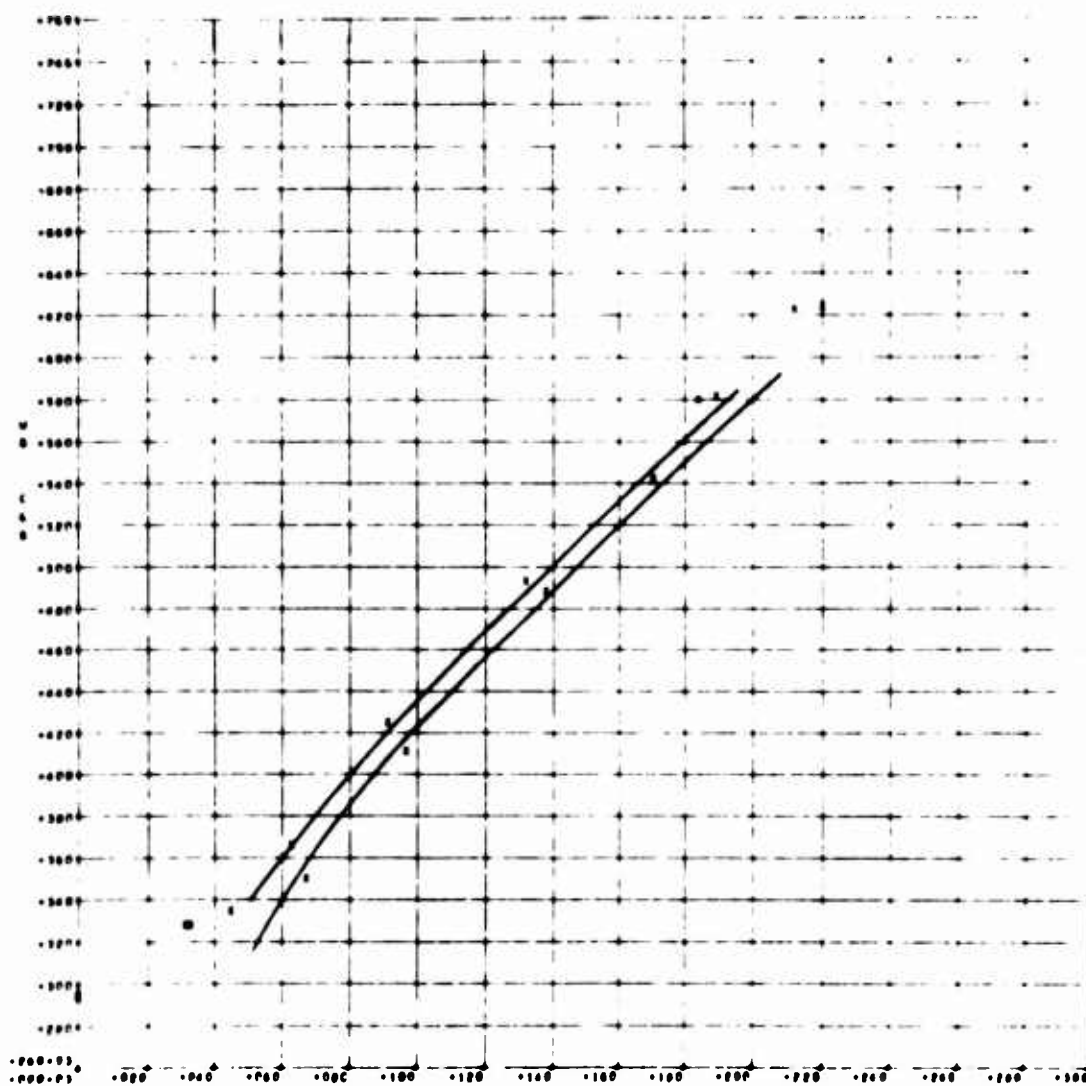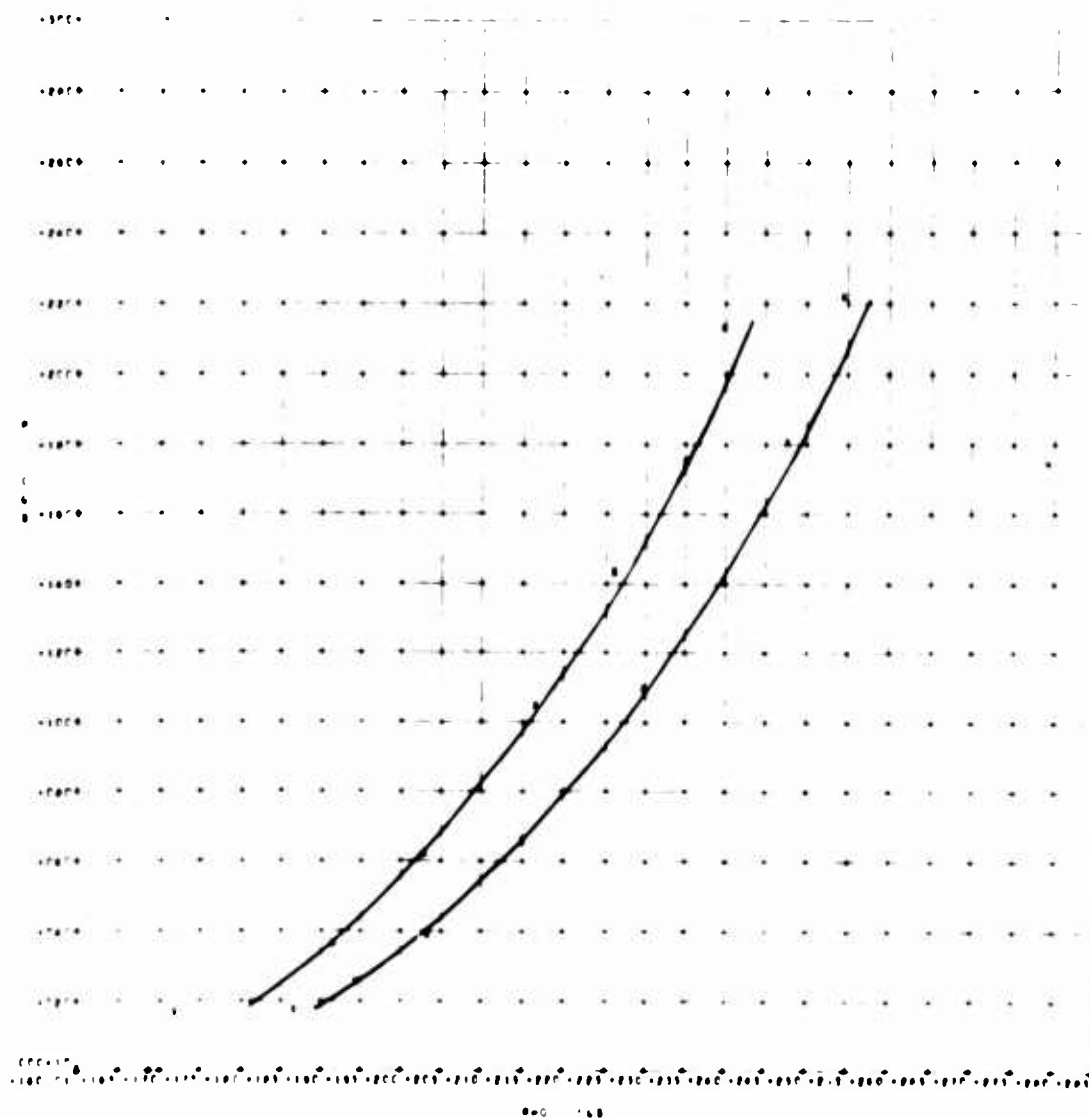Figure 18. Calculated pressure density Hugoniots and the experimental data for two Au-Ge alloys. It should be noted that these calculations represent a considerable extrapolation of the Ge data since the shock-wave data of Ge only goes to about one Mb.
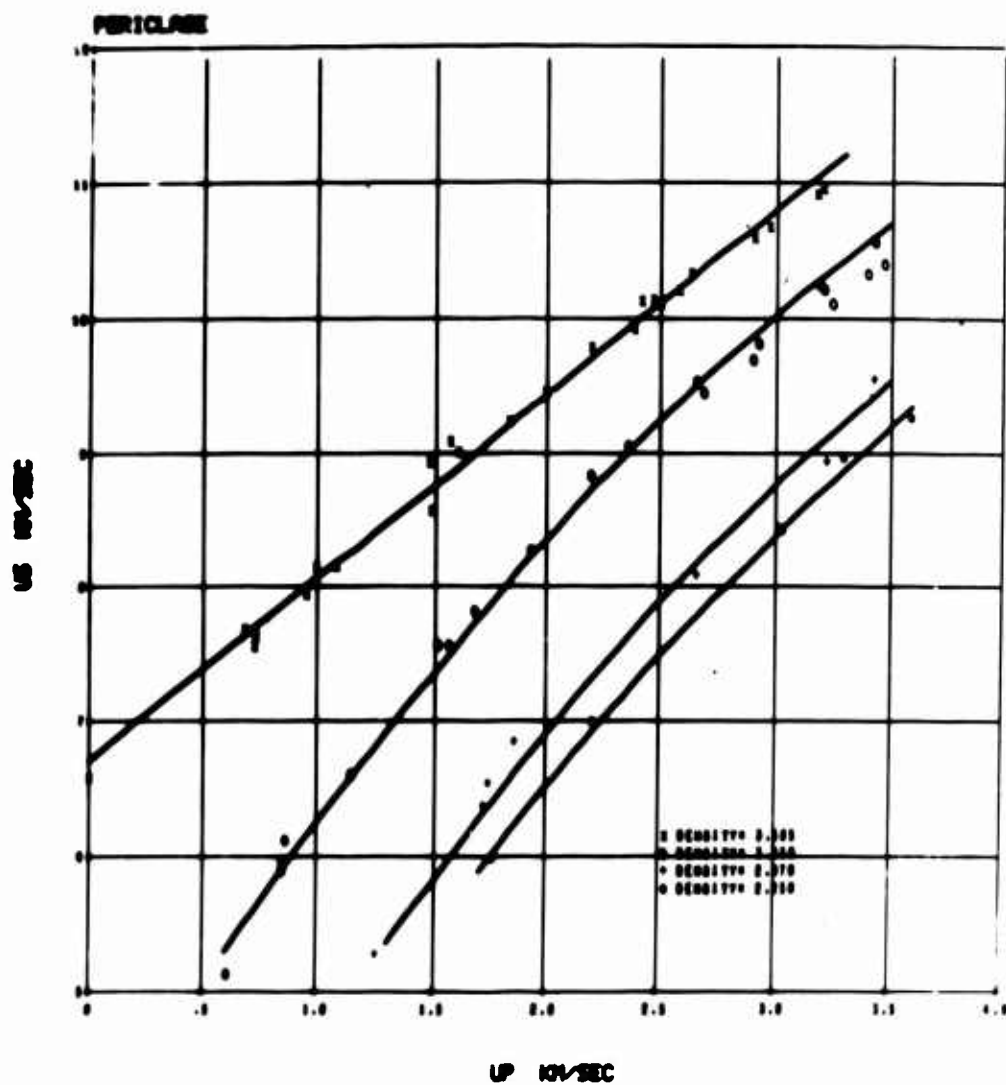
Figure 19. Shock-Particle Velocity Hugoniots for MgO. The high
density data (x) were obtained from single crystal specimens cut
at random orientation. The large number of available slip planes
in this system apparently allow the material to come to hydrodynamic
equilibrium. The other curves were calculated from the crystal
density Hugoniot but centered at the average density of each group
of samples.
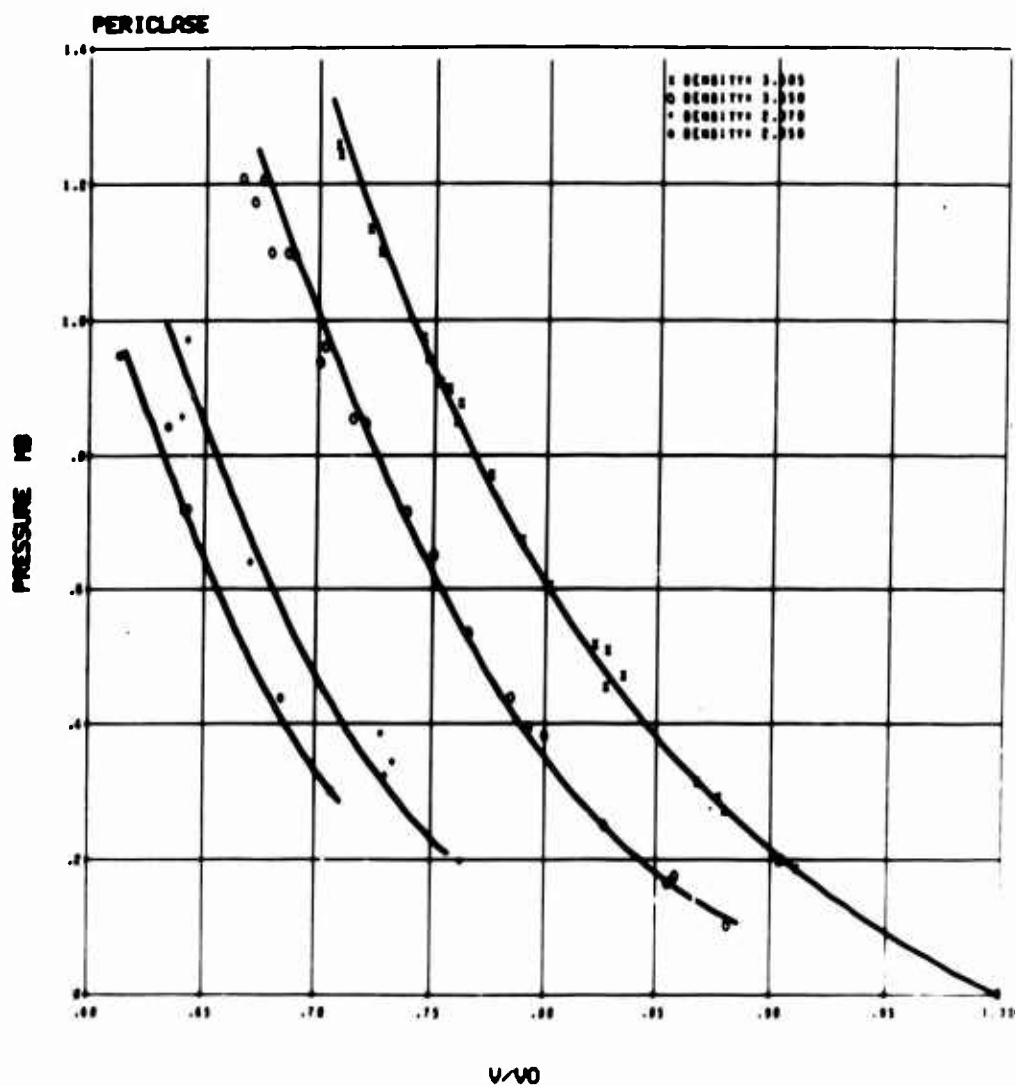
Figure 20. Pressure-Volume Hugoniots for MgO with Various Initial Densities. The calculated curves are the P-V/V_0 transforms of the U_s-U_p curves in Fig. 19.
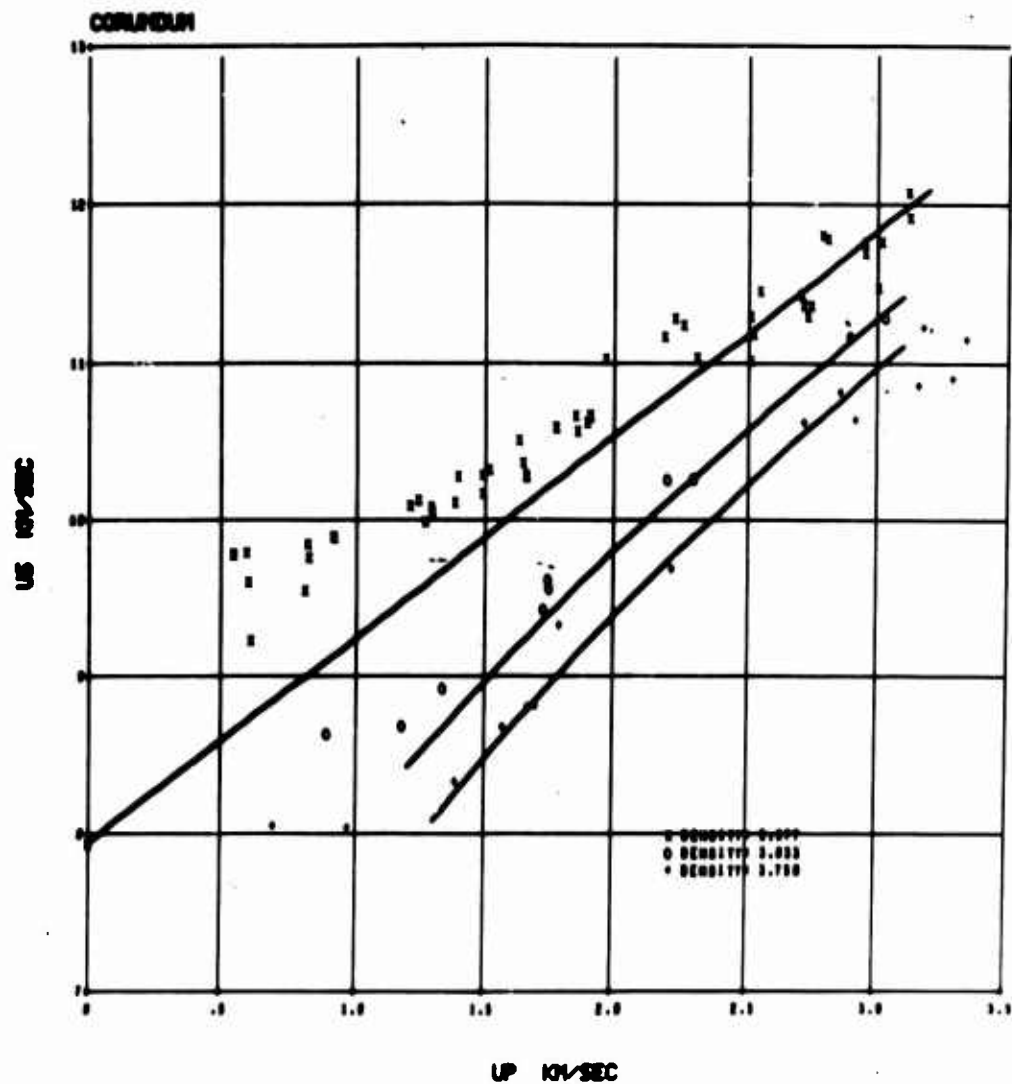
Figure 21. Shock-Particle Velocity Hugoniots for Al_2O_3 of Various Initial Densities. The high-density samples were made from General Electric's commercially available Lucalox. Although this is a ceramic material, the nearly perfect bonding results in a very strong material not too much weaker than the single crystal material. We have accordingly assumed that the equilibrium hydrodynamic curve (the linear curve) should be considerably softer than that indicated by the data. This curve is drawn through the measured zero-pressure bulk sound velocity. The other two curves were computed from this curve and the experimentally determined zero-pressure Gruneisen function.
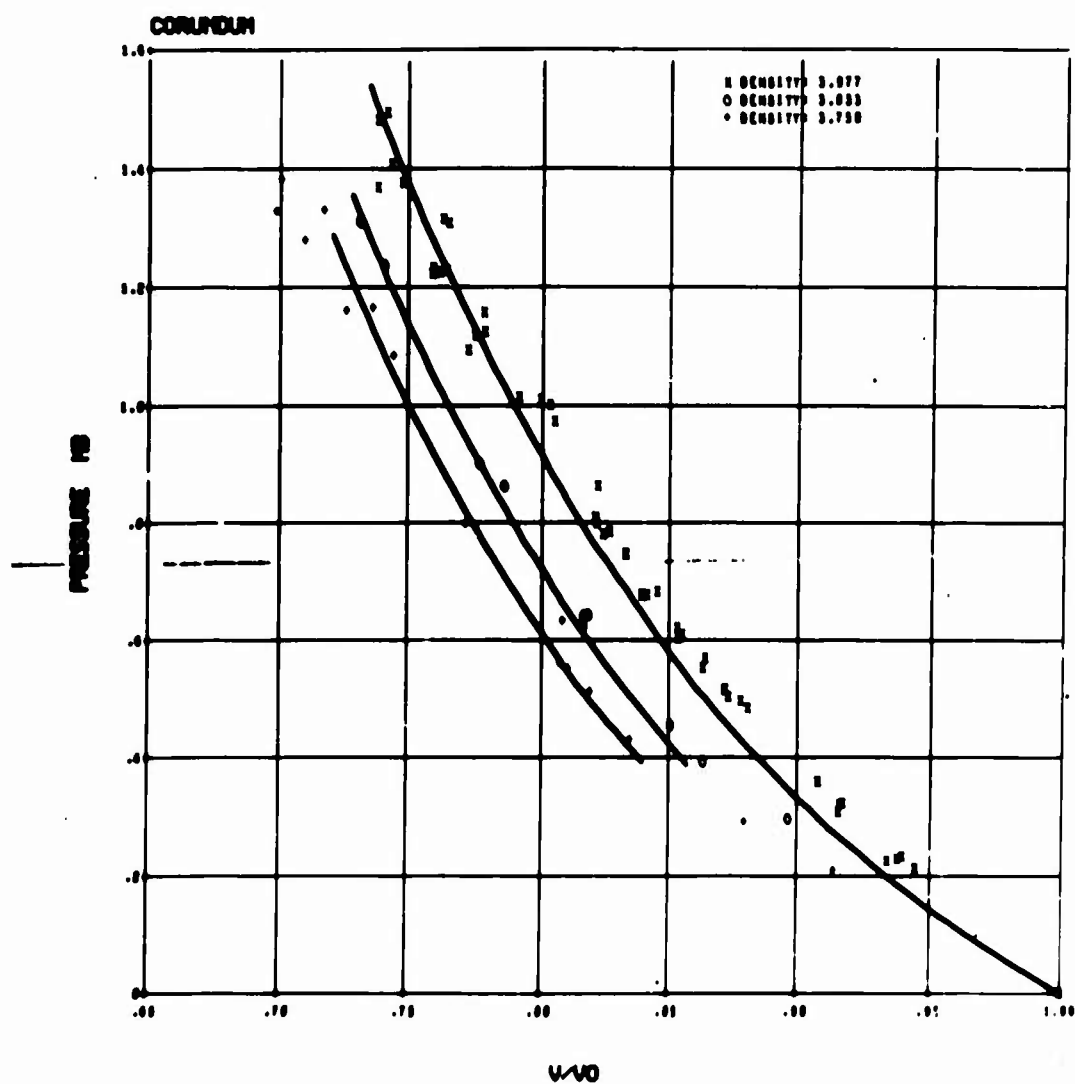
Figure 22. The Pressure-Volume Hugoniots for Al_2O_3 of Various
Initial Densities. The curves are the P-V transforms of the U_s-U_p
curves in Fig. 21. For the crystal-density curve it appears that
there is a residual shear stress in excess of 50 kb for practically
all the 3.98 g/cm^3 data points.

87
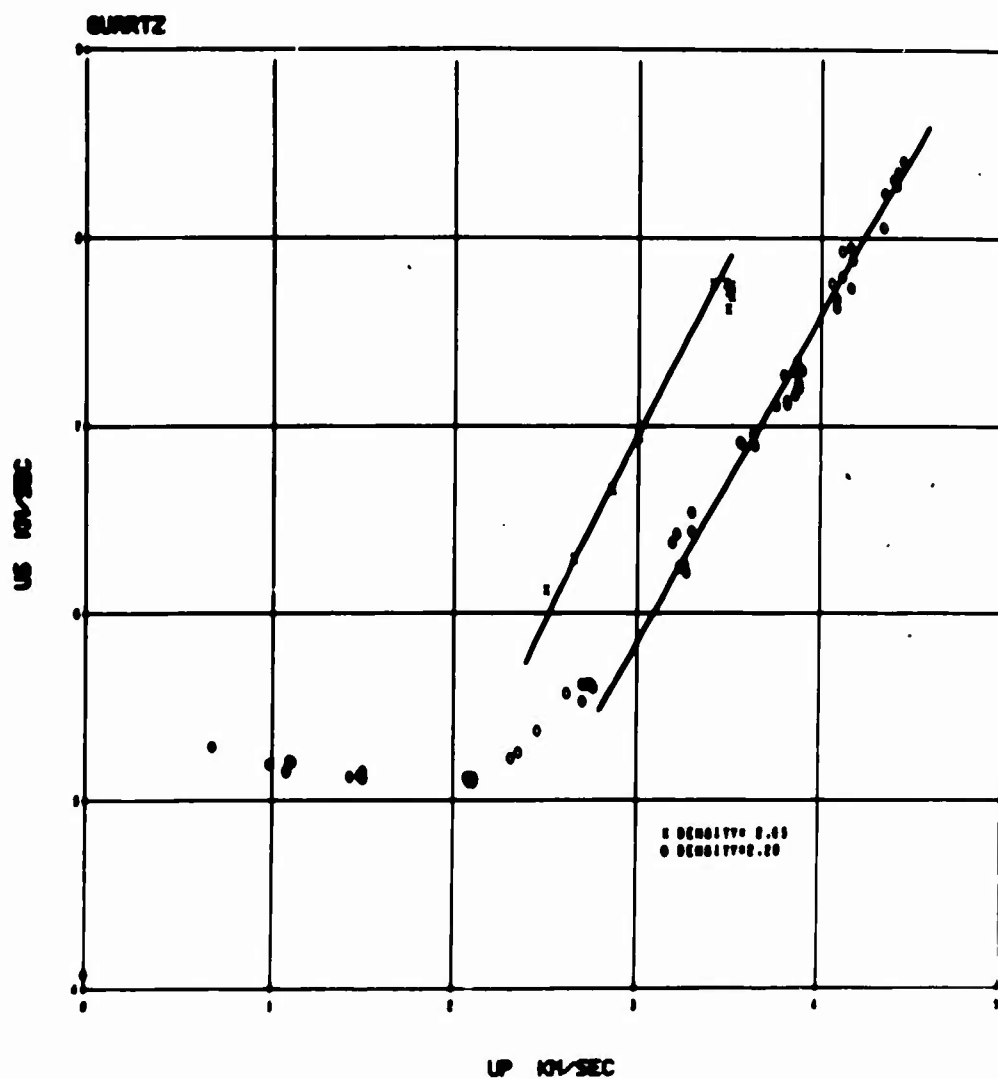
Figure 23. Shock-Particle Velocity Hugoniots for Wackerle's (3)
Crystal Quartz Data and Some More Recent Fused-Quartz Data.
The fused quartz data were used to determine the equation of state
parameters for stishovite. Only the data for $U_p > 3.0$ km/sec were
used. The curve through the crystal quartz data was calculated
from the derived stishovite Hugoniot.

88
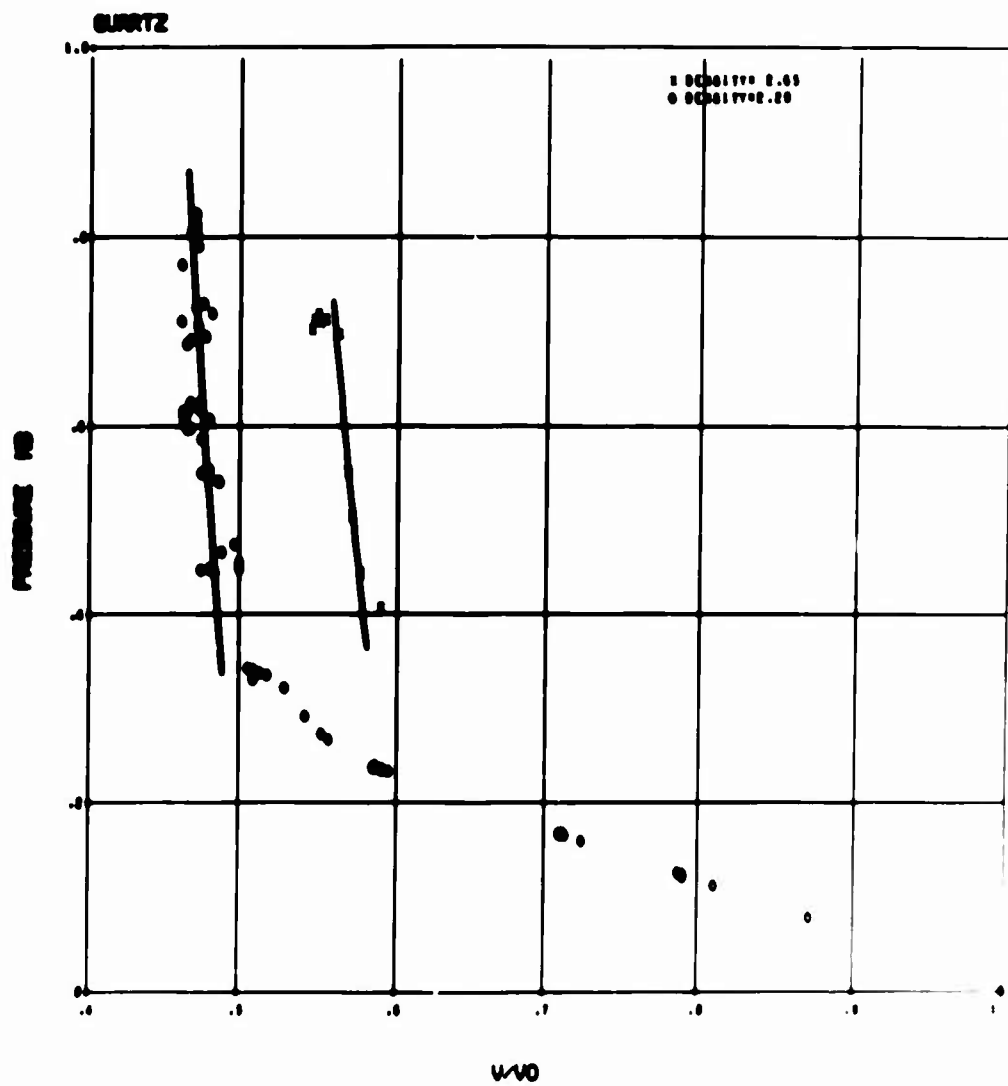
Figure 24. Pressure-Volume Hugoniots for SiO_2. The remarks for Fig. 23 apply here.
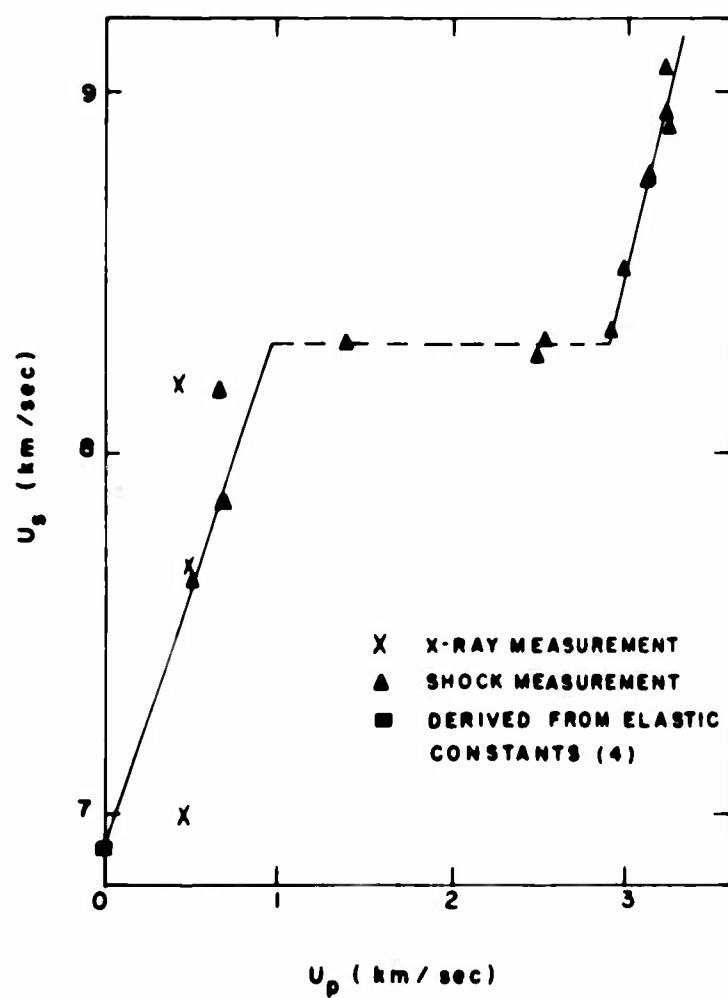
Figure 25. Shock-Particle Velocity Hugoniots for TiO_2. The dashed region at $U_s = 8.6$ km/sec has been interpreted to be due to a two wave structure caused by a phase change.
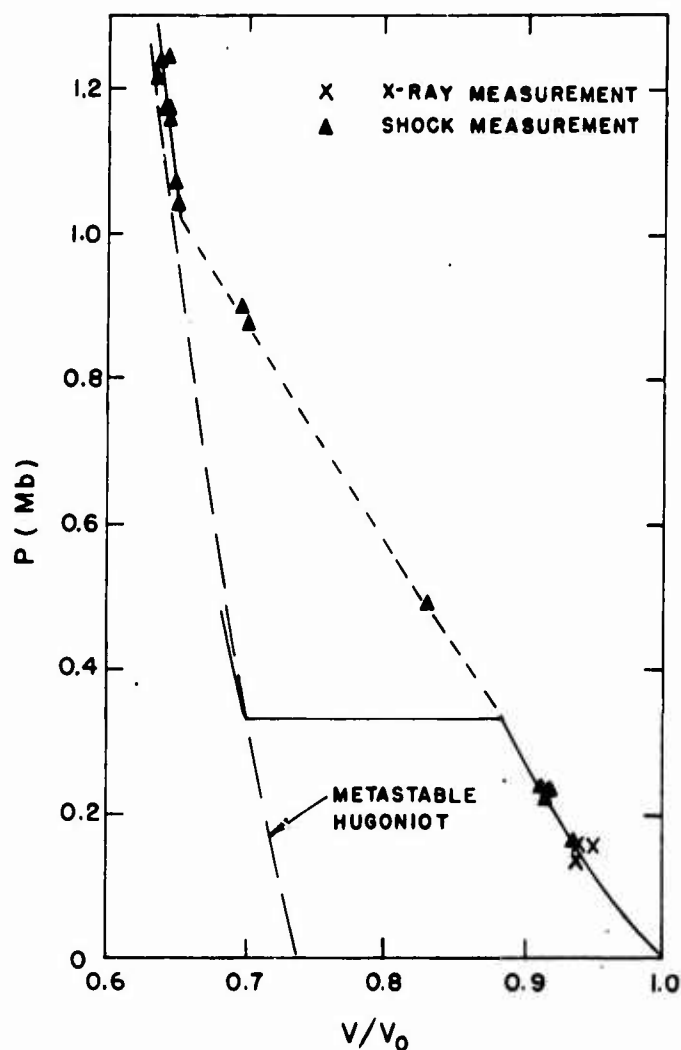
Figure 26. Pressure-Volume Hugoniot for TiO_2. The curve labelled "Metastable Hugoniot" is the one used (with the appropriate ΔE) in the mix calculations. It should be noted that only the data above 1.0 Mb is used in determining the metastable Hugoniot parameters C_0 and ρ_0 at $P = 0$. This looks like a rather insensitive way to determine these parameters and for this particular case indeed it is. However, for the present applications only the high-pressure regime is studied which is well represented by the calculated Hugoniot.
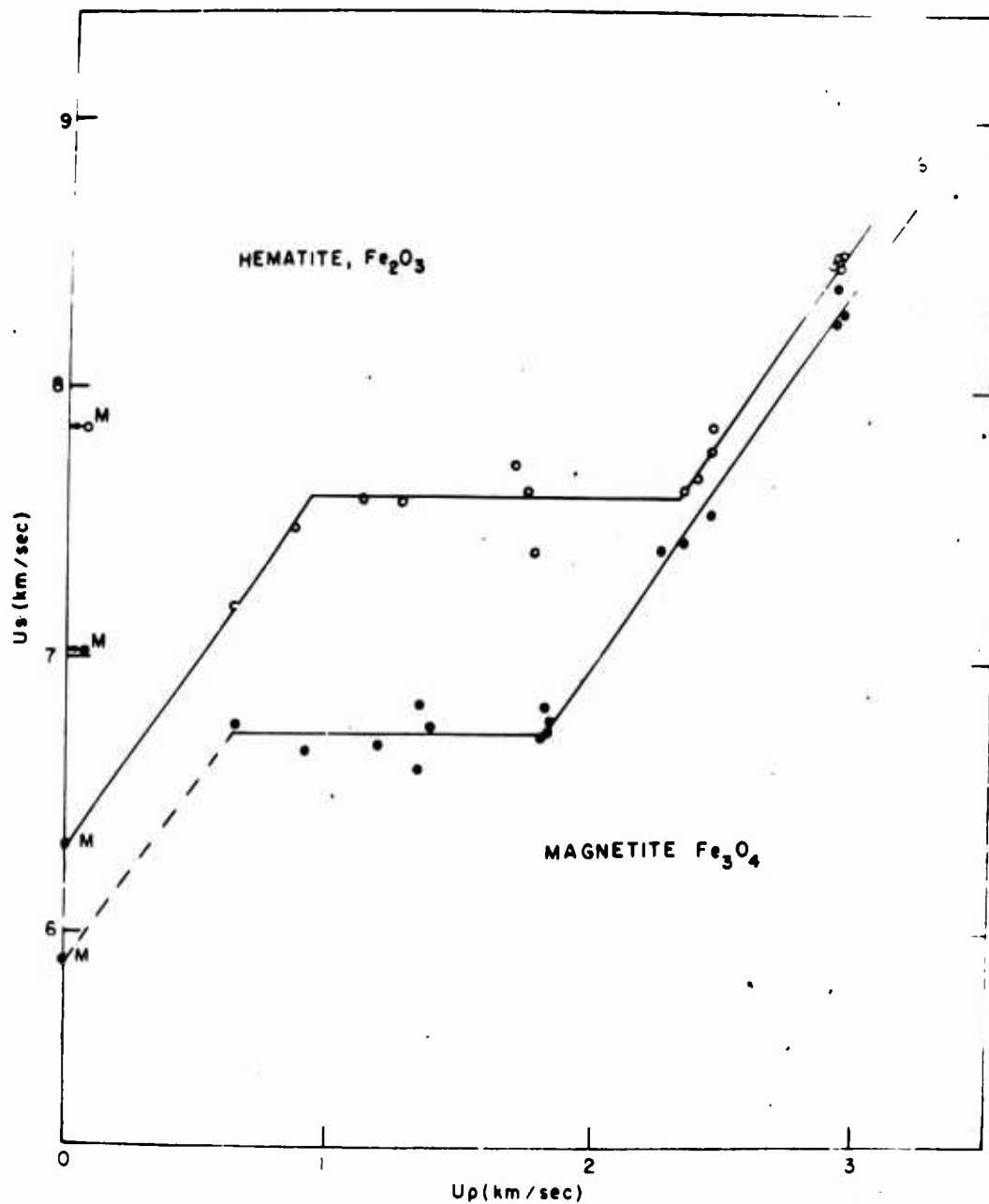
Figure 27. Shock-Particle Velocity Data for Hematite and Magnetite.
The upper data points above the transition region were used to
derive the metastable Hugoniots of these two materials. These
equations of state were then extrapolated on their "m" values to
obtain an estimate for the equation of state of FeO.
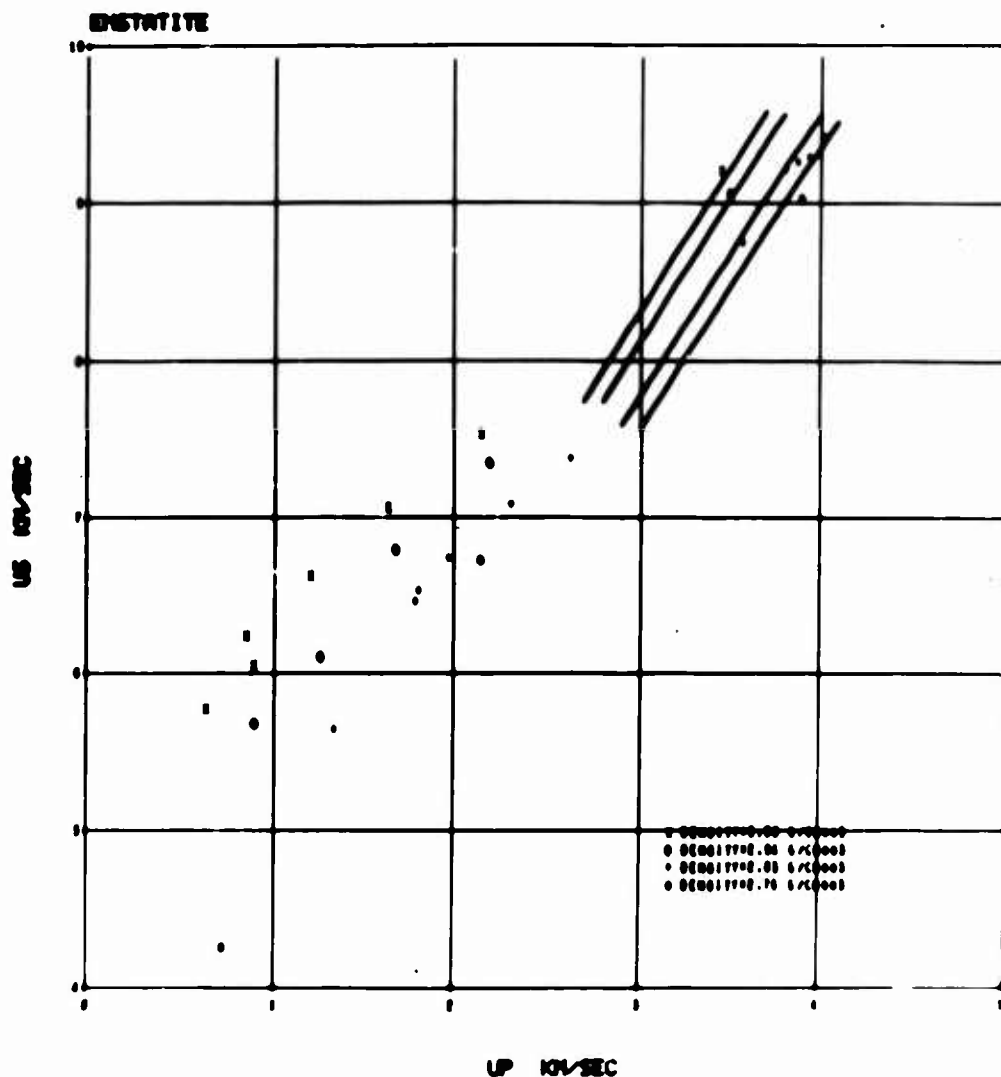
Figure 28. Shock-Particle Velocity Data for Enstatite. In this figure and those that follow the curves are the result of the mix calculation. Unfortunately, there is very little high-pressure data to compare with the calculations for this material, a situation that will be corrected. What there is does agree reasonably well with the calculated curves. It is felt that enstatite has at least one high pressure phase change and that these data are compatible with this assumption. It is very difficult to detect phase changes when using samples not at crystal density, especially if the volume change is small and if the phase changes do not go to completion in the shock front.

93
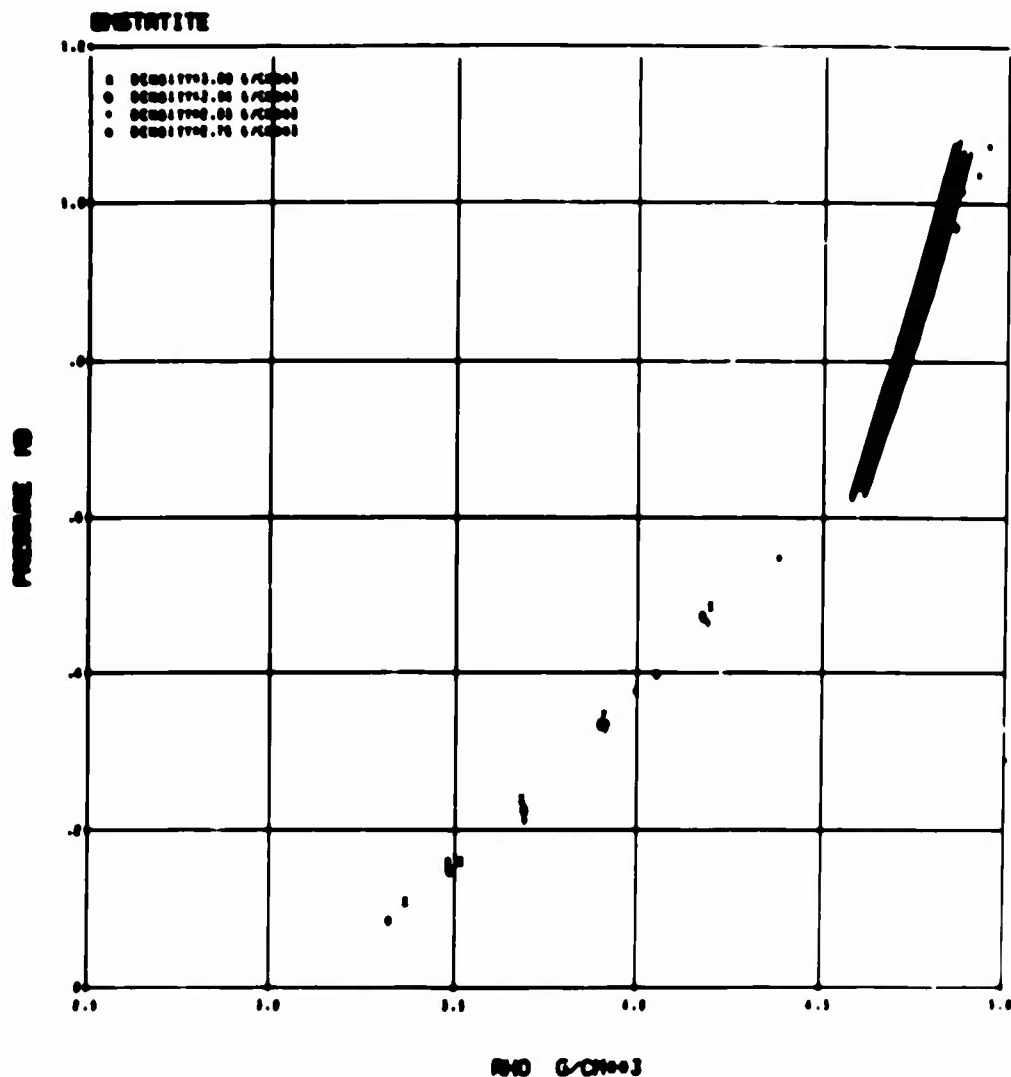
Figure 39. Pressure-Density Data for Enstatite. Remarks in
Fig. 38 apply here. A close examination of the data in the region
from 0.2 - 0.6 Mb reveals an apparent paradox, since in general
a material with a lower initial density should end up at a slightly
lower density. Since the data (Fig. 38) do not show evidence of
a two wave structure all points must be interpreted as representing
final states behind the shock front. The easiest explanation of this
dilemma is that thermodynamic equalibrium has probably not
been attained and that the higher temperatures reached for materials
with lower initial density has increased the reaction rates sufficiently
so that the phase change has gone more nearly to completion.

FORSTERITE

US KM/SEC

UP KM/SEC
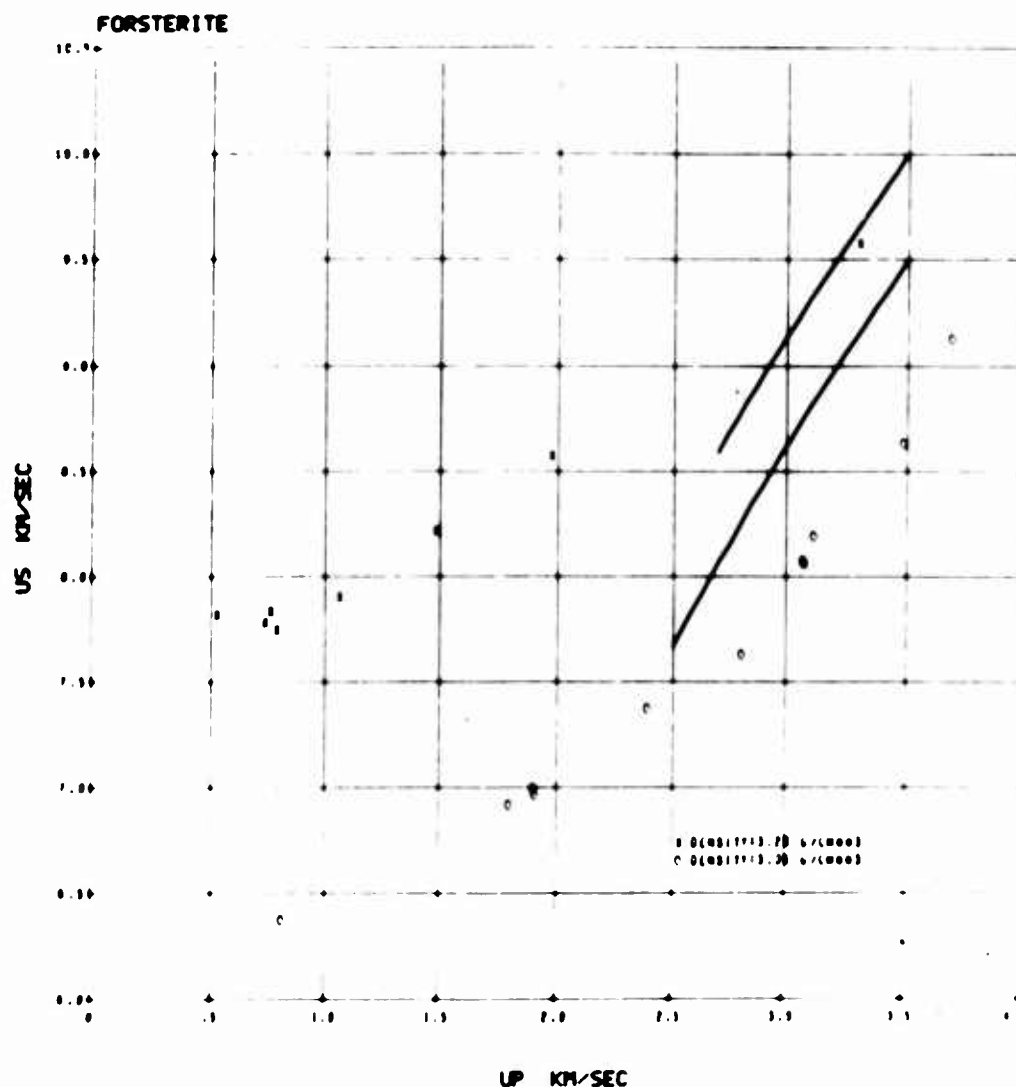
Figure 30 Shock-Particle Velocity Data for Forsterite. Remarks
in Figs. 28-29 are applicable here. Phase changes are indicated
by the data. The calculated curve is in reasonably good agreement
with the single high-pressure ρ_o = 3.2 g/cm^3 data point. However,
the ρ_o = 3.08 g/cm^3 data does not. The two sets of data are not
compatible since the effect of initial densities should not be this
large. This discrepancy is being investigated.
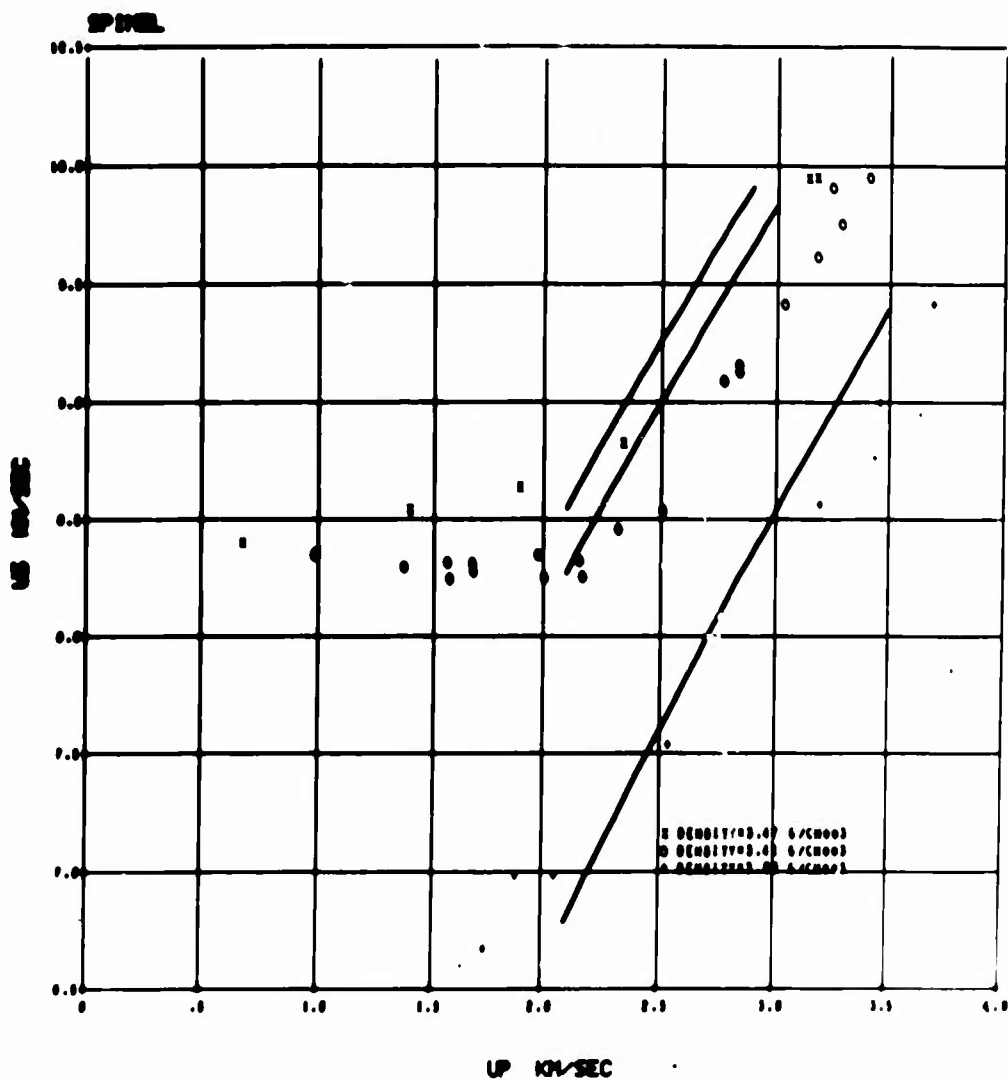
Figure 31. Shock-Particle Velocity Data for Various Initial Density
Spinels. The effect of density variations is adequately accounted
for but the calculated curves are all slightly too stiff showing that
the spinel lattice becomes slightly more compressible than predicted
by the straight forward mixing of MgO and Al_2O_3. The existence of a
transistion is well established.

96
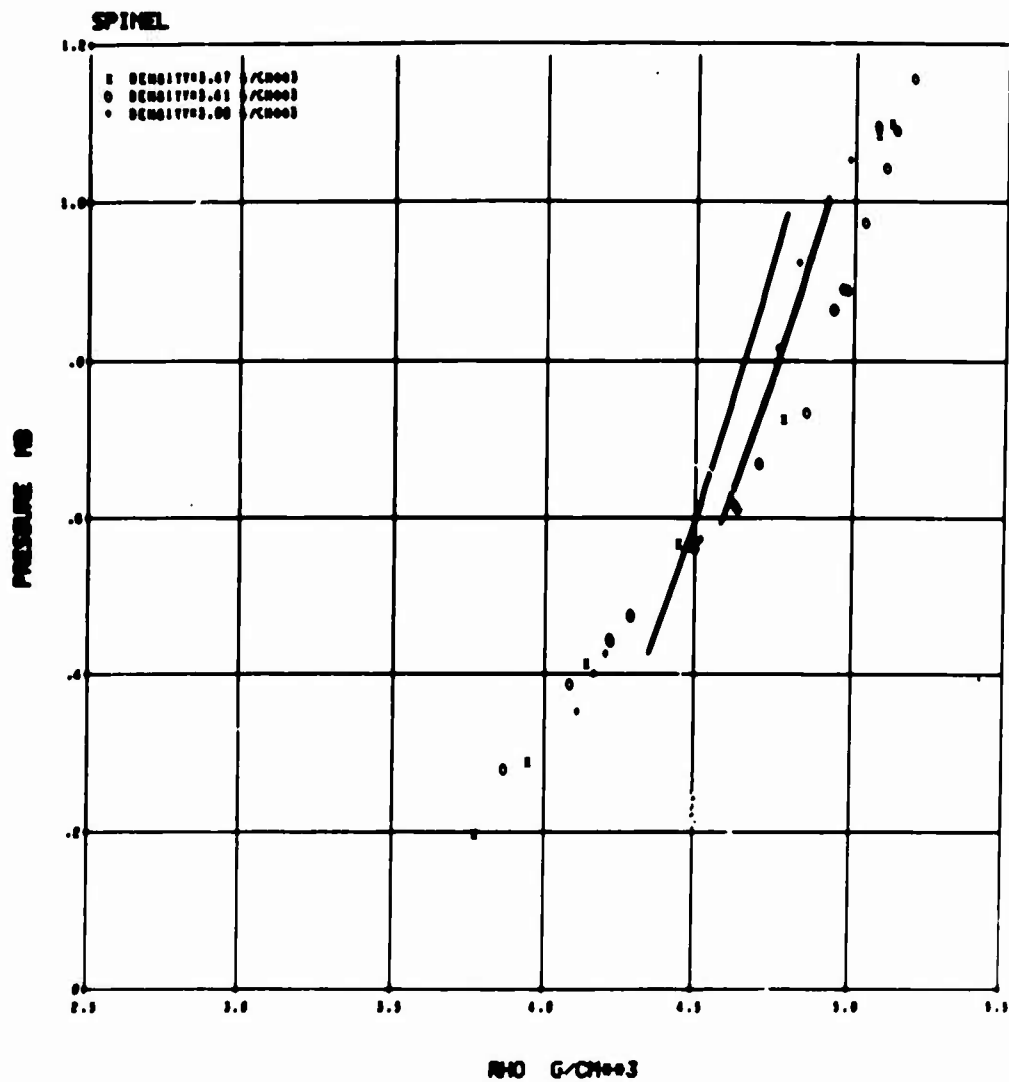
Figure 32. Pressure-Density Data for Spinel. This figure also
shows that the spinel structure becomes more dense after the
transition than would be indicated by simple mixing.
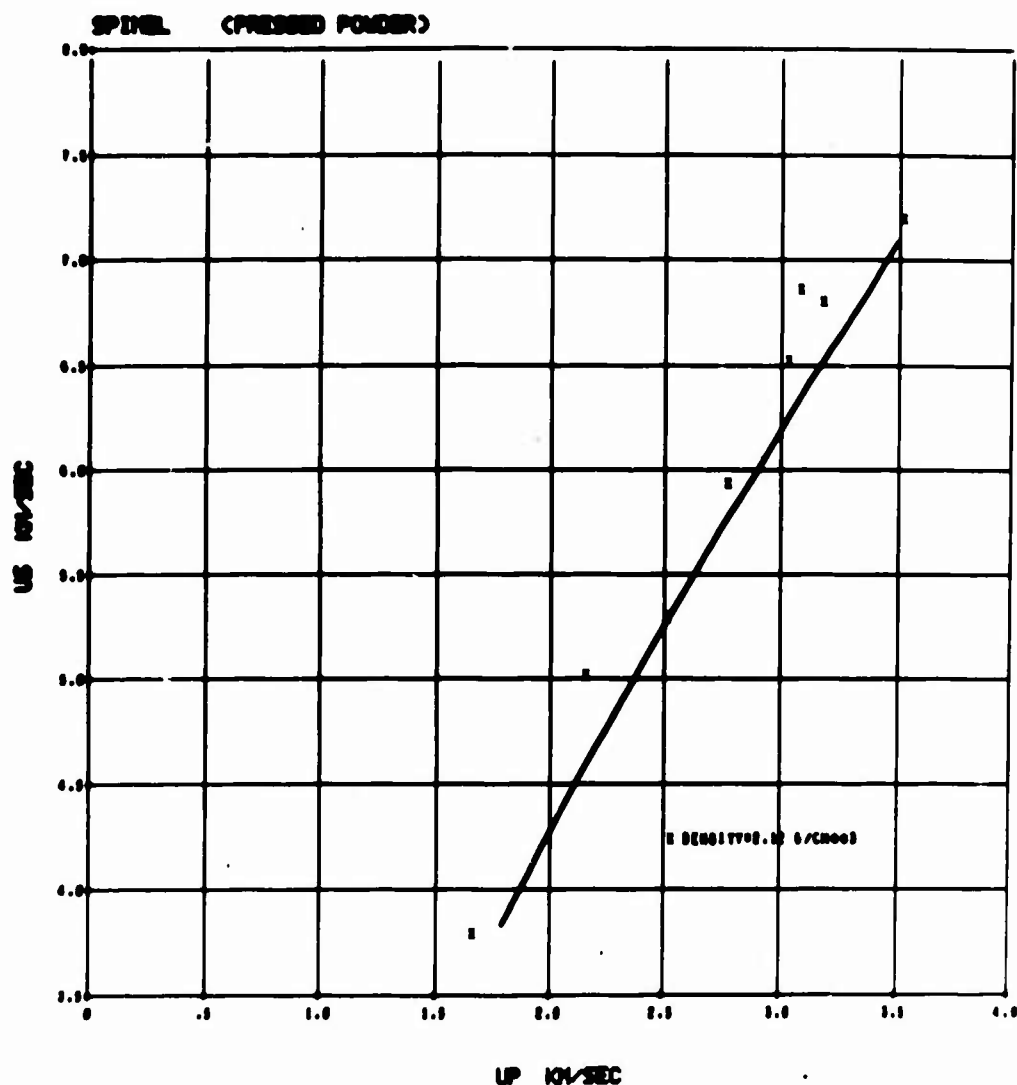
Figure 33. Shock-Particle Velocity Data for a Mixture of MgO and Al_2O_3 Powders. These samples used here were cold pressed from mixtures of MgO and Al_2O_3 with the spinel stoichiometric mass ratio. The calculated curve now lies slightly to the right of the data but in good agreement considering the large temperature correction requirement for the very low initial density of the pressed samples. These samples become very hot in the shock compression but it is felt that very little chemical reaction can occur in short time available in the shock front. The particle size is in the 10μ range.

98
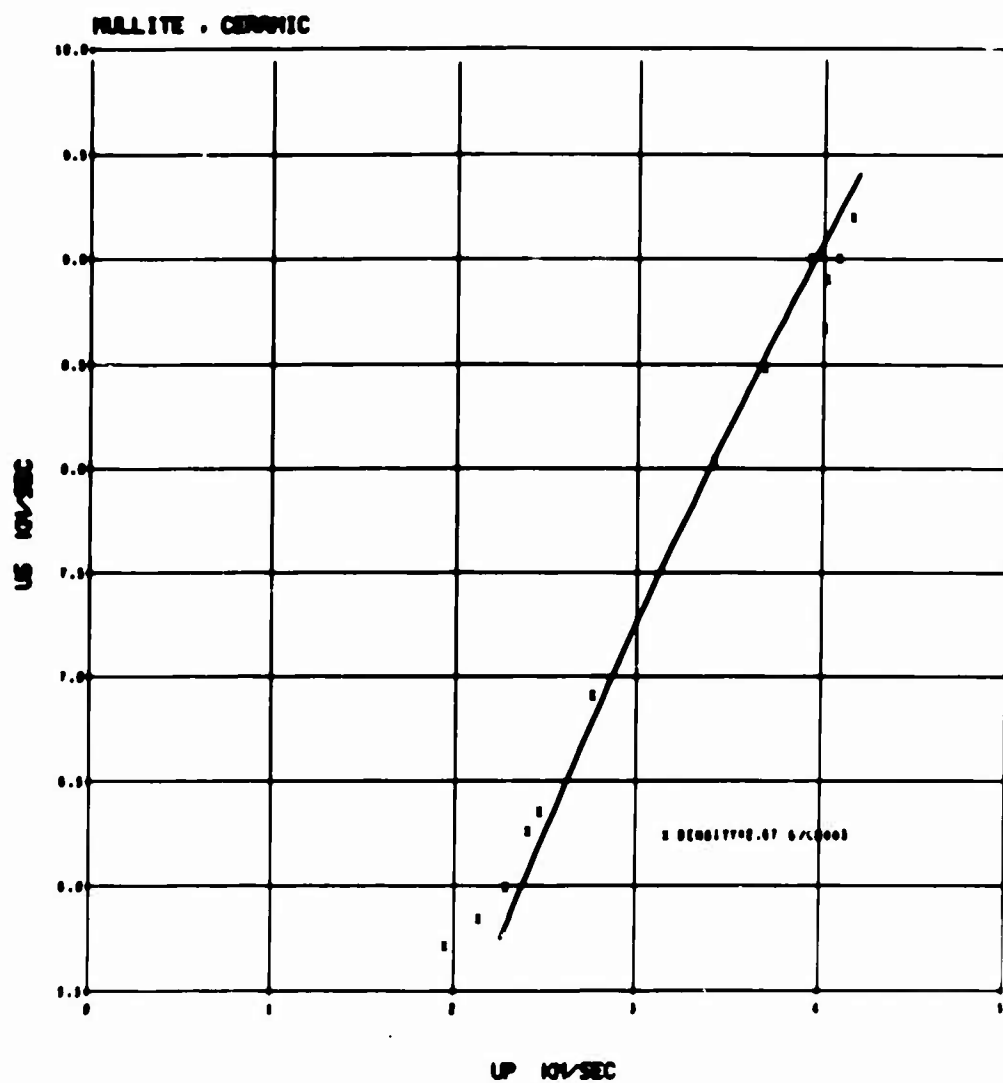
Figure 34. Shock-Particle Velocity Data for Ceramic Mullite.
The calculated curve is in good agreement with the data. The
low-pressure data points are high and are thought to be reflecting
the last bit of the phase change.
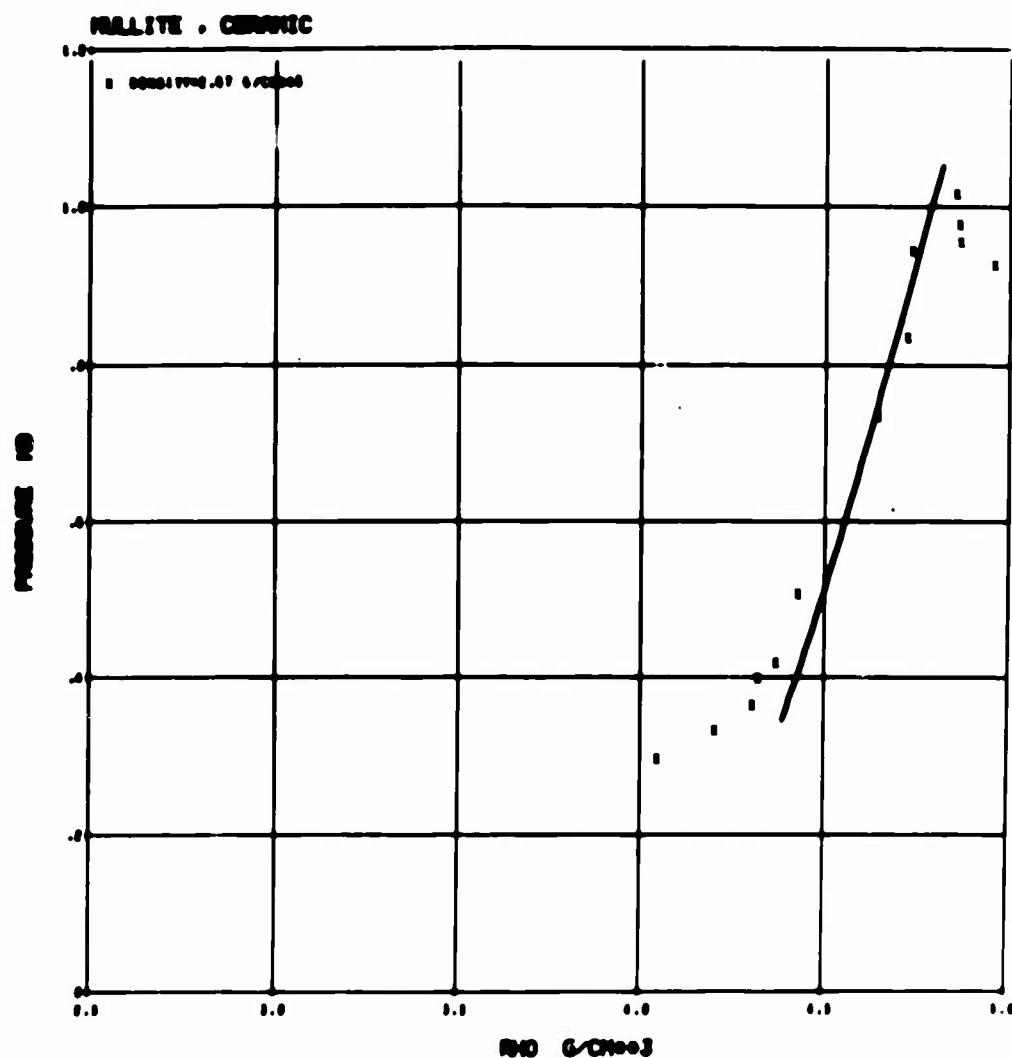
MULLITE . CERAMIC

Figure 35. Pressure-Density Data for Ceramic Mullite. The
agreement between this data and the calculated curve is judged
to be satisfactory here also. The low-pressure data again indicates
an incomplete transformation. The scatter in the high-pressure
data could be caused by the rarefaction release wave interacting
with the shock wave in samples with too great a thickness. This
is an extremely critical problem for materials that have transformation
with large density increases and the associated very high-velocity
sound waves.

100
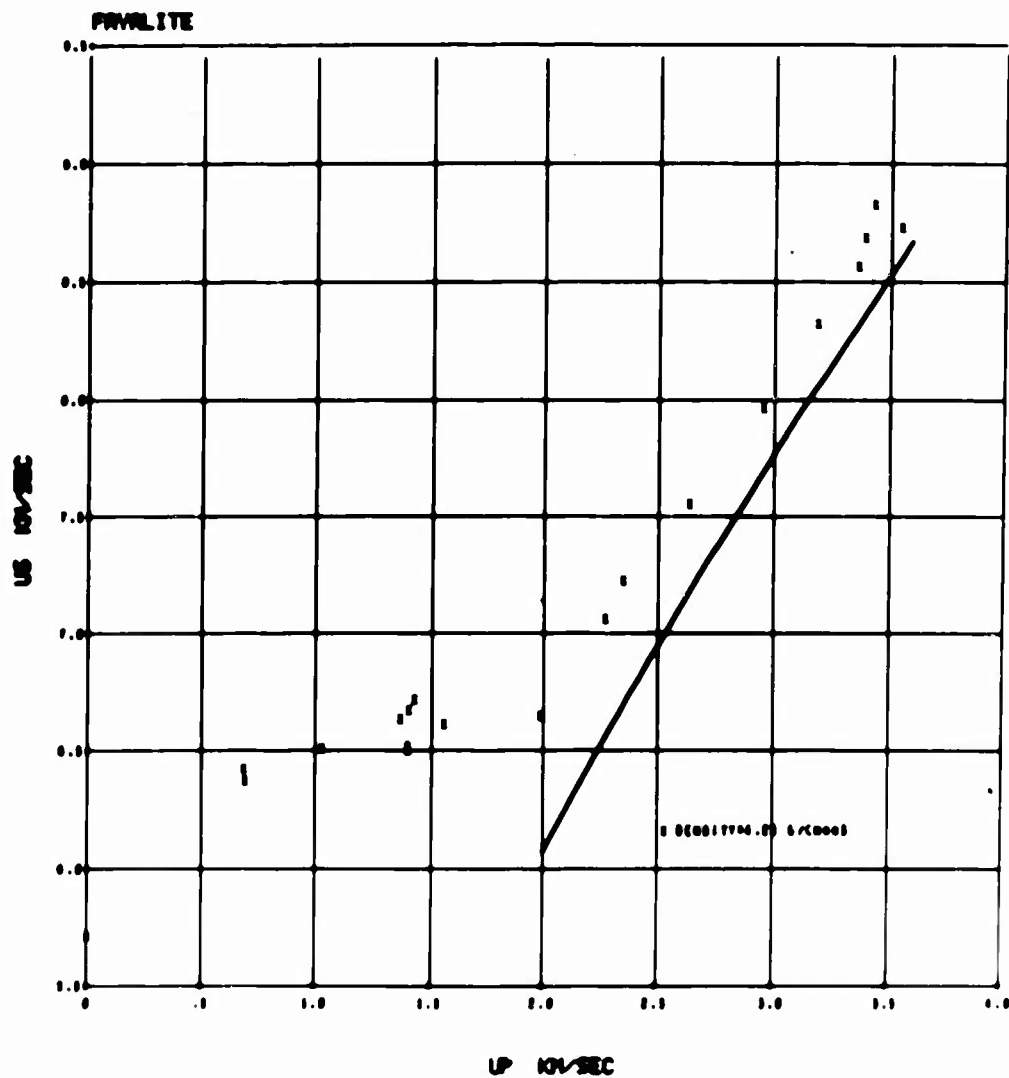
Figure 36. Shock-Particle Velocity Data for Fayalite. The
agreement is not as good as we would like for this important
geophysical material. The poor agreement can not be due to the
same effects seen for the spinels as the calculated curve is too
soft here. Most likely the difficulty lies in an incorrect equation of
state of FeO used in the calculations. A more direct determination
of the equation of state of FeO is certainly desired.

101
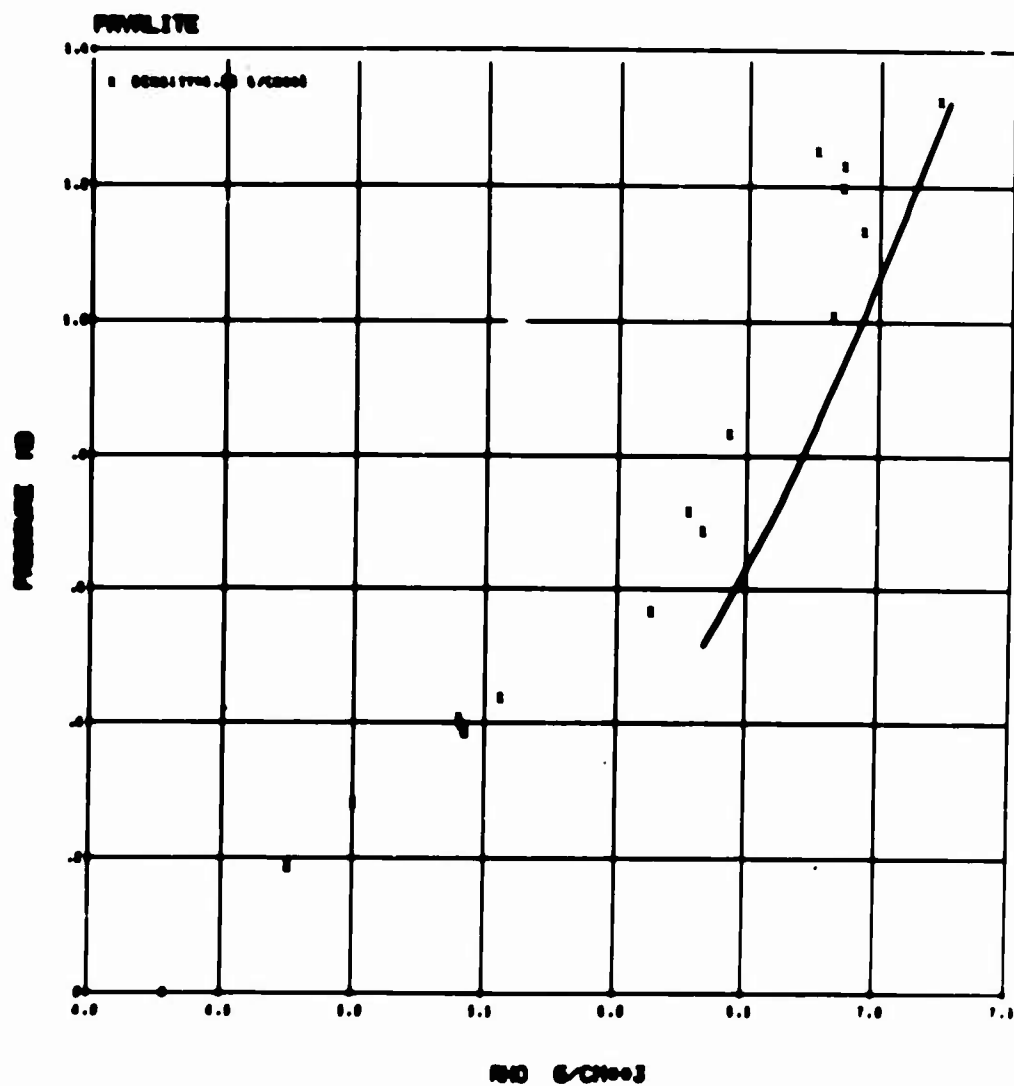
Figure 37. Pressure-Density Hugoniot for Fayalite. This again shows that perhaps the assumed equation of state for FeO is a bit too compressible.

102
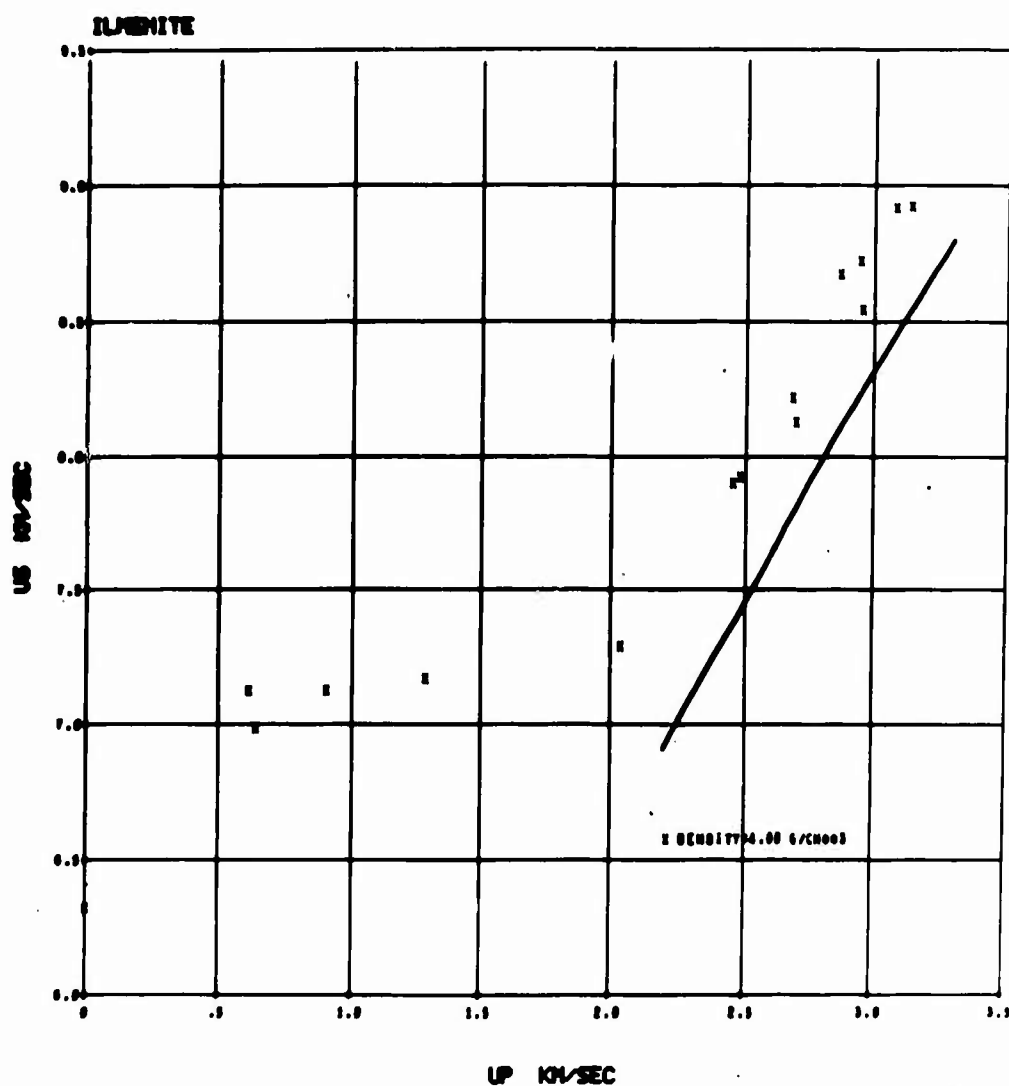
Figure 38. Shock-Particle Velocity Data for Ilmenite. The agreement with the data and calculated curve is remarkably similar to that of fayalite giving additional support to the idea that the equation of state of the FeO used in the calculation is a bit too soft. The existence of a phase change is well indicated here.

103
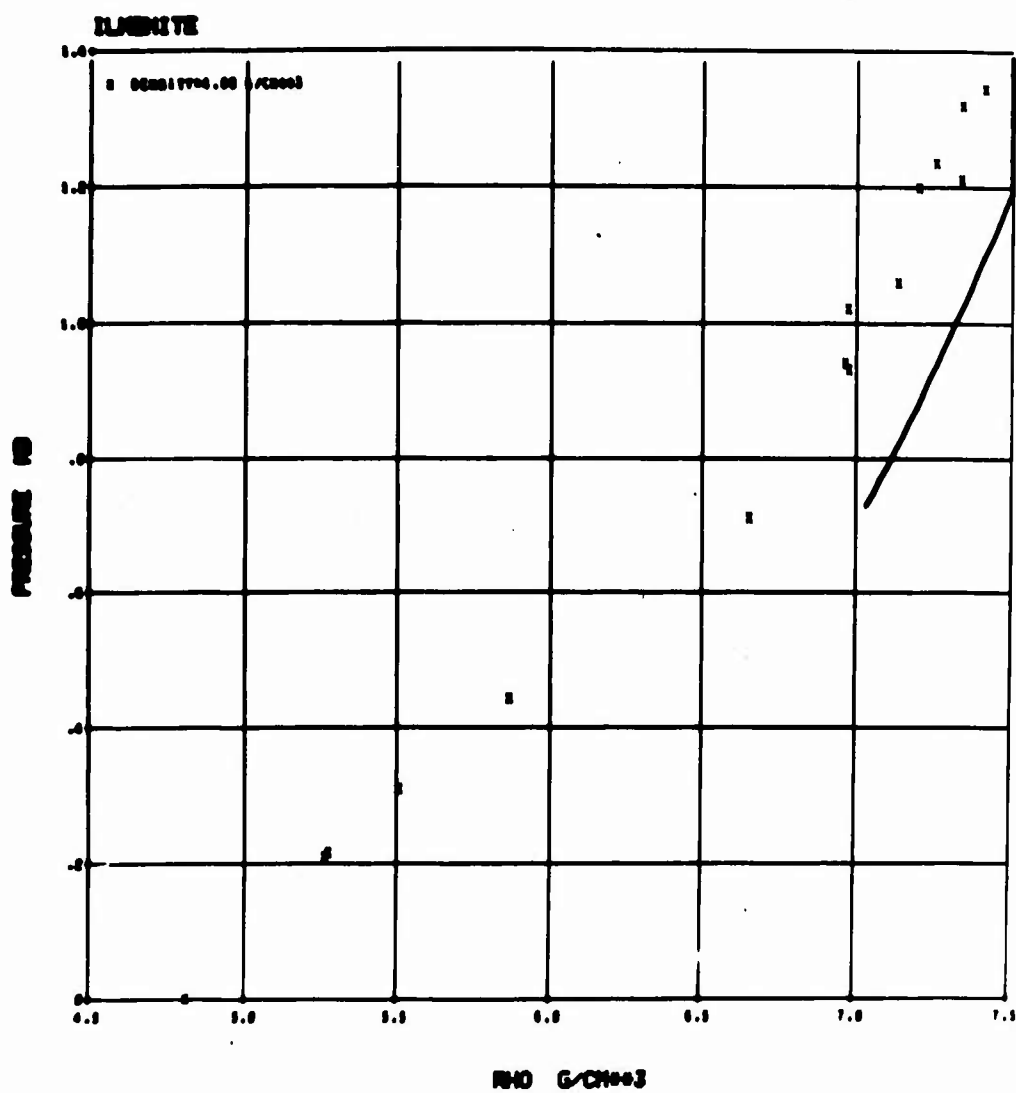
Figure 39. Pressure-Density Hugoniot Data for Ilmenite. Remarks in Figs. 37 and 38 are applicable here.

104
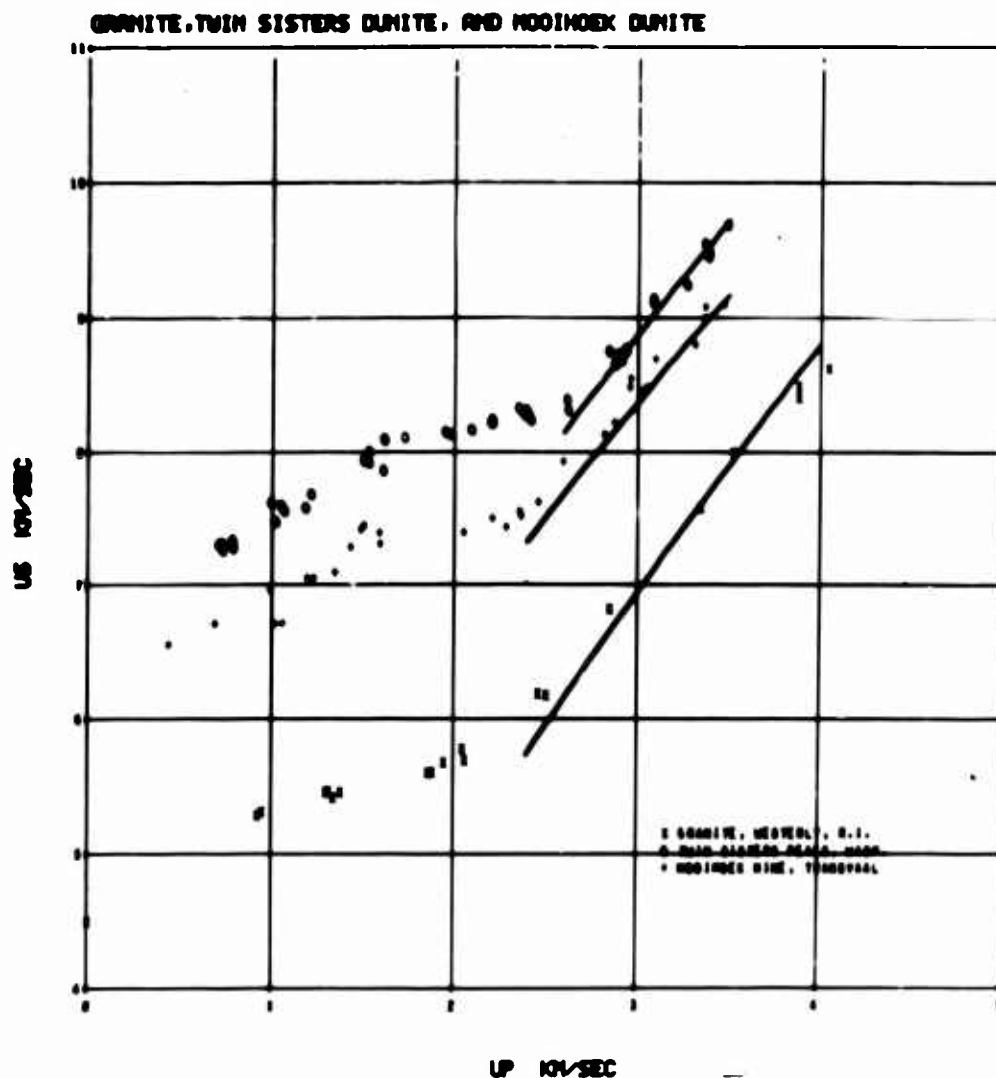
Figure 40. Shock-Particle Velocity Data for Two Dunites and One Granite. The agreement with the data and the calculated curves is as good as one could hope for. If the equation of state for FeO is made slightly stiffer the calculated curves for the two dunites will move to the left. The iron rich dunite (Mooihoek) will be displaced the most which could bring even these results into better agreement.
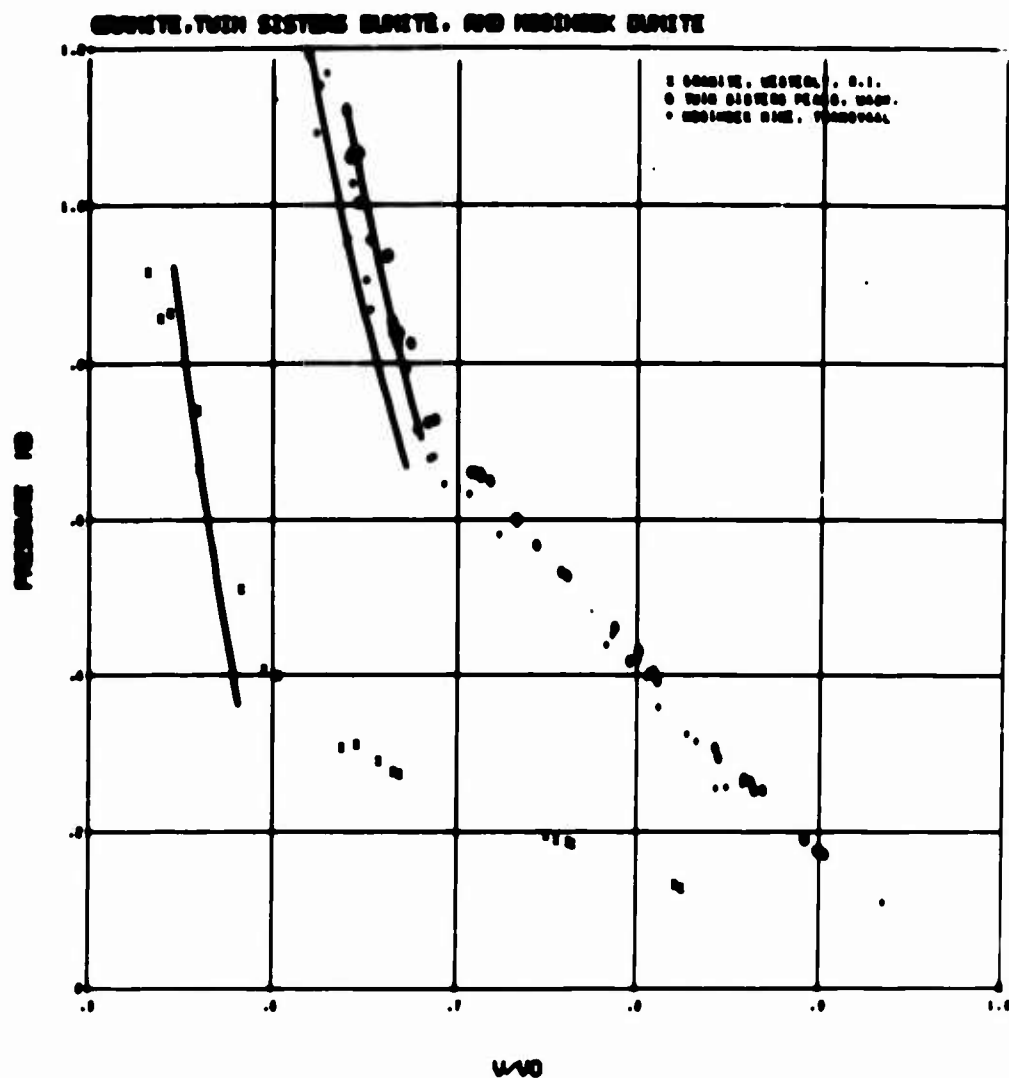
Figure 41. Pressure-Volume Hugoniot Data for Three Rocks.
Remarks for Fig. 40 are applicable here.

SHOCK WAVE EQUATIONS OF STATE FOR ROCKS AND MINERALS[*]

D. L. Anderson
Seismological Laboratory
California Institute of Technology
Pasadena, California

H. Kanamori
Earthquake Research Institute
University of Tokyo

ABSTRACT

Murnaghan, Birch-Murnaghan and linear U_s - U_p equations of state are fit to shock wave data for 9 rocks and 10 minerals. If a phase change occurs, parameters of the high-pressure phase are found from both the raw Hugoniot and an estimated metastable Hugoniot. Since the zero-pressure density of the high pressure phase is unknown, the equation-of-state parameters are found for a range of ρ_0. The zero-pressure densities of the high-pressure phases are estimated from an empirical relationship between the density and the zero-pressure slope of the Hugoniot. The parameter (dK dP), which is related to the Grüneisen ratio, is found to decrease across phase changes and upon iron substitution.

Most of the materials collapsed to a denser phase when shocked to sufficiently high pressure. These polymorphic transitions involve a considerable reduction in volume, ranging from 38 to 60% for feldspar and quartz rich rocks such as albitite, anorthosite and granite, to 20% for such basic rocks as diabase and dunite to about 12% for some dense, already closely packed minerals such as spinel, hematite and magnetite.

INTRODUCTION

Shock wave data is the only present source of information concerning the compressibility and polymorphism of silicates and oxides at pressures in excess of 300 kilobars. This data complements the lower pressure ultrasonic and x-ray diffraction data and the relatively low-pressure, high-temperature phase equilibria studies on silicates and analog compounds.

Prior to the availability of shock-wave data, discussions of the composition and crystal structure of the deep mantle relied heavily on the extrapolation of low pressure data by use of semi-empirical equations of state, ma   those due to Birch and Murnaghan, and on the study of materials thought to be useful analog   materials in the earth's mantle. It is now possible to make direct comparisons of seismic data with the density and compressibility of a variety of materials tested with shock-wave techniques.

Most silicates which have been shocked to sufficiently high pressure undergo solid-solid phase changes, supporting conclusions based on the behavior of analog compounds (Birch, [1]; Ringwood, [2]). The behavior of these high-pressure phases as a function of temperature and pressure and their zero pressure properties can be extracted from the present shock-wave data only after a variety of assumptions have been made.

As a first step in any reduction scheme it is convenient to fit the raw shock-wave data with a simple equation of state.

ANALYSIS

We have fitted the raw Hugoniot data with the Birch-Murnaghan equation of state

$$P_H = (3K_0/2)\left[(\rho/\rho_0)^{7/3} - (\rho/\rho_0)^{5/3}\right]\left\{1 - \xi\left[(\rho/\rho_0)^{2/3} - 1\right]\right\} \tag{1}$$

where the adjustable parameters are K_0, the zero pressure bulk modulus, and ξ which is $(3/4)$ $(4 - K_0')$ where K_0' is the pressure derivative of K at $P = 0$. As initially derived equation 1 is an isothermal equation of state but, as Clark [3] has pointed out it is also appropriate, with different K_0 and ξ, for adiabatic compression. It is also a useful two-parameter equation for fitting raw Hugoniot data. For most isothermal compression experiments $|\xi| < 0.5$ with zero being its most frequent value [1].

The raw Hugoniot data has also been fitted to a Murnaghan equation of state

$$P_H = (K_0/n)\left[(\rho/\rho_0)^n - 1\right] \tag{2}$$

where K_0 and n are the adjustable parameters. The parameter n is K_0', a number close to 4 for many elements and compounds. This form of the Murnaghan equation of state is based on the assumption that the bulk modulus is a linear function of pressure.

A third equation of state which has been used to fit Hugoniot data is the linear $U_s - U_p$ equation (McQueen, et al., [4]) which leads to

$$P_H = K_0[1 - (\rho_0/\rho)]/[1 - \lambda\{1 - (\rho_0/\rho)\}]^2 \tag{3}$$

This again is a two-parameter equation of state where K_0 and λ are the parameters to be found from the data.

When the shocked material transforms at high pressure to a new phase, the zero pressure density, ρ_0, of this new phase is usually not known. This turns equations 1, 2 and 3 into 3 parameter equations of state where ρ_0 must also be determined by the shock wave results. This places severe demands on available shock-wave data considering the small number of points and the scatter in the high-pressure regime. In some cases, the density of the presumed high-pressure phase is known, e.g., stishovite, in the case of shocked quartz. In most other cases, the shock-wave data itself is the only direct information regarding the properties of the high-pressure phase.

108

Our approach will be to fit the Hugoniot data with several values for ρ_0. In most cases, an equally good fit can be obtained for a fairly wide range of initial densities, indicating that this parameter cannot be determined with any precision directly from the data. In a later section we will invoke an empirical relationship between K_0 and ρ_0 to decide which ρ_0 is most appropriate.

An analytic expression for the raw Hugoniot data facilitates the reduction of this data to metastable Hugoniots, adiabats and isotherms. For example, the difference in pressure at a given ρ ρ_0 between the raw Hugoniot data, with the low-density phase as starting material and the metastable Hugoniot with the high-pressure phase as the starting material is (McQueen, et al., [5])

$$\Delta P = [\rho \gamma (x P - 2 \rho_b \Delta E_0)] [\rho_b (2 + \gamma) - \rho \gamma] \tag{4}$$

where x is the relative difference in density between the zero pressure densities of the high- and low-pressure phases $(\rho_b - \rho_a) / \rho_a$, γ is the Grüneisen ratio of the high-pressure phase. ΔE_0 is the difference in formation energy and ρ is the density at pressure P on the raw Hugoniot. There is a similar offset of the Hugoniot from the corresponding hydrostat due to one dimensional strength effects (Ahrens, personal communication).

EQUATION-OF-STATE PARAMETERS

Most of the shock-wave data used in the present analysis was supplied in preprint form by Robert G. McQueen and represents work done at Los Alamos by McQueen, Marsh and Fritz. Some of it has subsequently been published by McQueen, et al. [4] and Birch (Clark, [6]). The reader is referred to these two sources for tabulations of the original data.

All of the materials tested except MgO, Al_2O_3, MnO_2 and possibly eclogite, underwent phase changes at high pressure. The parameters in table I refer to the high-pressure phase. A starting density, ρ_0, is assigned and the Birch-Murnaghan parameters $\phi_0 = K_0 / \rho_0$ and ξ are found by a straightforward least squares fit to the raw Hugoniot data; these are tabulated in columns 2 and 3 of table I. The Murnaghan parameters $\phi_0 = (K_0 / \rho_0)$ and $n = (dK/dP)_0$, representing a least-squares fit of equation 2 to the data for an assigned ρ_0, are given in columns 4 and 5. The parameter $(\rho_0 / \overline{M})(\phi_0^{-1/3})$ will be discussed later. The last column in table I gives the pressure range over which the data was obtained. The relative standard deviation of the computed and measured densities is always less than 1% and usually less than 0.5%. There is very little difference in the goodness of fit over the adopted range of ρ_0. For example, the best fit Murnaghan equation to the iron rich dunite Hugoniot data with a zero pressure density of 4.5 gm/cm^3 gives a relative standard deviation of 0.785% in density. For an initial density for the high-pressure phase of 4.7 gm/cm^3, the best fit Murnaghan equation has a relative standard deviation of 0.782%. Comparable results are found for all the materials in table I. As far as providing an adequate fit to the experimental data itself, any of the combinations of ρ_0, K_0 and ξ or n can be considered equally satisfactory. However, quite different results would be obtained upon extrapolation or differentiation.

109

Note that ξ increases and n decreases as the trial ρ_0 is increased.

Table II gives an example for two starting densities of the computed versus the measured parameters as a function of pressure for the Twin-Sisters dunite. The measured compression, density and pressure are given in the first three columns. The pressure at corresponding compressions determined from the best fit Birch-Murnaghan equation with $\rho_0 = 3.90$ gm/cm^3 is given in the fourth column. The standard deviation in pressure is 28.5 kb or 3.10%. The slope of the fitted Hugoniot $(dP/d\rho) = \Phi$ is given in column five. The parameters of the best fit Birch-Murnaghan equation with $\rho_0 = 3.90$ gm/cm^3 are $\xi = 0.37$ and $\phi_0 = 51.6$ (km/sec)^2. The corresponding parameters with $\rho_0 = 4.00$ gm/cm^3 are $\xi = +0.20$ and $\phi_0 = 65.0$ (km/sec)^2. The computed pressures for this case are within 1 or 2 kb of those computed previously, and the standard deviation is 28.7 kb or 3.12%. The slope of the Hugoniot, as a function of pressure, is very similar for these two cases. The density and ϕ as a function of pressure computed from the best fit Murnaghan equation for these two densities are given in the last four columns. Again, the fits are equally satisfactory for both starting densities; note that the Φ's are 4 to 10% higher than given by the Birch-Murnaghan equation which indicates that some care must be taken when comparing seismic velocities with shock wave results. McQueen, et al. [4] give an equation for determining the adiabatic bulk sound velocity from the slope of the Hugoniot.

ESTIMATION OF METASTABLE HUGONIOT

McQueen, et al. [5] presented a method for correcting observed Hugoniot data of a high-pressure phase to the Hugoniot that would result if the high density phase were the (metastable) starting material. As formulated by [5], the correction involves the Grüneisen ratio, γ, at high pressure, the transition pressure, P_t and the difference of formation energy of the high pressure and low pressure polymorphs, ΔE_0 (see equation 4). McQueen, et al. [4] applied this technique in an elaborate study of twelve rocks of geophysical interest. In previous sections, we have fitted Birch-Murnaghan and Murnaghan equations of state to raw Hugoniot data, uncorrected for the effects of strength, phase changes and temperature.

In this section we estimate the offset of the metastable from the raw Hugoniot curve ana fit a linear U_s - U_p equation of state to this corrected data.

The transition pressures and density changes at the transition were estimated from the raw data; γ of the high-pressure phase was arbitrarily taken as unity. The change in entropy at the transition has been ignored. The results, however, are not very sensitive to ΔE_0. A complete discussion of more accurate reduction techniques are given in [4] and Ahrens and Anderson [7]. The present purpose is simply to investigate the difference in the inferred zero pressure properties when corrected, rather than raw, Hugoniot data are used.

Table III summarizes the parameters (λ, K_0) of linear U_s - U_p equations ate fit to the metastable Hugoniot data by least squares with different assumptions regarding the zero-

110

pressure density of the high-pressure phase. In this table, ρ_0 is assigned and λ and K_0 are determined by the data. The Grüneisen ratio of the high-pressure phase is determined with Slater's assumption

$$\gamma_0 = 2\lambda - 1$$

The trial range of ρ_0 was found by graphical extrapolation of the high pressure Hugoniot data. Other considerations, to be discussed later, indicate that, in most cases the zero-pressure density has been underestimated. The elastic parameter Φ_0 is simply K_0/ρ_0.

In figures 2 through 18 the region marked P_H is the range of metastable Hugoniots which corresponds to the indicated range of assumed zero-pressure densities (the heavy bar above the zero-pressure axis). In some of the figures, the points on the metastable Hugoniot calculated by McQueen, et al. [4] are shown by horizontal bars or crosses. The heavy bar below the zero-pressure axis is the range of ρ_0 determined by McQueen, et al. [4]. The X is the zero-pressure density found in the present paper.

The regions on these figures marked P_K are isotherms computed by integrating the Mie-Grüneisen equation of state (see, for example, Takeuchi and Kanamori, [8]). The assumed vibrational energy E_{HO} for each material is given in table III. The results are not very sensitive to the value of E_{HO}. Again, the range indicated corresponds to the range of initial densities.

ESTIMATION OF ZERO-PRESSURE PROPERTIES OF HIGH-PRESSURE PHASES

A wide range of zero-pressure densities and compressibilities satisfy the high-pressure shock-wave data equally well. The range can be considerably narrowed by invoked physical or intuitive constraints such as: (1) the density of the high-pressure phase should be greater than the density of the low-pressure phase; (2) the bulk modulus of the high-pressure phase should be greater than the low-pressure phase; (3) the pressure derivative of the bulk modulus is probably less for the more closely packed phase; and, (4) the bulk modulus probably increases with pressure at sufficiently high pressure. Some of these constraints may be violated if the high-pressure transformation has not gone to completion.

We invoke the seismic equation of state (Anderson, [9]), an empirical relationship between the zero-pressure density, ρ_0, mean atomic weight, $\overline{M}$, and the slope, at zero pressure, of the density-pressure curve, $\phi_0 = (\partial P/\partial\rho)_0$. A least-squares fit to ultrasonic data on 31 minerals and oxides with mean atomic weights between 18.6 and 33.1 yielded

$$\rho_0/\overline{M} = 0.048 \, \Phi_0^{0.323} \tag{5}$$

Alternatively, since $\Phi = K/\rho$, where K is the bulk modulus

$$K_0 = 20.8 \, \overline{M}^{-3.1} \rho_0^{4.1}$$

111

Figure 1 shows the experimental data which lead to this equation of state. Also shown are recent X-ray results of Mao [10]; these, of course, are measurements of the isothermal bulk modulus. For present purposes we ignore the slight difference between isothermal and adiabatic moduli. The dashed curve is an alternate fit to the data. The slope of this line was taken, for convenience, as one-third, and its level adjusted to fit the higher density, closely packed structures with compositions most pertinent to the majority of the shock-wave data. The equation of this line is

$$\rho_0/\overline{M} = 0.0475 \, \Phi_0^{1/3} \tag{6}$$

or

$$K_0 = 21 \, \overline{M}^{-3} \rho_0^4$$

for convenience we define

$$\psi_0 = (\rho_0/\overline{M})(1/\phi_0)^{1/3} \tag{7}$$

Table IV gives $\overline{M}$, ρ_0, ϕ_0 and ψ_0 for the low-pressure phases of the materials used in the present study and for some other oxides and silicates. For the rocks the presence of pores and cracks complicates the interpretation of both the density and the Φ_0 and introduces a scatter into the $(\rho/\overline{M})$ - Φ_0 relationship. The parameter $(\rho_0/\overline{M})\phi_0^{-1/3}$ is anamolously low for CaO and slightly lower for the CaO rich rocks albitite, anorthosite and diabase than for the remaining rocks. The eclogites, however, are also rich in CaO but the Sunnmore, Norway sample ($\overline{M}$ = 22.2) has a higher than average ψ_0 while the Heraldsburg, California sample has a near normal value. We will adopt the value of ψ_0 = 0.0475 as being fairly representative and will assume that the zero-pressure properties of the high-pressure phases satisfy equation 6. An alternate approach would be to assume that the relative changes in the density and Φ between the low-pressure and high-pressure forms of a given material are related by

$$\Delta\rho_0/\rho_0 = (1/3)(\Delta\phi_0/\phi_0) \tag{8}$$

A third approach would be to adopt the Murnaghan parameter, n, or the Birch-Murnaghan parameter, ξ, determined for, say, MgO which does not undergo a phase change and then determine ρ_0 and K_0 from the shock-wave data. This would be equivalent to the assumption that $(dK/dP)_0$ is a universal parameter.

Table V summarizes the estimated zero pressure parameters of the shock induced high-pressure phases with the constraint that the density and ϕ_0 of the high-pressure phases satisfy ψ_0 = 0.0475. Tabulated, for comparison, are the densities which would result if the rocks were made of the pure oxides MgO, FeO, Al_2O_3, NaO and SiO_2 (stishovite). This is simply a convenient high-pressure datum to which the densities of the high-pressure phases can be referred. The individual materials will be discussed in the following sections.

112

Except for eclogite, the inferred zero-pressure densities and ϕ's of the high-pressure phases are greater than the low-pressure phases. The higher pressure data for the eclogite is probably in a mixed phase region. Ignoring eclogite the range of ϕ_0 for the high-pressure phases is 42 to 87, compared to the range of 14 to 40 for the open structure silicates, and 31 to 63 for the low-pressure, but closely packed, oxides.

The Murnaghan parameter, n, and the Birch-Murnaghan parameter ξ for the high-pressure phases constrained by $\psi_0 = 0.0475$ can be estimated from the results in table I. Both of these parameters a₁ related to the pressure derivative of the bulk modulus at zero pressure

$$n = (dK/dP)_0$$

$$\xi = (1/4)[12 - 3(dK/dP)_0]$$

and, with Slater's assumptions, to the Grüneisen ratio, γ:

$$n = 2\gamma + 1/3$$

$$\xi = (1/4)[11 - 6\gamma]$$

The Grüneisen ratio is a small number that ranges roughly from 1 to 2. The range of the parameter n, therefore, is about 2.3 to 4.3 and the range of ξ is about -0.25 to +1.25.

Estimates of K_0, ξ, n, γ and ϕ_0 from the present work and from ultrasonic and X-ray measurements are given in table VI. The data is of variable quality but several trends seem to have been established. The related parameters n, ξ and γ seem to depend both on composition and on crystal structure. The parameter n is quite high for open packed structures such as quartz (6.4), Forsterite (4.8) and simple cubic compounds; CsCl (4.8), TlCl (6.0) and NH_4Cl (5.5). It is 4.19 for spinel, and ranges from 2 to 4 for the post-spinels and oxides.

There is a suggestion that in a given crystal structure n and γ decrease and ξ increases upon iron substitution. This is particularly evident in the post-spinel group where forsterite is the sole exception. The zero-pressure density of the high pressure form of forsterite is 31% greater than the starting density, compared with the 20-23% density increases for fayalite and the dunites. Forsterite is apparently going to a different, denser, phase than these other olivine rich materials; this is consistent with the lower n value.

DISCUSSION OF THE INDIVIDUAL MATERIALS

Figures 2 through 18 show the raw Hugoniot data (open circles); computed metastable Hugoniots (heavy curves labelled P_H) and computed isotherms (heavy curves labelled P_K) for the range of ρ_0 indicated by the heavy bar above the P = 0 line; the zero pressure density of the high pressure phase satisfying $\psi_0 = 0.0475$ (shown as X); the range of metastable Hugoniot's (shown as horizontal bars) calculated by McQueen, et al. [4] and the range of ρ_0 for the high pressure phase (heavy bar below the P = 0 line) calculated by McQueen, et al. [4]. Materials having the same crystal structure are discussed together.

113

PERICLASE

This material has been tested by ultrasonic, X-ray and shock wave techniques, and apparently remains in the starting structure to at least 2-1/2 megabars (figure 2). The parameter (dK_s/dP) for MgO found by ultrasonic techniques at low-pressure (Anderson and Schreiber, [11]) is 3.92 for ceramic MgO and 4.49 for single crystal MgO. dK_T/dP is less than 1% higher. The X-ray results of Perez-Albuerne and Drickamer [12] give 3.27 for this parameter from a Murnaghan fit to data to 350 kb. The raw Hugoniot data of McQueen, et al. [4] to 1258 kb gives 3.92. The Hugoniot data of Al'tshuler, et al. [13] to 2600 kb gives 3.65. The parameter dK/dP remains constant with pressure in the Murnaghan equation of state and decreases with compression in the Birch-Murnaghan equation of state.

An alternate method of fitting the post-phase change portion of a shock Hugoniot would be to adopt the n or ξ from a well determined material such as MgO, and determine ρ_o and K_o from the data.

The zero-pressure bulk modulus determined from the shock-wave results is 1710 kb which can be compared with 1717 kb found by ultrasonic techniques on polycrystalline MgO.

CORUNDUM AND HEMATITE

Both Al_2O_3 and Fe_2O_3 have been studied by static and shock compression. The Los Alamos group shocked single crystal and ceramic corundum. There is a break in the U_s - U_p curve for single crystal corundum that could indicate the beginning of a phase change; the ceramic data result in a fairly well defined Hugoniot (figure 3) that extrapolates by the present technique to a density of 3.91 gm/cm^3 which can be compared with the starting density, 3.83 gm/cm^3, and the theoretical density, 3.99 gm/cm^3. The zero pressure bulk modulus of the high-pressure data is 2581 kb using $\psi_o = 0.0475$. Low pressure ultrasonic data gives a value of 2521 kb for the adiabatic bulk modulus, and an estimate of 2505 kb for the isothermal bulk modulus. Within the accuracy of the X-ray diffraction studies of the lattice parameters of Al_2O_3 (Drickamer, et al., [14]), the compressibility is independent of pressure to 300 kbars, but the rhombohedral angle increases by about $1/2^o$.

The hematite (figure 4) goes through a phase change from 350 kb, the zero pressure density of which is about 5.90 gm/cm^3, 12% denser than the theoretical density of the low-pressure phase and about 18% denser than the original density of the starting mineral. In the X-ray work, the compressibility of Fe_2O_3 increases with pressure to 220 kb, and the rhombohedral angle decreases slightly. The bulk modulus of the high-pressure phase of hematite is about 3480 kb.

The X on the zero-pressure abscissa of this and the following figures is the zero-pressure density that satisfies $\psi_o = 0.0475$.

QUARTZ-STISHOVITE

The data of Wackerle [15] for shocked quartz is shown in figure 5. The evidence for the high-pressure phase being stishovite is summarized by McQueen, et al. [5]. This is one of the few materials for which the zero-pressure density of the high-pressure phase can be determined independently of the shock-wave data itself. Chao, et. al. [16] determined the density of stishovite to be 4.287 gm/cm^3. The zero-pressure density, of the high-pressure phase, presumably stishovite, found by the present technique, is 4.21 gm/cm^3 which is in error by less than 2%. The scatter of the raw data is considerable, so this is a severe test of the method.

McQueen, et al. [5] estimated ϕ_0 of stishovite to be 100 $(km/sec)^2$ for an assumed zero-pressure density of 4.35 gm/cm^3. The present estimate gives ϕ_0 = 87 $(km/sec)^2$ for ρ_0 = 4.21 gm/cm^3, and ϕ_0 = 91 $(km/sec)^2$ for ρ_0 = 4.287 gm/cm^3. The latter values correspond to a zero pressure bulk modulus for stishovite of 3922 kb.

RUTILE

McQueen, et al. [17] studied single crystal and polycrystalline TiO_2 both by shock wave and X-ray techniques. At zero pressure the low-pressure phase has ψ_0 = +0.0440, much lower than the other materials tested. If this value is conserved through the phase change, the high-pressure form has a zero-pressure density of 5.71 gm/cm^3, and a ϕ_0 of 116 $(km/sec)^2$. Because of the high quality of the starting material, and because of the accuracy with which ϕ_0 of the low-pressure form is known, we prefer this value to the 5.38 gm/cm^3 determined with ψ_0 = 0.0475. McQueen, et al. [17] estimated a density of 5.8 gm/cm^3 for the high-pressure phase assuming the slope of the phase line to be zero.

This remarkable 34% increase in density for an already closely packed, relatively incompressible structure is interesting since the low pressure for n of rutile was the model for Thomson's early suggestion [1] that quartz could transform at sufficiently high pressure to a rutile-like form (stishovite). There is, however, no evidence from shock-wave data for quartz for a phase change to a material denser than stishovite.

SPINEL AND MAGNETITE

The spinel was a ceramic material with density 3.41 gm/cm^3 compared to the theoretical density of 3.581 gm/cm^3. The magnetite samples were naturally occurring minerals with densities ranging from 5 to 5.14 gm/cm^3 compared to the theoretical density of single crystal magnetite of 5.21 gm/cm^3. The metastable Hugoniot data indicate that spinel and magnetite undergo phase changes involving 12% and 16% increases in density respectively, referred to zero pressure. The raw Hugoniot data give density increases of 10% and 13% respectively. The metastable Hugoniot data give densities for the high-pressure forms of spinel and magnetite which are, respectively, 2% and 7% denser than the oxides (figures 6 and 7).

The zero-pressure densities, estimated by extrapolating the metastable Hugoniot data for the high pressure phases, are 3.95 and 5.90 gm/cm^3 for spinel and magnetite. The value of

115

$(\rho/\overline{M})\left(\phi_{o}^{-1/3}\right)$ for the low-pressure forms of both spinel and magnetite is 0.0467. If this value is appropriate for the high-pressure phases, the inferred density will be raised by about 0.04 gm/cm^3. These values are 12% (spinel) and 14% (magnetite) denser than the theoretical densities of the low-pressure phases which have the spinel structure and 3% (spinel) and 7% (magnetite) denser than the mixture of oxides. Fayalite and the dunites, which presumably collapse to a spinel structure at high static pressure, apparently go directly to a phase, under shock loading, that has a density very near that of the component oxides. Forsterite, however goes to a phase about 9% denser than the oxides, and about 18% denser than the spinel form.

The two light lines in figure 6 are fits of the Murnaghan equation of state to the spinel data for two trial zero-pressure densities. They both satisfy the high-pressure data almost equally well. The range for P_H and P_K correspond to the range of ρ_o indicated at P = 0 by the heavy bar above the zero-pressure axis. For ρ_o = 3.60 gm/cm^3, n = 4.049 and ϕ_o = 55.6 $(km/sec)^2$, and the relative standard deviation in density is 0.6%. For ρ_o = 3.90 gm/cm^3, n = 5.26 and ϕ_o = 29.3 $(km/sec)^2$, and the relative standard deviation in density is 0.5%.

PYROLUSITE

This was a naturally occurring specimen purchased from Wards and seemed to be uniform, but there is appreciable scatter in the Hugoniot data (figure 8). The sample density was 4.35 gm/cm^3 compared with the theoretical density of 5.23 gm/cm^3. Assuming no phase change, a long extrapolation of the high-pressure data to ψ_o = 0.0475 gives a zero-pressure density of 5.05 gm/cm^3 with a large uncertainty. Pyrolusite crystallizes in the rutile structure.

OLIVINES

The fayalite is a naturally occurring specimen from Rockport, Mass., purity unknown. The forsterite is a synthetic ceramic. Both undergo phase changes under shock loading. The raw Hugoniot data for the fayalite extrapolated to zero pressure gives a density of 5.12 gm/cm^3 (figure 9). The calculated metastable Hugoniot extrapolates to 5.25 gm/cm^3, just slightly less than the 5.29 gm/cm^3 estimated for the density of the pure oxides, FeO and SiO_2 (stishovite). This represents a 19.6% increase in density over the theoretical density of fayalite in the low-pressure form.

The density of the high-pressure phase of the ceramic forsterite (figure 10) is 4.19 gm/ cm^3 which is 0.34 gm/cm^3 or 8.8% denser than the component oxides, MgO plus SiO_2 (stishovite). It should be pointed out that the starting forsterite material is 4.4% less dense than theoretical, while the starting fayalite material is 2.5% less dense. Assuming that the difference is due to porosity, this would result in higher temperatures and lower densities in the forsterite experiment, if the high-pressure phases have the same crystal structure.

Forsterite is anamolous when compared with results obtained with fayalite and the dunites all of which end up near the density of the component oxides. Unfortunately, the data for forsterite is very sparse and the Hugoniot for the high-pressure phase is not well defined.

116

The spinel form of forsterite has a density of about 3.54 gm/cm^3, so the high-pressure form is about 18% denser than the spinel form. This can be compared with the 12% and 16% density increases of spinel and magnetite which start in the spinel structure. The spinel form of fayalite has a density of about 4.85 gm/cm^3, 5.3% less dense than the high pressure shock phase.

DUNITES

These two rocks are over 90% olivine and transform at pressures above 0.45 Mb. Results are comparable to those on rocks of similar composition tested by Trunin, et al. [18]. The Twin Sister's dunite gives a zero-pressure density, determined from the metastable Hugoniot of the high-pressure phase, of 4.05 gm/cm^3; the raw Hugoniot data yield 4.01 gm/cm^3. The high-pressure phase is about 21% denser than the starting material, and has almost exactly the same density as the component oxides.

The iron rich dunite from the Transvaal contains 90% by volume of Fa$_{55}$ or 34 mole percent FeO. The density of the high-pressure phase, from the raw Hugoniot data, is 4.65 gm/cm^3, again virtually identical to the 4.64 gm/cm^3 for the oxides. This density increase corresponds to a zero pressure difference of 22.7%. If the original material was pore and crack free, the starting densities would be perhaps 1 to 2% higher.

Figure 11 shows the data for the Twin Sister's dunite and the fit, for two starting densities, of the Birch-Murnaghan equation of state to the high-pressure data. A wide range of starting densities would fit the high-pressure data equally well.

The heavy horizontal bar below the P = 0 line is the range of ρ_0 found by the analysis of McQueen, et al. [4]; the light horizontal bars are the range found for the corresponding metastable Hugoniots. Slightly lower densities are found in the present analysis.

DIABASE

The two diabase rocks give very similar results (figures 12 and 13). McQueen, et al. [4] discuss the complication of interpretation and point out the anamolous compressibility of this material compared with others they tested. These rocks contain quite a bit of CaO which, as an oxide, is more compressible than the other common rock forming oxides. The density of the high-pressure phase, computed as before, is about 3.6 gm/cm^3 or about 21% denser than the starting material, and some 0.4 gm/cm^3 less dense than the oxides. However, the presence of CaO also upsets the relationship between mean molar volume and elastic properties, as first pointed out by Simmons [19] CaO behaves as if it had a smaller mean atomic weight. Taking this into account would raise the estimated zero-pressure densities of the high-pressure phases by about 0.1 to 0.15 gm/cm^3.

There is very good agreement between the metastable Hugoniots calculated here and the more elaborate calculations of McQueen, et al. [4].

BRONZITITE

McQueen, et al. [4] shocked two bronzites which had nearly identical compositions. We analyzed the more complete set of data, that from the Stillwater Complex, Montana (figure 14). This rock contained 94% enstatite, 2% olivine and 4% hornblende. The analysis [4] yields zero pressure values for density and Φ for the high-pressure phase which are less than those for the low-pressure phase. We determined a density of 3.60 gm/cm^3 for the high-pressure phase, about 10% denser than the starting material, and 10% less than the oxides. Spinel plus stishovite is about 17% denser than the corresponding magnesium rich enstatite.

The decomposition, enstatite → forsterite + stishovite, results in a density increase of about 12%. The transformation enstatite → garnet would result in a density increase of about 9-1/2% (Ringwood and Major, [20]).

ALBITITE AND ANORTHOSITE

These rocks contain more than 90% feldspar and both undergo phase changes at relatively low pressures which involve large volume changes. The computed zero-pressure density of the high-pressure phase albilite (figure 15) which is 98% by volume an_{12} and 2% actinolite, is 3.75 gm/cm^3, a 43.7% increase over the starting density. This is about 0.1 gm/cm^3 less dense than the equivalent pure oxides, and about 0.25 gm/cm^3 denser than jadeite plus stishovite. Jadeite, however, itself undergoes a phase change above 0.55 Mb [4] but the density increase cannot be established with present data.

The zero pressure density of the anorthosite (figure 15) which is 90%, by volume feldspar (an_{49}) and 10% pyroxene (au) is 3.79 gm/cm^3. This represents a density increase of about 37.8% over the starting material and is 0.12 gm/cm^3 less dense than the oxides.

GRANITE

The granite sample (figure 17) was from Westerly, R. I., and contained about 28% quartz, 35% microcline and 31% plagioclase. The inferred zero-pressure density of the high-pressure phase is 3.85 gm/cm^3 or about 46% denser than the starting material. This can be compared with the 62% density increase for the quartz to stishovite transformation, 44% for albitite and 38% for anorthosite, the latter two being feldspar rich rocks. Apparently both the quartz and the feldspars in the granite have transformed to more dense phases. The high-pressure phase assemblage in granite is 6% less dense than the pure oxides.

ECLOGITE

We interpreted only the Sunnmore, Norway eclogite initial density about 3.56 gm/cm^3. McQueen, et al., believe that a phase change is indicated at about 0.37 Mb but that the high-pressure data may be still in the mixed phase region or that the phase change is second-order rather than first order. The high-pressure data is clearly anamolous in that the inferred zero-pressure density and ϕ_0 are both less than the low-pressure phase. Consequently the high-

118

pressure data is probably in the mixed phase region and the estimated zero-pressure param-
eters are not useful for present purposes.

ACKNOWLEDGMENTS

REFERENCES

1. F. Birch, "Elasticity and Constitution of the Earth's Interior," J. Geophys. Res., Vol. 57, 1952, pp. 227-286.

2. A. E. Ringwood, "Mineralogy of the Mantle," in Advances in Earth Science, ed. P. M. Hurley, M.I.T. Press, 1966.

3. S. P. Clark, Jr., "Equation of State and Polymorphism at High Pressures " in Research in Geochemistry, ed. by P. H. Abelson, John Wiley & Sons, New York, 1959.

4. R. G. McQueen, S. P. Marsh and J. N. Fritz, "Hugoniot Equation of State of Twelve Rocks," J. Geophys. Res., Vol. 72, 1967, pp. 4999-5036.

5. R. G. McQueen, J. N. Fritz and S. P. Marsh, "On the Equation of State of Stishovite," J. Geophys. Res., Vol. 68, 1963, pp. 2319-2322.

6. S. P. Clark. Jr. (ed.), Handbook of Physical Constants, Geol. Soc. of Am., New York, 1966.

7. T. J. Ahrens and D. L. Anderson, "Shock Wave Equations of State," 1968, in preparation.

8. H. Takeuchi and H. Kanamori, "Equations of State of Matter From Shock Wave Experiments," J. Geophys. Res., Vol. 71, 1966, pp. 3985-3994.

9. D. L. Anderson, "A Seismic Equation of State," Geophys. J., Vol. 13, 1967, pp. 9-30.

10. H. Mao, The Pressure Dependence of the Lattice Parameters and Volume of Ferromagnesian Spinels, and its Implications to the Earth's Mantle, Thesis, Univ. of Rochester, Rochester, New York, 1967.

11. D. L. Anderson and E. Schreiber, "The Pressure Derivative of the Sound Velocities of Polycrystalline Magnesia," J. Geophys. Res., Vol. 70, 1965, pp. 5241-5248.

12. E. A. Perez-Albuerne and H. G. Drickamer, "The Effect of High Pressure on the Compressibilities of Seven Crystals Having the NaCl Structure," J. Chem. Phys., Vol. 43, 1965, pp. 1381-1385.

13. L. V. Al'tshuler, R. F. Trunin and G. V. Simakov, "Shock-Wave Compression of Periclase and Quartz and the Composition of the Earth's Lower Mantle," Bull., Acad. Sci., USSR, Phys. Solid Earth, No. 10, 1965, pp. 657-660.

14. H. G. Drickamer, R. W. Lynch, R. L. Clendenen and E. A. Perez-Albuerne, "X-Ray Diffraction Studies of the Lattice Parameters of Solids Under Very High Pressure," Solid State Physics, Vol. 19, 1966, pp. 135-228.

15. J. Wackerle, "Shock-Wave Compression of Quartz," J. Appl. Phys., Vol. 33, 1962, pp. 922-937.

16. E. C. T. Chao, J. J. Fabrey, J. Littler and D. J. Milton, "Stishovite, SiO_2, a Very High Pressure New Mineral from Meteor Crater Arizona," J. Geophys. Res., Vol. 67, 1962, pp. 419-421.

17. R. G. McQueen, J. C. Jamieson and S. P. Marsh, "Shock-Wave Compression and X-Ray Studies of Titanium Dioxide," Science, Vol. 155, 1967, pp. 1401-1404.

18. R. F. Trunin, V. I. Gonshakova, G. V. Simakov and N. E. Galdin, "A Study of Rocks Under the High Pressures and Temperatures Created by Shock Compression," Bull., Acad. Sci. USSR, Phys. Solid Earth, No. 9, 1965, pp. 579-586.

19. G. Simmons, "Velocity of Shear Waves in Rocks to 10 Kilobars, 1," J. Geophys. Res., Vol. 69, 1964, pp. 1123-1130.

20. A. E. Ringwood and A. Major, "High Pressure Transformations in Pyroxenes," Earth and Planetary Sci. Letters, Vol. 1, 1966, pp. 351-357.

PREVIOUS TECHNICAL REPORTS
1964 - Present

Aki, K., "A Note on Surface Waves from the HARDHAT Nuclear Explosion," J. Geophys. Res., Vol. 69, 1964, pp. 1131-1134.

Alexander, S. S., Methods of Mode Separation of Seismic Surface Waves, Calif. Inst. Tech., Pasadena, Calif., 1964.

Allen, C. R., P. St. Amand, C. F. Richter and J. M. Nordquist, "Relationship Between Seismicity and Geologic Structure in the Southern California Region," Bull. Seism. Soc. Am., Vol. 55, 1965, pp. 753-797.

Anderson, D. L., "The Anelasticity of the Mantle," Geophys. J., Vol. 14, 1967, pp. 135-164.

Anderson, D. L., "Earth's Viscosity," Science, Vol. 151, 1965, p. 321.

Anderson, D. L., "Latest Information from Seismic Observations," Earth's Mantle, Academic Press, London, England, 1967.

Anderson, D. L., "Phase Changes in the Upper Mantle," Science, Vol. 157, 1967, pp. 1165-1173.

Anderson, D. L., Recent Evidence Concerning the Structure of the Upper Mantle from the Dispersion of Long Period Surface Waves, Rept. No. 4410-75-X, VESIAC, Willow Run Labs., Univ. of Mich., 1964.

Anderson, D. L., "Universal Dispersion Tables, 1. Love Waves Across Ocean and Continents on a Spherical Earth," Bull. Seism. Soc. Am., Vol. 54, 1964, pp. 681-726.

Anderson, D. L. and C. B. Archambeau, "The Anelasticity of the Earth," J. Geophys. Res., Vol. 69, 1964, pp. 2071-2084.

Anderson, D. L. and D. G. Harkrider, "Universal Dispersion Tables, II. Variational Parameters for Amplitudes, Phase Velocity and Group Velocity for First Four Love Modes for an Oceanic and a Continental Earth Model," Bull. Seism. Soc. Am., (in press).

Anderson, D. L. and H. Kanamori, "Shock Wave Equations of State for Rocks and Minerals," J. Geophys. Res., (in press).

Anderson, D. L. and R. L. Kovach, "Attenuation in the Mantle and Rigidity of the Core from Multiply Reflected Core Phases," Proc. Nat. Acad. Sci., Vol. 51, 1964, pp. 168-172.

Anderson, D. L., A. Ben-Menahem and C. B. Archambeau, "Attenuation of Seismic Energy in the Upper Mantle," J. Geophys. Res., Vol. 70, 1965, pp. 1441-1448.

Archambeau, C. B. and E. A. Flinn, "Perturbation Methods for the Inversion of Body Wave Travel-Time Data," J. Geophys. Res., (in press).

Ben-Menahem, A., Deformation of a Non-Gravitating Elastic Sphere by a Finite Internal Dislocation, Calif. Inst. Tech., Pasadena, Calif., 1965.

Ben-Menahem, A., "Mode-Ray Duality," Bull. Seism. Soc. Am., Vol. 54, 1964, pp. 1315-1321.

Ben-Menahem, A., "Observed Attenuation and Q Values of Seismic Surface Waves in the Upper Mantle," J. Geophys. Res., Vol. 70, 1965, pp. 4641-4651.

Ben-Menahem, A., Source Studies from Isolated Seismic Signals, Rept. No. 7845-1-X, VESIAC, Willow Run Labs., Univ. of Mich., 1965.

Ben-Menahem, A., "Spectral Response of an Elastic Sphere to Dipolar Point-Sources," Bull. Seism. Soc. Am., Vol. 54, 1964, pp. 1323-1340.

Ben-Menahem, A., Summation of Certain Legendre Series and Related Difference Equations, Calif. Inst. Tech., Pasadena, Calif., 1965.

Ben-Menahem, A. and D. G. Harkrider, "Radiation Patterns of Surface Waves from Buried Point Sources in a Flat Stratified Earth," J. Geophys. Res., Vol. 69, 1964, pp. 2605-2620.

Ben-Menahem, A., S. W. Smith and T. L. Teng, "A Procedure for Source Studies from Spectrum of Long-Period Seismic Body Waves," Bull. Seism. Soc. Am., Vol. 55, 1965, pp. 203-235.

Brune, J. N., "P and S Wave Travel Times and Spheroidal Normal Modes of a Homogeneous Sphere," J. Geophys. Res., Vol. 71, 1966, pp. 2959-2965.

Brune, J. N., "Regional Variations in the Structure of the Upper Mantle and the Propagation of the Sa Phase," Upper Mantle Symposium, Ottawa, Canada, 1965.

Brune, J. N., "The Sa Phase from the Hindu Kush Earthquake," Pure & Appl. Geophys., Vol. 62, 1965, pp. 81-95.

Brune, J. N., "Seismic Moment, Seismicity, and Rate of Slip Along Major Fault Zones," J. Geophys. Res., Vol. 73, 1968, pp. 777-784.

Brune, J. N. and C. R. Allen, "A Micro-Earthquake Survey of the San Andreas Fault System in Southern California," Bull. Seism. Soc. Am., Vol. 57, 1967, pp. 277-296.

Brune, J. N. and C. Y. King, "Excitation of Mantle Rayleigh Waves of Period 100 Seconds as a Function of Magnitude," Bull. Seism. Soc. Am., (in press).

Cisternas, A., Part I - The Radiation of Elastic Waves from a Spherical Cavity in a Half Space. Part II - Precision Determination of Focal Depths and Epicenters of Earthquakes, Thesis, Calif. Inst. Tech., Pasadena, Calif., 1964.

Davies, J. B. and S. W. Smith, "Source Parameters of Earthquakes, and Discrimination Between Earthquakes and Nuclear Explosions," Bull. Seism. Soc. Am., (in press).

Dewart, G. and M. N. Toksoz, "Crustal Structure in the East Antarctica from Surface Wave Dispersion," Geophys. J., Vol. 10, 1965, pp. 127-139.

Duda, S., "Regional Seismicity and Seismic Wave Propagation from Records at the Tonto Forest Seismological Observatory, Payson, Arizona," Annali di Geofisica, Vol. 18, 1965, pp. 365-397.

Hannon, W. J. and R. L. Kovach, "Velocity Filtering of Seismic Core Phases," Bull. Seism. Soc. Am., Vol. 56, 1966, pp. 441-454.

Harkrider, D. G., "Theoretical and Observed Acoustic Gravity Waves from Explosive Sources in the Atmosphere," J. Geophys. Res., Vol. 69, 1964, pp. 5295-5321.

Harkrider, D. C. and D. L. Anderson, "Surface Wave Energy from Point Sources in Plane Layered Earth Models," J. Geophys. Res., Vol. 71, 1966, pp. 2967-2980.

Johnson, L. R., "Array Measurements of P Velocities in the Upper Mantle," J. Geophys. Res., (in press).

Johnson, L. R., Measurements of Mantle Velocities of P Waves with a Large Array, Thesis, Calif. Inst. Tech., Pasadena, Calif., 1966.

124

Julian, B. R. and D. L. Anderson, "Travel Times, Apparent Velocities and Amplitudes of Body Waves," Bull. Seism. Soc. Am., (in press).

Kanamori, H., "Attenuation of P Waves in the Upper and Lower Mantle," Bull. Earthq. Res. Inst., Japan, Vol. 45, 1967, pp. 299-312.

Kanamori, H., "Spectrum of P and PcP in Relation to the Mantle-Core Boundary and Attenuation in the Mantle," J. Geophys. Res., Vol. 72, 1967, pp. 559-571.

Kanamori, H., "Spectrum of Short-Period Core Phases in Relation to the Attenuation in the Mantle," J. Geophys. Res., Vol. 72, 1967, pp. 2181-2186.

Kovach, R. L. and D. L. Anderson, "Attenuation of Shear Waves in the Upper and Lower Mantle," Bull. Seism. Soc. Am., Vol. 54, 1964, pp. 1855-1864.

Kovach, R. L. and D. L. Anderson, "Study of the Energy of the Free Oscillations of the Earth," J. Geophys. Res., Vol. 72, 1967, pp. 2155-2168.

Lehner, F. E. and F. Press, "A Mobile Seismograph Array," Bull. Seism. Soc. Am., Vol. 56, 1966, pp. 889-897.

Liebermann, R. C., C. Y. King, J. N. Brune and P. W. Pomeroy, "Excitation of Surface Waves by the Underground Nuclear Explosion LONGSHOT," J. Geophys. Res., Vol. 71, 1966, pp. 4333-4339.

McKenzie, D. P., "Forced and Free Convection within the Earth's Mantle," Geophys. J., (in press).

McKenzie, D. P., "Some Remarks on Heat Flow and Gravity Anomalies," J. Geophys. Res., (in press).

Niazi, M., "Corrections to Apparent Azimuth and dt d∆ of Teleseisms for a Dipping M-Discontinuity with Application to TFSO Data," Bull. Seism. Soc. Am., Vol. 56, 1966, pp. 491-509.

Niazi, M. and D. L. Anderson, "Upper Mantle Structure of Western North America from Apparent Velocities of P Waves," J. Geophys. Res., Vol. 70, 1965, pp. 4633-4640.

Nordquist, J., "A Catalog of Southern California Earthquakes and Associated Electronic Data Processing Programs," Bull. Seism. Soc. Am., Vol. 54, 1964, pp. 1003-1011.

Press, F., Dimensions of the Source Region for Small Shallow Earthquakes, Rept. No. 7885-1-X, VESIAC, Willow Run Labs., Univ. of Mich., 1965.

Press, F., "Seismic Wave Attenuation in the Crust, (Letter to the Editor)," J. Geophys. Res., Vol. 69, 1964, pp. 4417-4418.

Press, F. and S. Biehler, "Inferences on Crustal Velocities and Densities from P-Delays and Gravity Anomalies," J. Geophys. Res., Vol. 69, 1964, pp. 2979-2995.

Shimshoni, M. and S. W. Smith, "Seismic Signal Enhancement with 3-Component Detectors," Geophysics, Vol. 29, 1964, pp. 664-671.

Smith, S. W., Broadband Digital Recording, Rept. No. 4410-77-X, VESIAC, Willow Run Labs., Univ. of Mich., 1964.

Smith, S. W., "Free Oscillations Excited by the Alaskan Earthquake," J. Geophys. Res., Vol. 71, 1966, pp. 1183-1193.

Smith, S. W., "Seismic Digital Data Acquisition Systems," Rev. of Geophys., Vol. 3, 1965, pp. 151-156.

Teng, T. L., Amplitudes of Body Waves, Calif. Inst. Tech., Pasadena, Calif.

Teng, T. L., "Attenuation of Body Waves and the Q Structure of the Mantle," J. Geophys. Res., Vol. 73, 1968, pp. 2195-2208.

125

Teng, T. L., Body-Wave and Earthquake Source Studies, Thesis, Calif. Inst. Tech., Pasadena, Calif., 1966.

Teng, T. L., "Reflection and Transmission from a Layered Core Mantle Boundary," Bull. Seism. Soc. Am., Vol. 57, 1967, pp. 477-499.

Teng, T. L. and A. Ben-Menahem, "Mechanism of Deep Earthquakes from Spectrums of Isolated Body-Wave Signals. I. The Banda Earthquake of March 21, 1964," J. Geophys. Res., Vol. 70, 1965, pp. 5157-5170.

Teng, T. L. and F. T. Wu, "A Two-Dimensional Ultrasonic Model Study of Compressional and Shear Wave-Diffraction Patterns Produced by a Circular Cavity," Bull. Seism. Soc. Am., Vol. 58, 1968, pp. 171-178.

Thrower, E. N. and D. G. Harkrider, "A Note on the Existence Maxima and Minima on Phase Velocity Curves," Bull. Seism. Soc. Am., Vol. 55, 1965, pp. 971-974.

Toksoz, M. N. and D. L. Anderson, "Phase Velocities of Long-Period Surface Waves and Structure of the Upper Mantle," J. Geophys. Res., Vol. 71, 1966, pp. 1649-1658.

Toksoz, M. N. and A. Ben-Menahem, "Excitation of Seismic Surface Waves by Atmospheric Nuclear Explosions," J. Geophys. Res., Vol. 69, 1964, pp. 1639-1648.

Toksoz, M. N., A. Ben-Menahem and D. G. Harkrider, "Determination of Source Parameters by Amplitude Equalization of Seismic Surface Waves. I. Underground Nuclear Explosions," J. Geophys. Res., Vol. 69, 1964, pp. 4355-4366.

Toksoz, M. N., M. A. Chinnery and D. L. Anderson, "Inhomogeneities in the Earth's Mantle," Geophys. J., Vol. 13, 1967, pp. 31-59.

Vlaar, N. J., "The Field from an SH-Point Source in a Continuously Layered Inhomogeneous Medium. I. The Field in a Layer of Finite Depth," Bull. Seism. Soc. Am., Vol. 56, 1966, pp. 715-724.

Vlaar, N. J., "The Field from a SH-Point Source in a Continuously Layered Inhomogeneous Half-Space. II. The Field in a Half-Space," J. Geophys. Res., Vol. 56, 1966, pp. 1305-1315.

Wu, F. T., Energy of Earthquakes, Calif. Inst. Tech., Pasadena, Calif., 1965.

Wu, F. T., "The Inverse Problem of Magnetotelluric Sounding," Geophysics, (in press).

Wu, F. T., "Parkfield Earthquake of June 28, 1966, Magnitude and Source Mechanism," J. Geophys. Res., (in press).

Wu, F. T., Part I - Lower Limit of the Total Energy of Earthquakes and Partitioning of Energy Among Seismic Waves. Part II - Reflected Waves and Crustal Structures, Thesis, Calif. Inst. Tech., Pasadena, Calif., 1966.

Wu, F. T., A. Ben-Menahem, "Surface Wave Radiation Pattern and Source Mechanism of the September 1, 1962 Iran Earthquake," J. Geophys. Res., Vol. 70, 1965, pp. 3934-3949.

Wu, F. T. and W. J. Hannon, "PP and the Crustal Structure," Bull. Seism. Soc. Am., Vol. 56, 1966, pp. 733-746.

Wyss, M. and J. N. Brune, "Seismic Moment, Stress and Source Dimensions for Earthquakes in the California-Nevada Region," J. Geophys. Res., (in press).
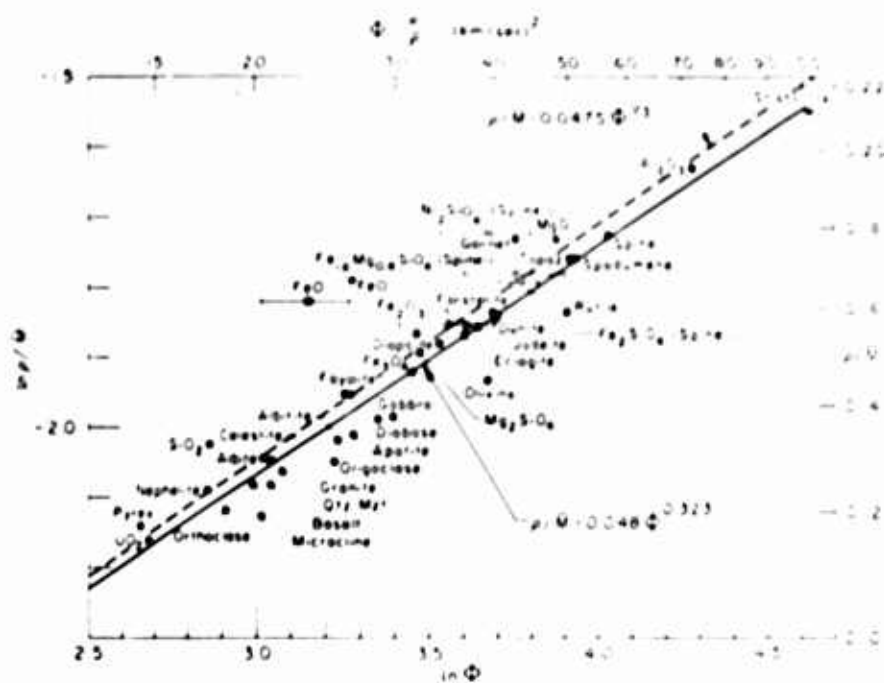
FIGURE 1. $\phi_0 = (dP\ d\rho)_0$ vs. $\rho_0/\bar{M}$ FOR OXIDES AND SILICATES. Data from Anderson [9], Mao [10] and Drickamer, et al. [14].
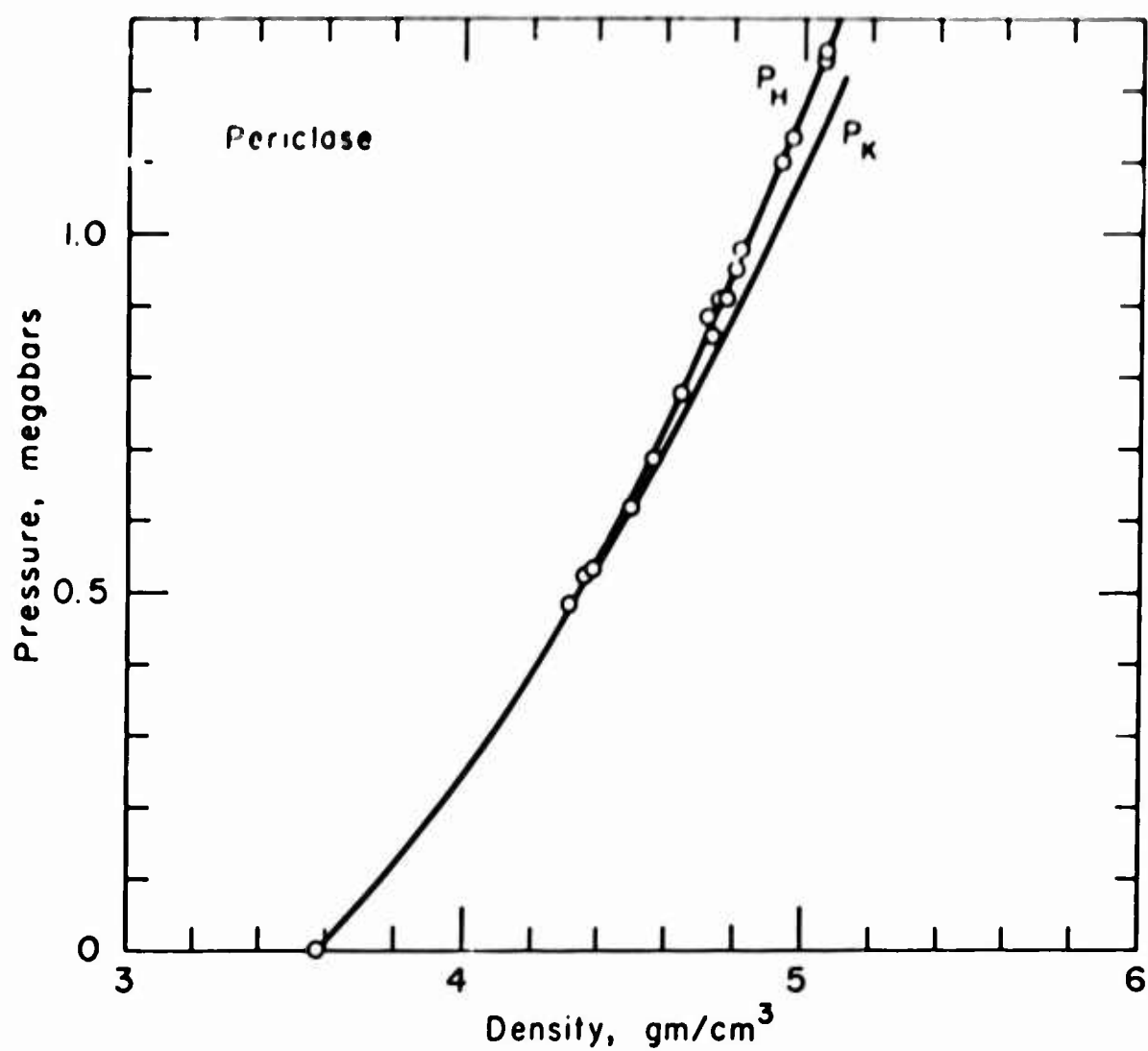
FIGURE 2. PRESSURE-DENSITY HUGONIOT FOR MgO. P_H is fitted Hugoniot, P_K is derived isotherm.
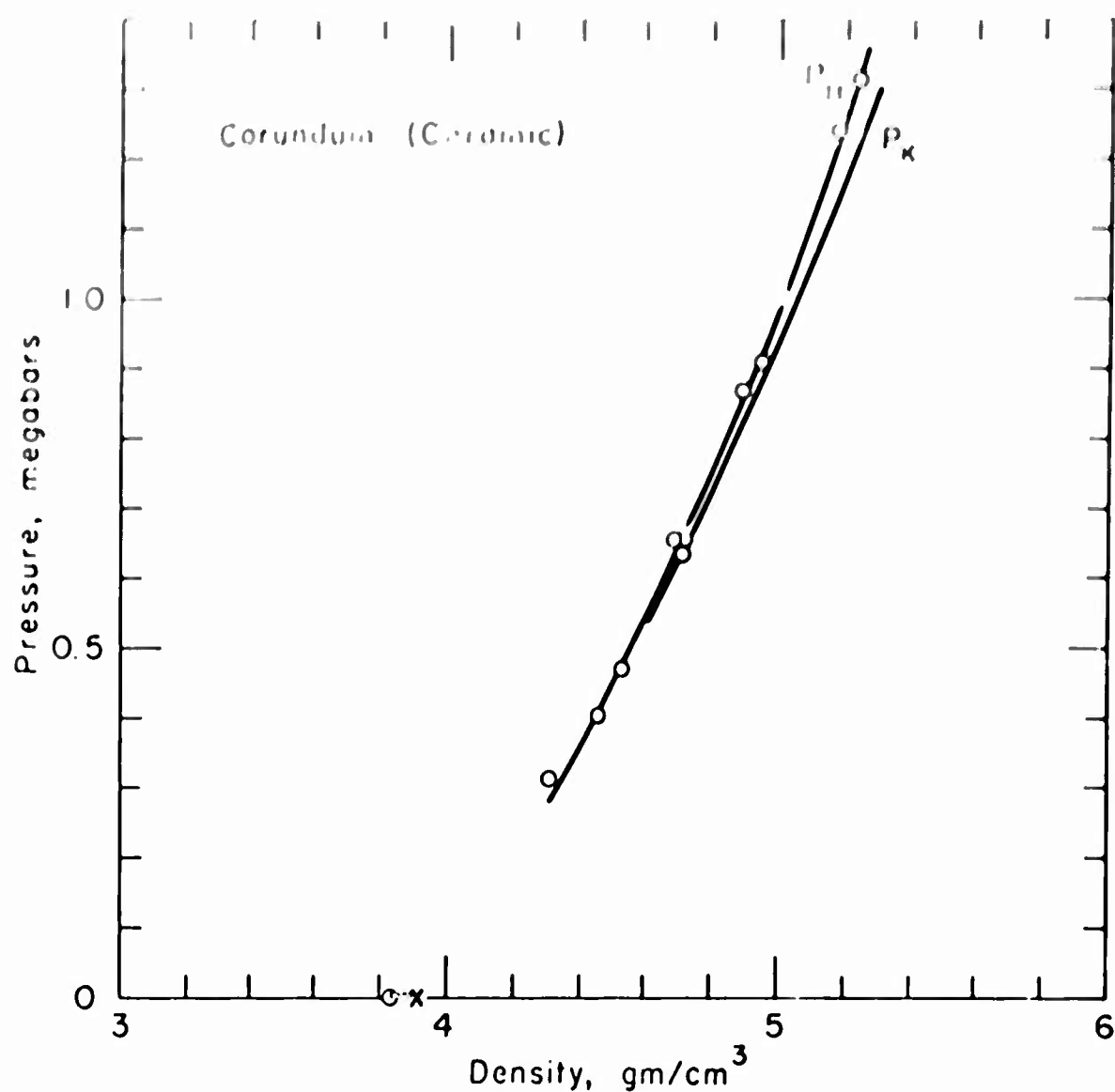
FIGURE 3. PRESSURE-DENSITY HUGONIOT FOR CERAMIC Al_2O_3. The heavy horizontal bar on the zero-pressure axis is the range of ρ_0 for which linear U_s-U_p fits have been obtained (table III). The X is the zero-pressure density satisfying $\mathcal{V}_0 = 0.0475$.
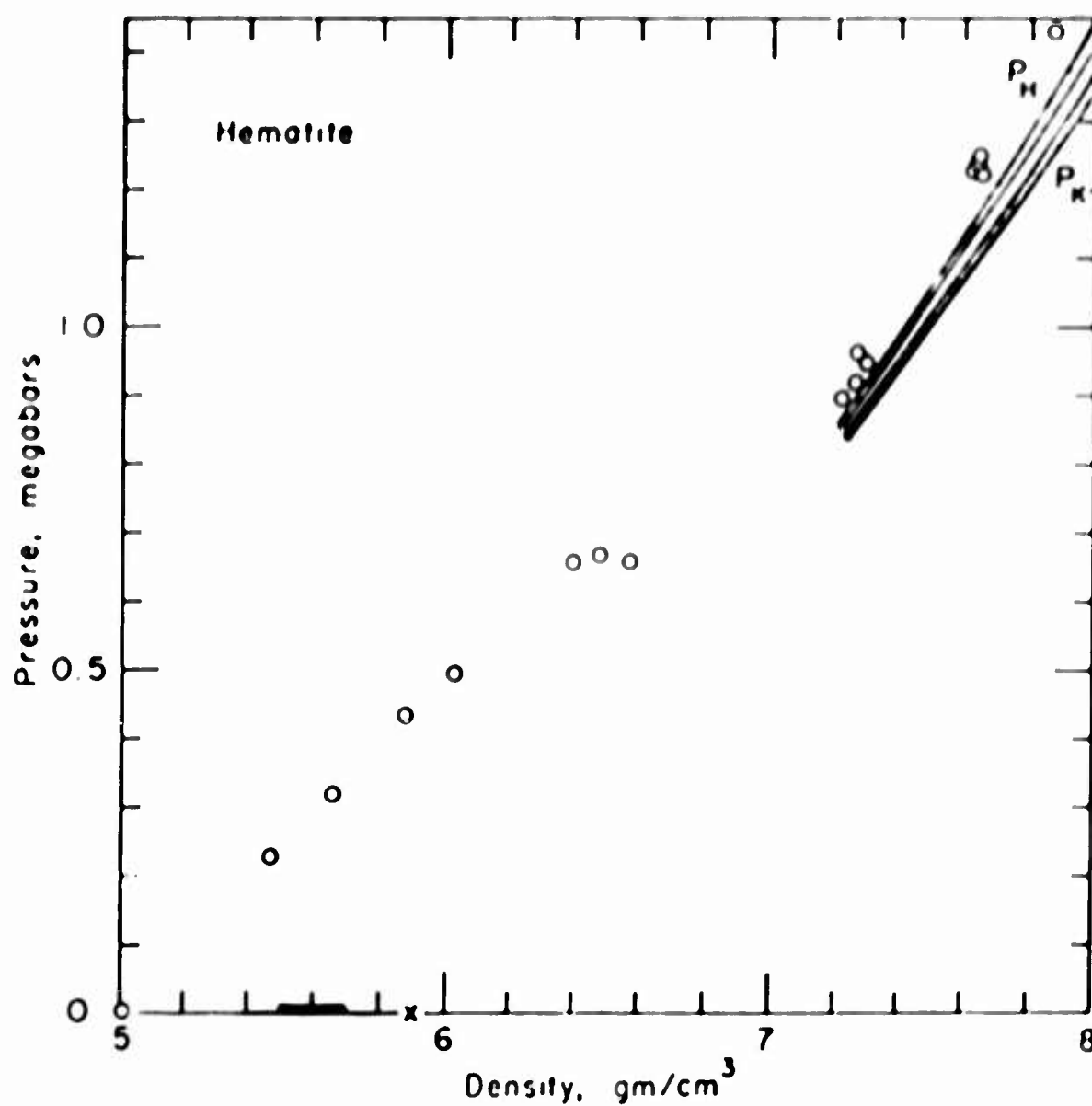
FIGURE 4. PRESSURE-DENSITY HUGONIOT FOR Fe$_2$O$_3$ AND DERIVED METASTABLE HUGONIOT, P$_H$, AND ISOTHERM, P$_K$ FOR ZERO-PRESSURE DENSITY RANGE INDICATED. In this and following figures we are concerned only with the high-pressure data.
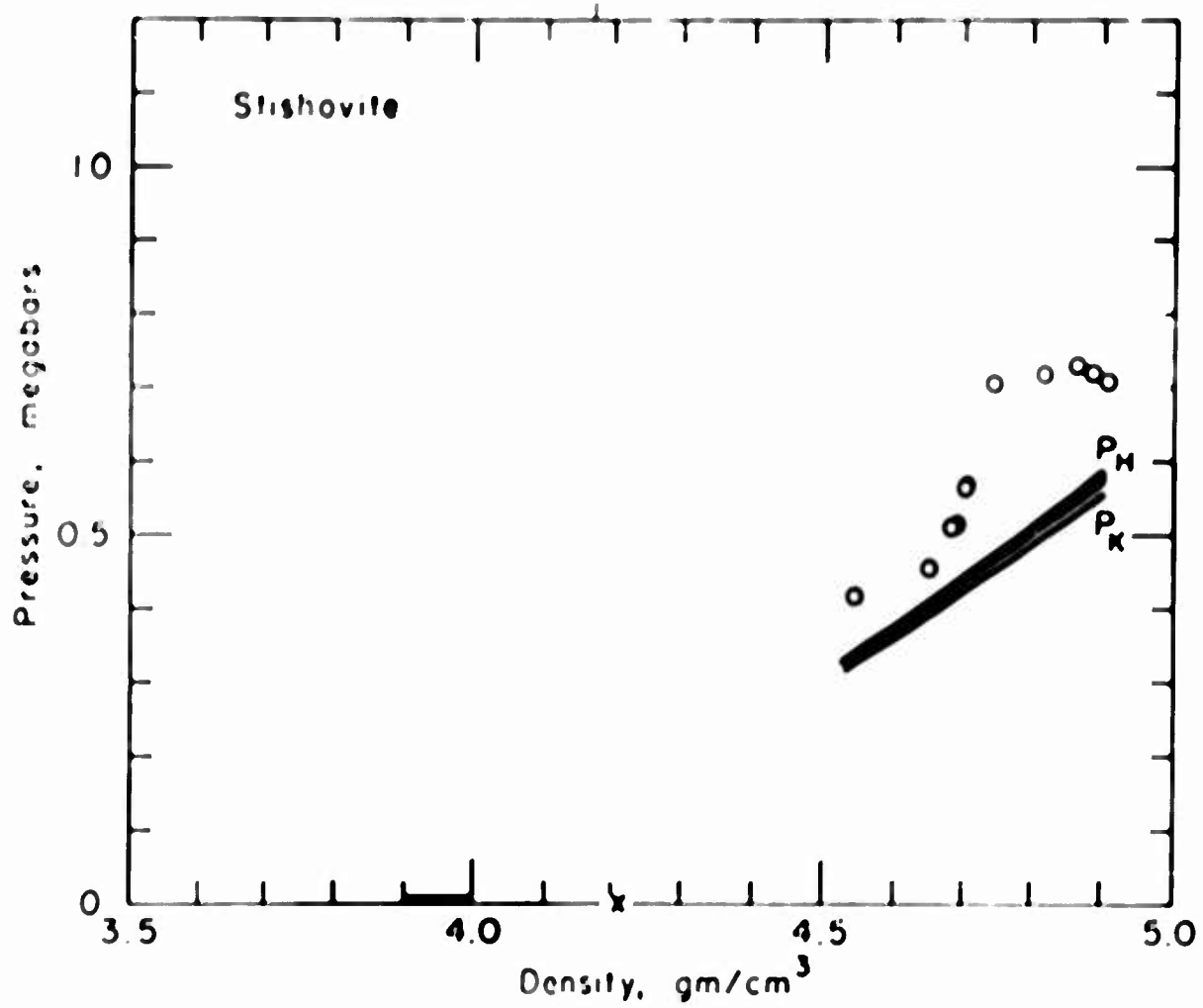
FIGURE 5. PRESSURE-DENSITY HUGONIOT FOR HIGH-PRESSURE PHASE OF SiO₂.
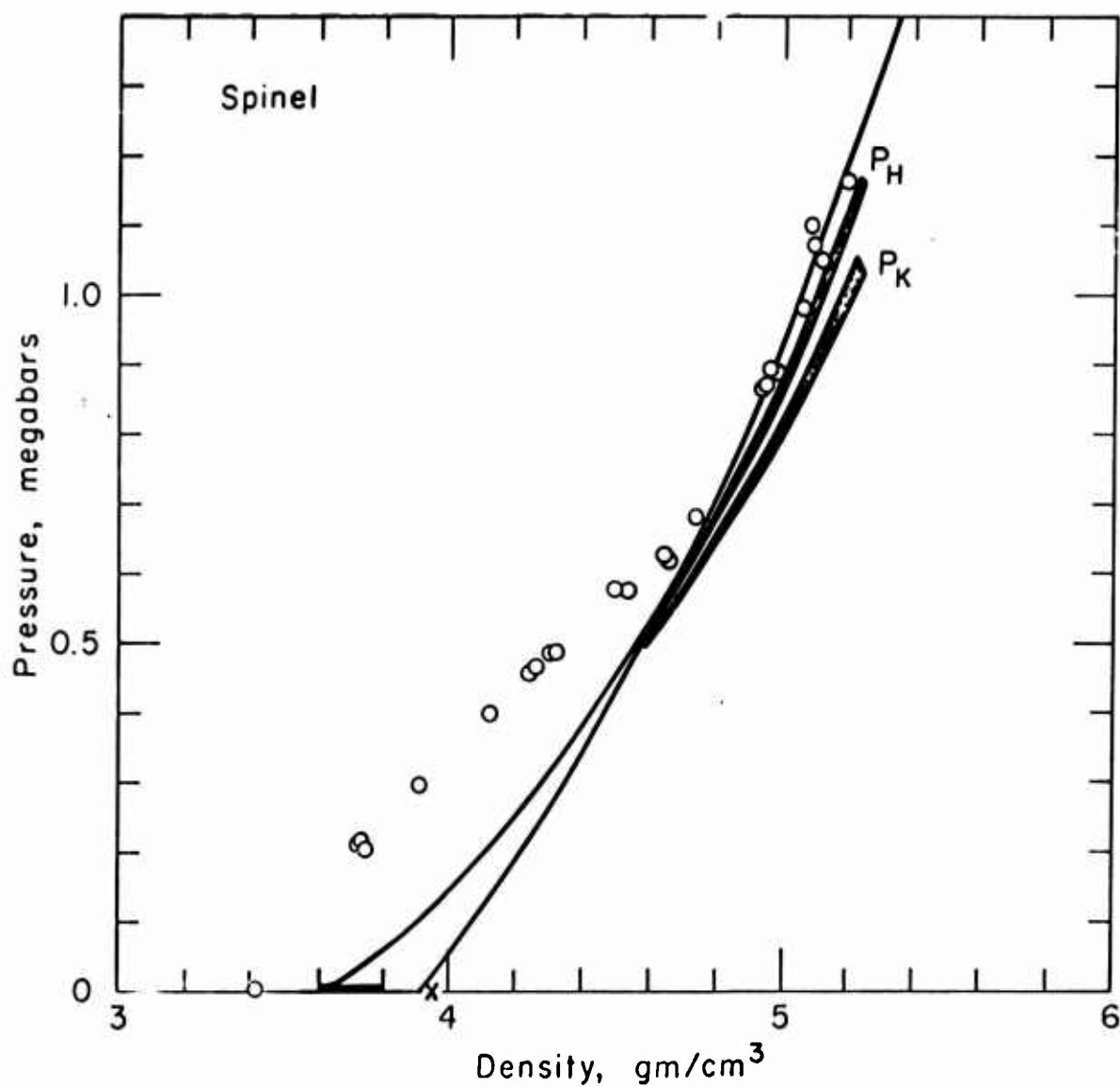
FIGURE 6. PRESSURE-DENSITY HUGONIOT FOR $MgAl_2O_4$ AND DERIVED METASTABLE HUGONIOT AND ISOTHERM. Also shown are least-square fits to the high-pressure data of Murnaghan equations for two assumed starting densities. This illustrates the difficulty of finding ρ_0 from the shock-wave data itself.

132
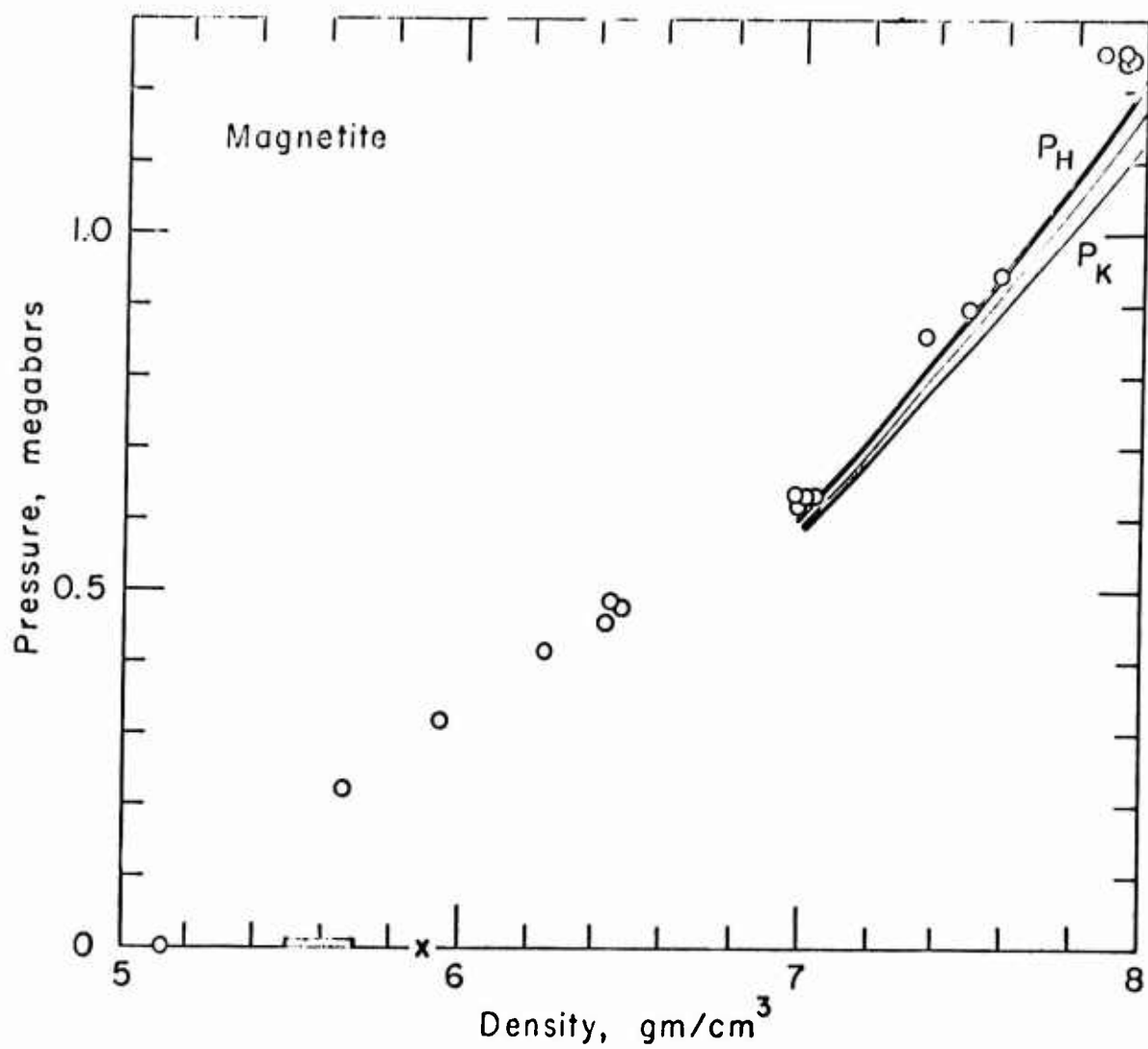
FIGURE 7. PRESSURE-DENSITY HUGONIOT FOR Fe₃O₄ AND DERIVED METASTABLE
HUGONIOT AND ISOTHERM

133
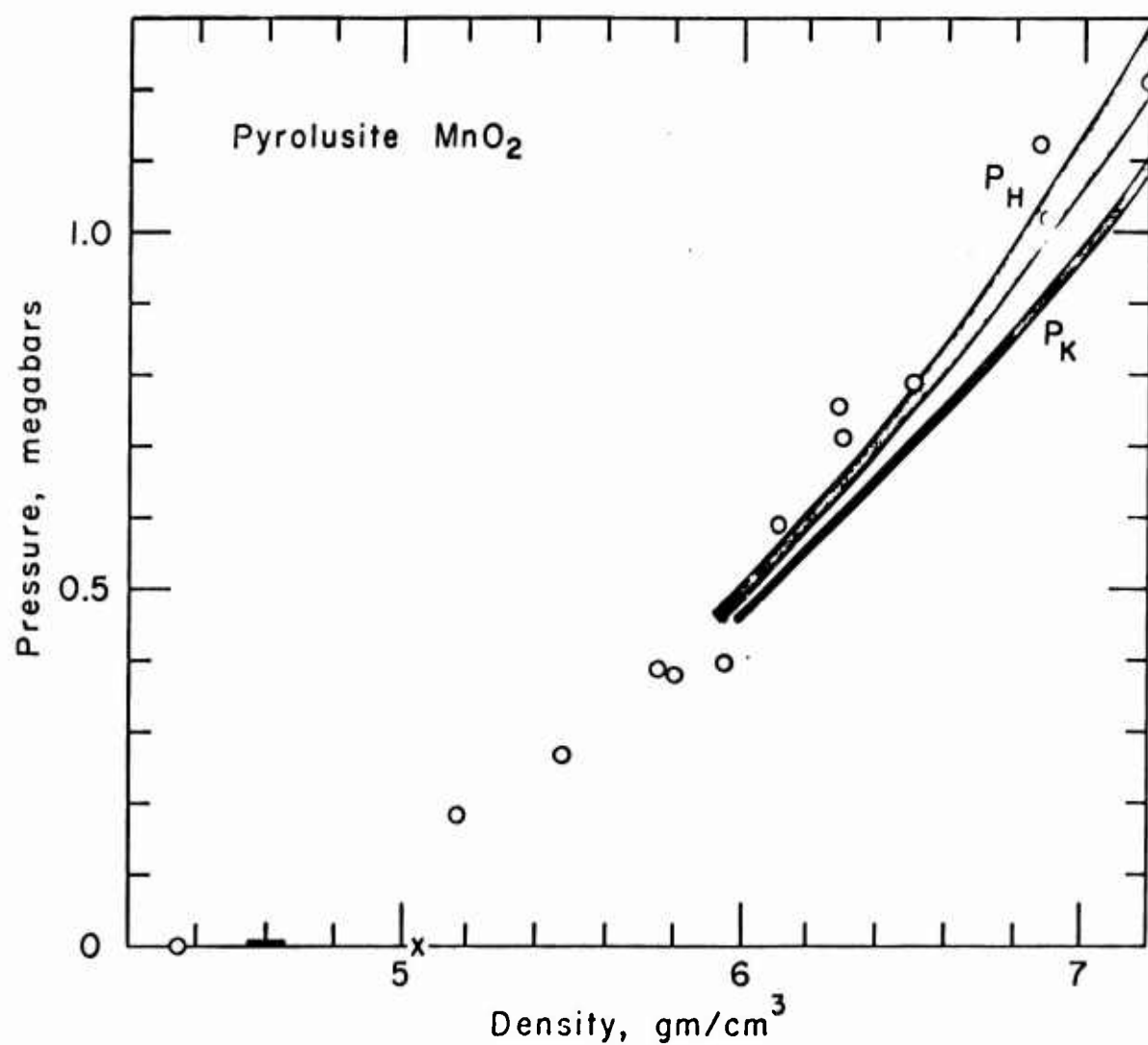
FIGURE 8. PRESSURE-DENSITY HUGONIOT FOR MnO_2 AND DERIVED HUGONIOT AND
ISOTHERM, ASSUMING NO PHASE CHANGE
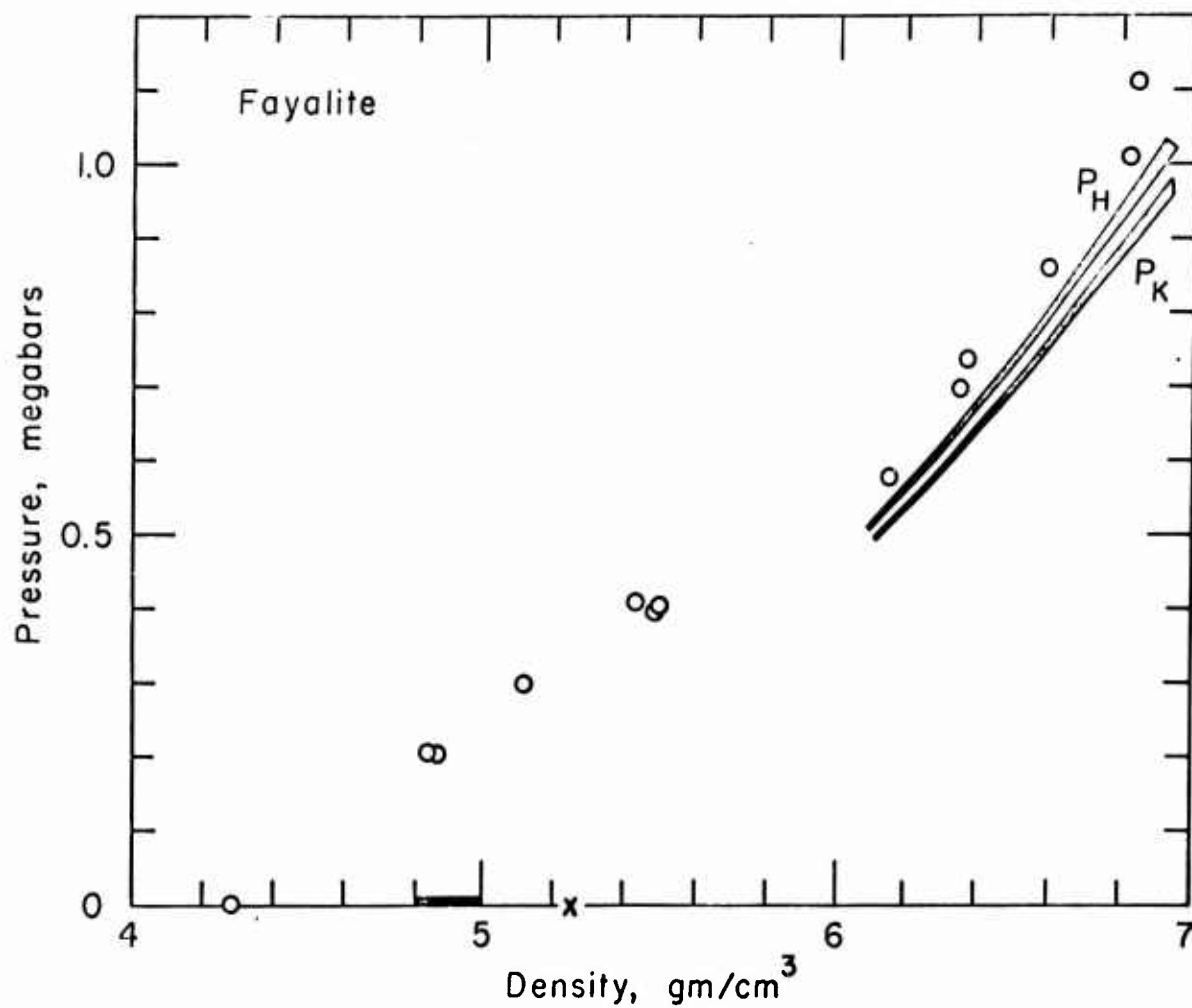
FIGURE 9. PRESSURE-DENSITY HUGONIOT FOR ROCKPORT FAYALITE AND DERIVED
METASTABLE HUGONIOT AND ISOTHERM FOR INDICATED RANGE OF ρ_0

135
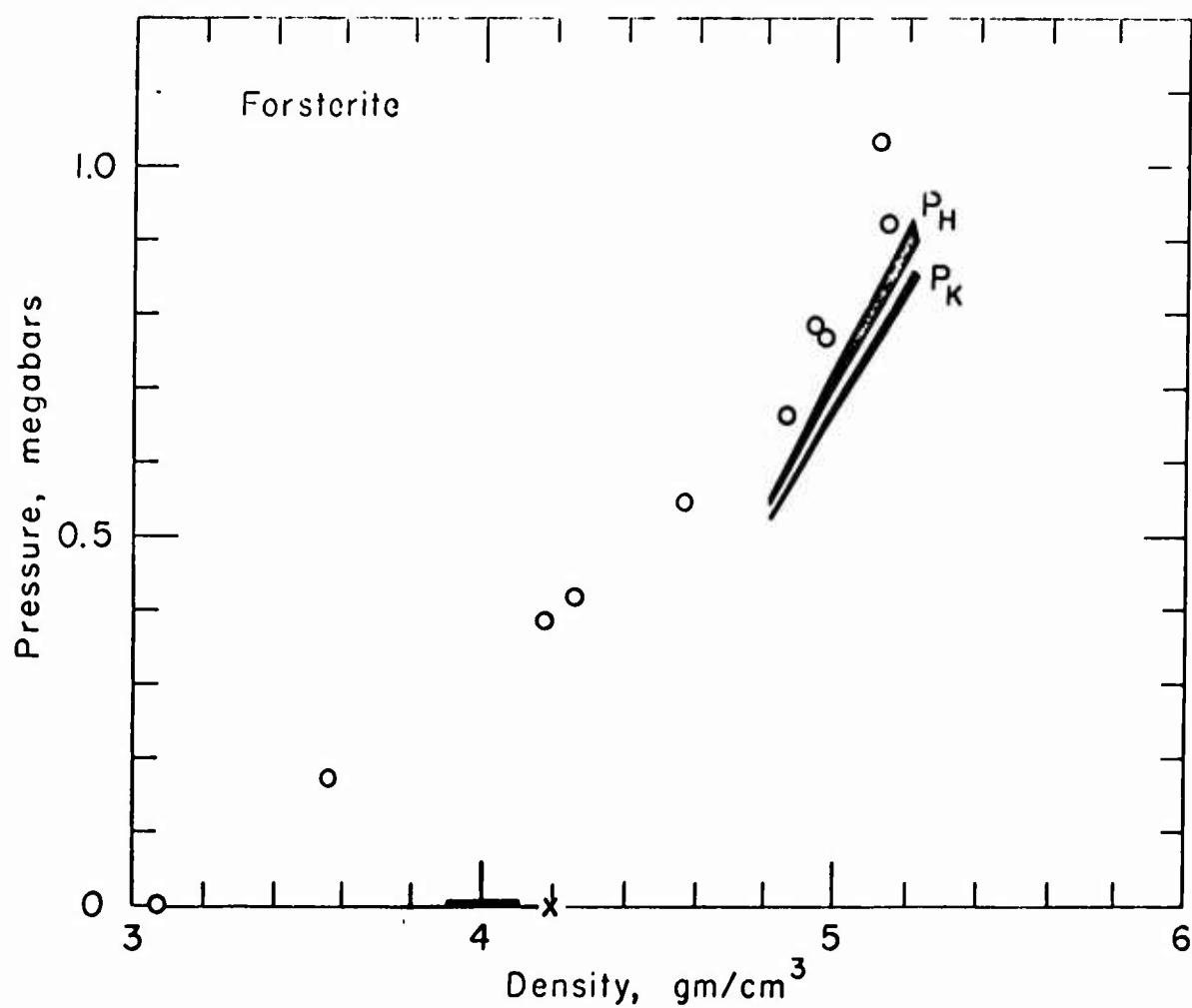
FIGURE 10. PRESSURE-DENSITY HUGONIOT FOR CERAMIC Mg_2SiO_4 AND DERIVED
METASTABLE HUGONIOT AND ISOTHERM FOR HIGH-PRESSURE PHASE
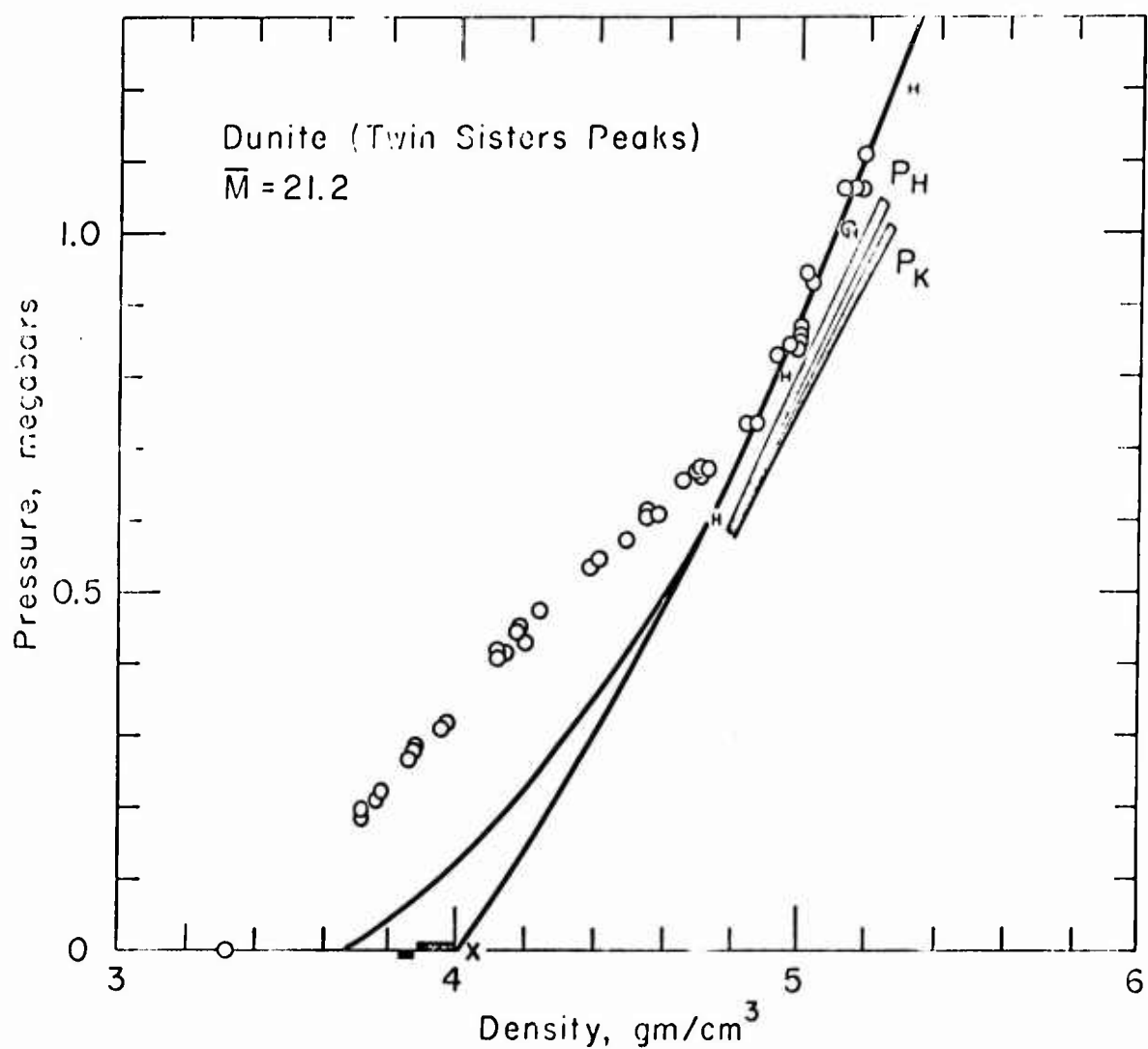
FIGURE 11. PRESSURE-DENSITY HUGONIOT FOR TWIN SISTERS DUNITE AND DERIVED
METASTABLE HUGONIOT AND ISOTHERM FOR INDICATED RANGE OF ρ_0. The heavy bar
below the P(0) axis is the range of ρ_0 estimated by McQueen, et al. [4]; the X is the ρ_0 esti-
mated in this paper. Also shown are Birch-Murnaghan fits to the high-pressure data for two
different ρ_0. The symbol (H) indicates the range of metastable Hugoniots calculated by
McQueen, et al. [4].

137

FIGURE 12. PRESSURE-DENSITY HUGONIOT FOR DIABASE FROM CENTREVILLE, VA.
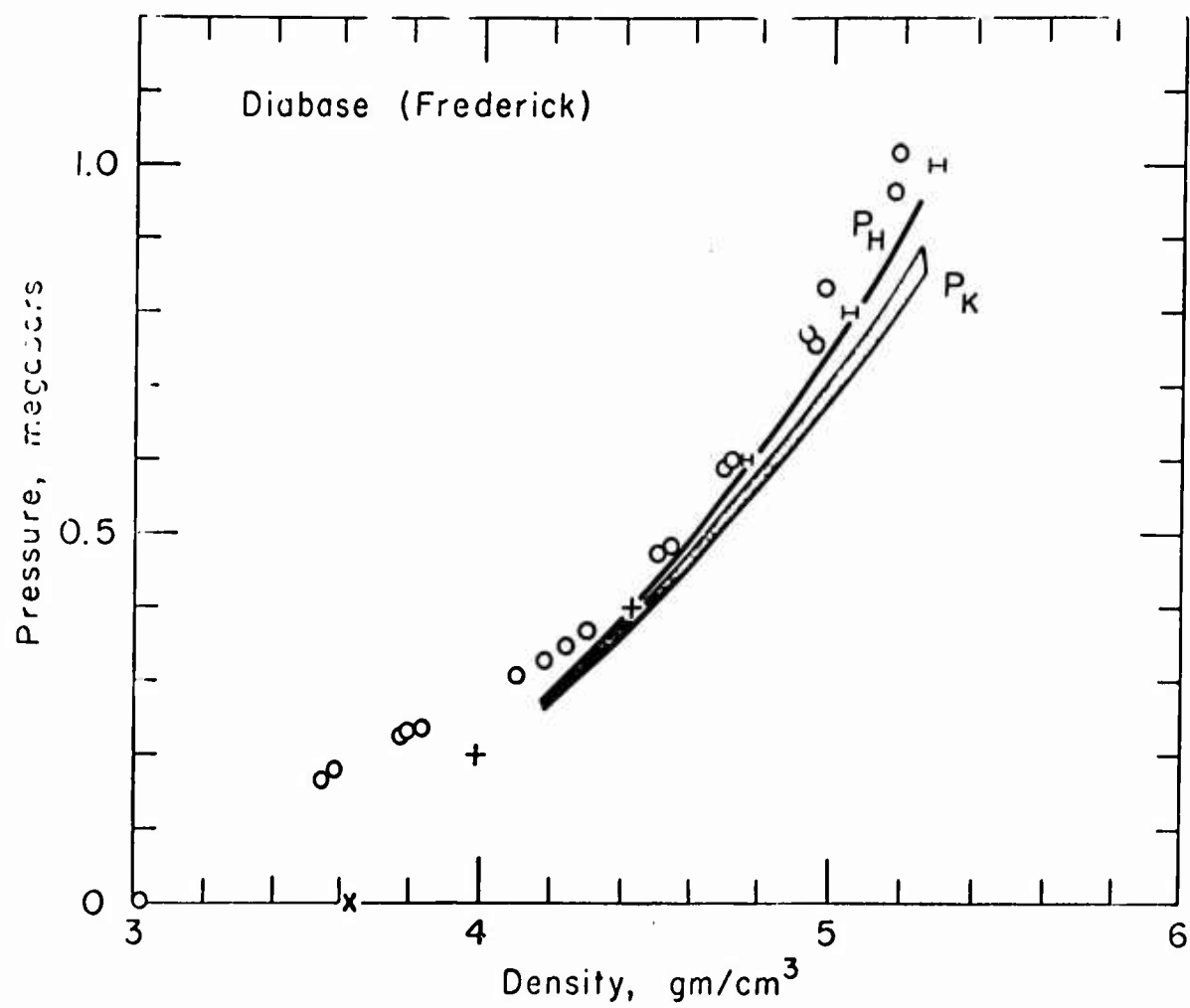
FIGURE 13. PRESSURE-DENSITY HUGONIOT FOR DIABASE FROM FREDERICK, MD.

FIGURE 14. PRESSURE-DENSITY HUGONIOT FOR BRONZITITE FROM THE STILLWATER COMPLEX
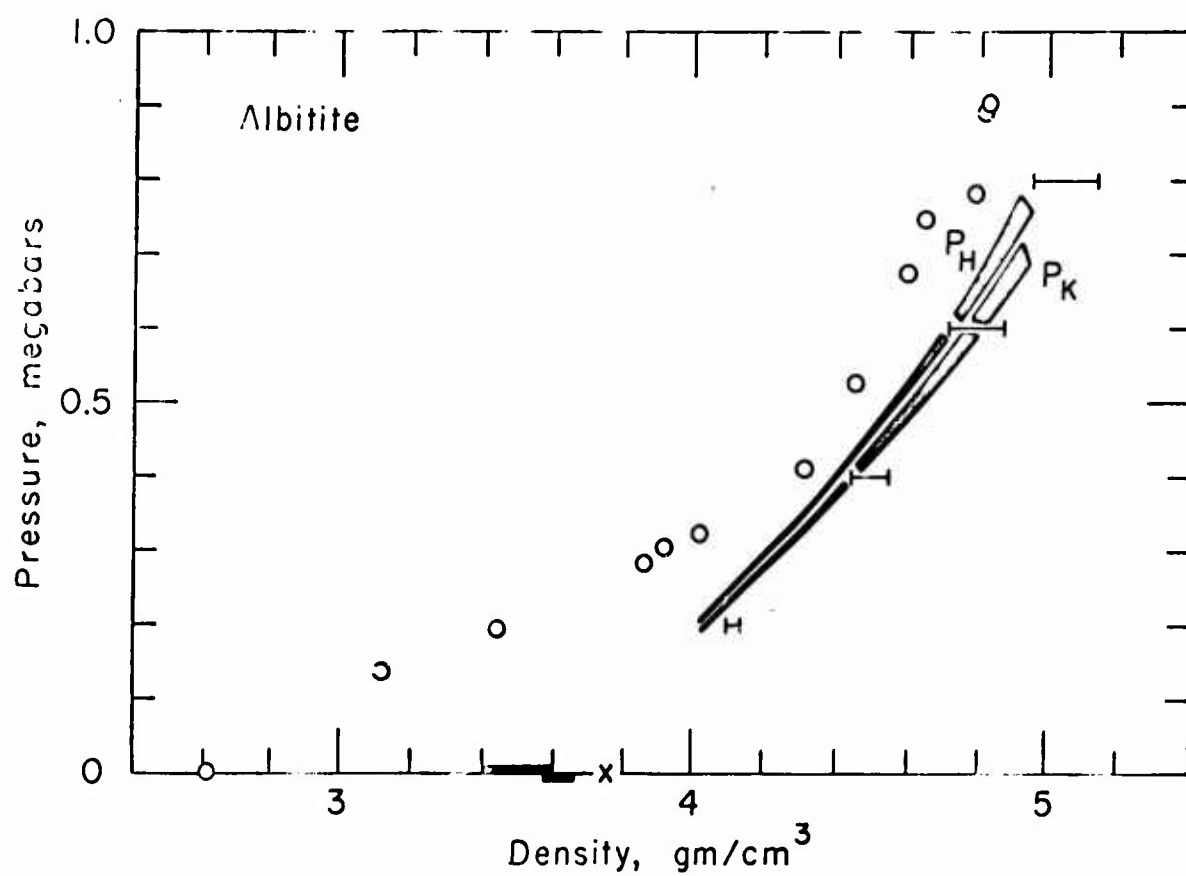
FIGURE 15. PRESSURE-DENSITY HUGONIOT FOR ALBITITE
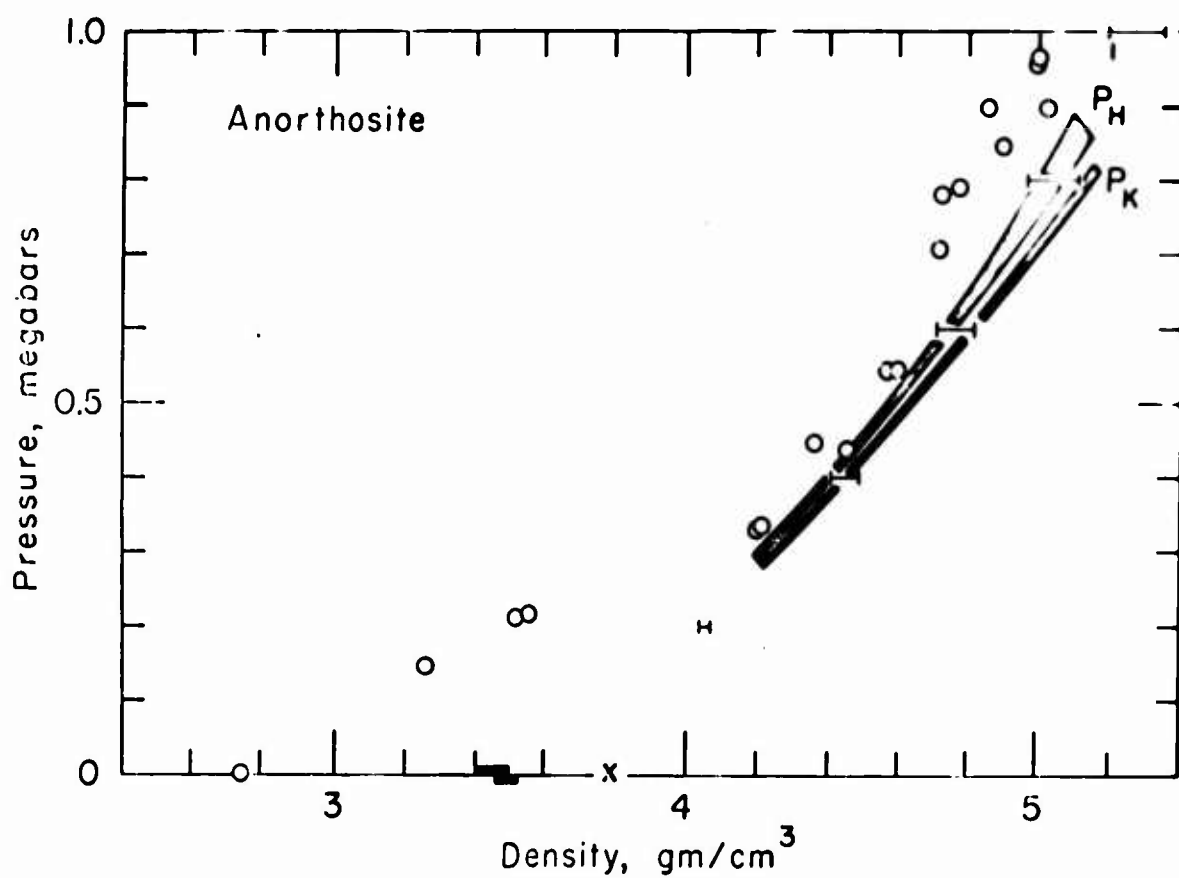
FIGURE 16. PRESSURE-DENSITY HUGONIOT FOR ANORTHOSITE

142
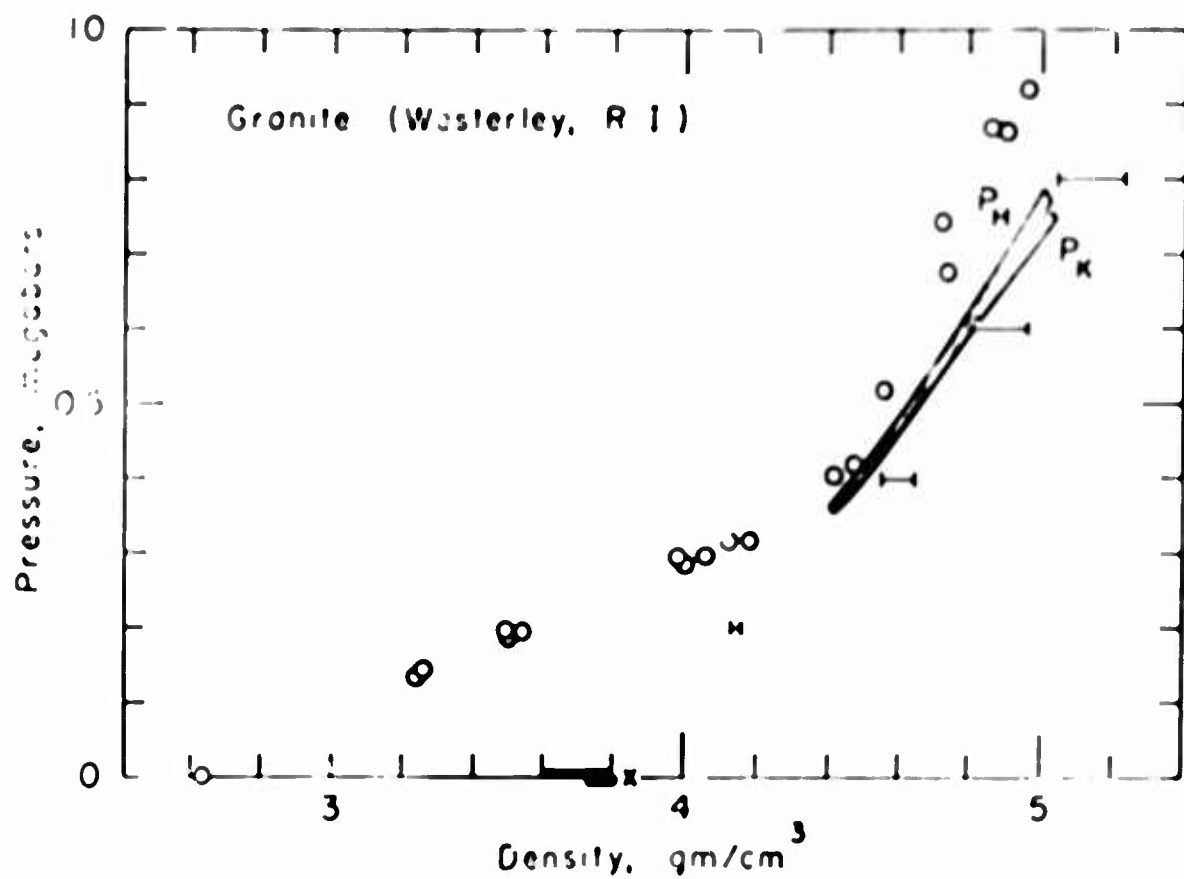
FIGURE 17. PRESSURE-DENSITY HUGONIOT FOR GRANITE.

FIGURE 18. PRESSURE-DENSITY HUGONIOT FOR ECLOGITE. Note that the high-pressure data extrapolate to a zero-pressure density which is less than the starting density, indicated that the transformation is probably not complete.

144

TABLE I. BIRCH-MURNAGHAN AND MURNAGHAN PARAMETERS FOR HIGH PRESSURE RAW HUGONIOT DATA [1]

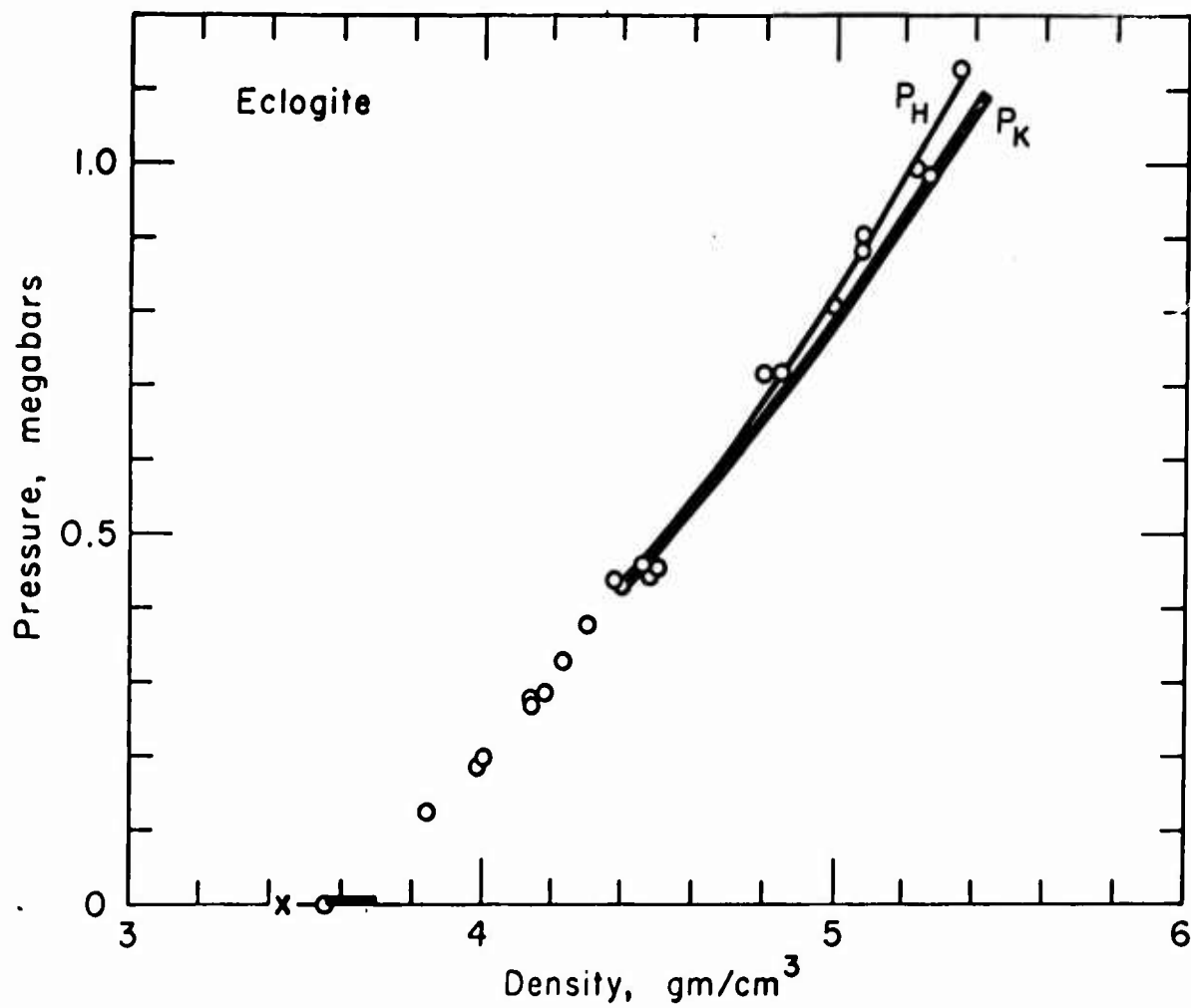| Material	ρ_0	Birch-Murnaghan ϕ_0	ζ	Murnaghan ψ_0	n	$(\rho_0/M)\phi_0^{-1/3}$	P(Mb)
Dunite	3.65	28.2	-1.89	29.1	5.37	0.0560	0.73-1.12
(Twin Sisters)	3.90	51.6	-0.37	49.5	4.42	0.0501	"
	4.00	65.0	+0.20	62.0	3.83	0.0477	"
	4.04 [5]	72.0	+0.46	68.8	3.51	0.0466	"
Dunite	4.50	47.9	+0.095	44.6	4.04	0.0506	0.65-1.19
(Iron Rich)	4.60	57.7	+0.51	54.0	3.50	0.0485	"
	4.63 [6]	61.7	+0.67	58.0	3.28	0.0477	"
	4.70	69.5	+0.96	66.0	2.82	0.0463	"
Diabase	3.40	24.8	-0.61	25.7	4.12	0.0528	0.36-1.02
(Centreville)	3.50	30.8	-0.20	31.6	3.75	0.0508	"
Diabase	3.40	26.2	-0.39	28.5	3.70	0.0518	0.33-1.03
(Frederick)	3.50	32.5	-0.00	34.8	3.30	0.0499	
Forsterite	3.33	3.2	-24.3	11.3	6.80	0.0738	0.66-1.04
(Ceramic)	3.85 [4]	35.8	-1.93	36.8	5.55	0.0578	
	3.90	40.6	-1.52	40.7	5.34	0.0564	
	4.00	53.1	-0.71	51.8	4.77	0.0534	
	4.10	68.9	+0.06	66.5	4.00	0.0503	
Fayalite	4.73	29.0	+0.04	28.3	3.70	0.0533	0.58-1.14
	4.80	32.0	+0.20	31.4	3.49	0.0522	
	5.00	42.7	+0.71	42.4	2.75	0.0493	
Spinel	3.60	27.1	-2.05	29.3	5.26	0.0575	0.68-1.16
	3.80	44.7	-0.75	44.7	4.55	0.0527	
	3.86 [4]	52.9	-0.38	51.4	4.23	0.0511	
	3.90	56.6	-0.17	55.6	4.05	0.0503	
Magnetite	5.40	23.7	-0.59	23.7	4.30	0.0568	0.62-1.31
	5.44 [4]	25.3	-0.47	25.1	4.22	0.0562	
	5.50	27.3	-0.32	27.0	4.09	0.0554	
	5.70	36.1	+0.22	35.2	3.53	0.0526	
	5.90	47.5	+0.79	46.6	2.75	0.0496	
	6.10	63.1	+1.43	62.7	1.64	0.0464	
Hematite	5.50	38.6	+0.38	39.3	3.07	0.0506	0.90-1.42
	5.70	49.3	+0.80	50.3	2.44	0.0483	
	6.00	72.1	+1.58 [1]				
Rutile	4.37 [4]	8.74	-7.15	5.68	9.20	0.0921	1.03-1.24
	5.10	38.0	+0.30	39.0	7.62	0.0484	
	5.80	174.1	+3.41 [1]	129.2	2.87	0.0431	
Periclase	1.62	44.6	-0.39	49.2	3.65	0.0489	0.3-2.6 (2)
	1.45 [5]	46.4	-0.24 *	50.6	2.92	0.0462	(3)
	1.62	48.4	-0.18 *	51.8	3.06	0.0481	(4)
	3.57 [7]	50.7	+0.36 *	51.1	3.27	0.0477	0-0.3 (5)
	3.57 [7]	47.8	-0.26	48.4	3.92	0.0486	0.2-1.26
	3.57	49.7	+0.29 *	51.5	3.09	0.0475	(6)
Corundum (Ceramic)	3.83 [3]	91.8	+1.83 [7]	28.9	7.94	0.0612	0.31-1.64
Pyrolucite	4.34	16.2	-0.76	15.4	4.57	0.0602	0.18-1.20
	4.36	14.8	-1.37	14.2	5.05	0.0621	
Stishovite	4.35	102.3	+0.79 *	106.7	2.29	0.0458	0.6-2.0 (2)
	4.35	104.5	+0.99 *	110.0	1.91	0.0453	(4)
	4.28	102.8	+0.96	107.9	1.97	0.0449	(3)

(1) Unless otherwise noted data from McQueen, et al. [4, 17]. McQueen (personal communication) and Clark [6]. ρ_0 in g/cm³, ϕ_0 in (km/sec)² or 10^{10} dy·cm/g

(2) Al'tshuler, et al. [13], Hugoniot

(3) Al'tshuler, et al. [13], 4000°K isotherm

(4) Al'tshuler, et al. [13], 0°K isotherm

(5) Perez-Albuerne and Drickamer [12], isothermal compression

(6) Isotherm, this paper

(7) ϕ decreases with pressure

* Isotherm

145

TABLE II. EXAMPLE OF BIRCH-MURNAGHAN AND MURNAGHAN FITS TO HIGH-PRESSURE PHASE OF TWIN SISTER'S DUNITE (ρ_0 = 3.90, ξ = 0.37, n = 4.42; and ρ_0 = 4.0, ξ = +0.20, n = 3.83)

| | | | Birch-Murnaghan | | | | Murnaghan | | | |
| | | | $\rho_0 = 3.90$ | | $\rho_0 = 4.0$ | | ρ_0 3.90 | | ρ_0 4.00 | |
V/V_0	ρ_3 (gm/cm³)	P (kb)	P_c (kb)	ϕ (km/sec)²	P_c (kb)	ϕ (km/sec)²	ρ_c (gm/cm³)	ϕ (km/sec)²	ρ_c (gm/cm³)	ϕ (km/sec)²
1.000	ρ_0	0	0	51.6	0	65.0	3.90	49.5	4.00	62.0
0.806	4.84	734	708	101.1	706	103.6	4.87	106.3	4.88	108.6
0.801	4.87	730	739	102.8	738	105.0	4.87	106.0	4.87	108.3
0.791	4.93	831	802	106.4	802	107.9	4.96	113.0	4.96	114.1
0.783	4.98	832	856	109.4	856	110.3	4.96	113.1	4.96	114.2
0.783	4.98	844	856	109.4	856	110.3	4.97	113.9	4.97	114.9
0.778	5.01	844	889	111.3	889	111.	4.97	113.9	4.97	114.9
0.780	5.00	858	878	110.7	878	111.2	4.99	114.9	4.99	115.7
0.778	5.01	857	889	111.3	889	111.7	4.99	114.8	4.98	115.6
0.777	5.02	941	900	111.9	901	112.2	5.06	120.5	5.06	120.4
0.775	5.03	940	911	112.5	912	112.7	5.06	120.5	5.06	120.3
0.759	5.14	1007	1039	119.3	1039	117.9	5.11	125.0	5.11	124.0
0.760	5.13	1070	1027	118.7	1027	117.5	5.16	129.2	5.16	127.5
0.753	5.18	1063	1087	121.9	1086	119.9	5.15	128.7	5.15	127.1
0.754	5.17	1068	1075	121.2	1074	119.4	5.16	129.0	5.16	127.4
0.753	5.18	1123	1087	121.9	1086	119.9	5.20	132.7	5.20	130.4
Standard deviation			28.5		28.7		0.0245		0.0247	
			3.10%		3.12%		0.488%		0.491%	

TABLE III. PARAMETERS OF LINEAR U_s-U_p FITS TO HIGH PRESSURE PHASES CORRECTED TO METASTABLE HUGONIOT[1]

Material	ρ_0	λ	γ_0	K_0	ϕ_0	ΔE_0	E_{HO}	$(\rho_0/M)\phi_0^{-1.3}$
Albitite	3.400	1 37	1.74	0.84	24.8	6	1.5	0.0572
	3.500	1.23	1.46	1.09	31.2	7	1.5	0.0545
	3.600	1.04	1.08	1.43	39.8	8	1.5	0.0517
Anorthosite	3.400	1.24	1.48	0.91	26.7	5	1.5	0.0542
	3.500	1.12	1.24	1.12	32.0	6	1.5	0.0525
Bronzitite	3.400	1.08	1.16	1.16	34.1	2	1.5	0.0507
	3.500	0.97	0.94	1.43	40.9	2	1.5	0.0491
Diabase (Centralville)	3.400	1.24	1.48	0.86	25.3	4	1.0	0.0531
	3.500	1.09	1.18	1.14	32.6	r	1.0	0.0503
Diabase (Frederick)	3.400	1.21	1.42	0.89	26.2	4	1.0	0.0532
	3.500	1.12	1.24	1.09	31.1	5	1.0	0.0518
Dunite (Twin Sisters)	3.900	1.26	1.52	1.96	50.3	8	1.3	0.0498
	3.970	1.18	1.36	2.29	57.4	9	1.3	0.0485
	4.000	1.10	1.20	2.40	60.0	9	1.3	0.0482
Eclogite*	3.56	0.97	0.94	1.49	41.8	0	1.'	0.0460
	3.70	0.79	0.58	1.95	52.7	0	1.0	0.0443
Granite	3.60	1.27	1.54	1.17	32.5	15	1.0	0.0548
	3.70	1.06	1.12	1.56	42.2	16	1.0	0.0516
	3.80	0.81	0.72	2.04	53.7	16	1.0	0.0489
Corundum*	3.833	1.38	1.76	1.95	50.9	0	1.0	0.0507
	3.900	1.20	1.40	2.47	63.4	0	1.0	0.0479
Fayalite	4.800	1.23	1.46	1.31	27.3	3	1.0	0.0548
	4.900	1.11	1.22	1.63	33.3	3	1.0	0.0524
	5.000	1.00	1.00	1.89	37.8	4	1.0	0.0512
Forsterite	3.900	1.34	1.68	1.63	41.8	10	1	0.0559
	4.000	1.18	1.36	2.05	51.2	11	1	0.0536
	4.100	0.09	0.80	2.70	65.9	11	1	0.0505
Hematite	5.500	1.15	1.30	1.92	34.9	4	1	0.0527
	5.600	1.06	1.12	2.22	39.6	5	1	0.0514
	5.700	0.96	0.92	2.58	45.2	5	1	0.0501
Magnetite	5.50	1.15	1.30	1.60	29.1	2	1	0.0541
	5.60	1.05	1.10	1.87	33.4	2	1	0.0526
	5.70	0.96	0.92	2.20	38.7	3	1	0.0509
Periclase*	3.585	1.23	1.46	1.79	49.9	0	1.3	0.0583
Pyrolucite*	4.55	1.28	1.56	0.90	21.8	0	1.3	0.0562
	4.65	1.15	1.30	1.19	25.6	0	1.3	0.0544
Spinel	3.600	1.39	1.78	1.19	33.1	1	1.3	0.0552
	3.700	1.30	1.60	1.48	40.0	2	1.3	0.0532
	3.800	1.18	1.36	1.87	49.2	3	1.3	0.0510
Quartz	3.900	1.25	1.50	1.60	41.0	12	1	0.0565
	4.000	0.97	0.94	2.06	51.6	13	1	0.0536

* No phase change assumed

(1) $V_s = \phi_0^{1/2} + \lambda U_p$

units $\rho_0 (g\ cm^{-3})$, $K_0 (Mb)$, $\phi_0 (km\ sec)^2$, $\Delta E_0 (10^9\ erg/g)$, $E_{HO} (10^7\ erg/g)$

(2) Wackerle [15]

147

TABLE IV. ZERO PRESSURE PARAMETERS

Material	$\overline{M}$	ρ_o	ϕ_o	$(\rho_o/\overline{M})\phi_o^{-1/3}$
		Ultrasonic Results[1]		
Jadeite	20.2	3.33	41.1	0.0478
Albitite	20.4	2.61	26.5	0.0429
Granite	20.6	2.63	20.2	0.0468
Bronzitite	20.7	3.30	34.2	0.0491
Bronzitite	20.7	3.23	30.2	0.0509
Anorthosite	21.0	2.72	30.7	0.0414
Dunite	21.2	3.32	38.4	0.0464
Diabase	21.5	3.01	26.6	0.0469
Diabase	21.8	2.99	27.1	0.0456
Eclogite	22.2	3.55	26.4	0.0535
Eclogite	22.3	3.42	34.5	0.0471
Dunite	25.1	3.79	32.8	0.0472
		Ultrasonic Results[2]		
Al_2O_3	20.03	3.97	63.1	0.0498
$MgO \cdot 2.61\ Al_2O_3$[4]	20.07	3.62	55.2	0.0473
Mg_2SiO_4	20.10	3.02	32.0	0.0473
MgO	20.16	3.58	44.6	0.0501
MgO	20.16	3.58	47.3	0.0491
"Garnet"	23.79	4.16	42.2	0.0502
ZnO	40.69	5.62	24.7	0.0474
		X-ray Results[3]		
MgO	20.16	3.58	49.7	0.0483
$Fe_1 \cdot 6MgO \cdot 4SiO_4$[4]	27.31	4.60	43.1	0.0480
CaO	28.04	3.35	33.5	0.0371
Fe_2SiO_4[4]	29.11	4.85	43.1	0.0475
Ni_2SiO_4[4]	29.93	5.35	39.5	0.0525
Fe_2O_3	33.08	5.20	35.2	0.0480
"FeO"	34.53	5.75	26.8	0.0556
"FeO"	35.13	5.69	23.4	0.0566
MnO	35.47	5.37	26.8	0.0504
NiO	37.35	6.81	29.2	0.0592
CoO	37.47	6.44	29.6	0.0556
CdO	64.20	8.24	13.1	0.0545

[1]Compiled by McQueen, et al. [4] adiabatic ϕ_o

[2]Compiled by O. L. Anderson (private communication, 1967); isothermal ϕ_o

[3]Drickamer, et al. [14] and Mao [10]; isothermal ϕ_o

[4]Spinel structure

Material	$\bar{M}$	Sample Density ρ_o^L	Theoretical Density ρ_o^L	High P Phase ρ_o^H	Oxides Density	Low P Phase ϕ_o	High P Phase ϕ_o
Albitite	20.4	2.61		3.75	3.85	25	58
Anorthosite	21.0	2.75		3.79	3.91	30	55
Bronzitite	20.7	3.28		3.60	4.08	33	49
Diabase	21.8	2.98		3.60	4.01	27	42
Diabase	21.8	2.98		3.67†			
Diabase	21.5	3.02		3.63†	4.08	27	52
Dunite	21.2	3.32		4.05	4.04	40	65
Dunite	21.2	3.32		4.01†			
Dunite	25.1	3.79		4.64†	4.64	33	59
Eclogite*	22.3	3.56		3.44	4.14	36	34
Granite	20.6	2.63		3.85	4.07	22	61
Fayalite	29.11	4.28	4.39	5.25	5.29	26	55
Fayalite	29.11	4.28	4.39	5.12†			
Forsterite	20.10	3.07	3.21	4.19	3.85	40	85
Forsterite	20.10	3.07	3.21	4.19†			
Hematite	31.94	5.00	5.27	5.90		31	59
Hematite	31.94	5.00	5.27	5.77†			
Corundum*	20.40	3.83	3.99	3.91		63	66
Spinel	20.32	3.42	3.58	3.95	3.86	56	69
Spinel	20.32	3	3.58	4.01†			
Magnetite	33.08	5.12	5.21	5.90	5.54	31	53
Magnetite	33.08	5.12	5.21	6.03†			
Pyrolucite*	28.98	4.35	5.23	5.05			49
Periclase*	20.20	3.59				47	50
Quartz	20.03		2.65	4.21	4.29	14	87
Rutile	26.63	4.25	4.25	5.38		49	77

*No phase change assumed

†Raw Hugoniot data

TABLE VI. BIRCH AND BIRCH-MURNAGHAN PARAMETERS[1]

Material	ρ_0 (g/cm^3)	$\bar{M}$	K_0 (K_b)	ℓ	n	γ	ϕ_0 (km/sec)^2
Olivine							
Mg_2SiO_4	3.02	20.1	967	-0.6	4.8	2.2	32
Spinels							
$MgO \cdot 2.61\ Al_2O_3$	3.62	20.1	2000	-0.1	4.19	1.9	55
$Fe_{1.6}Mg_{0.4}SiO_4$	4.60	27.3	1980	0*	4.00*	1.8	43
Fe_2SiO_4	4.85	29.1	2090	0*	4.00*	1.8	43
Ni_2SiO_4	5.35	29.9	2110	0*	4.00*	1.8	39
Fe_2FeO_4	5.20	33.1	1830	0*	4.00*	1.8	35
Post-Spinels							
Mg_2SiO_4	4.19	20.1	3561	+0.7	3.1	1.4	85
$MgAl_2O_4$	4.01	20.3	2767	+0.5	3.3	1.5	69
Dunite	4.01	21.2	2607	+0.3	3.7	1.7	65
Dunite	4.65	25.1	2743	+0.7	3.1	1.4	59
Fe_2SiO_4	5.12	29.1	2888	+1.0	2.2	0.9	56
Fe_2FeO_4	6.03	33.1	2767	+1.1	2.1	0.9	46
Oxides							
MgO	3.58	20.2	1780	0	4.0	1.8	50
FeO	5.75	34.5	1540	+0.5	3.4	1.5	27
SiO_2 †	4.28	20.0	4622	+1.0	2.0	0.8	108

[1]Compiled from O. L. Anderson (personal communication, Drickamer, et al. [14], Mao [10] and this paper.

*Assumed

† Stishovite (4000°K isotherm)

STABILITY STUDIES FOR PROJECT PAYETTE

K. Nair
Materials Research and
Oakland, Calif

ABSTRACT

This paper summarizes the investigations conducted to evaluate the structural stability of large (approximately 300 feet in diameter) underground cavities that have been proposed for construction in the Tatum Salt Dome in Mississippi.

A general (systems) approach to the problem of cavity stability analysis was developed. The advantages of such an approach have been established.

Four axisymmetric cavity shapes were analyzed. These shapes were chosen in accordance with criteria laid down by the Atomic Energy Commission and included shapes which might result if solution mining techniques were used. Based on a survey of the existing published information, appropriate assumptions were made with regard to the geologic profile and the initial stress (in-situ stress) conditions. It was concluded that the in-situ stresses were close to hydrostatic. For the purposes of analysis and in order to bracket the problem, the following values of the ratio (K) of initial horizontal to initial vertical stress were used: 0.75, 1.00, and 1.33.

Based on the assumption of an instantaneous creation of the cavity, the stresses and displacements in the surrounding salt medium were computed using the finite element method. The analyses were conducted for the four cavity shapes and the three initial stress conditions. Material behavior was represented by (1) Linear Elasticity, (2) Bilinear Elasticity, and (3) Linear Elasticity with Superimposed Creep. It was concluded that these representations of material behavior provided results which covered the range of stress and displacement values likely to occur in the field. Material constants for these models were obtained from existing experimental information.

Computed displacements were compared with those that have been observed in existing cavities in salt, and it was found that the theoretical results were of the right order of magnitude.

Material failure formed the basis of the performance criteria necessary to evaluate stability. It was concluded that creep rupture was the most likely mode of failure. A creep rupture criteria based on a life consumption hypothesis was used to evaluate stability.

Under the assumptions used in the investigation, it was found that for $K \leq$ 1.00, all the shapes analyzed would be stable with the sphere as the preferred shape. For $K = 1.33$, all the shapes analyzed were considered unstable.

Because of the general (systems) approach used for this investigation, it has been possible to identify those areas in cavity stability analyses where research is needed and to discuss the applications of the techniques used in this study to other investigations.

INTRODUCTION

In connection with Project Payette, which is concerned with the detection of underground nuclear explosions, it was necessary to determine the technical feasibility of constructing and maintaining a large (approximately 315 feet in diameter) unsupported underground cavity at a depth of approximately 2700 feet in the Tatum Salt Dome in Mississippi. The dimensions and the location of the cavity in the salt dome were governed by criteria laid down by the Atomic Energy Commission. Within the framework of the specified criteria, cavities of various shapes and dimensions could be utilized. One aspect of the feasibility study was to investigate the structural stability of various cavity shapes and to recommend a preferred shape.

The paper deals with the studies that were conducted to evaluate the structural stability of various proposed cavities. In order to aid future investigations, needed research in various aspects of stability analysis and the application of the method of analysis used in this investigation to other conditions are also briefly discussed.

APPROACH TO THE PROBLEM

Definition of Problem

For the purpose of this paper, it is convenient to regard the cavity and surrounding material as a "cavity system." The cavity system accepts certain inputs in the form of loads and environmental variables and responds by developing a mechanical state within its structure. The designer's problem is to determine if the cavity system can sustain the input satisfactorily over the design period.

The concept that the determination of the mechanical state, as defined by the matrices of stress and strain, is necessary to the evaluation of the structural stability of underground cavities is fundamental to this discussion. It is recognized that in some cases other states, e.g., the chemical state, might be the most significant. However, this study deals exclusively with the determination of the mechanical state.

Generalized (Systems) Approach

Because of the numerous factors that go into the stability analysis of an underground cavity, it was considered necessary to formulate a framework based on generalized analytical and systems concepts to enable one to look at the problem as a synthesized product of many different components. The approach to the problem is a general one and can be used in the investigation of the structural stability of any underground cavity. The following steps form the basis of such an approach which is depicted in figure 1.

1. Appropriate input and output variables must be defined.

2. The structure must be defined geometrically and the materials and construction techniques identified. This may be considered a description of the cavity system.

152

3. The response of the cavity system to all classes of input expected to occur in-service must be determined. This involves determination of the system function. There are two[*] general engineering approaches for determining the system function:

   (a) Testing Approach - This requires testing under service conditions (full scale and model) and results in various empirical design procedures.

   (b) Macroanalytical Approach - This forms much of the theoretical basis of most of the work in applied science and engineering. Continuum (solid) mechanics is the main discipline in this method, and the object may be considered to be the formulation and solution of an appropriate boundary value problem. It was this approach that was followed in the studies for Project Payette.

4. Appropriate criteria have to be formulated to judge the response of the system from the performance standpoint.

5. Modification of the cavity system must be permitted in order to attain as near an optimum condition as possible.

A general (systems) approach to the problem of cavity stability offers several advantages:

1. A good description of the problem is required. The development of such a description will provide an overall grasp of the complexity and breadth of the problem, including the need for a continuous feedback, which is essential to the development of improved methods of design.

2. The overall framework provided by such an approach will provide a means for coordinating and utilizing research from many sources and disciplines.

3. It will enable the profession to readily identify areas where research is needed.

4. Because of the complete description of the problem, it is possible to conduct investigations at two levels, (a) from a long-range standpoint, (b) to fulfill short-term needs. Methods involving the current state of the art can be utilized to develop immediate design methods without losing sight of needed improvements.

5. Such an approach also provides the framework for developing design optimization techniques.

DEFINITION OF INPUT AND OUTPUT VARIABLES

The input variables consist of loads (body forces and external loads)[**] and environmental factors. In defining the input variables, the limitations of the solution techniques available

---

[*]A third approach, the micromechanistic approach, which deals with behavior at the atomic or molecular level, is not considered here.

[**]Dynamic loads due to nuclear explosions and other loads that might occur in the future were not considered.

153

for solving appropriate boundary value problems should be kept in mind. The following assumtions were made for the input parameters:[*]

1. The Tatum Dome can be considered static for the purposes of analysis.

2. The vertical stress at a depth of 2700 feet was 2700 psi, i.e., 1 psi per foot of depth.

3. The unit weight of the salt was taken as 144 lbs/cu ft.

4. The existing state of stress in the salt at the proposed cavity depth of 2700 feet was assumed close to hydrostatic. For the purposes of analysis and in order to bracket the problem, the following values of the ratio of initial horizontal to initial vertical stress were used: 0.75, 1.00, and 1.33.

5. The temperature at the depth of the cavity is $125^{\circ}F$, and for the purposes of analysis, at least for the feasibility study, a uniform temperature field was assumed.

6. The nature of loads introduced by construction methods were not taken into account.[**] It was assumed the cavity was created instantaneously. This is considered a conservative assumption and suitable only for a preliminary feasibility study.

The output variables necessary to define the mechanical state of the salt surrounding the cavity were taken as the stress, strain, and the components of displacements in the surrounding salt.

DESCRIPTION OF CAVITY SYSTEM

The top of the salt dome is located approximately 1500 feet below the ground surface. At a depth of 2700 feet, which represents the location of the center of the cavity, the diameter of the dome is approximately 4000 feet. On the basis of experience with similar problems, it was assumed that the stability of a cavity approximately 315 feet in diameter will not be influenced significantly by the material outside the dome, i.e., the effect of the cavity will be relatively local and will not be felt outside the salt stock.[***] Therefore, in describing the cavity system from a geologic standpoint, only the salt stock is considered.

The description of the cavity system was divided into two phases:

1. Geologic description of the surrounding rock

2. Geometry of th proposed cavities

The following two assumptions were made with regard to the geologic description.

---

[*]A detailed discussion of the validity of these assumptions is given in Nair [1].

[**]In addition to loads introduced by the gradual creation of the cavity, the temperature gradient during construction could result in significant thermal stresses.

[***]This assumption will be verified by the solution of appropriate boundary value problems.

1. No faults, fractures, or other geologic discontinuities exist within the salt stock.

2. The salt was assumed to be a homogeneous and isotropic material, and hence, the cavity was assumed to be constructed in such a material.

The above assumptions were made after reviewing the literature and consulting with recognized authorities in engineering geology. While variations from these assumptions are always possible, no information which documented such variations could be found.

Since the problem is a three-dimensional one, the shapes that could be considered were classified into two broad categories.

1. Solids of revolution symmetrical about a vertical axis, i.e., axisymmetric shapes

2. Shapes without axisymmetry

Existing methods of analysis are limited to axisymmetric shapes, and hence, the choice of shapes for this study is limited to this class. It should be pointed out that it is possible to construct nonaxisymmetric shapes which meet the requirements set forth by the AEC for this project. From the stability standpoint, some of these shapes might possess advantages over the axisymmetric shapes considered in this investigation. It should also be recognized that the capability of being able to analyze any axisymmetric shape is a considerable advance over the capabilities that existed at the time of previous investigations when only very special axisymmetric shapes, e.g., prolate spheroid, oblate spheroid, and sphere, could be studied.

Within the framework of axisymmetric shapes, a great number of practical possibilities exist; however, due to the time limitations, only a few were analyzed. The shapes were selected to be representative of those which might result from solution mining and those shapes which might be desirable from a conventional mining standpoint.

The shapes analyzed in the study are shown in figure 2. They meet all the requirements specified by the Atomic Energy Commission. The egg and prolate spheroid represent those shapes which might develop in using solution mining techniques.

MATERIAL CHARACTERIZATION

As pointed out earlier, the approach followed in this investigation involved the determination of the mechanical state through the formulation and solution of appropriate boundary value problems. The determination of the mechanical state falls within the discipline of solid mechanics. Once this is recognized, then there is a logical sequence of steps governed by various rules which have to be followed in determining the mechanical state.

The starting point of solid mechanics is the basic laws of classical physics expressed in mathematical form. These la   include the laws of thermodynamics, laws of momentum and force (Euler's Laws) and the l   embodying the principles of conservation. If, in addition to this, one could formulate a comp ete mathematical description of the physical properties of the materials and the input variables, one could obtain the solution of any problem in continuum

155

mechanics from a general system of governing equations within the limitations of existing mathematical methods for the solution of these equations. At the present time, the lack of a general description of material properties and input variables in mathematical form does not permit such a general approach. "Completeness is impossible; physical reality is so complex that it must be idealized to be formalized," Drucker [2]. The approach utilized at present is to construct various simplified mathematical models for the materials; these are described mathematically in the form of constitutive equations, which in conjunction with the basic laws can be utilized to pose and solve a boundary value problem.

For this study, material characterization* is defined as the selection or formulation of constitutive equations to represent the behavior of the various materials which form part of the cavity system. These constitutive equations are really degenerate forms of general equations and only include (for the particular problem or aspect of a problem) those phenomena which are of importance.

The selection of a constitutive equation (mathematical model) to represent the behavior of a material is done through the systematic and logical study of experimental and field data on the performance of the material. Experimental observation is always limited in scope; the reduction of observations into a mathematical law can only be done through logic and in accordance with the general principles of continuum mechanics.

The approach followed in material characterization was to first develop the necessary theoretical framework and to examine the existing experimental information. Since it was not possible to perform additional tests for this study, the characterization was based exclusively on test results reported in the literature, Serata [4], U. S. Department of Interior, Bureau of Reclamation [5] and U. S. Army Engineers Waterways Experiment Station [6]. The principal information utilized was from the existing test data on salt specimens from the Tatum Salt Dome.

Based on an examination of these data and accounting for the limitations of the analytical methods, the following models were chosen under the general assumptions of homogeneity and isotropy:

1. Time-Independent Behavior

    (a) Linear Elasticity - The use of such a model would result in a conservative estimate for the stress distribution; displacements, however, would be underestimated. The results from such an analysis would give an upper bound on the stresses.

    The following material constants were chosen for the linear elastic analysis:

---

*Other definitions of characterization, which are more concerned with assisting in the development of new materials, are also used in the material science literature, Committee on Characterization of Materials Advisory Board [3].

156

$$E \text{ (Modulus of Elasticity)} = (1 \text{ and } 4) \times 10^6 \text{ psi}$$
$$\nu \text{ (Poisson's ratio)} = 0.2 \text{ and } 0.45$$

The range of values of the constants take into account different testing procedures and other variables, e.g., material variations.

(b) <u>Bilinear Elastic</u> - Such an analysis would permit some stress redistribution and is, therefore, more representative of the instantaneous behavior of salt. Because of the independence of the stress-strain curve from the confining pressures in the range of interest, the Von Mises criteria (octahedral shear stress) was used. Based on analyses of the data, a conservative estimate of the octahedral shear stress of 1400 psi was chosen. When the stress in the material exceeds this value, it is considered to have "yielded." The result is a decrease in modulus. The initial modulus and the modulus after yielding were chosen as follows:

$$E_1 \text{ (Initial Modulus)} = (1 \text{ and } 4) \times 10^6 \text{ psi}$$
$$E_2 \text{ (Final Modulus)} = (0.25 \text{ and } 1) \times 10^6 \text{ psi}$$
$$\nu \text{ (Poisson's ratio)} = 0.45$$

The change in modulus was determined from an effective stress-strain relation, and the material was assumed to remain isotropic.

2. Time-Dependent Behavior

<u>Linear Elasticity with Superimposed Creep</u> - Such an analysis would permit the closure of the cavity to be determined. Since linear elasticity is used, the stresses causing creep must be considered a conservative estimate. In reality, it is likely that some yield would occur before any significant creep could start; hence, the initial stresses would be lower than those predicted by linear elasticity. It may be assumed that the linear elastic with creep analysis will provide an upper bound on the displacements likely to occur.

For the elastic constants, the following values were chosen:

$$E_o \text{ (Initial Modulus)} = (1 \text{ and } 4) \times 10^6 \text{ psi}$$
$$\nu \text{ (Poisson's ratio)} = 0.45$$

In the creep equation $\epsilon_c = A\sigma^n t^m$

ϵ_c = effective strain

$A = 1.87 \times 10^{-13}$

σ = effective stress in psi

t = time in hours

157

n = 2.98

m = 0.36

The effective stress and strain is used as this permits generalization from the one-dimensional data to three dimensions.

These three models were chosen to give a spectrum of values which could be expected to bracket the problem from both a stress and displacement standpoint.

FORMULATION AND SOLUTION OF BOUNDARY VALUE PROBLEMS

Review of Previous Work

The first step in performing such an analysis was to review the literature with a view to determining the information that was available. Sources of literature in applied mechanics and rock mechanics were consulted. A summary of the results and the significant conclusions deduced from the review was prepared, [1].

It was found that the bell and the egg had not been analyzed by any of the mathematical models considered applicable to this project. For the bilinear elastic and the time dependent model, only the sphere had been analyzed for an initial stress condition of K = 1.00. Very little information was available on the variation of stress with distance from the cavity. No analyses were available for K = 0.75 and 1.33.

It was, therefore, concluded that the solutions to additional boundary value problems were necessary to perform an adequate stability analysis for Project Payette.

Formulation and Idealization of Problem

The additional boundary value problems to be analyzed were chosen on the basis of the selected shapes, mathematical models and material constants and the initial stress conditions. Various methods for the solution of these boundary value problems were reviewed. On the basis of this review, it was concluded that the finite element method of analysis was the best tool available for solving the boundary value problems applicable to this study. The finite element method, as a tool for the solution of boundary value problems, has been under intensive development for the past decade. Details of the method and its application to problems in rock mechanics have been discussed in many publications, e.g., Clough [7, 8], Wilson [9, 10], and Reyes [11].

As pointed out by Clough [8], the solution of boundary value problems using the finite element method may be divided into three basic phases:

1. Structural idealization
2. Evaluation of the element properties
3. Structural analysis of element assemblage

Items 2 and 3 deal with the details of the finite element technique and are discussed in the literature on the finite element method. Item 1 deals with the formulation of a particular

158

problem; therefore, it is considered appropriate to discuss it briefly here. The structural idealization involves the following steps:

1. Selection of boundary conditions
2. Selection of initial stress conditions
3. Choice of element and mesh layout

Selection of Boundary and Initial Stress Conditions - The finite element method provides a great deal of flexibility in the choice of boundary and initial stress conditions. In making this choice, an accurate representation of the actual conditions and convenience in analyses were the objectives.

In order to provide the initial stress condition existing prior to the construction, it was decided to introduce a stress field throughout the medium by imposing on each element an initial stress. This stress consisted of a vertical stress which is a function of the depth and unit weight and a horizontal stress which is given as a ratio of the vertical stress. This enables the initial stress to vary from element to element. The weight of the material is also taken into account during the analysis.

In idealizing the problem for the finite element method of analysis, the first step is to make the surrounding med'um of finite extent in all directions. It is necessary to decide on the extent of the surrounding medium as determined by its boundaries. The basic principle in this decision is that the boundaries should be sufficiently distant so that the creation of the cavity has a negligible influence on the conditions at the boundary and vice-versa. Experience with similar problems, Timoshenko and Goodier [12], Savin [13], Terzaghi and Richart [14], Mindlin [15], and Edwards [16], indicates that the effect of cavities on the surrounding material is relatively local; at distances of two to three diameters away, the material is very close to the undisturbed state. Therefore, it is assumed that at a sufficiently large finite distance from the cavity, there is no change from the conditions existing prior to the construction of the cavity. This assumption can result in three classes of boundary conditions:

1. Stress boundary conditions - The normal stresses on the boundaries are prescribed and are assumed equal to the stresses prior to the existence of the cavity.

2. Displacement boundary conditions - The vertical boundaries do not undergo any horizontal displacements, and the horizontal boundaries do not undergo any vertical displacements.

3. Mixed boundary conditions - Stresses are prescribed on some of the boundaries and the displacements on the others.

If the boundaries are sufficiently distant, these boundary conditions should give results which are not significantly different in the vicinity of the cavity. The boundaries chosen were at a distance of 1200 feet from the center of the cavity (see figure 2). This implies an average distance from the face of the cavity of approximately 8 radii. The effects of various boundary

159

conditions on stresses and displacements in the vicinity of the spherical cavity were investigated. It was found that the difference in the values of stresses and displacements obtained by using various boundary conditions did not exceed 2 to 3 percent.

For a distance of 1200 feet from the center of the proposed cavities, the surrounding material consists entirely of rock salt. The analysis was, therefore, conducted for a homogeneous, isotropic medium. Because of the convenience in data preparation, the displacement boundary conditions were used. In order to take into account the initial stress field, an initial stress has been imposed in each element.

Element Shape and Size and Mesh Layout - The choice of the shape of the element, i.e., if it was to be quadrilateral, triangular, or rectangular in shape, was not of concern in this project. The quadrilateral shape was predetermined by its use in the available computer program. It has been found from experience that it is desirable to keep the quadrilateral as close to a square as possible. Furthermore, it is not possible to determine an optimum shape a priori, as it depends on the stress di tribution. It is recommended (Rashid [17] that in the areas of maximum stress variation, the square or rectangular shape with a side ratio not exceeding 3 to 1 is desirable. In those areas where the stress variation is small, the element shapes may vary widely without causing any adverse effects.

The size of the element depends on the required accuracy of computations and the limitations of the computer. The basic principle is to have the smaller size in the areas of maximum stress variation. The only way in which to tell if the size of the mesh is adequate is to compare the results with closed-form theoretical solutions where possible.

Because of the time limitations on the project, it was considered desirable to try to lay out a mesh which could be used for all the shapes with a minimum of change. It was decided to keep the number of nodal points and elements the same for all shapes. Furthermore, from a distance of 500 feet away from the centroid to the exterior boundaries, the mesh layout for all the shapes was kept constant. All variations were kept in the first 500 feet. A typical mesh layout with the element and nodal point number is shown in figures 3 and 4.

To investigate the adequacy of the mesh size chosen, the finite element analysis for a spherical cavity, using a homogeneous stress field, and the closed-form analytical solution were compared. The results obtained from the finite element analysis do not differ from the exact solution by more than 2 to 3 percent.

Boundary Value Problems Analyzed

Having chosen the boundary conditions and the mesh layout, the factors left in defining the complete problem are:

1. Constitutive law for the salt, within this there is the further variation of material constants

2. Shape of cavity

3. Initial stress conditions

160

All these factors have been discussed in the earlier sections and have been defined for the present study.

Table I indicates the problems solved for this project. These analyses represent a level of effort which has not been previously applied to the problem.

The basic computer program used for the analysis was developed by Wilson [10]. Various modifications were made in the basic computer program for the specific problems of this project; these included the ability to take into account the initial stress condition in each element and the technique for analyzing the creep problem. A brief discussion of the principles involved in analyzing boundary value problems for the three mathematical models used to represent the salt is included in the appendix.

PRESENTATION OF RESULTS

The results from these analyses consisted of displacement and stress fields in the surrounding material which could be used in conjunction with failure criteria to evaluate the stability of the cavity. The stress and displacement fields obtained were summarized in graphical and tabular form. It is not possible in this paper to present the large volume of data obtained from the problems analyzed. For a detailed presentation of the data, reference should be made to Nair [1]. Some typical plots illustrating the types of information obtainable from the data are included in this paper.

1. Time-Independent Analysis - The main concern under the linear elastic assumption was the magnitude of the stresses that were likely to develop. Hence, the majority of the data presented deals with this aspect of the problem. Furthermore, since in the great majority of the cases the maximum stresses are at the cavity surface, it is the variation of stress at the surface which is of primary interest. This was examined by plotting variation of stresses with azimuth. Figures 5 and 6 show typical plots of stress conditions at various points in the surrounding salt mass and the variation of stress close to the cavity face with azimuth.

Under the bilinear assumption, the major interest was in the redistribution of stresses due to yielding and the zone of yielding. The yielded zone consists of elements where the stress state was such that the yield stress had been exceeded. Figure 7 is a summary plot of the yielded zones. The examination of results was largely confined to these items.

It should be pointed out that the stresses and displacements were obtained for the entire salt mass, and hence, the stress state throughout the salt mass was available for interpretation.

2. Time-Dependent Analysis - Under the assumption of linear elasticity with superimposed creep, the variations of deflections and stress with time were of major interest. The distribution of stress with time and shape was best illustrated by plotting

161

the stress with azimuth at various times. Deflection and rate of deflection at critical points of the various shapes were also examined. Some typical plots of the results are shown in figures 8 and 9.

DISCUSSION OF RESULTS

In summarizing the information obtained from the analyses, it is convenient to subdivide the discussion of results by considering individually the influence of the four major variables in the analysis on the results obtained. These four variables are:

1. Initial stress condition
2. Shape of cavity
3. Mathematical models and material properties
4. Analytical techniques

Initial Stress Conditions

The initial stress ratios (K) chosen for the analysis were 0.75, 1.00, and 1.33. Previous studies had indicated that for shapes similar to those chosen for this study, a value of K - 0.75 would not result in severe stress conditions. This was confirmed in all the analyses. The elastic stress, the yielded zones, and the creep deformation for K = 0.75 were favorable in comparison to the values for K = 1.00 and K = 1.33. A summary of the effect of the initial stress condition on the stress states at various selected locations near the face of the cavity for the linear elastic analysis is shown in figure 10. For the linear elastic analysis, the maximum values of the various stresses indicated that the horizontal stress, the tangential stress, and the octahedral stress were most influenced by the initial stress condition. There was an increase of 100 percent between values for K = 0.75 and for K = 1.33. For the bilinear analysis, the effect of the initial stress condition can be seen by examining the extent of the yielded zones summarized in figure 7. For all the shapes considered, an increase in K results in an increase in the extent of the yielded zone. The effect of the initial stress condition was very significant in the creep analyses, the maximum deflection for K = 1.33 (between 6 and 7 feet) being approximately three times that obtained for K = 0.75 or K = 1.00. The nonlinear nature of the creep relationship magnifies the effect of the high stress concentration which results from an initial stress condition of K = 1.33. It was significant that for K = 1.00 the creep deformation was not too different from that for K = 0.75. To investigate further the sensitivity of the creep deformation to the magnitude of K, an analysis of the spherical cavity with K = 1.16 was conducted. The results are presented in figures 11 to 13 and point out the rapid increase in deflection when the value of K exceeds unity.

This study indicated that the initial stress condition has a great influence on the stress and displacement pattern developed in the salt surrounding the cavity. Consequently, a correct estimate of the initial state of stress is of great importance in the evaluation of the stability of a large underground cavity. For the shapes analyzed in this study, values of K > 1.00 have an adverse effect on cavity stability.

162

Shape of Cavity

The four shapes chosen for this study were selected on considerations of ease in mining and stability. It is important to note that both the egg and the prolate spheroid are shapes which, when compared to a sphere, are elongated along the vertical axes. Previous investigations have shown that such shapes are preferable under initial stress conditions of $K < 1.00$. The bell has a narrow top, similar to the prolate spheroid, but has a flat bottom. None of the chosen shapes had any abrupt changes in curvature.

The distribution of stresses for the linear elastic case does indicate an effect of shape, especially in the case of the bell. The yielded zones are influenced by the shape, though not to such a significant extent. A study of the stress distribution curves along the face of the cavity and the extent of the yielded zones revealed those locations of the various shapes where excessive stresses occur. It would be possible by making suitable adjustments in these shapes at critical locations to obtain shapes with a more favorable distribution. These adjustments could be made directly in the numerical analysis. Such a concept would be useful in future investigations on stability analysis.

In the time-dependent study, the influence of shape is not as great for the downward displacement along the vertical axis and the horizontal displacement along the equator as for the upward deflection of the bottom along the vertical axis. In the latter case, a 33 percent increase between the extreme values is likely, approximately 0.5 feet in 1.5 feet for $K = 1.00$ and 2 feet in 6.0 feet for $K = 1.33$. The egg and prolate spheroid appear to have very similar deflection patterns and are more resistant to vertical deflection than either the bell or sphere. The bell and the sphere have better resistance to horizontal movement at the equator. Large-scale plots do not show any significant differences in the deformed shapes.

While the effects of shape are evident and they follow the general trend established from previous investigations, it does appear that for the range of K values considered and the shapes investigated, the effect of shape will not be the most critical factor in stability. This conclusion, while somewhat unexpected, appears reasonable if one considers the limited range of initial stress values and the absence of any radical changes in shape in the form of abrupt changes of curvature.

Mathematical Models and Material Properties

The three models chosen for the study under the general assumptions of homogeneity and isotropy were:

1. Linear elasticity
2. Bilinear elasticity
3. Linear elasticity with creep

The object of choosing these models was to obtain results which would cover the range of stress and displacement values likely to occur in the field. It is felt that this objective was

achieved. The linear elastic analysis gave the highest stress concentration. The bilinear elastic analysis resulted in the highest instantaneous displacement and also indicated the stress redistribution that might occur due to any yielding. The linear elastic analysis with creep superimposed permitted the computation of the stress relaxation with time and the increase in deflection with time.

Except for the creep data where the limited number of tests did not permit a range of values to be chosen, it was necessary to examine the effect of a variation in material constants on the results from the analysis.

In the linear elastic analysis, two constants (E and ν) can be varied. The magnitude of the stresses is not affected by E, and the deflection is inversely proportional to E, all other variables being held constant. The computations performed were for the lower value in the range of E values chosen. For the range of values of E used in this study, deflections associated with the linear elastic case were not of much interest.

A variation in the value of Poisson's ratio influences the magnitude of stress and deflection. The deflections are not of significance, and therefore, it is the stress variation that is of interest. It was found that a change in Poisson's ratio from the lower limit of 0.2 to the upper limit of 0.45 causes a maximum stress change of the order of 16 percent for K = 1.33; for other values of K, the change was less. It was felt that, within the accuracy of the knowledge of the material properties, this was not too significant.

For the bilinear elastic case, there are three important factors: the yield criteria, initial modulus, and the ratio of the initial to final modulus. The Von Mises (octahedral shear stress) criteria was used to determine when "yielding" would begin. The experimental justification for this choice appears fairly conclusive. The ratio of the initial to final moduli was varied from 2 to 4; this resulted in a minor change in the extent of the yielded zone and in the stress in the yielded zone near the face of the cavity. It was felt that the yielding would be slight because of the high degree of work hardening at the stress levels involved. This was indeed the case, and for future work at the stress levels utilized in this project, the bilinear elastic assumption would not be of much value.

Because of the limitations in the available experimental data, it was only possible to vary the initial elastic modulus in the time-dependent analysis (linear elasticity with superimposed creep). The majority of the computations were done for an initial modulus (E_o) of 4×10^6 psi. A decrease in the initial modulus by a factor of four caused an increase in the deflection by a maximum of 30 percent for the case investigated. However, it should be pointed out that the experimental data supports the choice of E_o as 4×10^6 psi. This was also the value used by Boresi and Deere [18]. Furthermore, the decrease by a factor of four is considered extreme; nevertheless, the possibility of unfavorable results compared to those presented here should be kept in mind.

164

It should be pointed out that if the assumptions of homogeneity and isotropy are not found to be true, the analytical results presented will have to be re-examined and modified where necessary.

Analytical Methods

The analytical method used for the solution of the additional boundary value problems needed for this project was the finite element method. A computer program utilizing the finite element method of analysis was used to conduct this study. The program was checked and found to be satisfactory. By its very nature, this is an approximate method. The accuracy of the solution obtained by the finite element method was investigated and found to be adequate.

Due to severe time limitations, it was not possible to study the effect of a variation in mesh size and shape. A mesh layout was chosen which would require the least modification for the various cavity shapes. The choice of size and shape of the elements and the mesh layout was based on past experience. Nevertheless, on the basis of the results, it can be concluded that the meshes utilized were satisfactory.

The linear elastic analysis is straight forward and the computation technique well established. For the bilinear case, an iterative procedure is utilized. For the cases studied, convergence to within one percent error was obtained in three or four iterations. Because of the particular nature of the problem, there is an absence of unloading, and the loading paths are likely to be close enough to radial to consider bilinear elastic analysis using a Von Mises yield criteria as a close approximation to an elasto-plastic analysis.

For the creep analysis, a total deformation method of computation was used. This was different from the incremental deformation technique used by Boresi and Deere [18]. An iterative method had to be used to get convergence within a prescribed tolerance (5 percent). In all cases, the convergence was obtained, though some of the cases did take an excessive amount of computer time.

It is realized that the analytical methods represent various approximations, and various improvements are possible in these techniques. Incremental theory, the gradual construction of the cavity, and the nonlinear analysis can all be accommodated within the finite element technique. It is felt that the finite element method proved entirely satisfactory in analyzing the problems associated with the present project, and the method also has the potential to take into account variables not considered in the analysis at the present time.

Before proceeding to an evaluation of stability, it was necessary to bring the analtyical results within the framework of the experience of the profession on similar systems.

PERFORMANCE OF SIMILAR SYSTEMS

A literature survey was made on the information available from the field and the laboratory on the behavior of salt. Because of time limitations, the review was confined to the most recently published data and with a view of obtaining data in two broad areas:

165

1. Time-dependent deformation
2. Modes of failure

A comparison of the data obtained from field measurements with the results of the theoretical studies in this project indicated that the theoretical values were of the right order of magnitude. Published information obtained from laboratory tests on the closure of spherical cavities in a uniform stress field gave results which were close to those obtained from theoretical studies. It was concluded that the theoretical results could be considered reasonable for the present feasibility study.

Very little information could be obtained on modes of failure in cavities in salt domes. Some spalling resulting from continuing creep has been reported. At large depths (> 1000 feet), shear fracture is extremely unlikely because, as observed from triaxial tests, salt under high confining pressure deforms without fracturing with increase in stress.

PERFORMANCE CRITERIA

The development of suitable performance criteria is essential to the evaluation of stability. The performance criteria for this study did not include cost and time of construction. The possibility that different shapes may require different construction times and cost was not considered. The performance criteria for this study were grouped into two categories:

1. Factors which impair the function of the cavity without loss of stability
2. Factors which could cause instability

In the first category, one may consider the possibility of excessive deformation and distortion without any breakage. The resulting change in shape may be large enough to make the cavity unsuitable for any experiment. Theoretical results and experimental evidence indicate that this is not a problem for this project.

Among the factors which could cause instability are:

1. Material failure
2. Geological factors such as weak seams, faults, fractures, etc.

It has been assumed that the salt dome is homogeneous, isotropic, and free from faults, fractures, and other discontinuities. The possibility that this assumption may be proved incorrect during construction of the cavity does exist, however, because of lack of quantitative information, variations from the above assumption cannot be taken into account at the present time. Therefore, material failure is the sole criterion for determining whether the proposed cavity will remain stable.

Two failure hypotheses were considered for material failure:

1. Shear fracture (using a Mohr Columb criteria)

2. Life consumption hypothesis using a relationship between the principal stress difference and time to rupture, Taira [19].

166

On examining the likely stress conditions and considering the yielding character of the salt under moderately high confining pressures, it was concluded that shear fracture was unlikely and that creep rupture was the likely mode of failure.

Under the life consumption hypothesis, fracture is assumed to occur when the damage ϕ_c accumulated in the material through creep reaches a critical value ϕ_o.

Assume that a material subjected to a stress σ at a constant temperature has a time-to-rupture t_c when the amount of accumulated damage ϕ_c reaches a critical value of ϕ_o. The amount of damage in a short interval of time dt may be expressed as

$$\Delta\phi_c = \phi_o \frac{dt}{t_c}$$

If it is assumed that load history has a negligible influence on creep rupture under varying stress, the amount of damage absorbed until time t can be written as

$$\phi_c = \phi_o \int_0^t \frac{dt}{t_c}$$

Fracture (rupture) is assumed to occur when

$$\frac{\phi_c}{\phi_o} = 1.00 \text{ that is, when } \int_0^t \frac{dt}{t_c} = 1.00$$

Based on experimental data from creep rupture tests, a relation between σ and t_c can be obtained, $t_c = f(\sigma)$. In a problem of stress relaxation, $\sigma = \sigma(t)$.

The previous equation can be written as

$$\int_0^t \frac{dt}{f[\sigma(t)]} = 1.00$$

If it is not possible to express $f[\sigma(t)]$ in a functional form, a numerical integration procedure can be used. The data available to develop a failure criteria, i.e., the determination of $f[\sigma(t)]$, consisted of five triaxial extension creep tests of which only two were run to failure. A straight line relationship obtained from the experimental data between the stress difference and the time-to-rupture on a logarithmic plot was used to determine $f[\sigma(t)]$. The creep rupture criteria developed on such a limited basis cannot be expected to command a high degree of confidence. It is recognized that much of this is speculative in its application in the field of rock mechanics. However, the approach appeared reasonable and offers a practical method for solving the problem.

PRELIMINARY CONCLUSIONS ON STABILITY

There were two main considerations in evaluating stability

1. Excessive deformation resulting in a significant change of shape or decrease in volume which would prevent the use of the cavity for its intended purpose

2. Instability resulting from material behavior leading to spalling and eventual collapse

The magnitude of the deflection and an examination of the deflected shapes lead to the conclusion that instability due to (1) is not likely.

Based on the theoretical results, failure criteria, and keeping in mind the assumptions and limitations of the analyses, the following preliminary* conclusions on the stability of the cavities investigated appear justified:

1. For K = 0.75 and K = 1.00, all the shapes analyzed would be stable, with the sphere as the preferred shape. It is recognized that for K = 1.00, the egg, prolate spheroid, and bell have potential local zones of failure. However, because of the beneficial effects of gradual construction and the location of the potential zones of failure below the equator, it is felt that all shapes are likely to be stable for K = 1.00.

2. For K = 1.33, there is considerable doubt regarding the stability of an unsupported cavity. For all the shapes analyzed, it appears that material failure progressing outward from the cavity, which could result in continued spalling, is likely to occur. Though failure appears likely for all shapes analyzed, the stress levels for the sphere are favorable in comparison to the other shapes.

3. Based on stability considerations, the spherical cavity appeared to be the best choice among the shapes analyzed in this study. However, this is a matter of degree; the egg, prolate spheroid, and bell would also be satisfactory for $K \leq 1.00$; and none of the shapes would be stable for K = 1.33.

4. Should any of the assumptions in the analysis, e.g., absence of faults, fracture, initial stress be found to be incorrect, the validity of the above conclusions should be re-examined.

Because of the uncertainties involved in dealing with the stability problem, and for the purpose of gathering information for future cavities, it has been recommended that the cavity and surrounding salt be instrumented to obtain pertinent data during and after construction. A comprehensive study of the instrumentation needs for a similar project is reported in United ElectroDynamics [20] and would serve as an excellent point of departure for a detailed instrumentation study for the subject cavity.

RECOMMENDATIONS FOR FUTURE RESEARCH

The selection of necessary topics for future research is based on an examination of all of the steps in the investigation which were detailed in the discussion of the generalized approach.

---

*These are preliminary in the context of figure 1. Final conclusions can be made only after obtaining data during construction.

168

As pointed out earlier, one of the advantages of the generalized (systems) approach followed in this project is that it enables one to identify areas where research is needed. The various steps that lead up to a decision on the stability of the cavity can be likened to links in a chain, the chain being only as strong as the "weakest link." To improve the design, it is necessary that the "weak links" in the chain leading to the stability decision be identified.

All phases of the investigation were studied with the object of identifying those phases in which the level of confidence needed improvement. It was felt that additional research in the following three areas would be of maximum benefit to the project described in this paper:

1. Development of material failure criteria

2. Development of techniques for incorporating the construction sequence into the analysis

3. Development of methods for determining the initial stress conditions

Each of these areas are discussed briefly below:

1. Development of Material Failure Criteria - The development of suitable performance criteria is essential to the evaluation of the stability of the cavity. For the present project, material failure is the criterion which has been used to perform this evaluation. The experimental and field information available to determine a material failure criterion was extremely limited.

   Two avenues of research could be pursued:

   (a) Laboratory testing - This requires the setting up of properly designed testing programs and an analysis of the data obtained with the object of developing an applicable failure theory.

   (b) Field information - In order to obtain field information, it would be necessary to study existing information on performance and to consult with people engaged in the operation and maintenance of similar cavities.

   The lack of a satisfactory material failure hypothesis is the "weakest link" in the stability studies undertaken for the project described in this report.

2. Development of Techniques for Incorporating the Construction Sequence into the Analysis - The gradual creation of the cavity has a considerable influence on the resulting displacements and stress, [18]. In this study, it was assumed that the cavity is created instantaneously. This is a conservative assumption, and results based on this assumption overestimate the stress and displacements in the medium surrounding the cavity. Not much attention has been paid to the loading patterns imposed by different construction schemes. Furthermore, for various initial stress conditions and shapes, it may be beneficial to follow a certain mining pattern to prevent excessive stress concentrations. The availability of theoretical results for the stresses and displacements of the surrounding salt during construction would enable the interpretation and evaluation of data obtained from instrumentation during the construction

169

peiiod. Therefore, it is extremely desirable that the effect of construction be incorporated into the analysis.

The program modifications necessary to take into account construction effects could be combined with modifications necessary for optimizing the shape of the cavity. Optimization of shape would include the removal of those areas of salt where the material had failed and is likely to spall so that the cavity could take a shape best suited to the stress and displacement field.

3. Development of Methods for Determining the Initial Stress Condition - Previous studies and the results of the analysis as described in this paper have pointed out the extreme importance of knowing the correct state of stress that exists in a medium prior to the creation of a cavity. As shown in this study, presently available analytical methods have the capability of taking into account a variety of initial stress conditions. However, methods of determining the initial stress condition, especially at large depths, are not well developed.

Research in this area is urgently needed; such research would be of great value to the design and construction of underground structures. As a first phase, it is recommended that a complete survey of the existing methods of determining the initial stress be made by studying the literature and by consulting with those who have actually used various methods in the field. A study of this type would also be of considerable help in the development of instrumentation for the project described in this paper and would be the logical first step in the development of new methods for determining the state of stress in any type of rock.

COMMENTS ON THE APPLICATION OF THE METHODS OF ANALYSIS USED IN THIS STUDY TO OTHER CONDITIONS

There are two basic considerations in applying the methods of analysis used in this investigation to other conditions:

1. The capabilities of the analytical techniques, in this case the finite element method
2. The applicability of the generalized (systems) approach

The capabilities and potential of the finite element method are very great. Nonlinearity, anisotropy, nonhomogeneity in material characteristics can be readily incorporated into the analysis. With the restriction of axisymmetry, this drawback will probably be removed in a few years; faults, fractures, weak seams, and reinforcement patterns can be readily investigated. In addition to elasto-static analysis, dynamic problems can also be investigated. A wide range of initial stress conditions, cavity shapes, and material properties can be readily investigated. Various failure and yield criteria can be readily incorporated into existing computer programs.

170

The general (systems) approach presented in figure 1 has the advantage that it is applicable to all cavity stability problems. The definition of the various quantities might change with a different situation, but the basic steps outlined in figure 1 have to be completed in every case.

The following discussion wil illustrate the procedure that would be followed in the investigation of a cavity stability problem in which some conditions might be at variance with those assumed in the Payette study. The discussion will be in general terms and will emphasize the logical approach to the problem rather than specific details.

Consider a cavity stability problem identical in all aspects to that considered in the investigation reported earlier with the following exceptions:

1. Different range of initial stress conditions

2. Existence of faults and weak seams in the geologic profile

3. A different material, e.g., granite

The problem would be approached by following the sequence of steps outlined in figure 1.

1. <u>Different Range of Initial Stress Conditions</u> - In the definition of the input, the load variance would be modified to take into account the new range of initial stress conditions.

2. <u>Existence of Faults and Weak Seams</u> - The existence of faults and weak seams would require a change to be made in the description of the cavity system. In the layout of the mesh for the finite element idealization, it will be necessary to allow for faults; this can be done through linkages which allow free movement along the fault. Weak seams are accounted for by assigning very low modulus and strength values to the elements located at the seams.

3. <u>A Different Material, e.g., Granite</u> - This would require modifications in three areas of the investigation:

   (a) Material characterization
   (b) Information on the performance of similar systems
   (c) Material failure criteria

<u>Material Characterization</u>

Existing experimental data will have to be examined to choose a suitable mathematical model(s) to represent the behavior of the granite. It might be necessary to perform additional tests to obtain more information. It will be necessary ɔ have a clear understanding of the capabilities and limitations of mathematical models and the experimental methods currently available. Consideration must also be given to the existing analytical capabilities in solving boundary value problems. As pointed out earlier, the finite element method is extremely versatile in this aspect.

Information on Performance of Similar Systems

It is necessary to evaluate the ability of the chosen mathematical models to predict the behavior of surrounding rock and to check the "reasonableness" of the theoretical results. This can be most readily done by comparing the results of the analyses with the observed performance of underground cavities in a similar material. This is essential to establishing confidence in the theoretical results.

Material Failure Criteria

Computations of stress, strain, and displacement in the surrounding granite would be of little use for stability evaluation unless suitable failure criteria could be developed. Existing experimental data and records of failures in the field will have to be studied in order to develop an understanding of failure mechanisms in the granite. Additional tests might have to be performed. It might be necessary to select more than one failure theory to allow for different modes of failure. Existing computer programs using the finite element method can account for a wide range of failure criteria. Once these modifications have been made, the analyses will follow the steps outlined in figure 1.

In summary, the general principles used for the analysis of underground cavities in salt could be readily applied to the analysis of cavities in other media. The major effort would be in characterizing the material, developing suitable constitutive equations to represent its behavior, and in defining adequate failure criteria. The finite element method for solving boundary value problems represents the most powerful tool that is available to tackle the problem of cavity stability. It is felt that the methods of analyses used in Project Payette can be readily applied, with minor modifications, to the stability analysis of underground cavities in other media under different conditions.

172

ACKNOWLEDGEMENTS

REFERENCES

1. K. Nair, Stability Studies for Project Payette, Final Report Submitted to Fenix & Scisson, Inc., Woodward-Clyde-Sherard & Associates and Materials Research & Development, Inc., Oakland, Calif., 1967.

2. D. C. Drucker, "Survey on Second-Order Plasticity," Second-Order Effects in Elasticity Plasticity and Fluid Dynamics, Pergamon Press, New York, 1964.

3. Committee on Characterization of Materials Advisory Board, Characterization of Materials, Publication MAB-229-M, National Academy of Sciences - National Academy of Engineering, Washington, D. C., 1967.

4. S. Serata, Transition from Elastic to Plastic States of Stress of Rocks Under Triaxial Compression, Proceedings, 4th Symposium on Rock Mechanics, College of Mineral Studies, Penn. State Univ., Univ. Park, Penn., 1961.

5. United States Department of Interior, Bureau of Reclamation, Triaxial Compression Tests of Salt Rock Cores for USAEC Project DRIBBLE, Rept. No. C-1043, Washington, D. C., 1962.

6. United States Army Engineer Waterways Experiment Station, Project DRIBBLE, Petrographic Examination and Physical Tests of Cores, Tatum Salt Dome, Mississippi, Vicksburg, Miss., 1963.

7. R. W. Clough, The Finite Element in Plane Stress Analysis, Proceedings, 2nd ASCE Conference on Electronic Computation, Pittsburg, Penn., 1960.

8. R. W. Clough, "The Finite Element Method in Structural Mechanics," Stress Analysis, Zienkiewicz and Hollister, eds., John Wiley and Sons, New York, 1965.

9. E. L. Wilson, Finite Element Analysis of Two-Dimensional Structures, Report 63-2, Structural Engineering Laboratory, Univ. of Calif., Berkeley, Calif., 1963.

10. E. L. Wilson, "Structural Analysis of Axisymmetric Solids," AIAA J., Vol. 3, 1965.

11. S. F. Reyes, Elastic Plastic Analysis of Underground Openings by the Finite Element Method, Thesis, Univ. of Ill., Urbana, Ill., 1966.

12. S. Timoshenko, and J. N. Goodier, Theory of Elasticity, Second Edition, McGraw-Hill Book Co., New York, 1951.

13. G. N. Savin, Stress Concentration Around Holes, Pergamon Press, London, England, 1961.

14. K. Terzaghi, and F. E. Richart, "Stresses in Rock About Cavities," Geotechnique, Vol. III, 1952.

15. R. D. Mindlin, "Stress Distribution Around a Tunnel," Trans. Am. Soc. of Civil Eng., Vol. 105, 1940.

16. R. H. Edwards, "Stress Concentrations Around Spherical Inclusions and Cavities," J. of Appl. Mech., Vol. 18, 1951.

17. Y. R. Rashid, Solution of Elasto-Static Boundary Value Problems by the Finite Element Method, Thesis, Univ. of Calif., Berkeley, Calif., 1964.

174

18. A. P. Boresi, and D. U. Deere, Creep Closure of a Spherical Cavity in An Infinite Medium (With Special Application to Project DRIBBLE, Tatum Salt Dome, Mississippi, Holmes & Narver, Inc., Las Vegas Div., 1963.

19. S. Taira, Thermal Fatigue and Its Relation to Creep Rupture and Mechanical Fatigue, Proceedings, 3rd Symposium on Naval Structural Mechanics, Columbia Univ., Pergamon Press, New York, 1964.

20. United ElectroDynamics, Inc., Final Report, Project DRIBBLE - Phase 1, Cavity Stability Instrumentation and Observation, Contr. No. AT (29-2)-1312, Two Volumes, USAEC Nevada Operations Office, Las Vegas, Nevada, 1963.
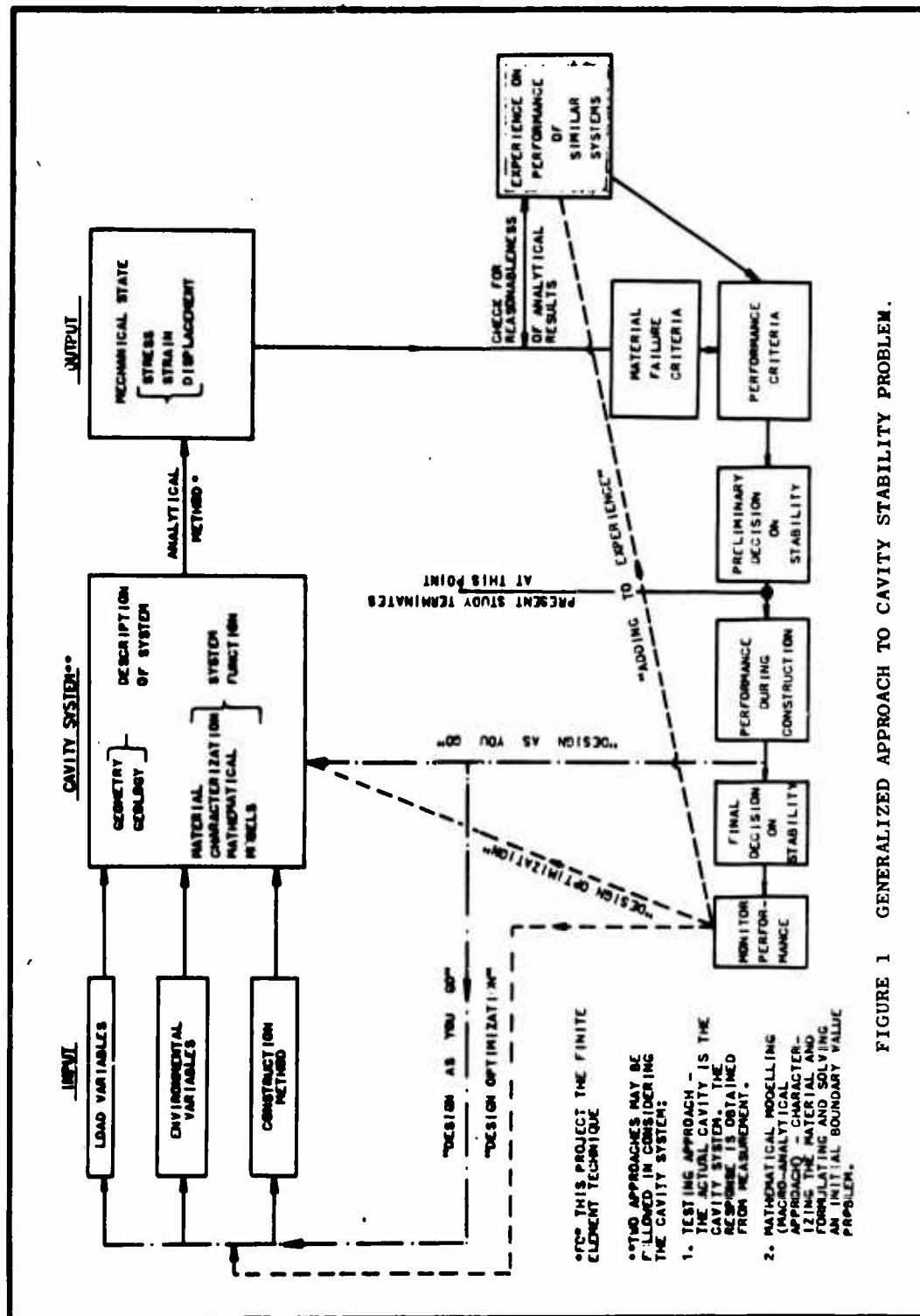
FIGURE 1   GENERALIZED APPROACH TO CAVITY STABILITY PROBLEM.

Figure 2. SHAPES CHOSEN FOR CAVERN STABILITY STUDY.

177
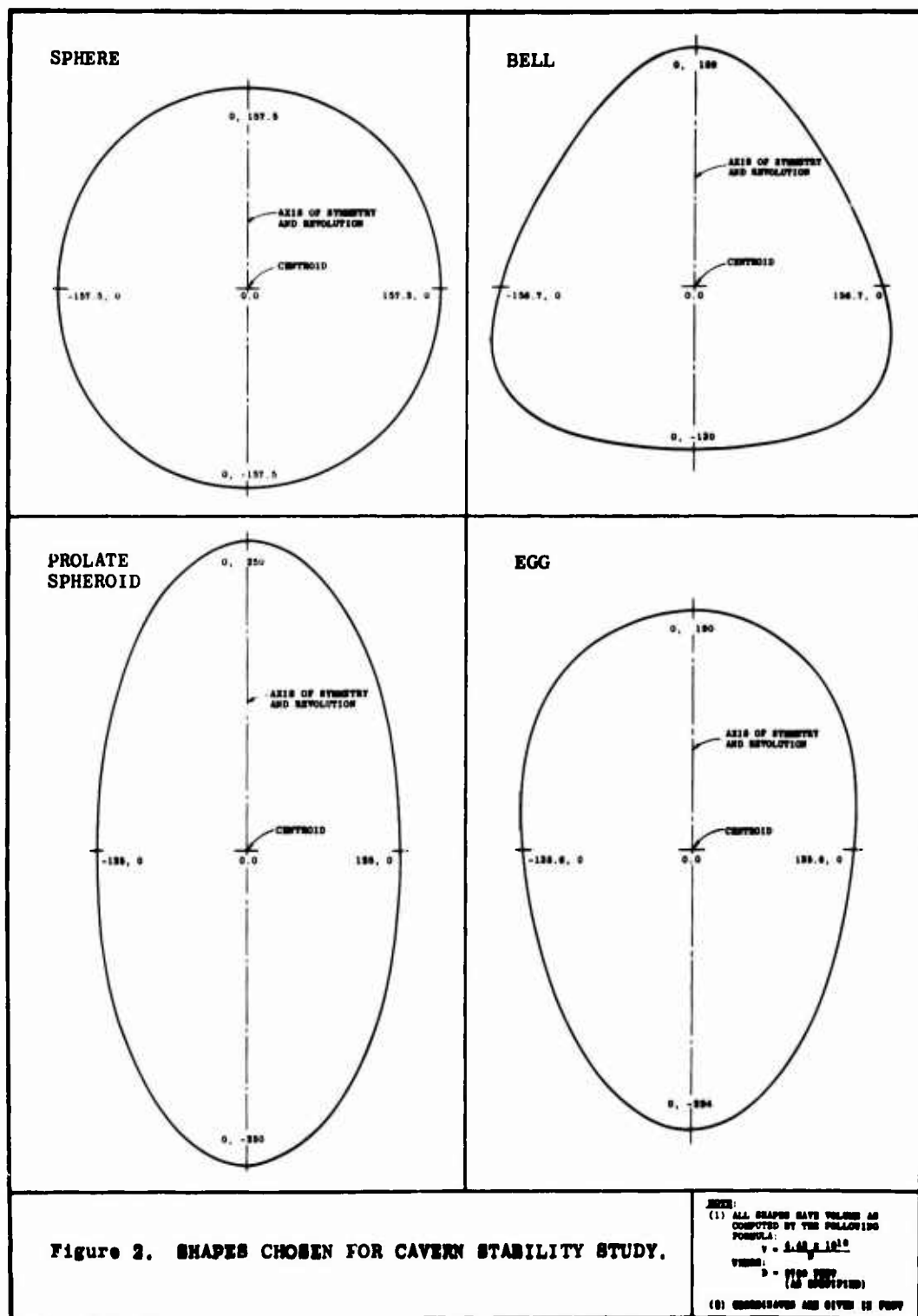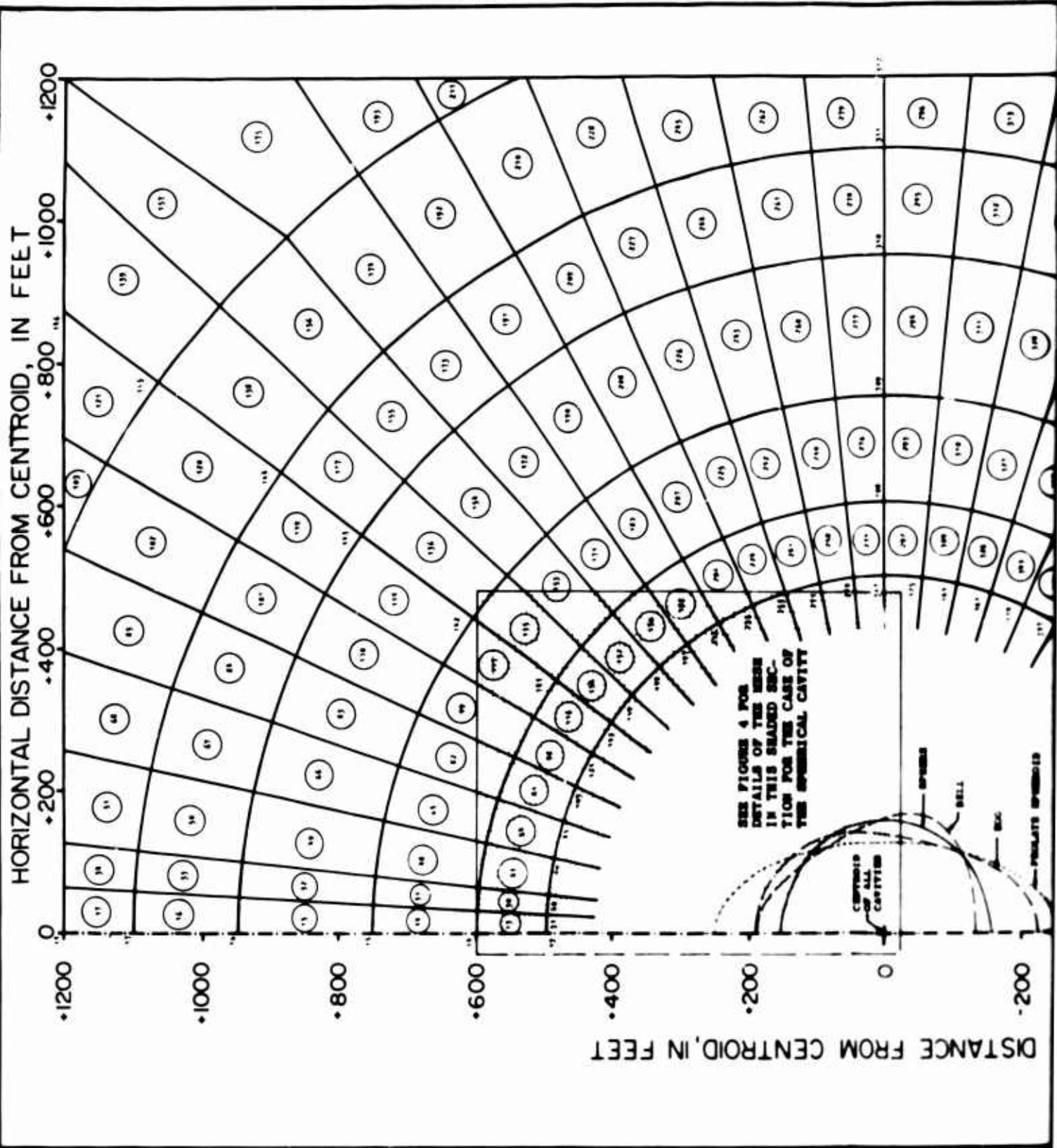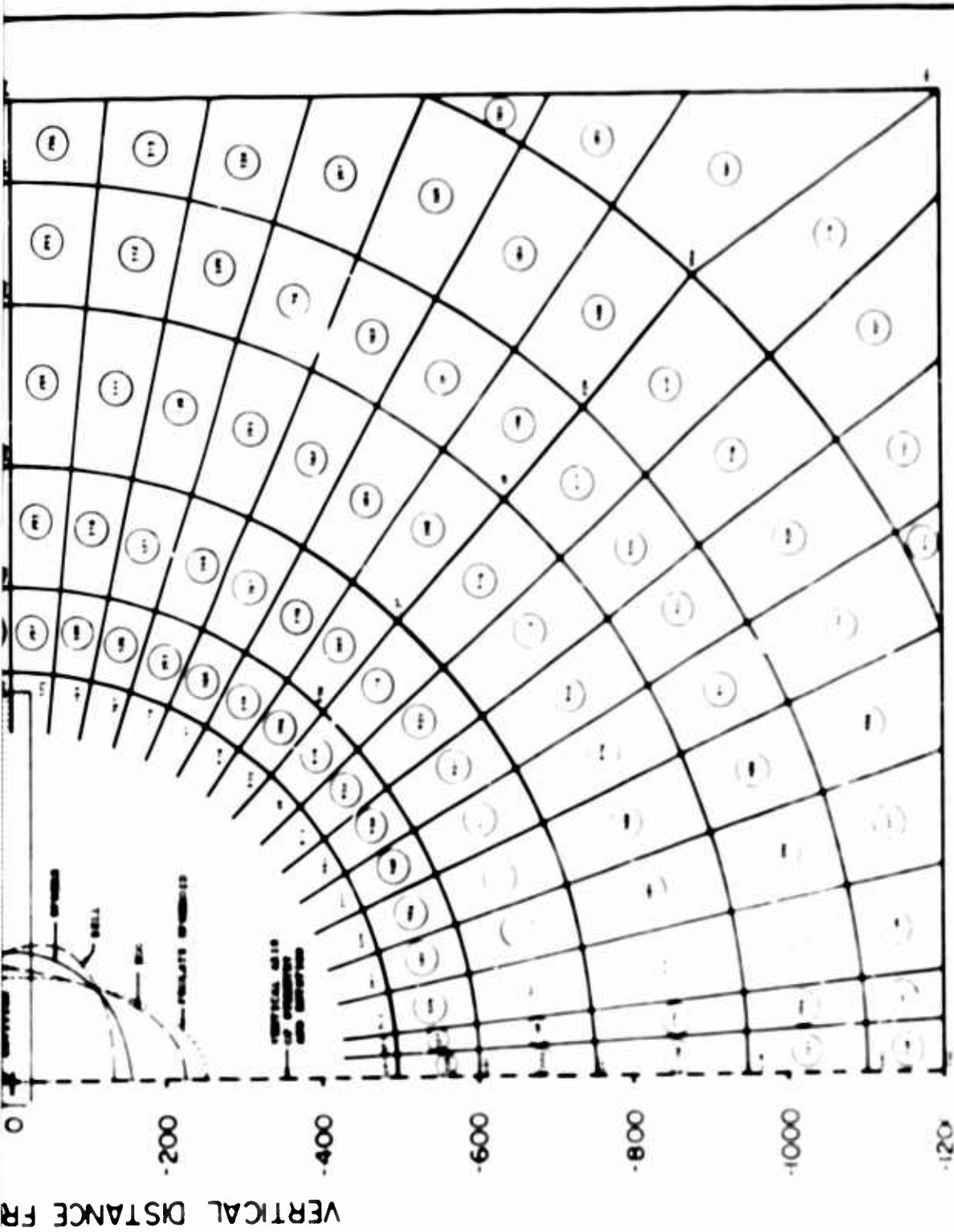
Figure 3. FINITE ELEMENT MESH FOR ALL SHAPES FROM A RADIUS OF 500 FEET TO THE EXTERIOR BOUNDARIES.

VERTICAL DISTANCE FR

HORIZONTAL DISTANCE FROM CENTROID, IN FEET

...ICAL DISTANCE FROM CENTROID, IN FEET
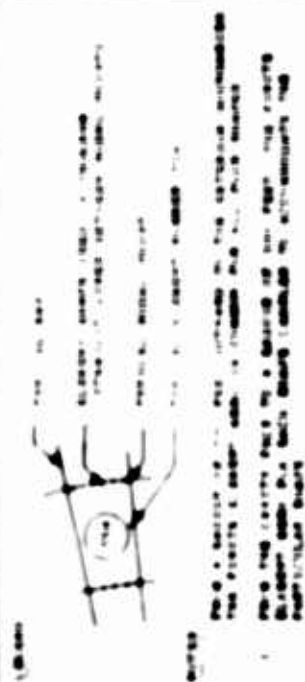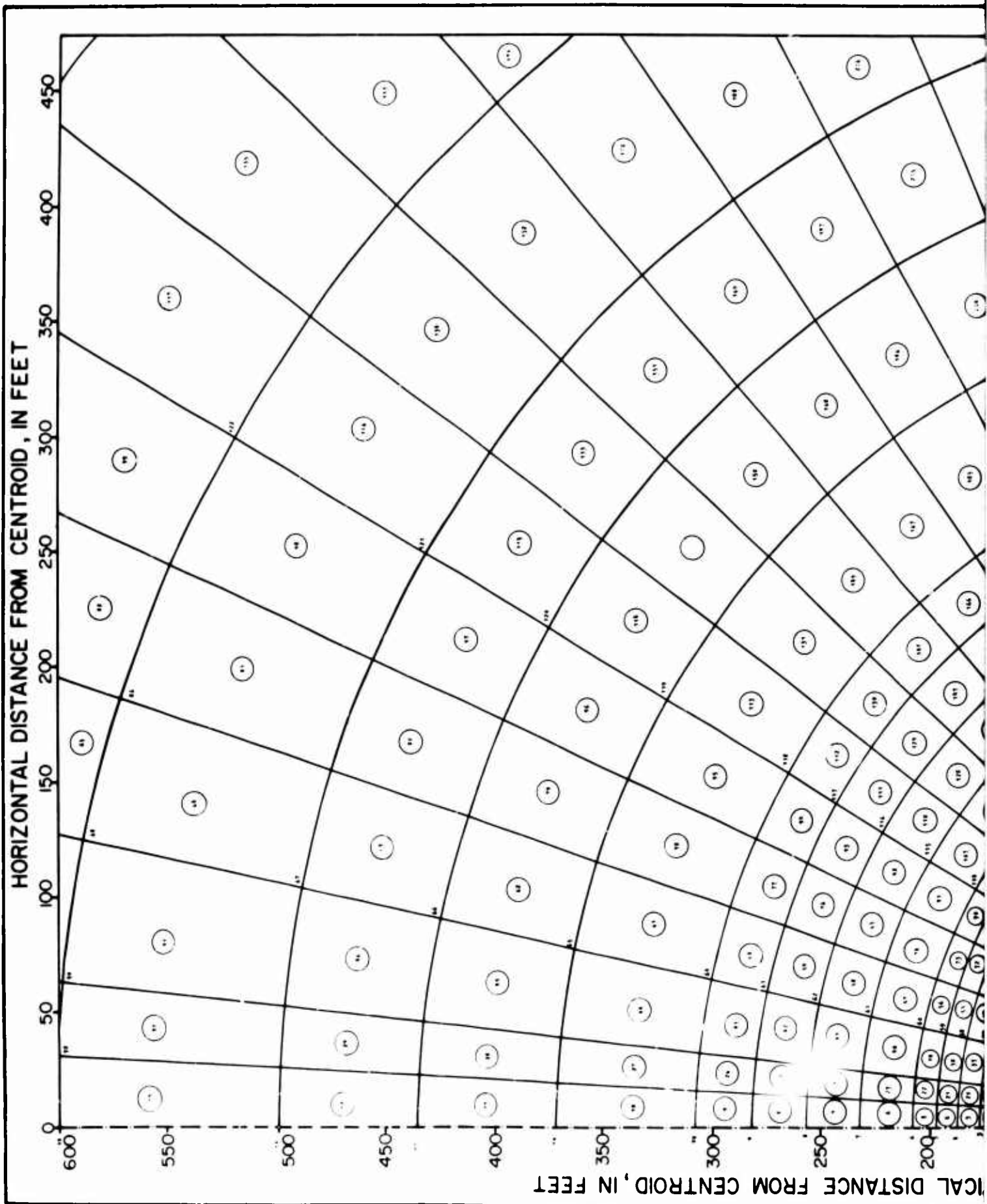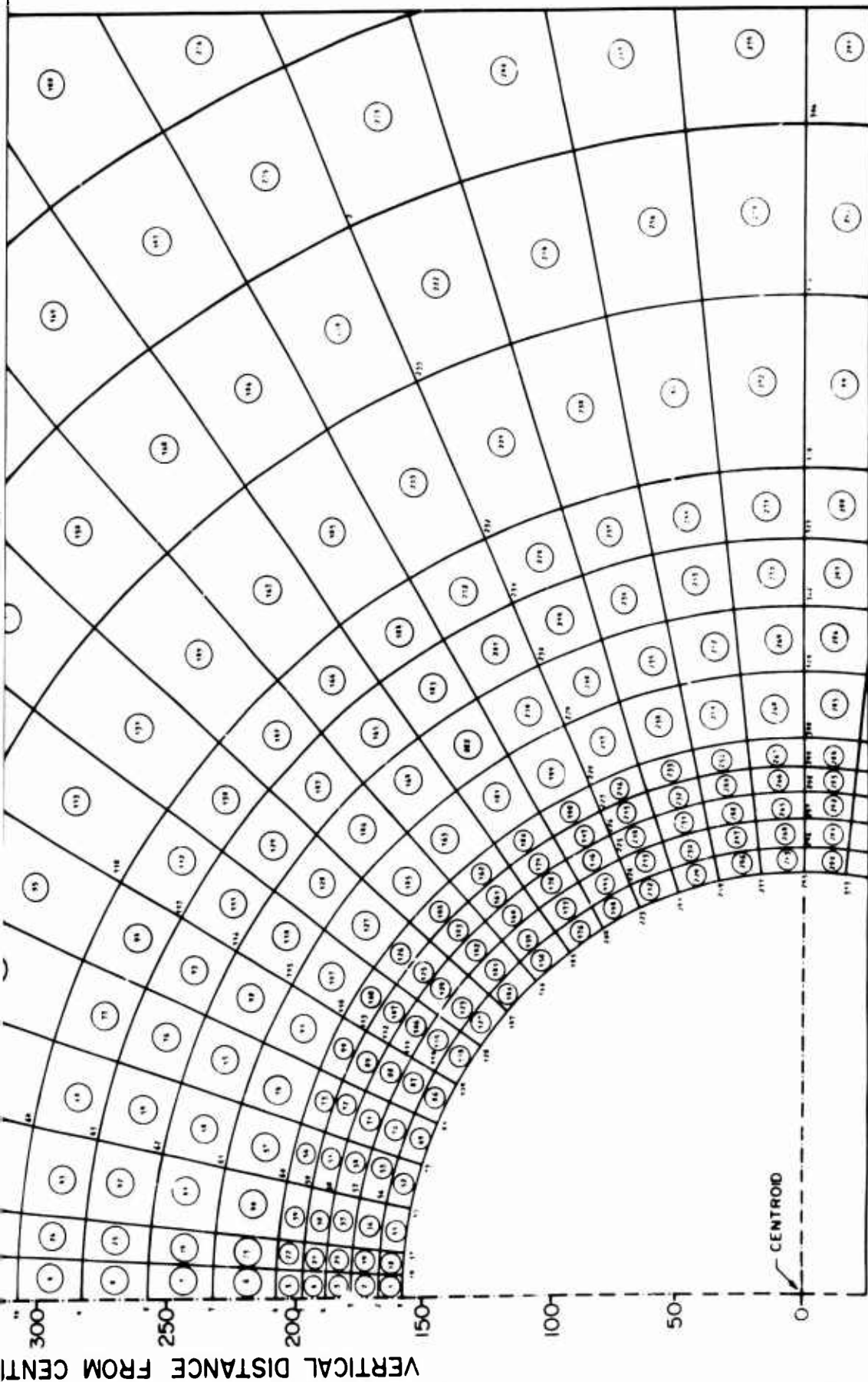
Figure 4. FINITE ELEMENT MESH FOR SPHERE IN THE VICINITY OF
THE CAVITY FACE (ENLARGEMENT OF THE SHADED SECTION
SHOWN ON FIGURE 3

BELL

EGG
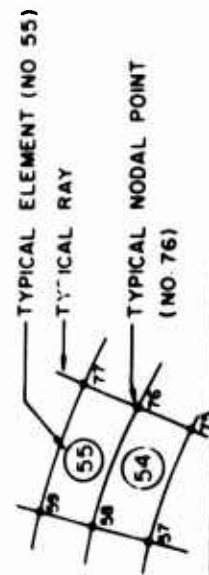
SPHERE

PROLATE
SPHEROID
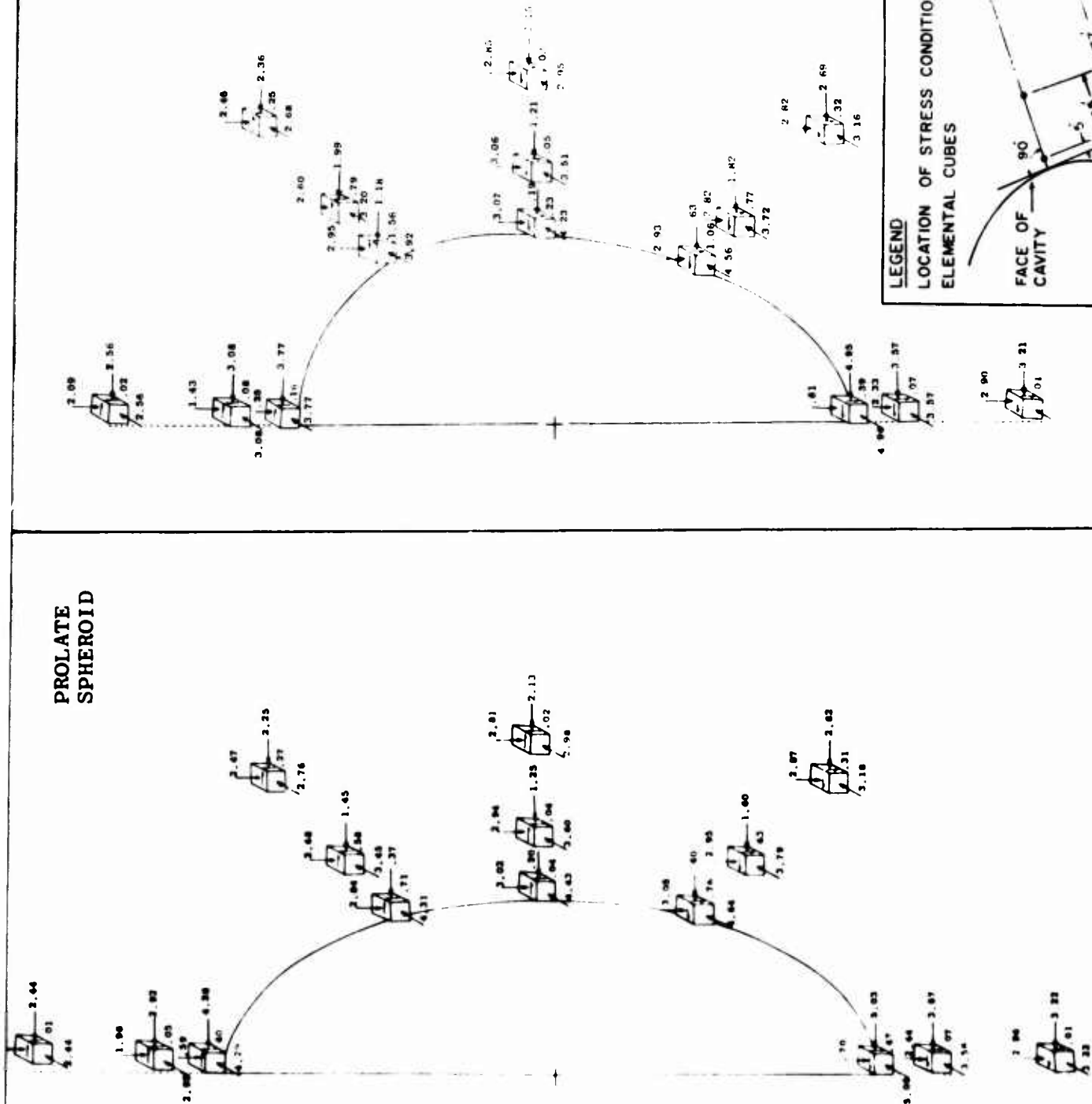
Figure 5. STRESSES ON SELECTED ELEMENTS IN THE SURROUNDING MEDIUM FOR VARIOUS SHAPES AND K=1.00. (LINEAR ELASTIC ASSUMPTIONS, E=1x10⁶ PSI, ν=0.20).

183
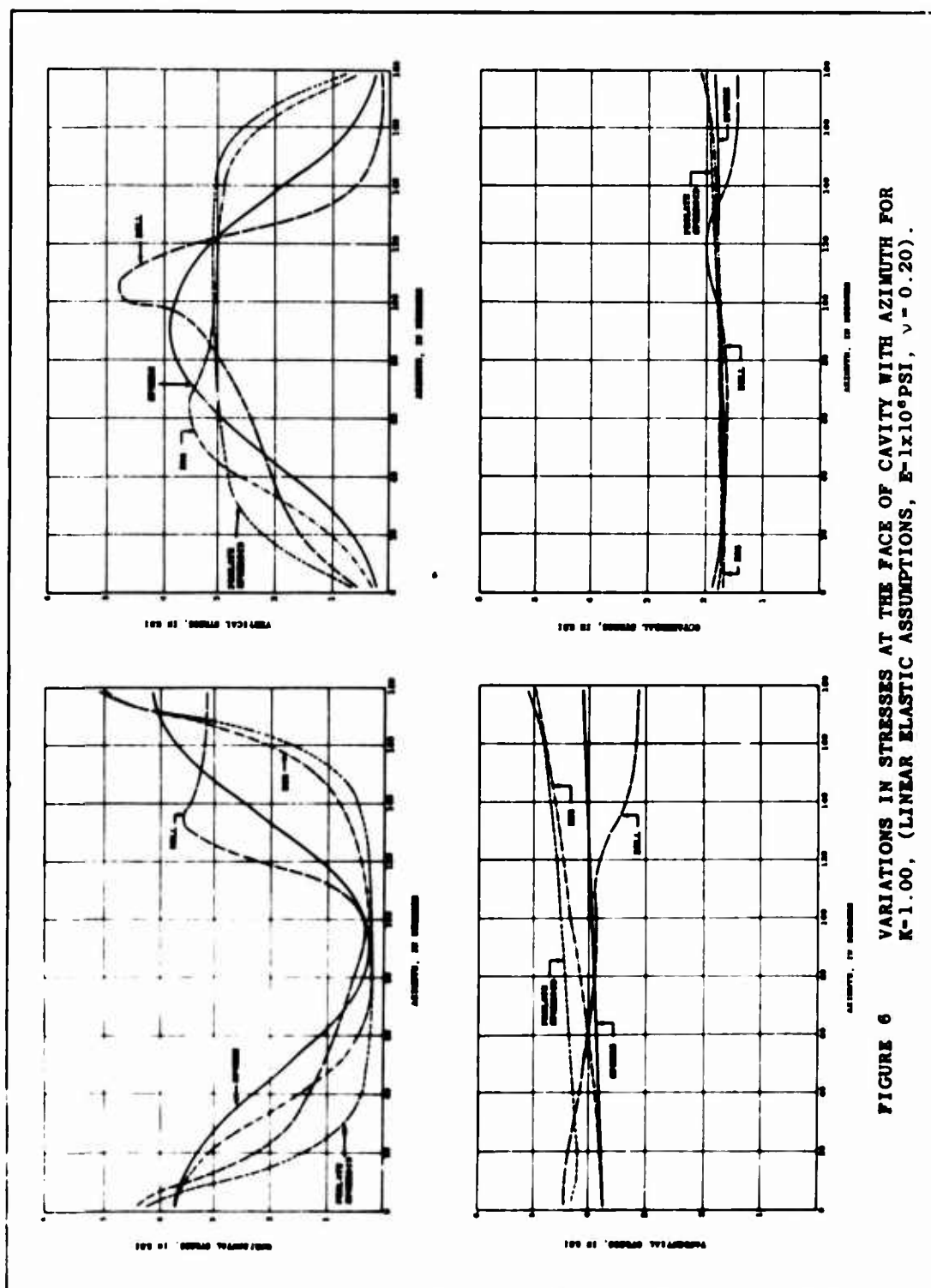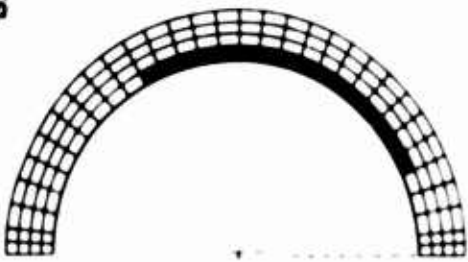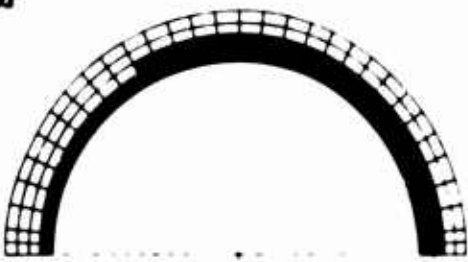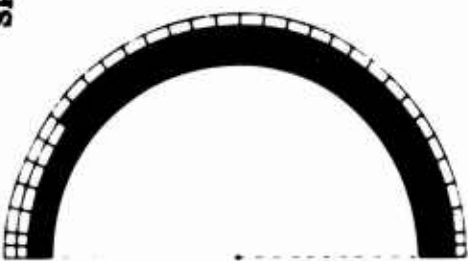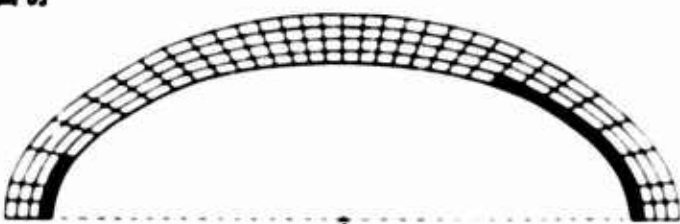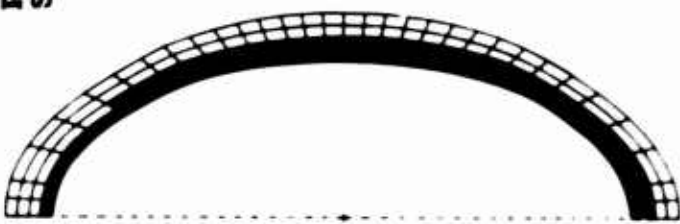
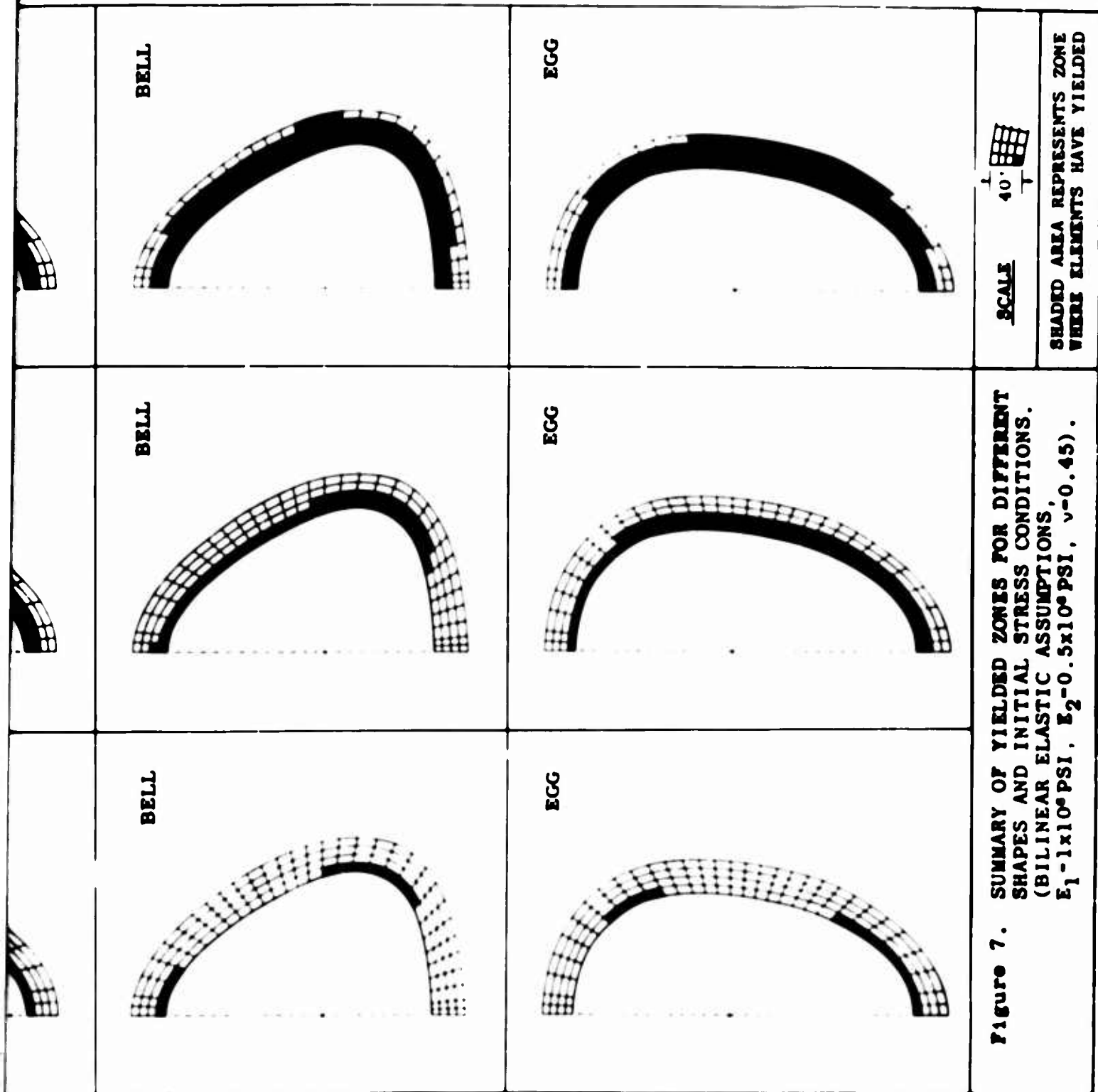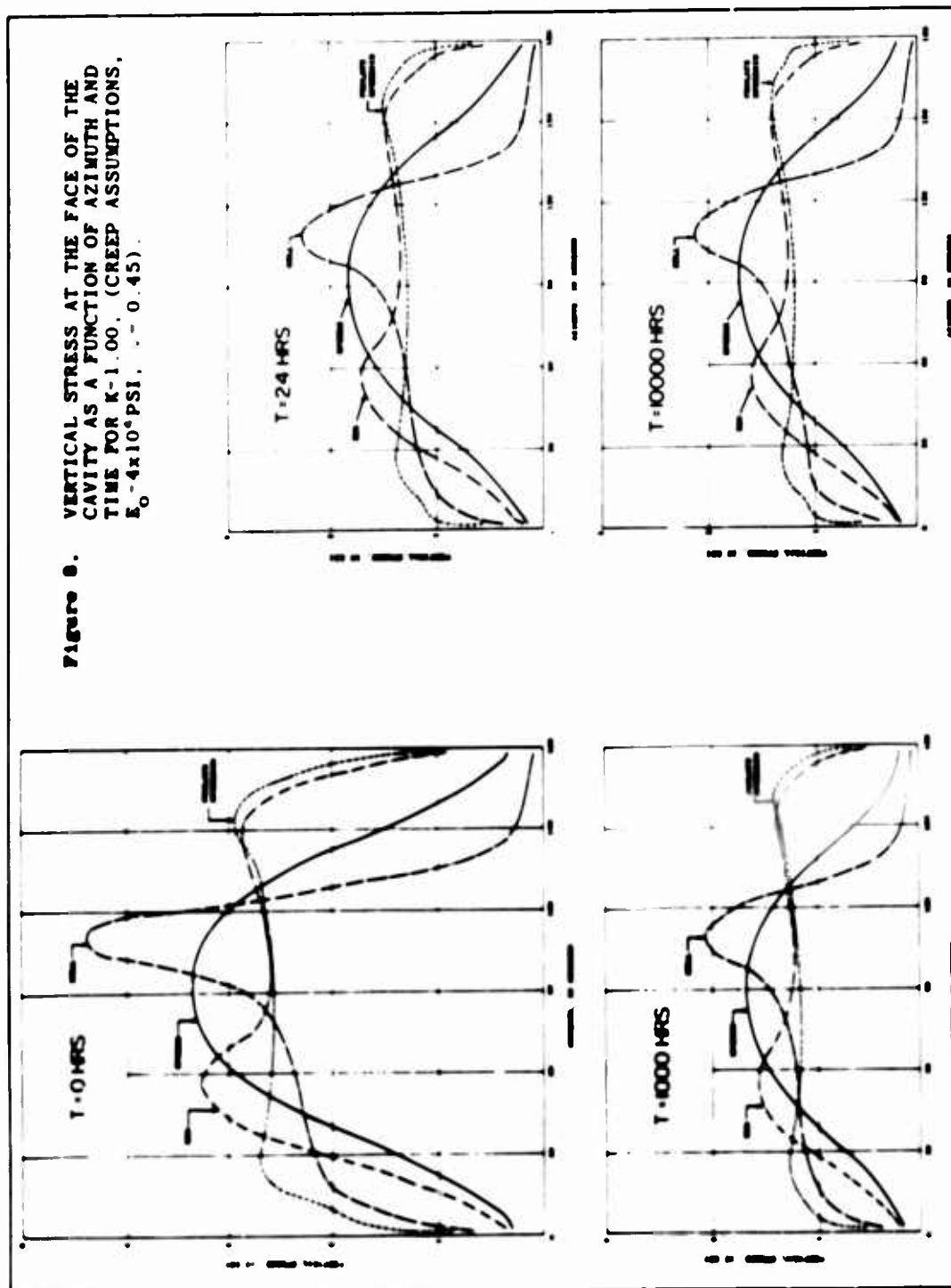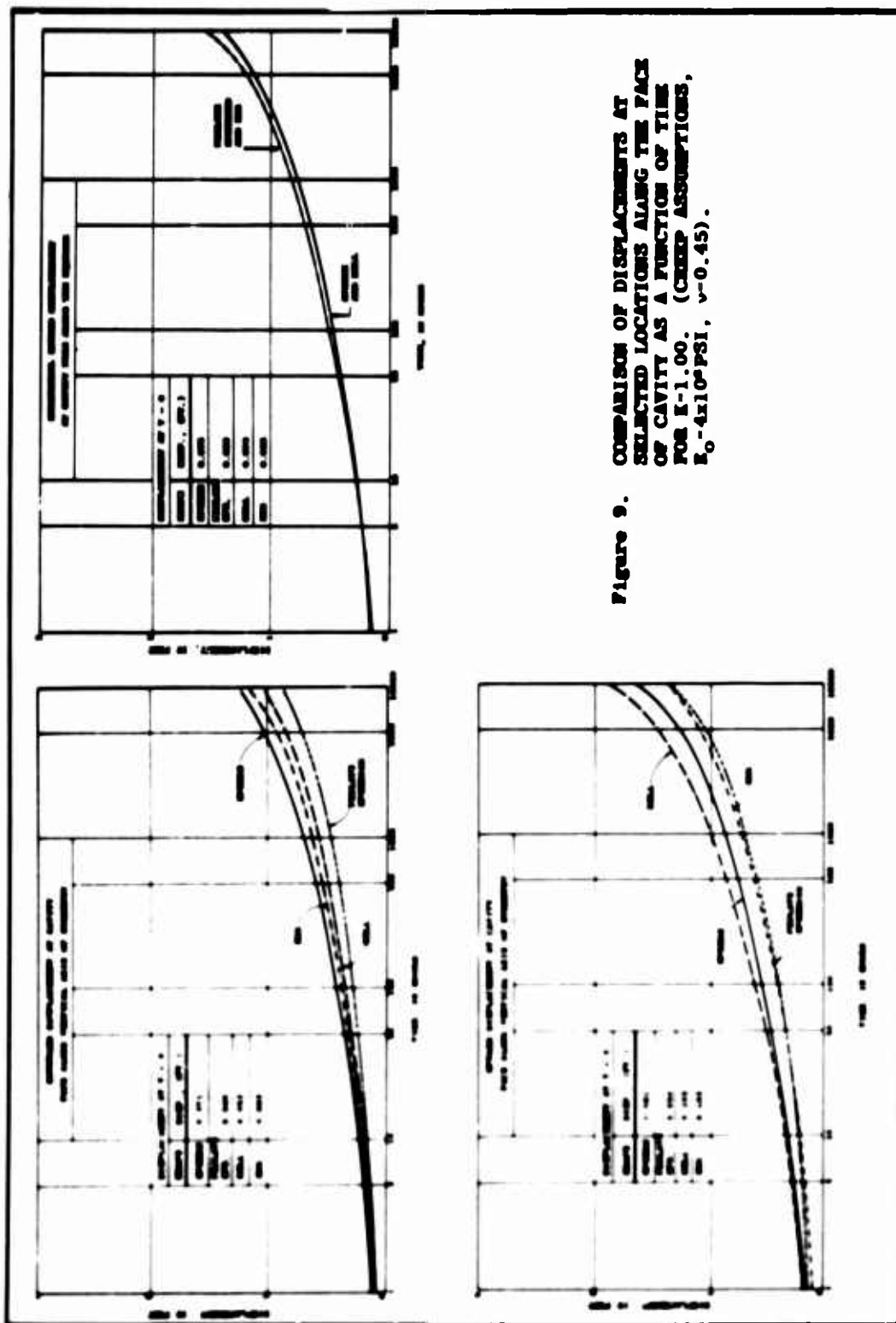FIGURE 6   VARIATIONS IN STRESSES AT THE FACE OF CAVITY WITH AZIMUTH FOR
K=1.00, (LINEAR ELASTIC ASSUMPTIONS, E=1x10⁶PSI, $\nu = 0.20$).

Initial Horiz. Stress = 0.75 / Initial Vert. Stress	Initial Horiz. Stress = 1.00 / Initial Vert. Stress	Initial Horiz. Stress = 1.33 / Initial Vert. Stress
SPHERE	SPHERE	SPHERE
PROLATE SPHEROID	PROLATE SPHEROID	PROLATE SPHEROID
BELL	BELL	BELL

Figure 7. SUMMARY OF YIELDED ZONES FOR DIFFERENT SHAPES AND INITIAL STRESS CONDITIONS. (BILINEAR ELASTIC ASSUMPTIONS. $E_1-1 \times 10^6$ PSI, $E_2-0.5 \times 10^6$ PSI, $\nu-0.45$).

SCALE

SHADED AREA REPRESENTS ZONE WHERE ELEMENTS HAVE YIELDED

187

Figure 8. VERTICAL STRESS AT THE FACE OF THE CAVITY AS A FUNCTION OF AZIMUTH AND TIME FOR K-1.00. (CREEP ASSUMPTIONS, E_o-4x10^{6}PSI. ν - 0.45).

Figure 9. COMPARISON OF DISPLACEMENTS AT SELECTED LOCATIONS ALONG THE FACE OF CAVITY AS A FUNCTION OF TIME FOR K=1.00. (CREEP ASSUMPTIONS, $E_0=4 \times 10^6$ PSI, $\nu=0.45$).

Figure 10. SUMMARY OF STRESS CONDITIONS AT CAVITY FACE. (LINEAR ELASTIC ASSUMPTIONS, $E=1\times10^6$ PSI, $v=0.20$)

Figure 11. DOWNWARD DISPLACEMENT AT CAVITY FACE ALONG VERTICAL AXIS OF SYMMETRY FOR SPHERE (CREEP ASSUMPTIONS WITH $E_0 = 4 \times 10^6$ PSI, $\nu = 0.45$)

Figure 12. UPWARD DISPLACEMENT AT CAVITY FACE ALONG VERTICAL AXIS OF SYMMETRY FOR SPHERE (CREEP ASSUMPTIONS WITH $E_0 = 4 \times 10^6$ PSI, $\nu = 0.45$)

193

Figure 13. HORIZONTAL INWARD DISPLACEMENT AT CAVITY FACE ALONG THE EQUATOR FOR SPHERE (CREEP ASSUMPTIONS WITH E_o=4x10⁶ PSI, ν=0.45).
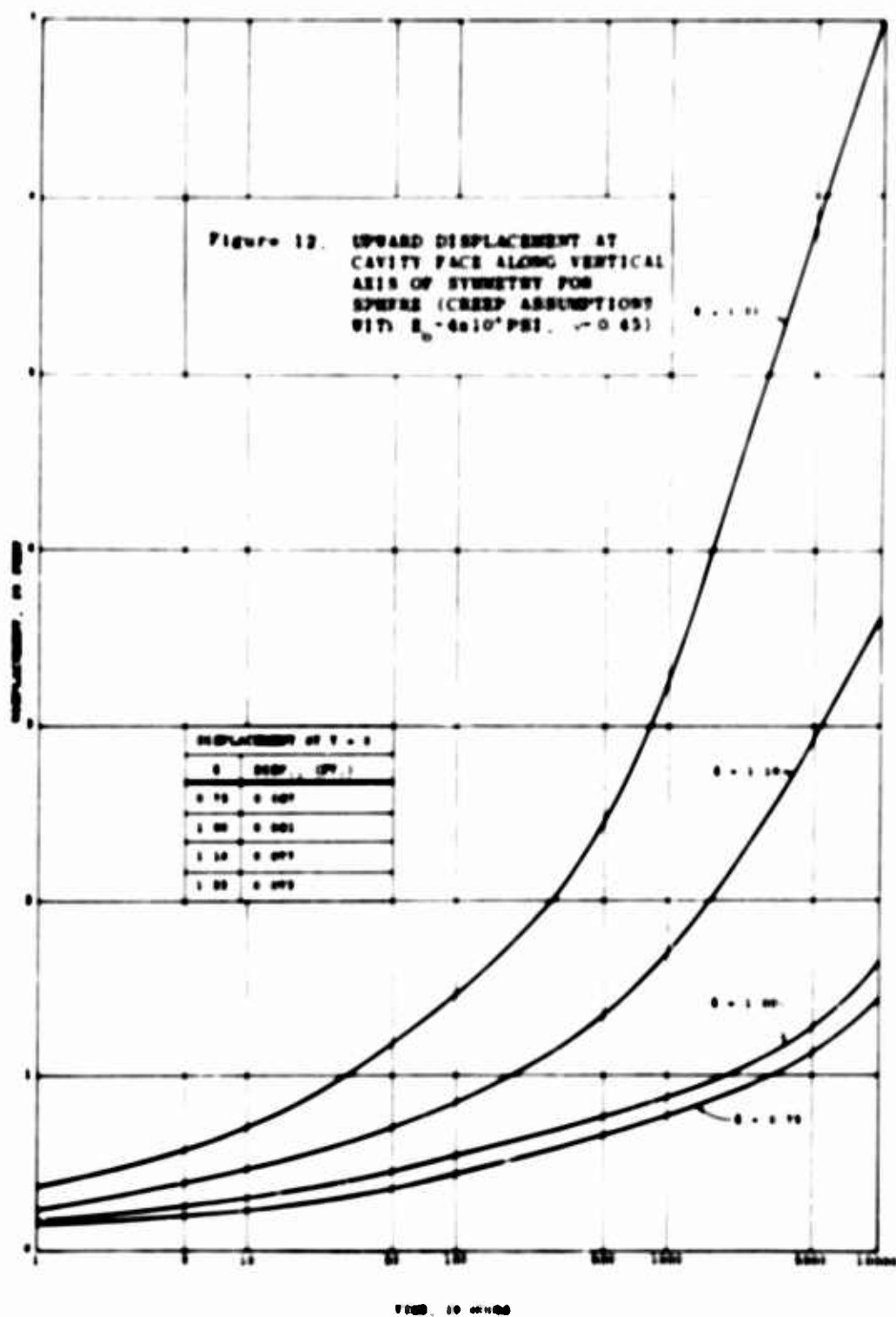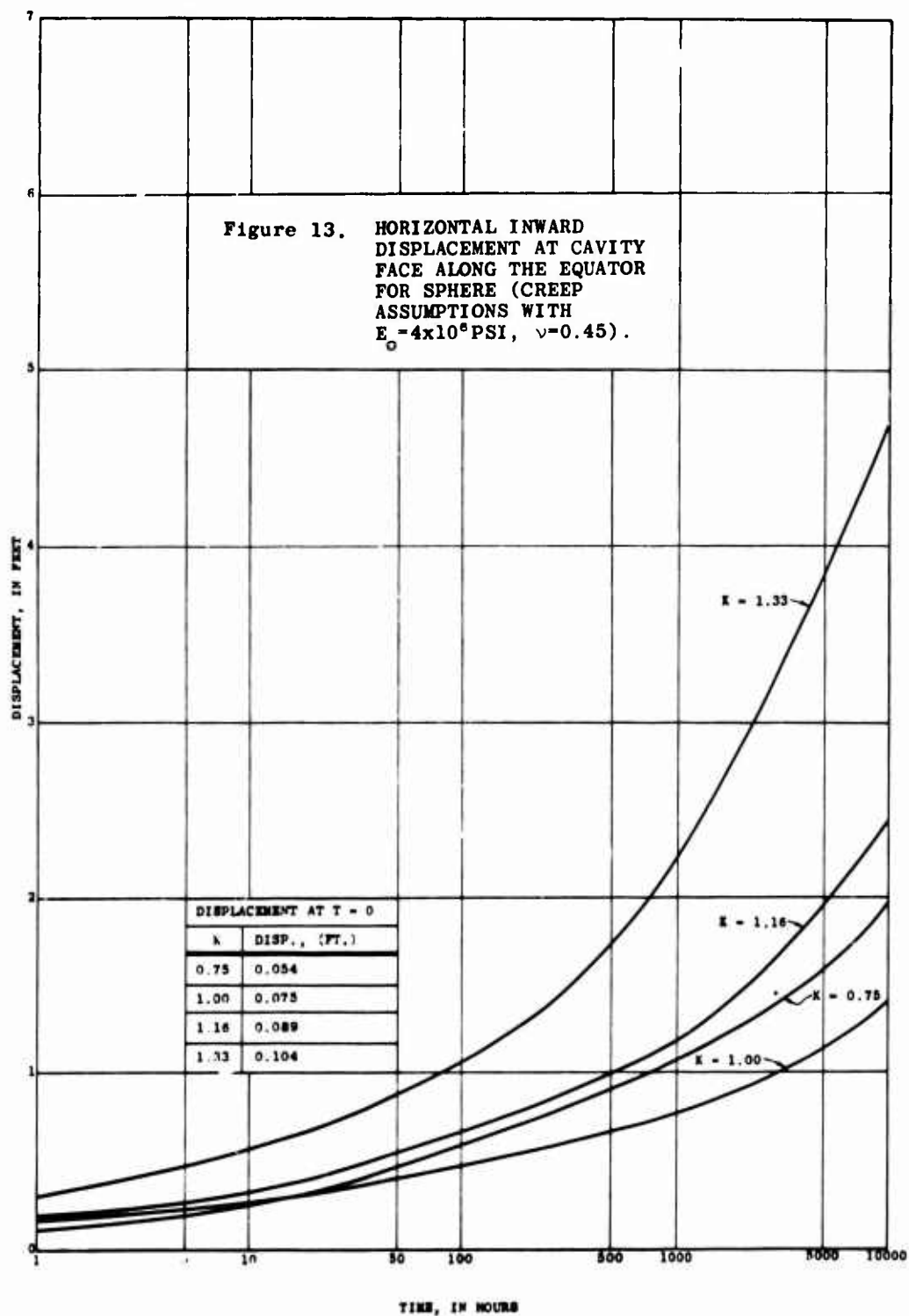
194

TABLE 1. SUMMARY OF CAVITY STUDIES

LINEAR ELASTIC ANALYSIS

Shape of Cavity	Material Constants and Initial Stress Field					
	$E=1 \times 10^6$ psi $v=0.20$ $K=0.75$	$E=1 \times 10^6$ psi $v=0.20$ $K=1.00$	$E=1 \times 10^6$ psi $v=0.20$ $K=1.33$	$E=1 \times 10^6$ psi $v=0.45$ $K=1.00$	$E=.5 \times 10^6$ psi $v=0.20$ $K=1.00$	$E=4 \times 10^6$ psi $v=0.45$ $K=1.33$
Sphere	X	X	X	X	X	X
Prolate Spheroid	X	X	X	X		
Bell	X	X	X	X		
Egg	X	X	X	X		

BILINEAR ELASTIC ANALYSIS

Shape of Cavity	Material Constants and Initial Stress Field					
	$E_1=1 \times 10^6$ psi $E_2=.5 \times 10^6$ psi $v=0.45$ $K=0.75$	$E_1=1 \times 10^6$ psi $E_2=.5 \times 10^6$ psi $v=0.45$ $K=1.00$	$E_1=1 \times 10^6$ psi $E_2=.5 \times 10^6$ psi $v=0.45$ $K=1.33$	$E_1=4 \times 10^6$ psi $E_2=.1 \times 10^6$ psi $v=0.45$ $K=1.00$	$E_1=1 \times 10^6$ psi $E_2=.25 \times 10^6$ psi $v=0.45$ $K=1.00$	$E_1=1 \times 10^6$ psi $E_2=.5 \times 10^6$ psi $v=0.45$ $K=1.75$
Sphere	X	X	X	X	X	X
Prolate Spheroid	X	X	X	X		
Bell	X	X	X	X		
Egg	X	X	X	X		

LINEAR ELASTIC WITH SUPERIMPOSED CREEP ANALYSIS

Shape of Cavity	Material Constants and Initial Stress Field					
	$E_o=4 \times 10^6$ psi $v=0.45$ $K=1.00$	$E_o=4 \times 10^6$ psi $v=0.45$ $K=0.75$	$E_o=4 \times 10^6$ psi $v=0.45$ $K=1.33$	$E_o=1 \times 10^6$ psi $v=0.45$ $K=1.00$	$E_o=4 \times 10^6$ psi $v=0.45$ $K=1.18$	
Sphere	X	X	X	X	X	
Prolate Spheroid	X		X			
Bell	X		X			
Egg	X	X	X			

APPENDIX

The finite element method, which was employed for the analytical aspects of this project, is a technique for determining the stresses and displacements which develop during arbitrary loading of solid bodies.

In the application of the finite element method, the solid body to be analyzed is idealized by dividing it into a series of discrete, finite-sized elements, interconnected at their corners so that the assemblage of elements forms the shape of the original solid body. For axisymmetric solids, the elements have the shape of rings; in a cross-sectional cut the ring elements have straight sides. The corners of the elements are called nodal circles or nodal points.

The method employed to analyze the assemblage of elements is the direct stiffness method wherein the internal stresses and nodal circle displacements are determined. Equilibrium equations, expressed in terms of unknown nodal circle displacements, are developed at each nodal circle. A solution to this set of equations constitutes a solution to the system.

The method of analysis can be outlined as follows:[*]

1. Derivation of element stiffness matrix $[k^m]$.

2. Determination of stiffness matrix $[K]$ for the total assemblage of elements.

3. Formulation and solution of the equilibrium equation $[K][u] = [Q]$, where $[u]$ and $[Q]$ are the nodal point displacement and force vectors respectively. The solution of the equilibrium equations is performed by a Gauss elimination process.

4. Evaluation of the element strains from the computed nodal point displacements. The element stresses are computed from the element strains by means of the stress-strain relations.

BILINEAR ANALYSIS

A method of successive approximations is used to solve the problem for a material with bilinear properties. This involves the repeated solution of the equation:

$$[Q]_{i-1} = [K]_{i-1}[u]_i \quad \ldots \ldots \ldots \ldots \ldots \ldots \ldots \ldots \ldots \ldots \ldots \ldots \ldots \quad (1)$$

$[K]_{i-1}$ = stiffness based on previous solution

$[Q]_{i-1}$ = loads acting on system

$[u]_i$ = the new displacements

---

[*]This applies for the linear elastic case; the modifications for the bilinear and creep analysis are discussed later.

This approach is not guaranteed to converge. However, experience has indicated that for materials with small nonlinear effects, the procedure will converge. The method is restricted to materials with single valued stress-strain relationships.

The effective strain for each element is calculated from the expression:

$$\epsilon_i = \left[\sqrt{\frac{1}{2}\left[\left(\epsilon_{rr}^{i-1} - \epsilon_{zz}^{i-1}\right)^2 + \left(\epsilon_{rr}^{i-1} - \epsilon_{\theta\theta}^{i-1}\right)^2 + \left(\epsilon_{zz}^{i-1} - \epsilon_{\theta\theta}^{i-1}\right)^2 \right]} \right] \frac{1}{(1+\nu)} \quad \dots \dots (2)$$

ϵ_i = effective strain

$\epsilon_{rr}, \epsilon_{\theta\theta}, \epsilon_{zz}$ = radial, tangential, and vertical strain respectively
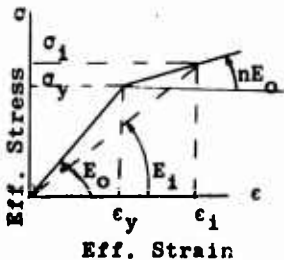
ν = Poisson's ratio

The value of effective strain is compared with the yield strain. If the yield strain is exceeded, the effective modulus for the next element is calculated from the following expression (see sketch)

$$E_i = E_o n + \frac{\sigma_y}{e_i}(1 - n) \quad \dots \dots \dots \dots \dots \dots \dots \dots \dots \dots \dots \dots (3)$$

E_0 = initial elastic modulus

σ_y = uniaxial yield stress

n = ratio of plastic to initial modulus

The procedure is repeated until a converged solution is found. The number of approximations depends on the particular problem.

The use of the effective stress-strain relation to generalize one-dimensional results to three-dimensional stress-strain relationship assumes that the material remains isotropic after the change in modulus. This is not necessarily true in non-linear elastic analysis.

TIME-DEPENDENT (CREEP) ANALYSIS

A method of successive approximation is used to solve this problem. This requires, that at each time, the repeated solution of the following equation be obtained:

$$Q_{i-1}^{t_n} = [K]_{i-1}^{t_n} [u]_i^{t_n} \quad \dots \dots \dots \dots \dots \dots \dots \dots \dots (4)$$

The above equation indicates the ith approximation at the nth time.

The relationship between stress, strain, and time is given by:

$$\epsilon = \epsilon_o + K\sigma^n t^m \quad \dots \dots \dots \dots \dots \dots \dots (5)$$

$$\epsilon = \sigma E_o + K\sigma^n t^m \quad \dots \dots \dots \dots \dots \dots \dots (6)$$

197

$$E(t) = \frac{\sigma}{\epsilon} = \frac{E_o}{1 + E_o K \sigma^{n-1} t^m} \quad \cdots \cdots \cdots \cdots \cdots \cdots \quad (7)$$

where

E_o = initial modulus

σ = effective stress

ϵ = effective strain

It is assumed that the change in modulus with time is such that the material remains isotropic. The first computation is made at $t = 0$ and is the simple elastic solution. At the next time interval, a new modulus is computed from equation 7, and a new stress distribution obtained. This is checked for convergence with the previous stress distribution. Convergence is measured by the change in effective stress. If convergence is not satisfactory, the new stress distribution is used to compute a new modulus for every element and the analysis repeated. When satisfactory convergence is found, the analysis moves to the next time interval. The procedures used in this project employ a total deformation type of theory.

8
DESIGN OF UNDERGROUND OPENINGS TO WITHSTAND STATIC LOADS[*]

W. R. Judd
School of Civil Engineering
Purdue University
Lafayette, Indiana

ABSTRACT

The efficient design and construction of underground openings requires that a theoretical method be found that will permit a reliable prediction of safe spans and shapes and efficient supports for such openings. Although many theories exist that purport to accomplish these objectives, most underground openings still are built on the cut and try or empirical method. A primary difficulty in obtaining the necessary theory has been an inability to validate the theory by measurements on the prototype. The present research project is attempting to overcome this difficulty. Strain measurement data from seven underground openings of various size, shapes and geology are being analyzed. Concurrent with this analysis, a modified finite-element is being used to predict the same strain data for each of the openings. When the finite-element method and prototype measurement data are not similar, geological data for each of the openings are being introduced into the finite-element method. By this latter approach, it is hoped that a suitable finite-element method can be formulated to predict the desired parameters for under-ground openings.

INTRODUCTION

Many underground openings have been and are being built for various purposes. The most permanent of these house underground power stations, military and civil defense command and control centers, and military and industrial archives. Of a somewhat less permanent nature are the variety of openings required for the extraction of ore. And, of least permanency, are those required for housing underground nuclear tests. However, regardless of the requirements for permanency and although innumerable openings have been excavated successfully, they commonly present an unsolved problem: the lack of a reliable theory for the efficient design and construction of an underground opening.

199

THEORETICAL APPROACHES

Many theories have been proposed for the correct design of underground openings. The objectives of these theories are to permit selection of the correct shape, span, and type of support that will maintain a stable opening under static loads. However, there is wide variance in the philosophy of these theories. For example, one of the earliest and most frequently used theories requires that the full weight of rock that overlies the opening per se has to be supported either by fabricated supports or by the rock around the periphery of the opening. This theory generally results in an inefficient design because it does not consider certain inherent properties of the rock, such as its shear strength. Other theories have been developed that presume to compensate for this latter factor by making the assumption that the burden above an opening will be supported by various-sized blocks of rock that extend beyond the boundaries of the opening. One of the earliest examples of the latter approach was the theory developed by Bierbaumer.[*] He proposed that the load acting on the tunnel has a parabolic configuration. The base of the parabola was at the roof of the tunnel and the width of the base (B) was determined by subtending an angle of $45^O + \frac{\phi}{2}$ upwards from a horizontal line coincident with the floor or invert of the tunnel as shown in figure 1. (ϕ is the measured or estimated angle of internal friction for the rock.) The height of the parabola was assumed to be equal to the depth of the tunnel roof beneath the ground surface times a coefficient K. For tunnels whose depth is less than five times the width of the base of the parabola, the value for this coefficient seems to be determined primarily by experience. However, Bierbaumer did propose the following formula for K:

$$K = 1 - \frac{\tan \phi \, \tan^2 \left(45^O - \frac{\phi}{2}\right) H}{b + 2 \tan \left(45^O - \frac{\phi}{2}\right)}$$

where b is the proposed width for the tunnel, h is the proposed height of the tunnel, and H is the distance between the ground surface and the roof of the tunnel. Bierbaumer also indicated that K would have a value of 1 for very "small"[**] overburden depths and whenever H is greater than 5B, $K = \tan^4 \left(45^O - \frac{\phi}{2}\right)$.

A number of other theories presume the formation of a pressure bulb above the tunnel and relate the roof load to the depth of the tunnel beneath the surface. This type of approach was followed by theories that ignored the depth of the tunnel beneath the surface and assumed there would be natural arching in the rock above the tunnel. The problem thus becomes one of calculating the shape of this arch to determine the weight of the rock within the bounds of the arch. An example of this approach is the theory proposed by the Soviet investigator, M. M.

---

[*]Szechy, K., The Art of Tunnelling, Akademiai Kiado, Budapest, 1966, pp. 191-194.

[**] The term "small" is not given a numerical value.

Protodyakonov.[*] His theory presumes that the area of the parabolic arch immediately above the tunnel is equal to $\frac{2}{3}$ bh, where b is the width of the roof of the tunnel and h is the height of the parabola or $\frac{b}{2 \tan \phi}$. The load per unit length on the roof is $\frac{2}{3}$ bhγ wherein γ is the unit weight of the rock (in Kg/m^3) or $\frac{1}{3} \gamma \frac{b^2}{\tan \phi}$. Protodyakonov established the tan ϕ value as follows:

$$\text{Tan } \phi = \frac{\text{Unconfined Compressive Strength (Rock) (kg/cm}^2)}{100}.$$

The above-described theories and their numerous modifications occasionally produce satisfactory designs for underground openings. However, these theories all have the common fallacy of not providing for the geological defects that normally are present in a rock system.[**] Furthermore, in practice there have occurred geological situations where a flat-or trapezoidal-shaped roof was stable whereas an arch-shaped roof in the same rock system had tended to be unstable. An example of the latter occurred during the pilot excavations for the Poatina underground power station in Tasmania. Despite several attempts to excavate pilot tunnels with an arch roof, the roof continually broke away toward a flat roof. Based upon these field experiences and upon laboratory simulations by photoelastic models, the chamber was constructed with a trapezoidal roof. This roof has proved stable during the past three years of operation. In this case, the rock system primarily was constituted of a series of horizontal sedimentary rocks that were relatively free of vertical discontinuities. A curious point raised by this latter experience and one that indicates the weaknesses in our theories is that generally theory and laboratory experiments show that a rectangular-shaped opening will have undesirably high stress concentrations at the corners of the rectangle; theoretically, the most desirable distribution of stresses occurs around a circular-shaped opening.

The fundamental difficulty with the described theoretical approaches is that unrealistic assumptions have to be made before a numerical result can be obtained. For example, all of these theories presume a material that has a linearly elastic response and is homogeneous and isotropic. Thus, these assumptions disregard the following conditions that almost always prevail in the prototype: (1) geological defects or discontinuities in the rock system that can inhibit or overwhelm the elastic response of the real media; and (2) the effect of time on the strain distribution around an opening that has to maintain stability for a considerable period of time. An almost equally significant factor that would have to be considered in a realistic theory is the ambient-stress condition in the rock system. That is, the walls or invert of the opening may be considerably deformed by lateral pressures that are considerably higher than

---

[*]Ibid, Szechy, pp. 213-217.

[**]"Rock system" designates the mass within which the opening is located, and includes the physio-mechanical properties of the rock, all geologic discontinuities, ambient stresses, and other environmental factors that can influence the distribution of strain around the opening.

the vertical pressures; and this may occur even for those openings that are located in reasonably flat topography and at moderate depths. Another influence can be anisotropy in the physico-mechanical properties of the rock element* and the rock system, and the resultant response to external loads. For example, it has been theorized that when Young's modulus of a rock element is at least 25 percent greater in one direction than in a direction normal to it, there can be a significant redistribution of stress around an opening excavated in such material. [1]

THE FINITE ELEMENT METHOD OF ANALYSIS

In conducting the stress analysis of continuous, or quasi-continuous bodies it is frequently necessary to seek appropriate solutions. One such approximation is the discretization of the body into a number of simple elements of finite size which are interconnected at a finite number of points. The approximation becomes useful when the individual elements are required to deform (or transmit stress) in such a way that the assembled elements respond to imposed conditions in approximately the same fashion as the actual body for which the approximation has been developed. The primary advantage of such an approach is that the partial differential equations describing the solution of a stress analysis problem in a continuum can, for suitably chosen elements, be reduced to a number of simultaneous algebraic equations. The availability of large high-speed digital computers makes the solution of such equations a much simpler problem than direct solution of the governing differential equations.

If proper consideration is to be given to all of the factors that can influence the behavior of a rock system, the analytical method selected for the opening design must be capable of the following:

1. Numerical simulation of the physico-mechanical properties of individual rock ele·ments;

2. Numerical simulation of the behavior of a system that is comprised of an agglomeration of such elements; and

3. The transference of deformation of each rock element to each adjacent element and subsequently to the boundary of an opening excavated in such a system.

Therefore, because of the discretized nature of the rock system the finite element approach makes it possible to consider the response of such anisotropic, inhomogeneous, discontinuous and multiply-connected bodies. The details of the basic method of finite analysis have been presented by Zienkiewicz and Cheung in a 1967 publication [2]. For purposes of this discussion it is sufficient to note that a wide variety of plane stress, plane strain, and axisymmetric stress analysis problems for linearly elastic continuous media have been solved. For example, in 1906 there were a series of papers published that used the finite-element method to investigate stresses around cavities of arbitrary shape in an elastoplastic material; [3] to analyze circular

---

*The "rock element" is one of the intact pieces of rock that comprise the rock system.

tunnels in layered rock systems; [4] to analyze a square opening in a system that contains faults [5] and to study the effect of inhomogeneity and nonlinear behavior in the rock system [6, 7].

The finite element method selected for our study was developed at the IIT Research Institute by Constantino and Wachowski [8, 9]. This program initially was developed to predict free-field response to shock effects, however, we have adapted it for the static load condition and for operation on the CDC 6500. When possible, consideration is being given to horizontal prestress in the rock mass, and anisotropic response of the solid rock material.

A major difficulty with this and other finite-element methods is that total deformation in a system generally is computed by permitting movement only at the nodal points of the elements. Therefore, there is no input of the effect of shear friction forces that would exist along the interfaces between the discrete elements in the grid. And yet, such forces may exercise a significant influence on the ultimate deformation behavior of the rock system. For example, there are numerous underground openings with relatively large spans where the roof is intersected by faults or fractures that resulted in prismatic or wedge-shaped blocks; yet these blocks remain in place because of the frictional forces on the block interfaces. Furthermore, the present code may be inadequate to predict the measured response of the rock mass to tunneling because of the time-dependent response of the rock mass as measured in the field.

THE EMPIRICAL APPROACH

The present research project has been undertaken with a full awareness of the inherent weaknesses in the theoretical methods that will be investigated. However, we believe that if the existing methods do not provide the desired results, they can be suitably modified to produce the correct answers. This latter belief brings us to what might be termed the proof of the pudding.

The obvious method for evaluating the accuracy of any theory on stress distribution around an opening is to compare the theoretical prediction with actual measurements of strains around an as-built underground opening. For some time it has been possible to measure the deformation on the skin of the opening by various types of strain measuring devices. However, it was not until the comparatively recent development of such instruments as measuring bolts, [10] the CSIR "Doorstopper" Gauge, [11] and borehole extensometers that it has been possible to measure deformations and strains at some distance into the rock away from the opening boundary. Thus, currently there are available strain data at varying distances from an opening boundary; this now makes it possible to verify the validity of current theories that purportedly predict stresses around openings.

To establish some standardization in our approach, that is, to minimize the number of variables, we decided to use measurement data from underground openings that had been instrumented with the multiple borehole extensometer or the "MPBX," as it is commonly called

203

(figure 2). This type of instrument provides a direct measurement of deformation or strain on the walls of the borehole into which the instrument is inserted. Secondly, the MPBX can be anchored at a depth in the borehole where the ambient stress field can be expected to not be influenced by the presence of opening. (Theoretical analyses, that have been supported by occasional field measurements, indicate that the influence of the opening on the ambient stress field can be expected to considerably diminish and probably become negligible at a distance from the opening boundary that is equal to approximately one and one-half times the diameter of the opening.)

To accomplish our objectives, the initial step in our research has been to select a group of excavated openings that have the following characteristics:

(1) They are instrumented with MPBX's,

(2) They have commonly constructed shapes such as circular and horeshoe cross-sections, and,

(3) They vary in total span or width.

Although it would have been desirable, it was not possible to select openings that were all in the same type of rock. The openings that were selected as meeting these requirements are illustrated in figure 3. They range from the almost rectangular Straight Creek Pilot Bore Tunnel that is 12-ft high by 14-ft wide to the Swiss Veytaux Underground Power Plant Chamber that is 98-ft wide and 91-ft high. In addition, although not instrumented with the MPBX, it was considered desirable to include measurement data from portions of the NORAD Underground Control Center Complex. This Complex has chambers that range from 32-ft wide by 56-ft high to 45-ft wide by 60.5-ft high, and, as shown in figure 3, have chamber intersections with considerably greater spans. The rock types in the openings that were selected range from shales and sandstones to granites and granite-gneisses. The geological situations vary from horizontally layered sediments to complexly jointed igneous rocks.

At the present time the measurement data from the instruments in these tunnels is being analyzed on a CDC 6500 computer and the resulting strain diagrams are being drawn by a CALCOMP plotter attached to the computer. To obtain a reasonable evaluation of these plots, it is necessary to select those readings in the continuous rate-of-strain diagrams that will be most useful for comparison with theoretical predictions. (A typical set of such diagrams is shown in figure 4.) Therefore, it was decided to select the strain readings at three different time periods for each instrumented cross-section: the first set would be those obtained immediately after initiation of the instrument readings; the second set would be those readings that appear to represent the maximum strain measured; and the final set would be those that represent the strain situation after the stresses at the selected location appear to have stabilized. During the evaluation, the selected strain diagrams will be compared with the position of the working face at the time the strains were measured.

Concurrent with these evaluations, the finite-element method will be used to predict the strain distribution at each of these instrumented cross-se 'ions. Input data for the initial prediction will be the opening geometry and the actual rock properties that have been determined by the laboratory and or field tests. The results from the finite-element analyses then will be visually compared to each of the three sets of CALCOMP strain plots. If, as we suspect, the finite-element results show evident dissimilarity to the prototype measurement plots, modifications will be introduced into the finite-element code. The first such modification will be an attempt to simulate in the finite-element model any geological discontinuities or features of rock element behavior that seem most likely to influence the response of the rock system in the vicinity of the instrumented cross-sections. These features include non-linear constitutive relationship (i.e., elastoplastic), joints and faults, [12], and time-dependent material response.

CONCLUSION

We expect this study to determine if varying the size of an opening will cause an appreciable perturbation in the strain-distribution pattern. According to elastic theory, the size should have no influence on the stress-concentration factors nor on the strain-distribution pattern; however, practical experience has shown that the larger the span of the opening, the greater the number of geological defects that will be encompassed by the opening boundary. Therefore, at some presently unknown but critical ratio between opening size and size of geological defects, the latter should dominate any elastic influence that might occur in the rock system surrounding the opening. In addition, the analyses of several openings that have increasingly larger maximum spans will permit us to evaluate the feasibility of extrapolating the behavior of small openings to those that are considerably larger. And, finally, the overall results from the research should enable us to evaluate the reliability of finite-element methods in predicting the static stability of an underground opening that is located in a rock system that contains discontinuities.

For this meeting on seismic coupling, we were asked to comment on results from our current research in the use of statistical methods to correlate rock properties. The initial detailed results from this research currently are being published as a separate unclassified document that will be available from the DDC. This document also will contain the format and coding used for the analysis. The title of this document is "Correlating Rock Properties by Statistical Methods The Computer Format and Some Initial Results," this report will be published by the Purdue Research Foundation in February 1968.

REFERENCES

1. W. R. Judd, R. H. Merrill and J. W. Workman, The Vulnerability of Underground Facilities - Geologic and Rock Mechanics Factors, Air Force Rept. No. BSD-TR-67-241, Space and Missile Systems Organization, Air Force Systems Command, Norton AFB, Calif., 1967, p. 53.

2. O. C. Zienkiewicz and Y. K. Cheung, The Finite Element Method in Structural and Continuum Mechanics, McGraw-Hill Publishing Co., New York, 1967.

3. S. F. Reyes, Elastic-Plastic Analysis of Underground Openings by the Finite Element Method, Unpublished Ph.D. Thesis, Univ. of Ill., Urbana, Ill., 1966.

4. R. E. Goodman, "On the Distribution of Stresses Around Circular Tunnels in Non-homogeneous Rocks," Proc. 1st. Cong. of ISRM, Vol. II, 1966, p. 249.

5. H. W. Anderson and J. S. Dodd, "Finite Element Method Applied to Rock Mechanics," Proc. 1st. Cong. of ISRM, Vol. II, 1966, p. 317.

6. O. C. Zienkiewicz and Y. K. Cheung, "Application of the Finite Element Method to Problems of Rock Mechanics," Proc. 1st. Cong. of ISRM, Vol. I, 1966, p. 661.

7. R. W. Clough and R. J. Woodward, III, "Analysis of Embankment Stresses and Deformations," J. Soil Mech. and Foundations Div., ASCE, Vol. 93, 1967, p. 529.

8. C. J. Constantino, Auto. Design of Advanced Hardened Facilities Study, Final Report, Vol. I, Air Force Ballistic Systems Div., Norton AFB, Calif., 1966.

9. A. Wachowski and C. J. Constantino, Computer Program Description for Free Field Stress Wave Problems Using Finite Element Technique, Final Res. Rept., Air Force Ballistic Systems Div., Norton AFB, Calif., 1966.

10. T. A. Lang, "Testing of Rock In-Situ for Foundations and Underground Excavations," Soil Mech. and Foundation Div., ASCE, Preprint for October 1963 meeting in San Francisco, Calif., pp. 22-24.

11. Staff, CSIR Strain Gauge Strain Cell ("Doorstopper") Equipment, CSIR Rept. MEG 417 (Instruction Manual), Rock Mechanics Div., National Mechanical Research Institute, Council for Scientific and Industrial Research, Pretoria, South Africa, 1966.

12. R. E. Goodman, Analysis of Structures in Jointed Rock, Research on Rock Bolt Reinforcement and Integral Lined Tunnels, Tech. Rept. No. 3, Omaha District Corps of Engineers, Omaha, Neb., 1967.
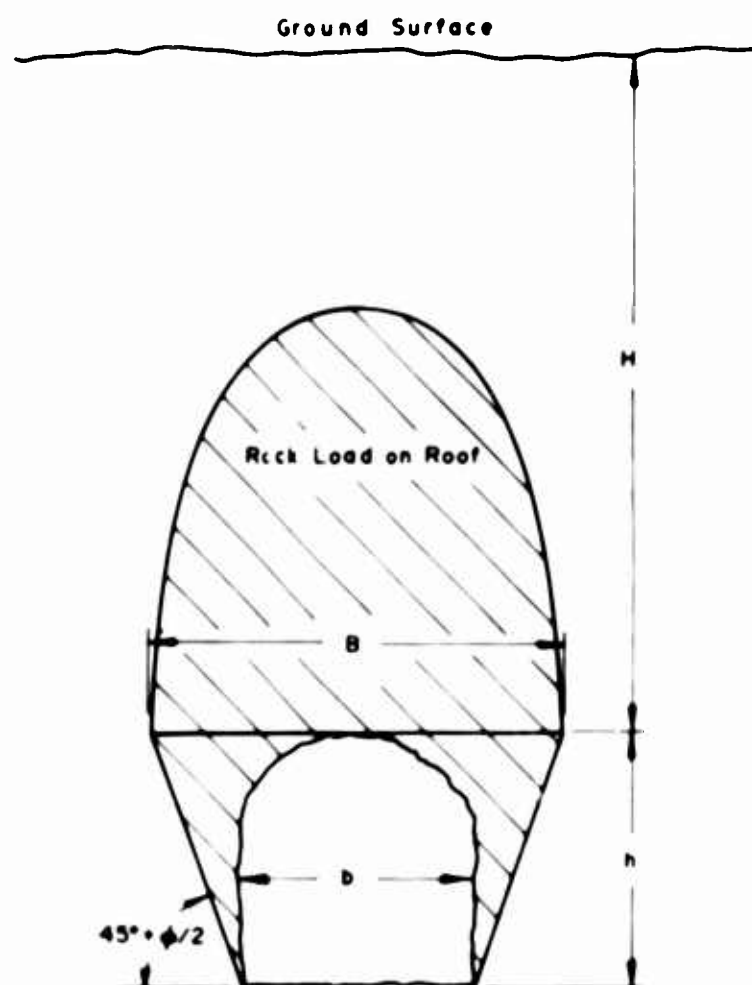
Ground Surface

Rock Load on Roof

B

b

H

h

45° + φ/2

Figure I   Bierbaumer Theory *

*After Figure 3/30 in "The Art Tunneling" by K Széchy,
Akadémiai Kiadó, Budapest 1966

207

A - Measurement Cantilever

B - Attachment Point for
Movement Wire

SENSOR HEAD

(ENLARGED VIEW)

Movement Wires

Flat, Wedge-Spring Anchors

Sensor Head

Cover
Plate

8 Stainless Steel Cantilevers
With Transducers Attached

Readout Cable

Measuring Points:
Eight Fixed Anchor
Points Spaced Along
Borehole Axis
Movement Range
± 0.40 in
Sensitivity
0.001"
Borehole Diameter
Percussion Drilled,
2-1/4 in.
Diamond Drilled,
EX, BX, NX

Figure 2 Multiple Borehole Extensometer*

*Courtesy, Terrametrics, Inc., Golden, Colorado
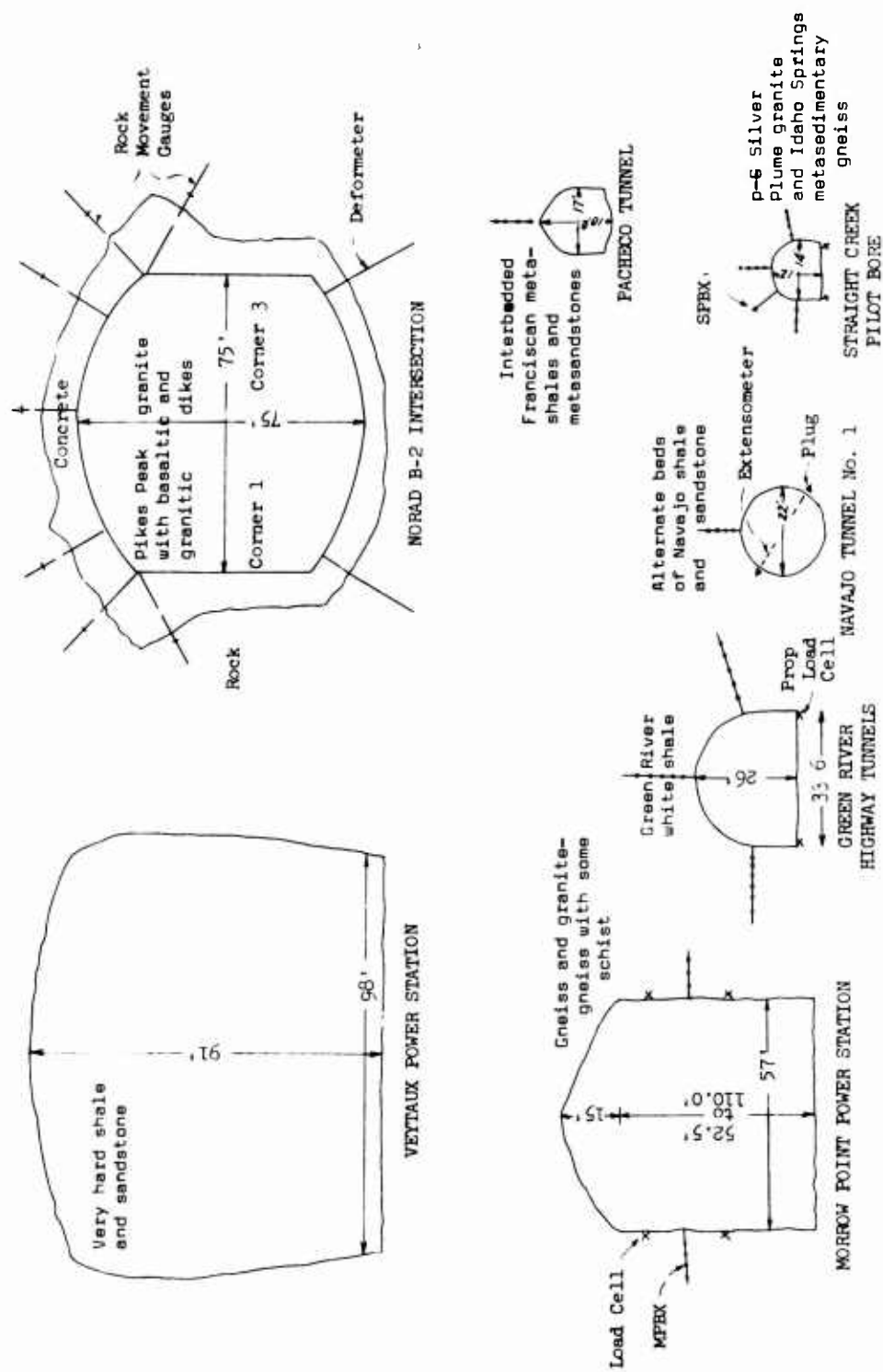
Figure 3. INSTRUMENTED UNDERGROUND OPENINGS

TUNNEL- STRAIGHT CREEK
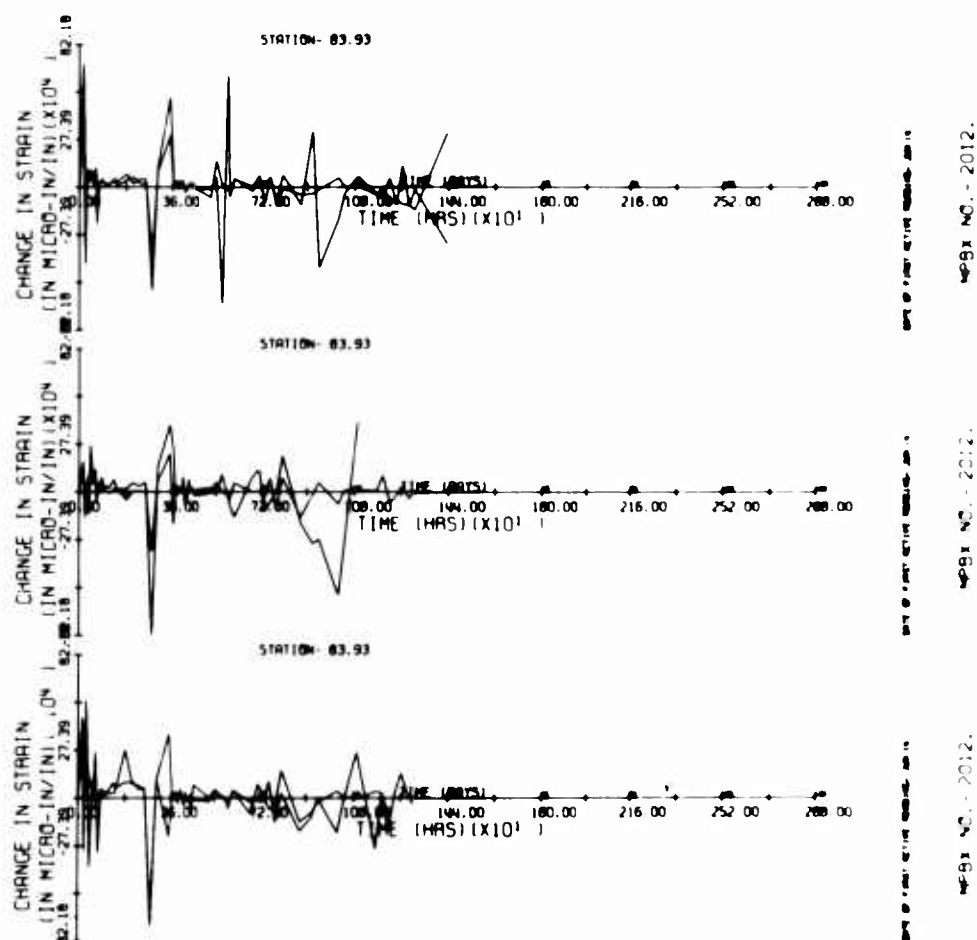
Figure 4. EXAMPLE OF STRAIN MEASUREMENTS AT SIX ANCHOR POINTS IN MPBX No. 2012. (Each diagram contains the strain readings from 2 anchors.*)

* At the time of preparation of this figure, we had not completed the "dash-line routine" for the computer program. In the working drawings, one of the two curves on each diagram will be plotted as a dashed line.

210

A NEAR FIELD STUDY BY OPTICAL TECHNIQUES OF THE GENERATION AND PROPAGATION OF SEISMIC WAVES FROM EXPLOSIONS IN PRESTRESSED MODELS

K. C. Thomson
Air Force Cambridge Research Laboratories
L. G. Hanscom Field
Bedford, Massachusetts

T. J. Ahrens
California Institute of Technology
Pasadena, California

M. N. Toksoz
Massachusetts Institute of Technology
Cambridge, Massachusetts

ABSTRACT

A number of theoretical calculations have been made of anticipated isochromatic and 45° isoclinic effects to be expected when P and S waves propagate in med a prestressed in tension or shear. The results are shown as cross sections of the waveform with maximum shearing stress plotted as a function of distance from the shotpoint with azimuth, time, and amplitude as parameters. On the basis of these special cases a number of distinctive optical phenomena are predicted. A 45° discontinuity between P and S wave isoclinics for the unstressed case, a tendency for the isoclinics to broaden and envelop the isochromatics in regions where P and S are superimposed, the development of serrations in the dynamic isoclinics in the presence of a prestressing field yielding a pseudo-isochromatic appearance to the isoclinics when viewed monochromatically and a general similarity between the dynamic optical effects observed in tensile and shear prestressed media.

A model study of the generation and propagation of seismic waves from explosions in glass and Plexiglass models prestressed in tension and shear at various levels was made using dynamic photoelasticity and a high speed motion picture camera to record the observations. The isochromatic and isoclinic effects theoretically predicted were observed.

Analysis of the dynamic cracking phenomena in the vicinity of the shot point indicated good agreement between the observed terminal velocities of cracks and those predicted by Mansinha, and Dulaney and Brace only at the higher prestress levels. In other respects there was less agreement between the observed cracking phenomena and available crack propagation theories.

INTRODUCTION

Not infrequently the seismic radiation from underground nuclear explosions contains strong horizontally polarized components. The question of the relative significance in producing this anomalous radiation of possible mechanisms such as source irregularities, local inhomogeneity and anistropy in the shot point vicinity, mode conversion along the travel path and tectonic

prestress in the source region has never been fully evaluated. For a more detailed discussion of the problem as viewed at teleseismic distances reference is made to Toksoz [1].

In order to better understand the complicated near source phenomena which might be contributing to the anomalous far field observations a model study has been undertaken by the authors. Figure 1 shows the essential elements of the apparatus. The argon bomb light source presents a brilliant 100 μsec flash to the focus of the Fresnel lens, the front surface mirror turns the light parallel to the main optic axis of the system and a paraxial beam is projected through the system. The polarizer and analyzer can be of either the linear or circularly polarizing type. When linear polarization was used the optical elements were maintained at 45^0 to the horizontal. The model was supported inside a framework (see figure 2) which permitted the development of a wide range of prestress types and intensities. Dynamic loading of the model was achieved by means of mild detonating fuze as shown. The fuze length was cut and detonated so that the shock entered the glass simultaneously from both sides. Recording of the detailed dynamic cracking and wave generation phenomena in the immediate vicinity of the shot point was obtained by the high speed camera which took 25 pictures with exposure times from 0.02 to 0.7 microseconds. The far field phenomena at 20 cm from the shot point were recorded by means of strain gauges disposed along a circular arc about the shot point and oriented usually at 45^0 to the radius vector from the shot point. Figure 2 is a photograph of the straining frame actually developed for the project. Note the hydraulic pumps and rams used to synthesize tension and shear at various intensities within the model. Most of the other elements of the system, except the framing camera, are also visible. The mild detonating fuze system of dynamic loading used in this experiment was arrived at after considerable testing, looking for the most truly radial source available. The success of this effort can be judged from figure 3 which is a shot in 1 8 in. glass without prestress and using circularly polarized light. Further details of the apparatus used are given in Ahrens [2].

The optical effects observed on the high speed photographs from this experiment were rather complicated and evaluation of these is still taking place. This paper is a progress report on the results to the time of writing.

CALCULATION OF SPECIAL CASES

Theoretical calculation from mathematical models of anticipated optical results were made.

A polar coordinate system (r, θ) was used in which the direction θ = 0 corresponded to the applied compression axis in the real model and $\theta = \frac{\pi}{2}$ to the tension axis. In figure 4 these relationships are clarified and the basic quantities being calculated indicated. The radius of the shot hole is "a" and its center is taken as r = 0. A plane stress situation at any point (r, θ) can be adequately described by the three stress components $(\sigma_r, \sigma_\theta, \tau_{r\theta})$ from which the orientation of the plane across which the maximum shearing stress occurs $\left(\phi \cdot \frac{\pi}{4}\right.$ relative to the radius vector from the shot point$\left.\right)$ and its magnitude $|\tau_m|$ can be calculated from the formulae of figure 4. 212

When monochromatic circularly polarized light is used to view a stress situation in the optical path the light passing through the stressed model emerges polarized in two orthogonal directions parallel to the principal stress directions in the plane of the plate. Each of the two polarized beams experiences a different velocity in traversing the model so that an interference effect is observed when the beams are combined by passage through the analyzer. The fringes so produced are called isochromatics and are proportional to the maximum shearing stress. The constant of proportionality is wavelength dependent so that in white light the isochromatic effect is a multi-colored interference pattern. For purposes of theoretical calculation the isochromatics can be adequately described (i.e., to within a multiplicative constant) by calculating τ_m. In plane polarized light the isochromatics are also observed but an additional set of extinctions, called the isoclinics, is seen wherever the principal stress directions are parallel to the pass directions of the polarizer and analyzer. If θ' is the orientation of the polarizer it will be apparent from figure 4 that the isoclinic condition is

$$\phi = \phi$$

or

$$\phi = \frac{\pi}{2} + \phi$$

or

$$\phi = \phi + \pi$$

or

$$\phi = \pi + \phi + \frac{\pi}{2}$$

$$(1)$$

Obviously an adequate description of the isoclinics is obtained by calculating ϕ as shown in figure 4. A more detailed quantitative description of dynamic photoelasticity for seismic modelling is given in Thomson [3].

The stress conditions in simple cylindrical P and S waves can be approximately described as in figure 5 where

A_p, A_s are the amplitudes of P and S

σ is Poisson's ratio

F and G are the unit time functions described in figure 6. (Simply being 360° of a sine wave in each case.)

Numerical values used are

$$L_p \quad C_p \quad 12.8$$

$$L_s \quad C_s \quad 6.9$$

$$\sigma \quad 0.4$$

213

No attempt was made to match these values to any specific case, however they bear some similarity to the waveforms, duration, Poisson's ratio and velocities actually obtained in Plexiglass in this experiment.

Two types of prestress have been primarily used: tension and shear. The stress distribution around a hole is given in figure 7 for each of these static cases.

In all calculations the unit of distance is the hole radius. The unit of stress used was chosen such that for both tension and shear prestress fields

$$\lim_{r \to \infty} (\sigma_r)_{\theta = \frac{\pi}{2}} = 1$$

(i.e., $\sigma = 1$ in figure 7).

The simple case of the P and S waves of figure 5 propagating from a common source was considered first. Amplitude levels chosen were $A_p = 1.0$ and $A_s = 0.1$. Calculations were performed digitally at six times and the results presented in analog form in figure 8. At each time a graph or a cross section is shown giving the absolute value of the maximum shearing stress $|\tau_m|$ as a function of distance from the shot point, and a contour map of $|\tau_m|$ on the (r, θ) plane with a contour interval of $|\Delta \tau_m| = 0.02$. Note that at a time $T = 3.0$ the two waves P and S are separated but that at earlier times more complicated $|\tau_m|$ cross sections are obtained due to interaction between the two wave types. The maps are in all cases simple concentric rings for both P and S so we would anticipate that distinction between the two wave types on the basis of the isochromatic effects displayed here could only be obtained through the use of time distance plots for successive fringes. Figure 3 shows observed P and S isochromatics which should be compared with those predicted for ideally simple P and S waves in figure 8.

In all of the experimental work the orientation ϕ of the polarizer and analyzer pass directions was at 45^0 to the horizontal so that it is adequate for isoclinic purposes here to calculate only the 45^0 isoclinic. Figure 9 shows the results of this calculation for the simple P and S wave situation described above. At all points of the digital data where the condition

$$\sigma = \alpha + \phi = \frac{\pi}{4} \tag{2}$$

was fulfilled, a solid circle was drafted onto figure 8. The results are shown in figure 9. The black circles are then the points actually calculated for a continuous locus the 45^0 isoclinic. In a simple cylindrical P wave with the displacement normal to the wave front and of the same value for all when r is constant then the principal stress directions are radial and tangential and the corresponding isoclinics lie along radii inclined at 45^0 to the horizontal. Similarly in a simple S wave with displacement tangential to the wavefront the principal stress direction will be at 45^0 to it and the resulting isoclinics should lie along radii inclined at 0^0 and 90^0 to

214

the horizontal. This sharp discontinuity of 45° between P and S wave isoclinic behaviour is readily observed in figure 9 particularly at later times such as T = 3.0 where the two waves are clearly separated. Study of figure 9 gives an indication of the isoclinic effects to be anticipated when P and S waves overlap. Note how the isoclinics tend to wrap around the isochromatics at the times from 1.0 to 2.0 where the more rapidly propagating and spreading P wave has undergone sufficient geometric attenuation for its amplitude levels to be comparable to S. At times earlier than 1.0 the superior amplitude of P relative to S (i.e., 10 to 1) overrides any contribution from S and the only isoclinics observed are those characteristic of P.

Figure 10 is a framing camera sequence with interframe time of 4.162 microseconds in unstressed 1/16 in. Plexiglass. The amplitude level produced is not high enough at any point to observe a single isochromatic fringe, the optical intensities observed being due to fractional fringe orders and the optical minima being either zero order isochromatics, isoclinics, or smoke from the mild detonating fuze. Comparison between the observations of figure 10 and the predictions of figure 9 enable the details of the former to be uniquely identified. These include the tensile and compressive portions of P, the zero order isochromatic separating them, the P isoclinic, the S wave and its associated isoclinic. Confirmation of these identifications was made by making time distance plots of all phases. Plate P and S wave velocities observed on this shot were 237,000 cm/sec and 128,000 cm/sec.

The next step in calculational complexity was taken by adding the P wave of figures 5 and 6, with $A_p = 10$, to the tension field of figure 7. The resulting $|\tau_m|$ effects vary with azimuth (θ) so figure 11 has been prepared showing cross sections in two orthogonal directions parallel $\left(\theta = \frac{\pi}{2}\right)$ and perpendicular to the tensile axis and for seven sequential times. Inspection of successive $|\tau_m|$ cross sections (for any one θ) in figure 11 will enable the reader to easily identify the static and dynamic portions of the field. Note that the original time function is recovered in the direction $\theta = 0^O$ for times of T = 3.5 or more where excursions of the dynamic waveform are not less than the average value of the static field. Closer in (i.e., at shorter times) this condition is violated and the lower half of the wave is distorted. At even shorter times (T = 1.0 or less) the apparent distortion of the waveform becomes even more marked. Note that at times greater than T = 1.0 the dynamic effects observed at any one time for $\theta = 0$ are reversed with respect to those at $\theta = \frac{\pi}{2}$.

As an additional test of the ability of the method to recover the original time function in the presence of a static prestress figure 12 was prepared. At seven times and using the same prestress for a fixed azimuth $|\tau_m|$ cross sections are displayed for two amplitude values of the P wave. Note that to within an additive constant of π the original waveform is immediately apparent at T = 1.5 for the lower amplitude level of $A_p = 1.0$ but that it does not become apparent at the higher level of $A_p = 10.0$ until the later time T = 3.0.

In order to better understand the effects of P and S waves propagating together in a medium stressed in tension, figures 13, and 14, were prepared. A fixed time has been taken of T = 2.0.

215

For this situation the P wave exists for $26 \leq r \leq 13$ while the S wave lies in $14 \leq r \leq 7$ so that the entire waveform is defined for $26 \leq r \leq 7$. The P and S amplitude used are $A_p = -10$ and $A_s = 10$. In both figures cross sections have been prepared at θ intervals of 10° to give an indication of the azimuthal variation. In figure 13 the ordinate for each cross section is $|\tau_m|$ while in figure 14 it is $(\theta + \phi)$. The isoclinic condition of equation 1 is indicated in figure 14 by heavy dotted lines. Whenever the solid curve $(\theta + \phi)$ intersects these dotted lines the isoclinic condition will be fulfilled. All such points have been noted on figure 13 by superimposing a little circle on the $|\tau_m|$ curve at the isoclinic position indicated by figure 14. By careful inspection of figure 13 it will be apparent that the isochromatics associated with the P wave will consist of two roughly elliptical minimum contour regions followed by an elliptical maximum contour region in the direction $\theta \cong 0$ while in the direction $\theta = \frac{\pi}{2}$ a similar sequence of contours will be observed except that the order is reversed with the maximum contour leading rather than trailing. This should be compared with figure 8 to understand the changes in the isochromatics produced by the prestress. The change in the isoclinics is even more marked. Now instead of being segments of straight lines as in figure 9 they form elliptical closures with centers on $\theta = 0$ in one case and $\theta = \frac{\pi}{2}$ in the other. In the one direction the isoclinic closure is in the leading portion of P and in the other it is trailing. The S wave also is characterized by elliptical isochromatic closures but in this case the centers lie along the line $\theta = \frac{\pi}{4}$. The S wave isoclinic should be compared in figure 13 and figure 14 with figure 9. The most noticeable difference is that the prestress causes "notching" of the isoclinic. Instead of the isoclinic being a pair of continuous lines at $\theta = 0$ and $\frac{\pi}{2}$ as in figure 9 it is now a set of broken lines appearing at isochromatic peaks for $\theta = 0$ and along the points of inflection for $\theta = \frac{\pi}{2}$; in addition there is some spreading of the isoclinics to angles other than 0 and $\frac{\pi}{2}$.

In order to test the sensitivity of the observations discussed in the preceding paragraph to amplitude variations, the calculations on which figures 13 and 14 were based were rerun at three amplitude levels of $(A_p = 10, A_s = 10)$, $(A_p = -10, A_s = 10)$ and $(A_p = -100, A_s = 100)$ for a single azimuthal angle $\theta = 0$. The results are displayed in figure 15. Consider the P, or leading half of the wave first. At high amplitude levels $(A_p = -100)$ the P waveform given by the isochromatics is not noticeably different than that for the unstressed case shown in figure 8. The isoclinic picture for P in figure 15 is slightly different from the unstressed case in that a hint of a very "thin" isoclinic $\left(\text{i.e., } \frac{\partial(\theta + \phi)}{\partial r} \to \infty\right)$ is indicated at isochromatic minimum positions $(r = 19$ and $26)$ whereas no such isoclinic exists at $\theta = 0$ in the unstressed case. Note that reversing the sign of A_p (from 10 to -10) reorganizes the appearance of the waveform in such a way that formerly trailing features become leading. As the amplitude level of P drops to $A_p = 10$, a level more comparable with the amplitude of the prestress, then the deviation of the waveform from the unstressed case becomes more marked. The behavior of the S wave isochromatics at all amplitude levels for the stressed case of figure 15 differs little from the unstressed case of figure 8; however the S wave isoclinic behavior differs markedly. At intermediate amplitude levels $(A_s = 10)$ the S wave isoclinic has a "notched" or "broken"

216

appearance as noted previously. As the amplitude level rises to high levels (A_s = 100) the amou.t of notching is reduced but not eliminated so that this effect seems to be a fairly sensitive test for the presence of a weak prestressing field. On the other hand when the S amplitude level drops to low levels (A_s = 1.0) such that the trace excursions of S are less than the static level of the prestress no isoclinics at all are produced, and the isoclinic test for S earlier indicated in figure 9 is no longer valid.

Frontispiece displays a framing camera sequence in tension stressed 1/8 in. Plexiglass using plane polarized white light. The interframe time is 4.158 microseconds. Distance can be obtained from the two little triangles shown on each frame as these are ten centimeters apart. The prestress level is $(\sigma_r)_{\theta=\frac{\pi}{2}}$ = 114 bars. Due to the use of white light, rather than the monochromatic green used in figure 10, an isochromatic effect is observable giving some dynamic amplitude information.

The P wave can be immediately identifed by the four leading elliptical closures (isoclinics) two in the leading (compressive) portion of the P wave in the direction of the prestress tensile axis $\left(\theta = \frac{\pi}{2}\right)$ and two in the trailing tensile portion of the P wave ($\theta = 0$) as predicted in figures 14 and 15. The S wave is immediately identifiable in the trailing portion of the waveform by its "notched" isoclincs. This suggests an amplitude level of the same order of magnitude as the prestress and certainly greater than that produced in the unstressed case of figure 10.

Calculations were also performed to estimate anticipated effects when the prestress in the medium was shear rather than tensile as in the cases so far discussed. The same P wave, with A_p = 10.0, used to calculate figure 11 was used for figure 16 but with the prestress field being shear as shown in figure 7. Note the general similarity to figure 11. It should be further observed that the time function is obtained undistorted in the shear case at shorter times than for the tension case. This is due to the higher value of the prestress assymptote $|\tau_m|_{r\to\infty}$ for the shear case where $|\tau_m|_{r\to\infty} \to 1$ than for the tension case where $|\tau_m|_{r\to\infty} \to 1/2$. Consequently a wider dynamic excursion of $|\tau_m|$ around the static prestress value (i.e., unity in the shear case for large r) is permitted for shear than for tension.

The same combined P and S wave used in figures 13 and 14 (i.e., A_p = -10, A_s = 10, T = 2.0) in conjunction with tension prestress has been used in figure 18 in association with a shear prestress for two azimuthal angles θ = 0 and $\frac{\pi}{2}$ to show the isochromatics (i.e., $|\tau_m|$) as a function of distance from the shot point. The analogous graphs for the tension case are juxtaposed with the shear results for comparison. As in the previous figure the differences between the tension and shear cases are very slight. For the S wave, any wave form differences in the isochromatics are not discernible by eye. For the particular amplitude used (A_p = -10) the isochromatic minima for P show differences because of the lower static value of $|\tau_m|$ in tension permitting negative excursions in P of any particular value to approach closer to the axis

217

$|\tau_m| = 0$ in the tension case than in the shear case. At a lower amplitude level of A_p this effect would not be observed. The differences in the P waveform between $\theta = 0$ and $\theta = \frac{\pi}{2}$ for a fixed prestress type are greater than they are between the two prestress types at a given azimuth.

Figure 17 is a framing camera sequence from a shot in 1/8 in. Plexiglass prestressed in shear such that $(\sigma_r)_{r\to\infty} = 98$ bars. The interframe time is 18.32 microseconds. Recording was on color film, with figure 17 being obtained by rephotographing the color prints. The view is a closeup of the source region. The leading edge of the P wave is partially visible in the first frame but only the trailing edge of the S wave is apparent in the last frame. Comparison of Frontispiece with figure 18 does not disclose appreciable differences in the P portion of the waveform. Surprisingly there is clearly less S wave produced in the shear prestressed medium than in the tension prestressed medium although the prestress levels were comparable when characterized by $(\sigma_r)_{\substack{\theta=\frac{\pi}{2} \\ r\to\infty}}$.

One of the anticipated problems in this research was that of extracting a possibly small dynamic field from a relatively larger static one. The preceding theoretical calculations suggest an approach analogous to the problem of determining the response of a vacuum tube from its characteristic curves. Figure 19 will make this clear. In this figure note the relationship between the principal stress difference $(\sigma_1 - \sigma_2)$, the maximum shearing stress $|\tau_m|$, the stress optic coefficient f_s, the fringe order number j, and the model thickness d. Both glass and Plexiglass, the principal model materials used in this experiment, have about the same value for f_s for monochromatic green illumination (5460 Å) taken to be 816 psi per fringe per inch for purposes of the following calculation. A family of straight lines, of slope $\frac{f_s}{2d}$ can obviously be drawn relating $|\tau_m|$ to j for various model thicknesses. The two members of this family used in the experiment, that is d = 1/8 in. and 1/16 in. are shown. Any particular value of the tension or shear prestress set in the model by the prestressing frame can be characterized by the $(\sigma_r)_{\substack{\theta=\frac{\pi}{2} \\ r\to\infty}}$ value it produces. This in turn can be characterized by a $(\tau_m)_{r\to\infty}$ value since for tension (or compression) and shear respectively

$$\left.\begin{array}{c} (\tau_m)_{r\to\infty} = \frac{1}{2}(\sigma_r)_{\substack{r\to\infty \\ \theta=\frac{\pi}{2}}} \\[2em] (\tau_m)_{r\to\infty} = (\sigma_r)_{\substack{r\to\infty \\ \theta=\frac{\pi}{2}}} \end{array}\right\} \tag{3}$$

Horizontal lines are drawn on figure 19 at $|\tau_m|_{r\to\infty}$ values for each shot as determined from equations 3. The numbers on these lines are the shot numbers, the letters G or P indicate whether

218

glass or Plexiglass was used and the letters T, C or S indicate whether the prestress type was tension, uniaxial compression or shear. The horizontal line corresponding to a particular prestress intersects the characteristic line at an operating point as indicated in figure 19. This point will correspond to a background fringe order which should agree with that seen in the high speed photographs at portions of each frame to which dynamic effects have not yet reached. At points reached by the wave the fringe order will rise or fall above or below the operating point along the characteristic line for the model thickness and material used so that the stresses corresponding to these fringe orders can be identified.

In white light slightly different considerations are required since a colored interference pattern is observed rather than the fringe pattern seen in monochromatic light. Tables are available which relate the subjective effect of color to the relative retardation R between two beams of recombined white light. The first two orders of this table are shown as the abscissa of figure 19 so that an observed color can be related to the retardation. The formulae in figure 19 show the retardation to be directly proportional to the product of the model thickness d and the maximum shearing stress $|\tau_m|$. The constant of proportionality c is independent of the wavelength of light used, but is not generally tabled. It can be readily determined from knowledge of the stress optic coefficient f_s at a particular wavelength. The values used for calculating the characteristic lines in figure 20 were $f_s = 816$ psi per fringe per inch and $\lambda = 5460$ Å. As in the preceding figure an operating point is determined by comparison of the prestress set into the model with the observed background color in the high speed photographic frames and color changes about this background give a roughly quantitative measure of the stress changes in the model.

CRACKING PHENOMENA

A prominent feature on all shots in glass was dynamic cracking. Figure 21 is a selection of six frames, separated by 8.32 microseconds, of a shot in 1 8 in. glass prestressed in tension such that $(\tau_r)_{2} = 118$ bars for r large. Note the distinct preference for crack directions orthogonal to the tensile axis, whereas in figure 3 where no prestress was used it is quite apparent that the cracks have no preferred direction but have a more or less random radial character. Observe the darkening of the optical field behind the crack tips, probably indicative of stress relaxation in the shattered region.

A number of features of figure 21 display rather clearly theoretical results predicted in earlier figures. Note the 45^0 separation between P and S wave isoclinics, and the spreading of the isoclinics where P and S overlap as predicted in figure 9. Observe the serration of the isoclinics, an effect which was anticipated on the basis of figure 13 and is due to the interaction between the dynamic and static fields.

Several writers indicate that a limiting velocity for the crack tip in brittle tensile fracture should exist regardless of the prestress conditions. Mansinha [4] gives this value as 0.631 the

219

transverse wave velocity in the medium. Dulaney and Brace [5] give the following relationship:

$$\dot{C} = V_t\left(1 - \frac{C_o}{C}\right) \tag{4}$$

where $\dot{C}$ is the crack velocity, C_o is the initial half crack length, C is the instantaneous half crack length and V_t is the limiting velocity given as 0.38 of the bar wave velocity for Poisson's ratio = 1 4. Broberg [6] predicts a limiting crack tip velocity equal to the Rayleigh wave velocity in the medium.

Figure 22 shows the limiting velocities discussed above as dotted lines while the observed crack velocities are plotted as closed circles, as a function of the prestress measured by $|\tau_m|_{r-c}$ as given from equation 3. The more intense the prestress the better defined was the observed slope of the crack tip time distance plots. Time distance plots of six prominent cracks in figure 22 showed velocity deviations from the mean of no greater than 4%. A very much larger range of velocities was observed at zero prestress as indicated in figure 21. At the higher prestress levels the observed velocities agreed very well with the limiting velocity predictions indicated by both Mansinha [4] and Dulaney and Brace [5], but deviations became more marked at lower stress levels. No agreement with Broberg was observed. There was no evidence for the curved time distance plots of crack tips which might be anticipated on the basis of equation 4. Cracks parallel to the tensile axis propagated much slower than those perpendicular to it. The observed crack velocities showed a convex upward increase with pre-stress. DeNoyer and Pollack [7] in their study of the cracking of glass plates in flexure also found the fracture velocity to increase with the available strain energy of the field into which the fracture was propagating. Since the boundary conditions under which these explosion generated cracks are produced are greatly different than the conditions considered in references [4], [5] and [6], the measure of agreement observed is probably more surprising than the disagreement.

220

REFERENCES

1. M. N. Toksoz, Radiation of Seismic Surface Waves from Underground Explosions, in VESIAC Rept. 7885-1-X, VESIAC, Willow Run Labs., Univ. of Michigan, Ann Arbor, Mich., 1967.

2. T. J. Ahrens, Stress Wave Propagation in a Prestressed Medium, Final Rept. on Contract AF 19(628)-6048, Document No. AFCRL-67-0529, 1967.

3. K. C. Thomson, A Study in Viscoelastic Wave Propagation by Photo-Viscoelasticity, D. Sci. Thesis T-1016, Colorado School of Mines, Golden, Colo., 1965.

4. L. Mansinha, "The Velocity of Shear Fracture," Bull. Seism. Soc. Am., Vol. 54, 1964, pp. 369-376.

5. E. N. Dulaney and W. F. Brace, "Velocity Behaviour of a Growing Crack," J. Appl. Phys., Vol. 31, 1960, pp. 2233-2236.

6. K. B. Broberg, "The Propagation of a Brittle Crack," Arkiv För Fysik, Vol. 18, 1960, pp. 159-192.

7. J. DeNoyer and H. Pollack, "Measurement of the Velocity of Crack Propagation in Glass Plates," Bull. Seism. Soc. Am., Vol. 53, 1963, pp. 87-93.
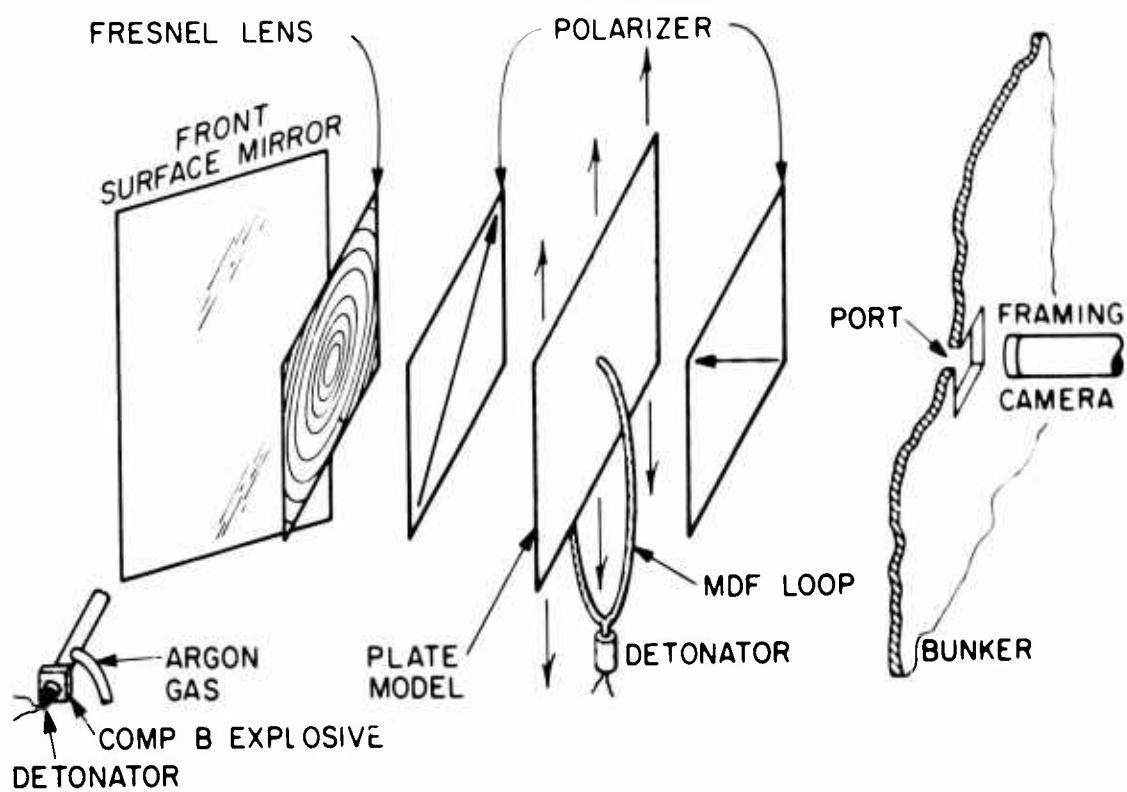
FIGURE 1. APPARATUS FOR THE STUDY OF STRESS WAVE PROPAGATION IN A PRE-STRESSED MEDIUM

222

FIGURE 2. PRESTRESSING FRAME

FIGURE 3. DYNAMIC LOADING OF UNSTRESSED GLASS AS SEEN IN CIRCULARLY POLAR-
IZED LIGHT

COORDINATE SYSTEM, PRINCIPAL STRESS DIRECTIONS AND MAXIMUM SHEARING STRESS

$$\phi = \frac{1}{2} \tan^{-1} \frac{2 \, \tau_{r\theta}}{\sigma_r - \sigma_\theta}$$
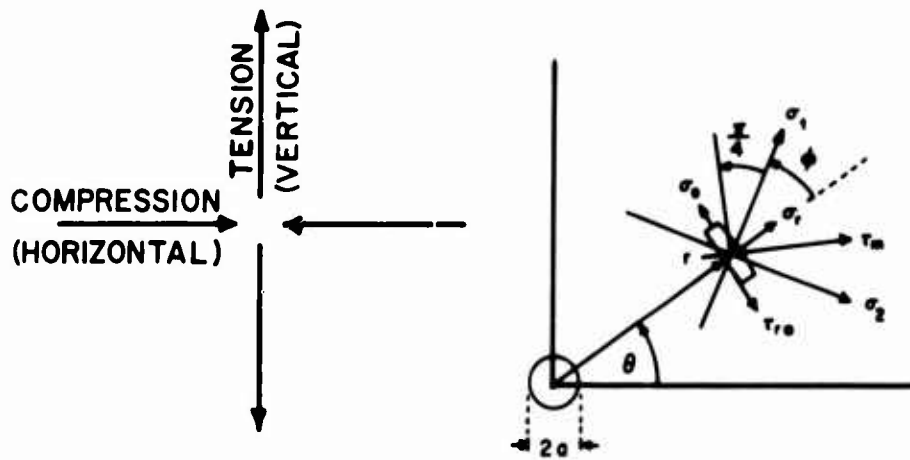
$$\tau_m = (\sigma_\theta - \sigma_r) \sin\left(\phi \pm \frac{\pi}{4}\right) \cos\left(\phi \pm \frac{\pi}{4}\right)$$
$$+ \tau_{r\theta} \left[\cos^2\left(\phi \pm \frac{\pi}{4}\right) - \sin^2\left(\phi \pm \frac{\pi}{4}\right) \right]$$

FIGURE 4. COORDINATE SYSTEM

225

DYNAMIC STRESS FIELDS

1. "P" WAVE

$$\sigma_r = \frac{A_P}{\sqrt{r}} \cdot F(r - c_P t)$$

$$\sigma_\bullet = \frac{\nu A_P}{\sqrt{r}} \cdot F(r - c_P t)$$

$$\tau_{r\bullet} = 0$$

2. "S" WAVE

$$\sigma_r = 0$$

$$\sigma_\bullet = 0$$

$$\tau_{r\bullet} = \frac{A_S}{\sqrt{r}} \cdot G(r - c_s t)$$

FIGURE 5. DYNAMIC STRESS FIELDS

226

TIME FUNCTIONS

P WAVE

If $\qquad -L_p \leqslant (r - c_p t) \leqslant 0$

then $\qquad F(r - c_p t) = \sin \dfrac{2\pi}{L_p} (r - c_p t)$

otherwise $\quad F(r - c_p t) = 0$

S WAVE

If $\qquad -L_s \leqslant (r - c_s t) \leqslant 0$

then $\qquad G(r - c_s t) = \sin \dfrac{2\pi}{L_s} (r - c_s t)$

otherwise $\quad G(r - c_s t) = 0$

FIGURE 6. TIME FUNCTIONS

227

STATIC FIELDS

TENSION AROUND A HOLE

$$\left(\frac{\sigma_r}{\sigma}\right) = \frac{1}{2}\left[1 - \left(\frac{a}{r}\right)^2\right] - \frac{1}{2}\left[1 - 4\left(\frac{a}{r}\right)^2 + 3\left(\frac{a}{r}\right)^4\right]\cos 2\theta$$

$$\left(\frac{\sigma_\theta}{\sigma}\right) = \frac{1}{2}\left[1 + \left(\frac{a}{r}\right)^2\right] + \frac{1}{2}\left[1 + 3\left(\frac{a}{r}\right)^4\right]\cos 2\theta$$

$$\left(\frac{\tau_{r\theta}}{\sigma}\right) = \frac{1}{2}\left[1 + 2\left(\frac{a}{r}\right)^2 - 3\left(\frac{a}{r}\right)^4\right]\sin 2\theta$$

SHEAR AROUND A HOLE

$$\left(\frac{\sigma_r}{\sigma}\right) = -\left[1 - 4\left(\frac{a}{r}\right)^2 + 3\left(\frac{a}{r}\right)^4\right]\cos 2\theta$$

$$\left(\frac{\sigma_\theta}{\sigma}\right) = \left[1 + 3\left(\frac{a}{r}\right)^4\right]\cos 2\theta$$

$$\left(\frac{\tau_{r\theta}}{\sigma}\right) = \left[1 + 2\left(\frac{a}{r}\right)^2 - 3\left(\frac{a}{r}\right)^4\right]\sin 2\theta$$

FIGURE 7. STATIC FIELDS

228

ISOCHROMATICS OF A P AND S WAVE
PROPAGATING FROM A COMMON SOURCE
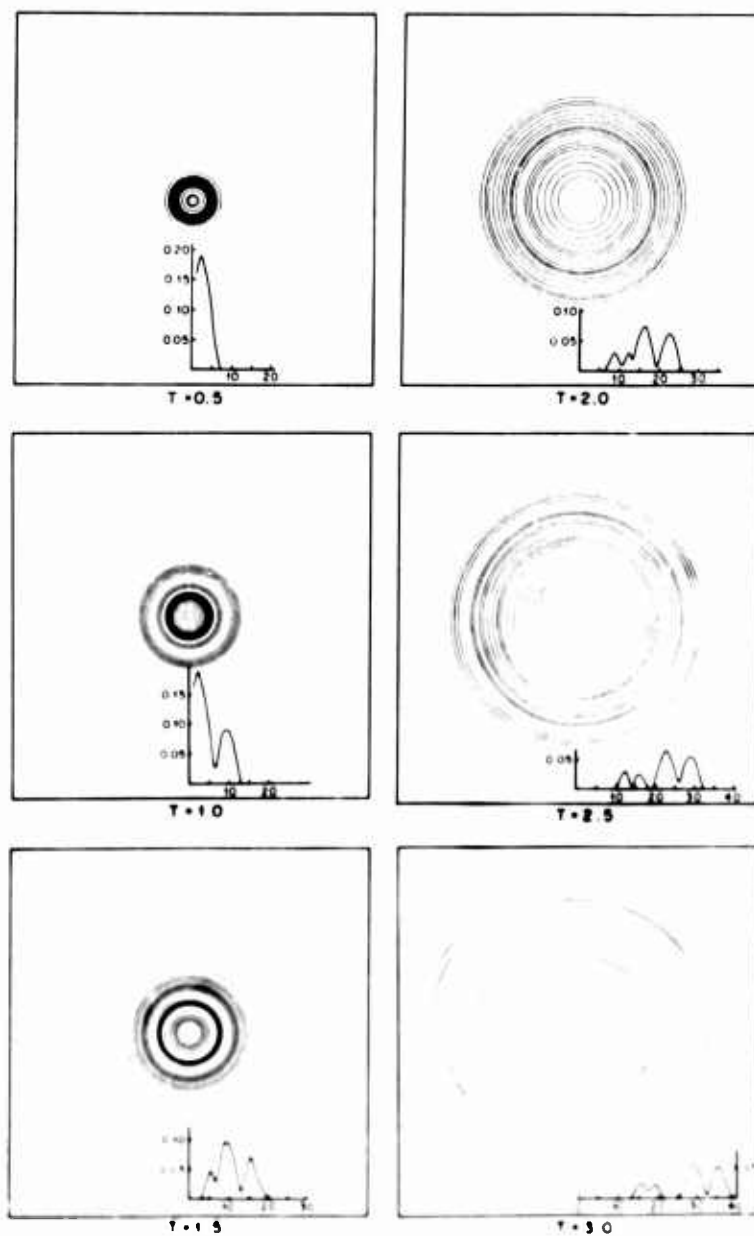
FIGURE 8. ISOCHROMATICS OF A P AND S WAVE PROPAGATING FROM A COMMON
SOURCE

ISOCLINICS OF A P AND S WAVE PROPAGATING FROM A COMMON SOURCE
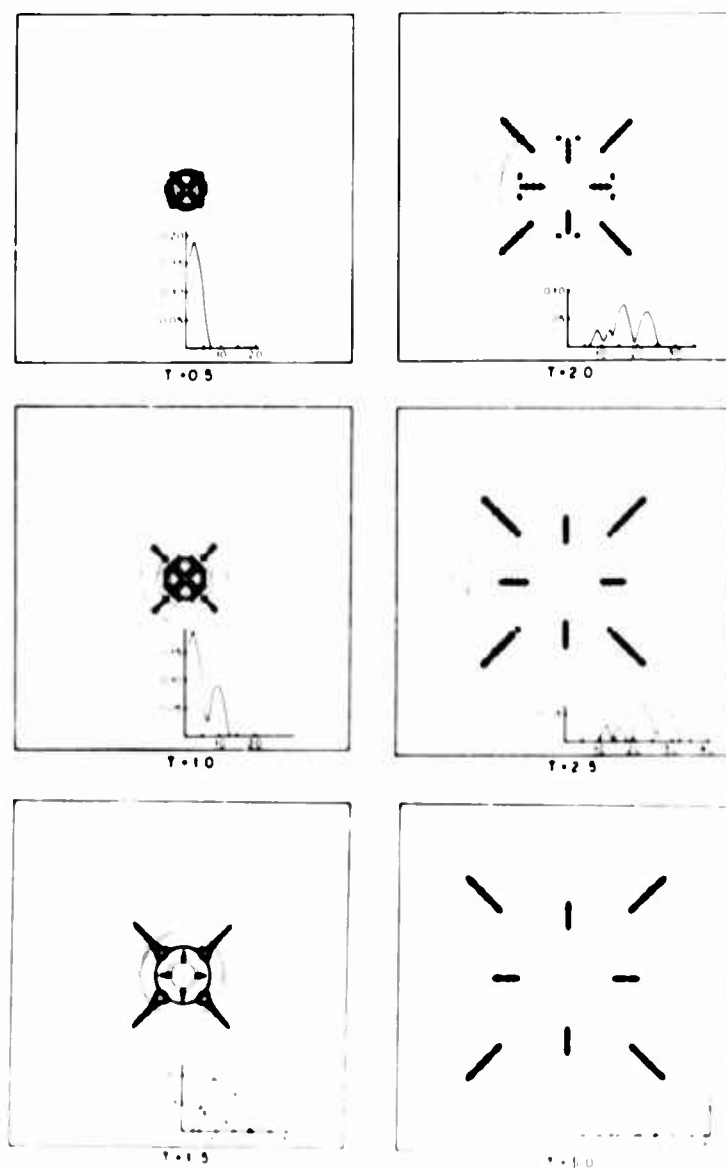
FIGURE 9. ISOCLINICS OF A P AND S WAVE PROPAGATING FROM A COMMON SOURCE
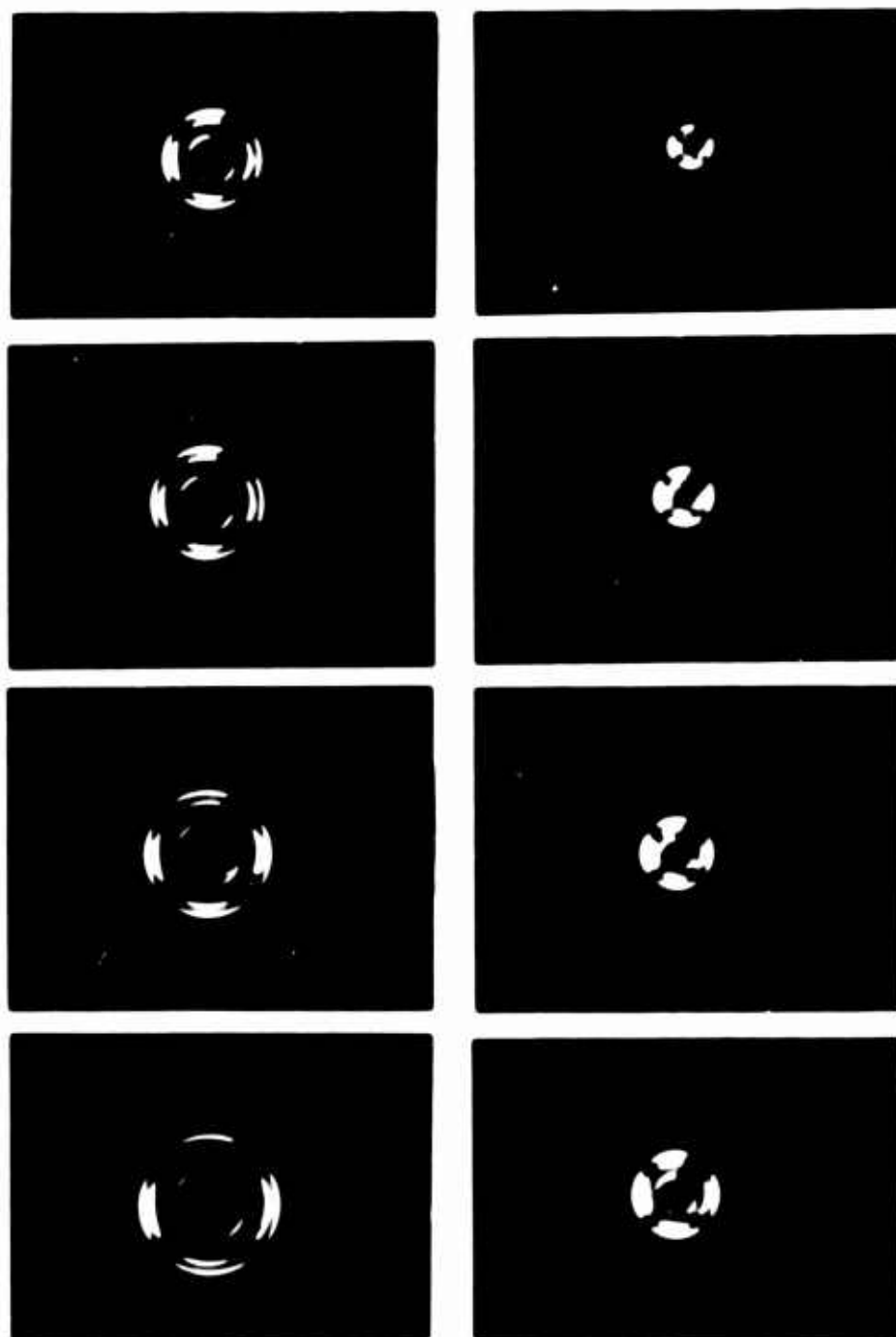
FIGURE 10. FRAMING CAMERA SEQUENCE IN UNSTRESSED PLEXIGLASS USING PLANE POLARIZED LIGHT

RADIALLY SPREADING P WAVE PROPAGATING
IN A MEDIUM STRESSED IN TENSION
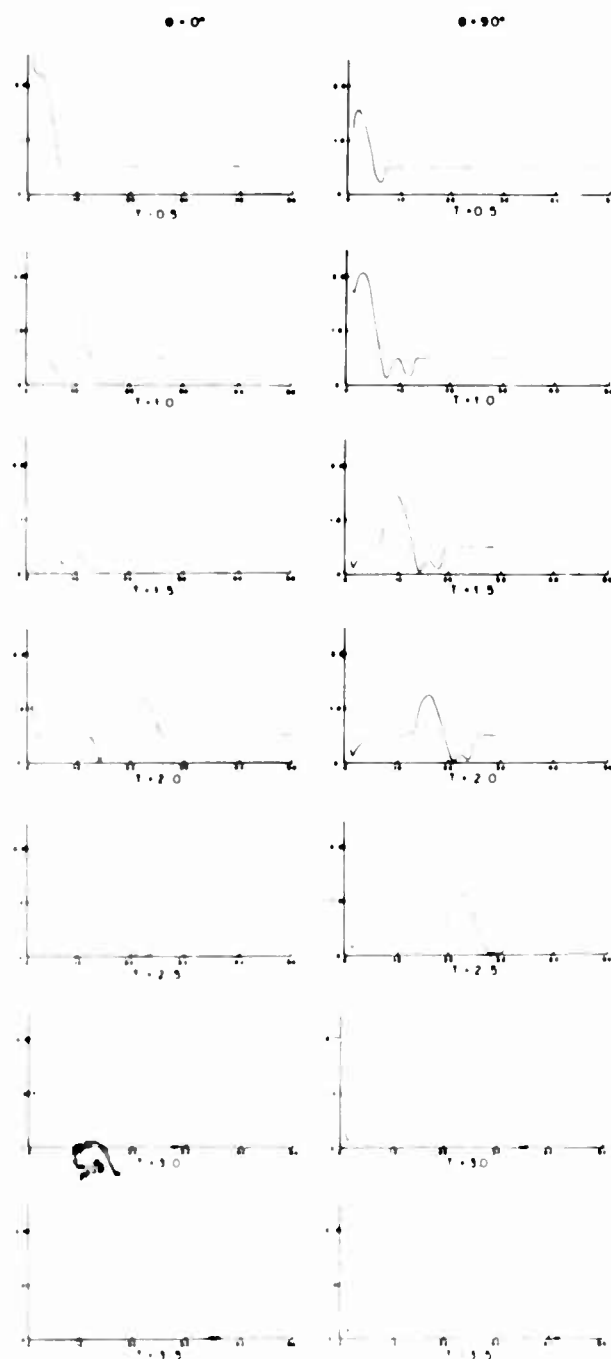
FIGURE 11. RADIALLY SPREADING P WAVE PROPAGATING IN A MEDIUM STRESSED IN
TENSION

232

RADIALLY SPREADING P WAVE PROPAGATING
IN A MEDIUM STRESSED IN TENSION,
AT TWO AMPLITUDE LEVELS
Θ = 90°
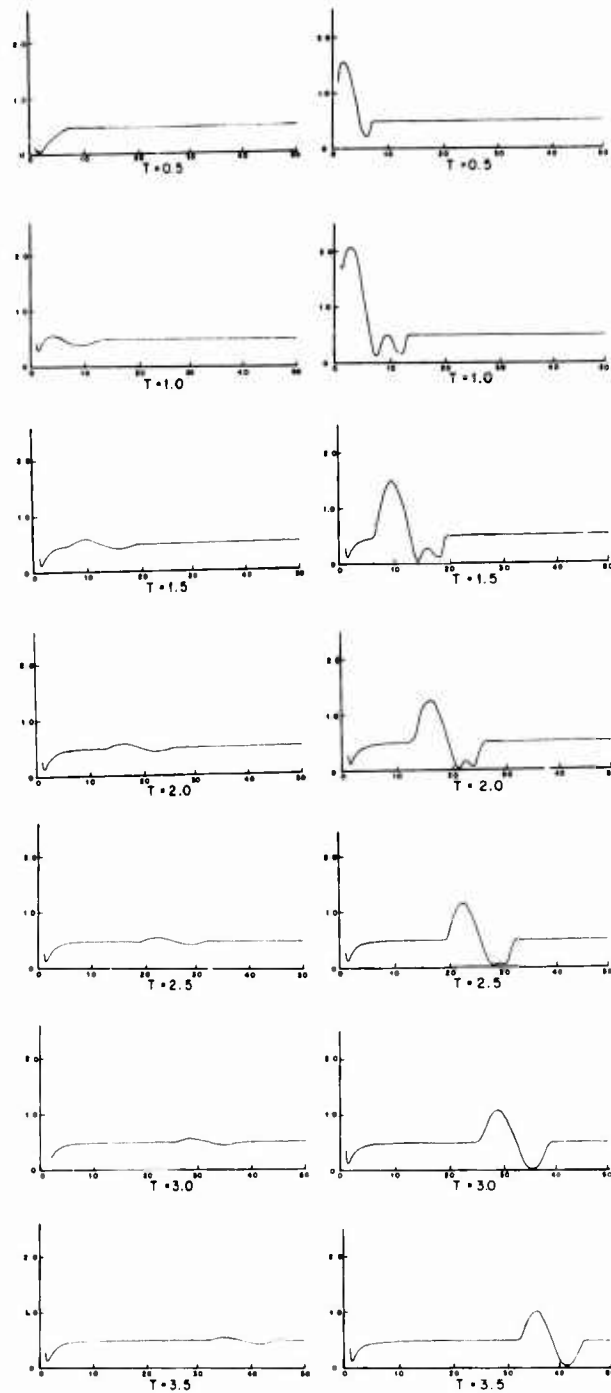
FIGURE 12. RADIALLY SPREADING P WAVE PROPAGATING IN A MEDIUM STRESSED IN
TENSION AT TWO AMPLITUDE LEVELS

233

MAXIMUM SHEARING STRESS FOR P AND S WAVE PROPAGATING IN A MEDIUM PRESTRESSED IN TENSION.

$A_p = -10$ $A_s = 10$ $T = 2.0$
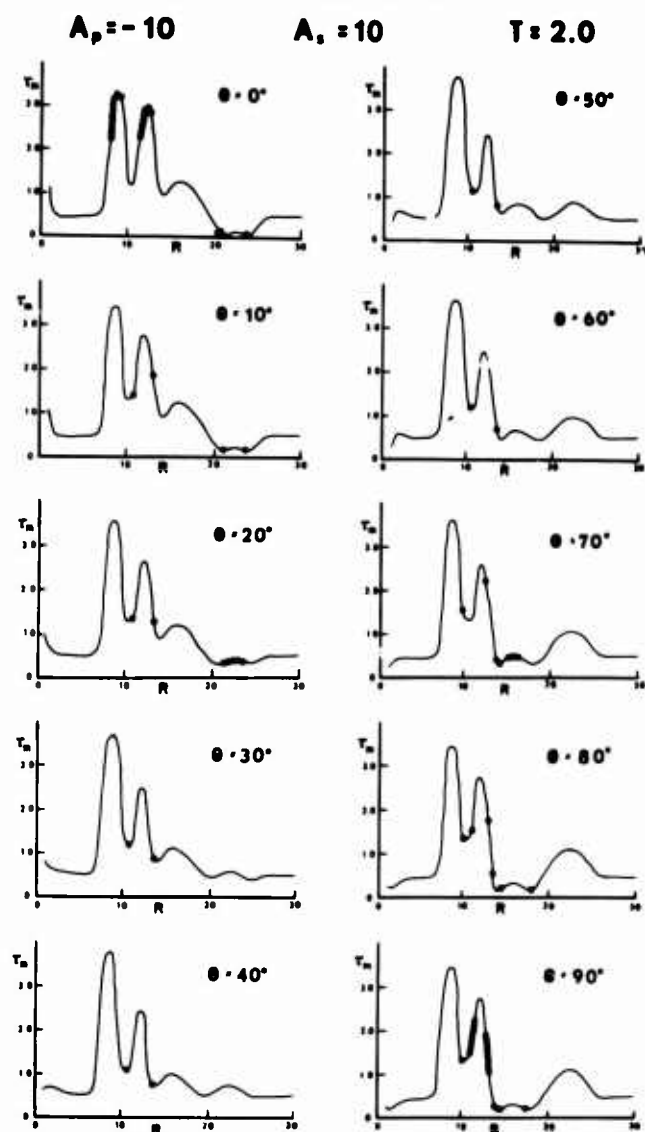
FIGURE 13. MAXIMUM SHEARING STRESS FOR P AND S WAVES PROPAGATING IN A MEDIUM PRESTRESSED IN TENSION

Θ + Φ FOR P AND S WAVES PROPAGATING IN A MEDIUM STRESSED IN TENSION.
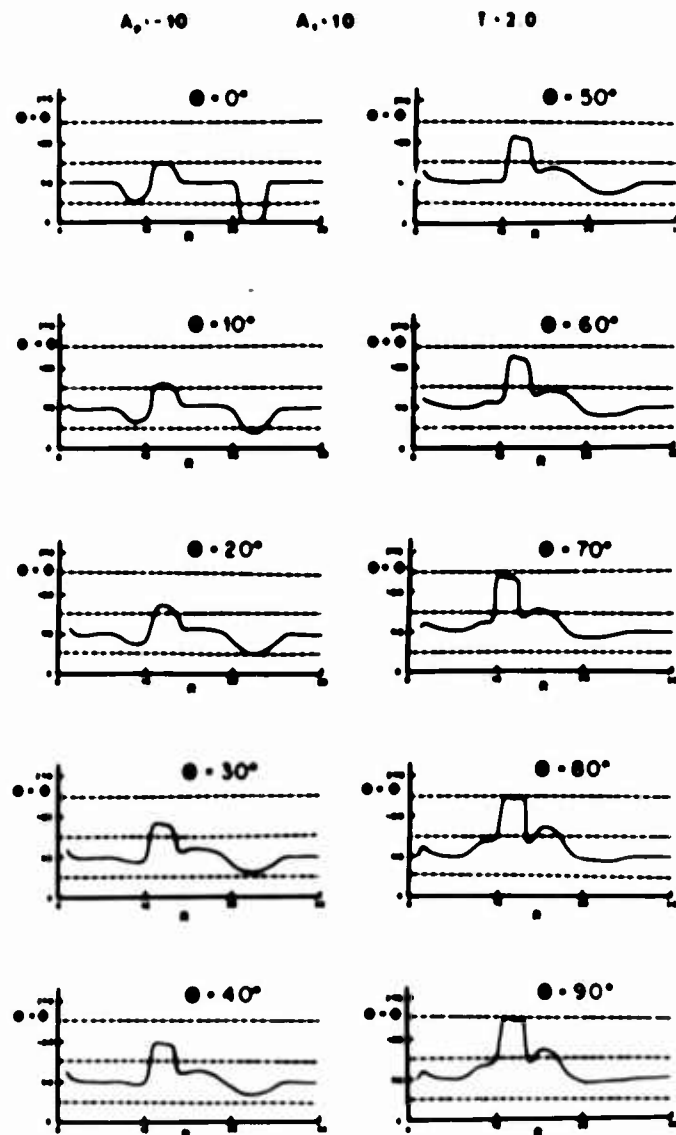
FIGURE 14. Θ + Φ FOR P AND S WAVES PROPAGATING IN A MEDIUM STRESSED IN TENSION

EFFECT OF P AND S AMPLITUDE VARIATION ON τ_m AND $\theta + \phi$ FOR A MEDIUM STRESSED IN TENSION.

T = 2.0 $\theta = 0°$

$A_p = 10$ $A_s = 1.0$

$A_p = -10$, $A_s = 10$

$A_p = -100$, $A_s = 100$
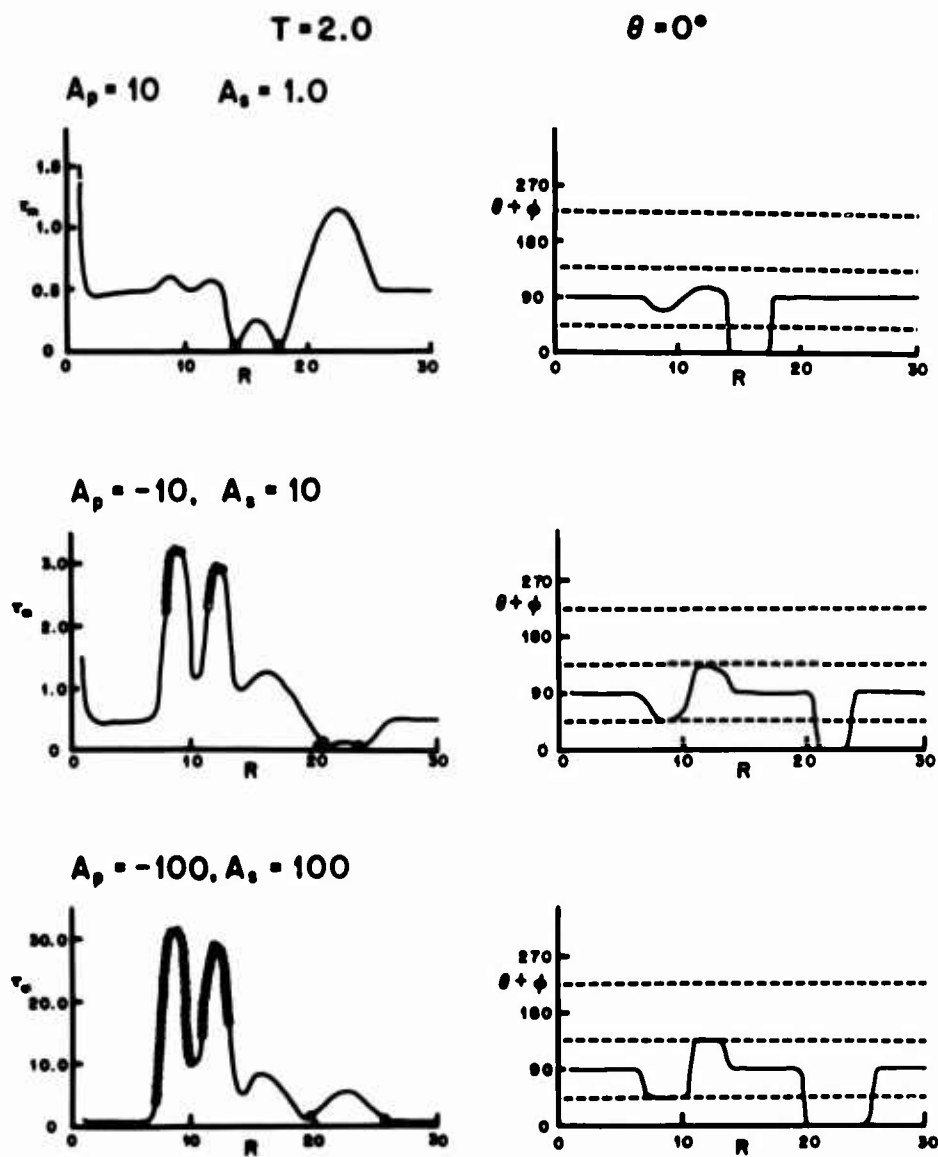
FIGURE 15. EFFECT OF P AND S AMPLITUDE VARIATION ON τ_m AND $\theta + \phi$ FOR A MEDIUM STRESSED IN TENSION

P WAVE PROPAGATING IN A MEDIUM
PRE STRESSED IN SHEAR
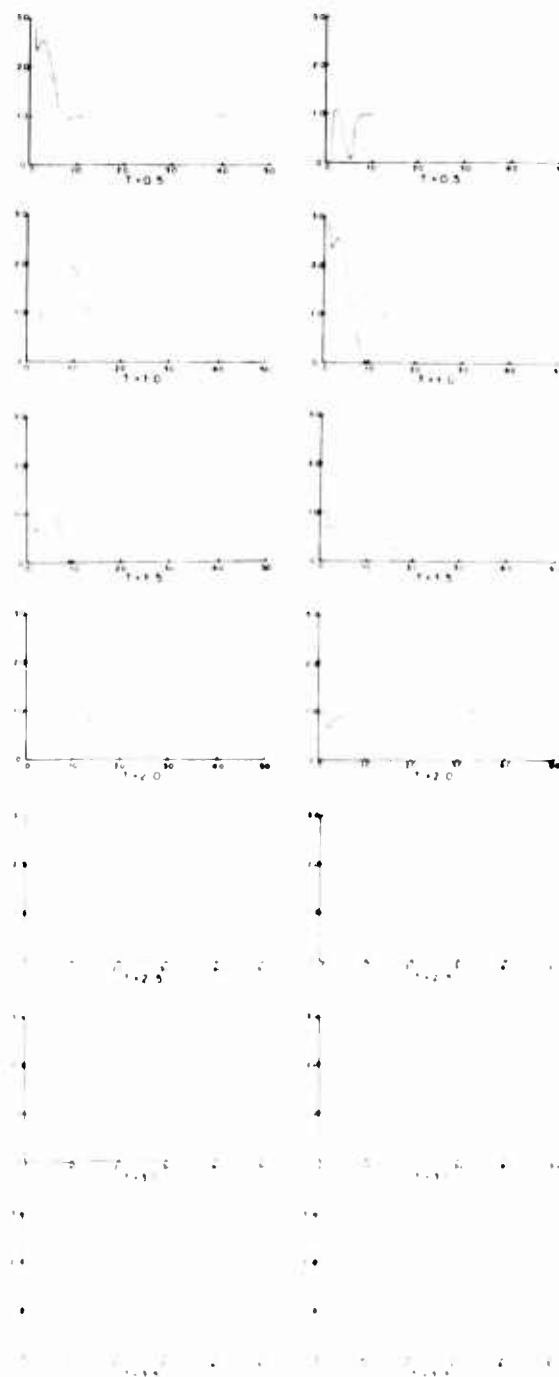
FIGURE 16. P WAVE PROPAGATING IN A MEDIUM PRESTRESSED IN SHEAR

237

ISOCHROMATICS FOR P WAVE + S WAVE + VARIOUS STATIC FIELDS
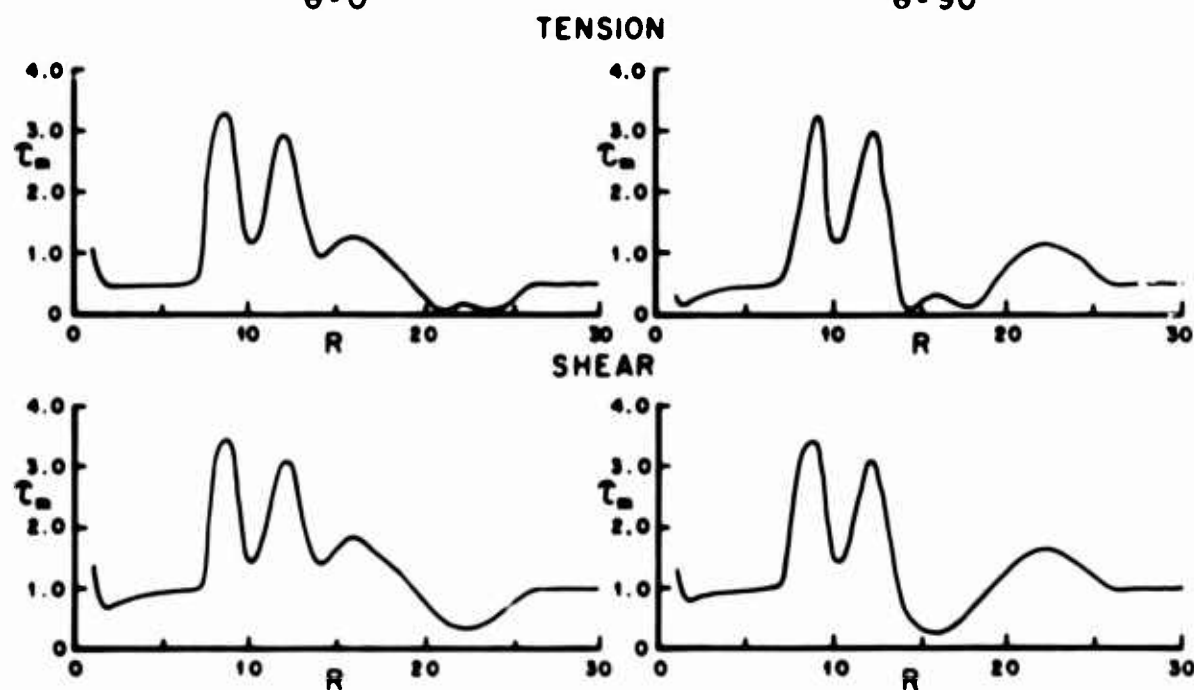
FIGURE 17. ISOCHROMATICS FOR P AND S IN TWO TYPES OF PRESTRESS FIELDS

FIGURE 18. FRAMING CAMERA SEQUENCE OF A SHOT IN SHEAR STRESSED PLEXIGLASS
USING PLANE POLARIZED LIGHT
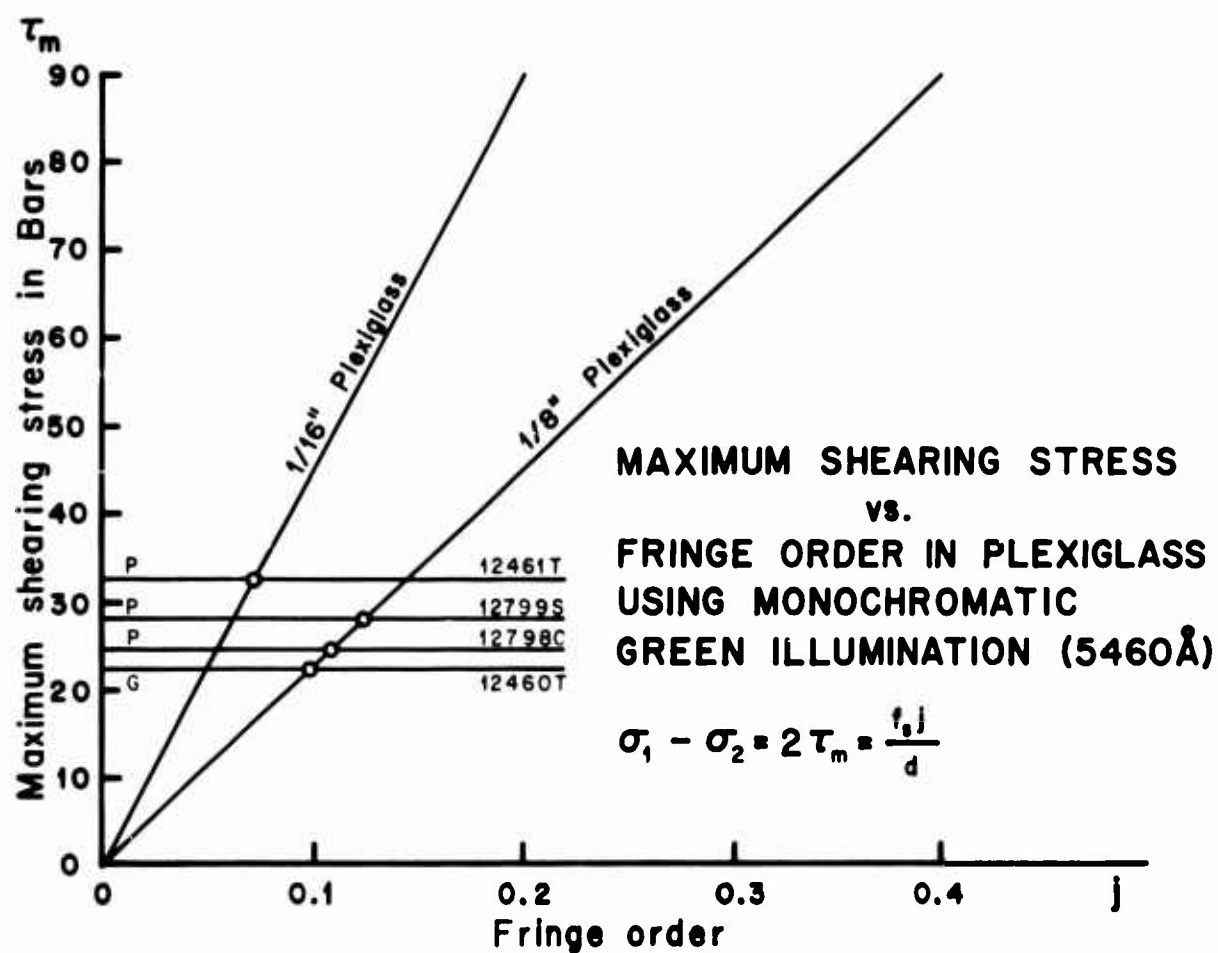
FIGURE 19. MAXIMUM SHEARING STRESS vs. FRINGE ORDER

240
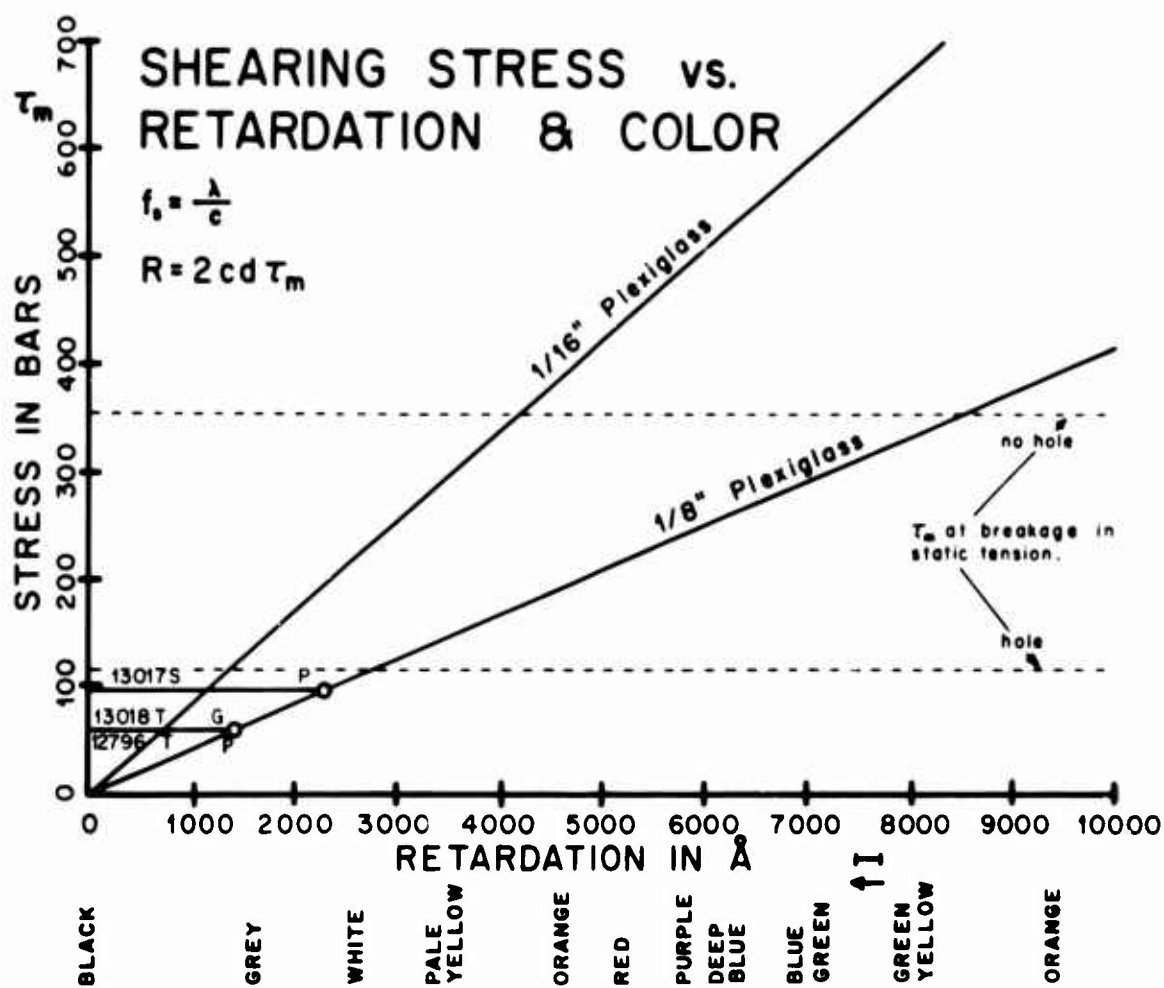
FIGURE 20. MAXIMUM SHEARING STRESS vs. RETARDATION AND COLOR
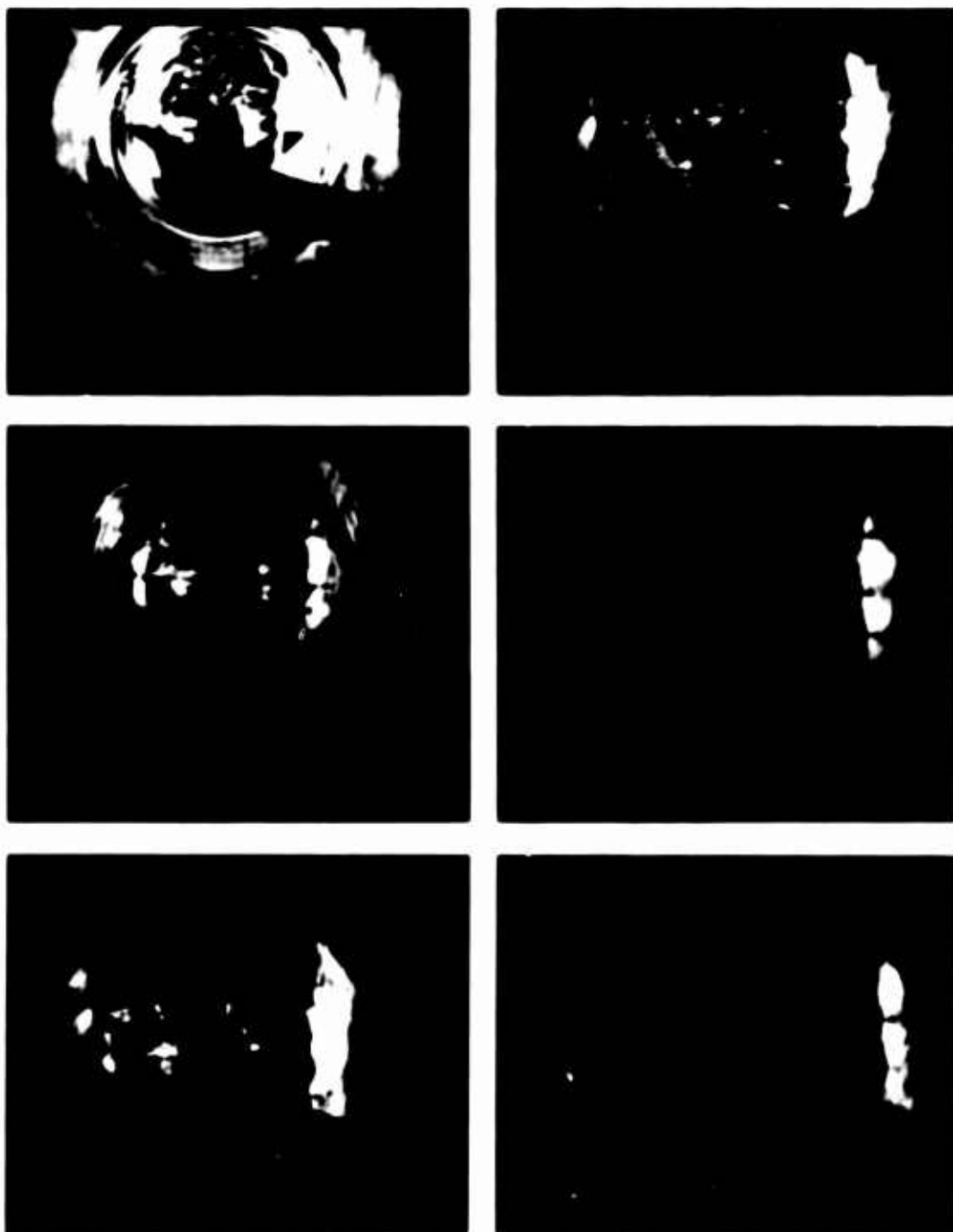
FIGURE 21. FRAMING CAMERA SEQUENCE IN TENSION STRESSED GLASS USING PLANE POLARIZED LIGHT
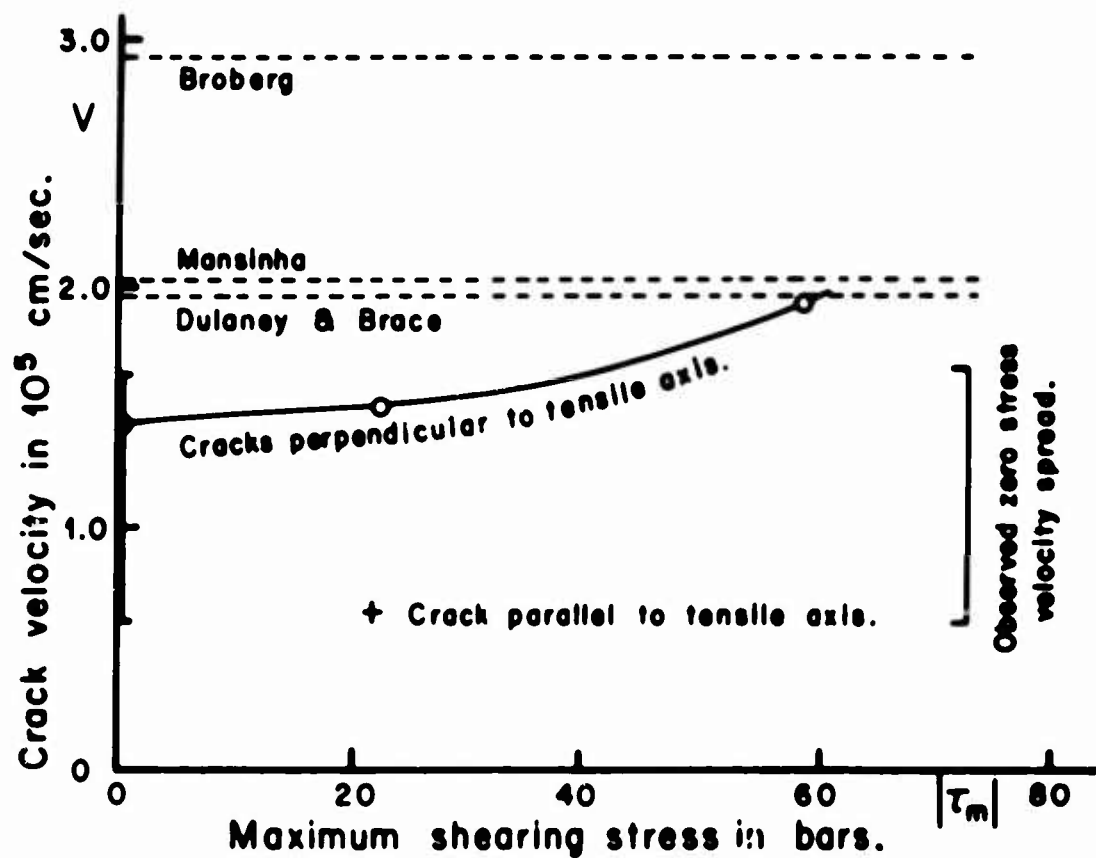
FIGURE 22. CRACK VELOCITY vs. TENSILE PRESTRESS

10
HIGH PRESSURE DATA AND EARTHQUAKE MECHANISMS

R. E. Riecker
Air Force Cambridge Research Laboratories
L. G. Hanscom Field
Bedford, Mass.

SUMMARY

Since 1961, we have performed experimental rock deformation tests on deep crust and upper mantle rock-forming minerals under geophysically realistic conditions of very high temperature and pressure in order to learn more about the earthquake source mechanism. Our objectives included determination of the mechanical properties, modes of deformation and polymorphism for enstatite, olivine, plagioclase feldspar, diopside, garnet, a suite of NTS rock samples, and several other minerals and rocks. We performed the tests in a high pressure opposed anvil shear apparatus, a Birch-type shear squeezer, a 20-kb constant strain-rate solid-pressure-medium device, and a large tetrahedral press. Maximum simultaneous conditions achieved were 100 kb and $1000^{\circ}C$ with strain rate variation from $10^{1}/sec$ to $10^{-8}/sec$.

Two significant results have application to the source mechanism problem. We have observed dehydration weakening in olivine associated with minor amounts of hydrous serpentine, in serpentine, and in NTS tuffs. The dehydration gives rise to increased pore pressure which reduces the effective confining pressure and therefore lowers rock strength (Riecker and Rooney, [1]; Riecker and Rooney, [2]). Dehydration weakening may be an important process in causing otherwise strong crust and mantle rocks to yield to low stresses. The weakening noted in NTS tuffs from the Rainier Mesa is of importance near the shot point of underground nuclear explosions in tuff, where the ambient temperature rises above the dehydration temperature of clinoptilolite (200-$300^{\circ}C$).

Studies on the mechanical behavior of enstatite reveal a possible earthquake source mechanism. Under small shear stresses applied for short duration (as little as one second) orthorhombic enstatite inverts to monoclinic clinoenstatite with a small reduction in volume. This highly shear sensitive reaction can produce moderate seismic energy, and runs rapidly enough to be considered as one possible source mechanism in the mantle (Riecker and Rooney, [3]).

Our research program in rock mechanics continues with emphasis on improving understanding of the seismic source mechanism. Special attention is directed toward study of dehydration weakening in other hydrous rockforming mineral groups, such as the important mantle mineral group amphiboles, and toward a search for additional potential seismic sources as suggested by anomalous mechanical behavior at high pressure and temperature.

REFERENCES

1. R. E. Riecker and T. P. Rooney, "Weakening of Dunite by Serpentine Dehydration," *Science*, Vol. 152, 1966, pp. 196-198.

2. R. E. Riecker and T. P. Rooney, "Shear Strength and Weakening of Zeolitized Tuffs From the Nevada Test Site, Nevada," *Am. Mineralogist*, Vol. 52, 1967, pp. 1174-1178.

3. R. E. Riecker and T. P. Rooney, "Deformation and Polymorphism of Enstatite Under Shear Stress," *Bull. Geol. Soc. Am.*, Vol. 78, 1967, pp. 1045-1054.

11
INELASTIC DEFORMATION OF ROCK

John Handin
Center for Tectonophysics
Texas A&M University

ABSTRACT

When the deformations are inelastic, solutions to problems in rock mechanics
are most difficult and can seldom be exact for the following reasons. 1) The mate-
rial is structurally and compositionally complicated, and is never ideally and rare-
ly even statistically homogeneous and isotropic, especially in domains of a few
cubic meters or more. 2) The mechanical equation of state of even a uniform ele-
ment of rock depends at least upon the states of stress and strain, their time deriv-
atives, and temperature. 3) When one attempts to describe the deformations at all
realistically, the solutions very soon become mathematically intractable.

This is not meant to imply that we should not try to obtain meaningful solutions.
Thus when the rock is in the brittle state and fails wholly or even predominantly by
shear fracture, we can use the Coulomb-Mohr criterion of internal friction with an
uncertainty that is probably small relative to the many other simplifying assump-
tions necessarily introduced into a typical problem. On the other extreme, when
the rock is fully ductile, we can use the Mises criterion of ideal plasticity. How-
ever, the uncertainty is larger because we have ignored the strain hardening and
time dependence of yield stress of real rocks. Furthermore, at the relatively low
temperatures and mean pressures of the transition between the hydrodynamic and
elastic zones associated with a nuclear explosion, the deformational behavior of
most rocks is neither purely brittle nor fully ductile. Our knowledge of what hap-
pens here is entirely empirical and still highly limited. Predictions should be
fashioned with caution.

THE INELASTIC DEFORMATION OF ROCK

John Handin
Center for Tectonophysics
Texas A&M University
College Station, Texas

When the deformations are inelastic, solutions to problems in rock mechanics are most difficult and they can seldom be exact. To help assess the uncertainties, let us refer to figure 1 which was designed to outline the rationale of tectonophysics, but which applies at least in part to any boundary-value problem in rock mechanics, including that of the inelastic deformation of the shell around a cavity in which a nuclear device is detonated.

Suppose we were asked to derive the deformation associated with a geologic structure — a fault or a fold — from the first principles of mechanics. Beginning in the upper right corner with the causative body and surface forces acting on an element of the earth's crust, we would follow the ideal path along the solid lines. We could specify these forces if we fully understood the energetics of the problem, that is if we knew the detailed thermal history of the earth. We would then prescribe the boundary conditions in terms of stresses, displacements, their time derivatives, or some combination of them. Unfortunately, the origin of tectonic forces and the proper natural boundary conditions are in fact conjectural with rare and relatively trivial exceptions. On the other hand, our procedure with respect to the seismic coupling problem would be straight forward so far. The energy source is well known, and the boundary conditions are simple.

If any problem involving the failure or potential failure of rock — earthquake prediction, seismic coupling of explosions, stability of underground openings, and many more — the next step is the most difficult. We must select the proper equation of state to connect the stress and strain or strain rate tensors. If our material were ideal, we could choose a relatively simple fracture criterion for the brittle state or rheological "law" for the ductile state and then solve for the stress and strain fields in space and time. But our material is rock. It is structurally and compositionally complicated, and it is never ideally and rarely even statistically homogeneous and isotropic, especially in domains of a few cubic meters or more. The deformation mechanism — fracture, faulting, or flow — is determined by the mineral content and fabric of the rock, together with the rate of strain and the natural environmental factors of effective confining pressure and temperature. The pressure tends to increase ultimate strength and ductility. Decreasing the strain rate or increasing the temperature tend to lower the strength but to enhance the ductility.

The equation of state is in turn intimately related to the deformation mechanism, and so we face a bewildering complexity. The equation properly describing the behavior of even a uniform element of our real material depends at least on the state of stress, the state of strain (because of strain hardening and softening) the rate of deformation, and temperature. And even if we could choose a realistic and general equation, the solution to our problem would very soon become mathematically intractable.

In tectonics we can directly observe only the state of general strain at the present instant of geologic time. All else is a matter of inference as indicated by the broken lines. Having inferred the initial undeformed state of the rock, we can determine the permanent deformation from laboratory and field studies of certain fabric elements, and from in situ stored strain measurements we can determine what remains of the recoverable viscoelastic deformation (not reformation). Stratigraphic and radiometric dating can enhance our knowledge of the kinematics of the deformation, even so we can only rarely work out the path from the initial to the final (present) states.

From the results of laboratory experiments simulating the natural environment as realistically as possible and reckoning favorably with the facts of nature, we can connect many fabric elements with the directions and relative (if not absolute) magnitudes of the principal stresses, with temperature, and less frequently with strain rate. This allows us to work part of the problem backwards, as currently we must, if we hope to improve our understanding of the dynamics. Our inferences about the environment and the nature of the rock at the time of deformation are reasonably good. But our estimates of the boundary conditions and of the proper equation of state are not at all adequate.

Somewhat similar attempts have been made to solve the coupling problem. That is to say, the coefficient of internal friction in the Coulomb yield condition has been calculated on the basis of measured close-in displacements. The values derived for granite (of the order of 0.1) are unbelievably low.

As an example let us consider the failure of limestone. Figure 2 shows a plot of the octahedral shear stress as a function of the mean pressure at the ultimate strength of Solenhofen limestone in compression ($\sigma_1 > \sigma_2 = \sigma_3$), extension ($\sigma_3 < \sigma_1 = \sigma_2$), and torsion ($\sigma_1 > \sigma_2 > \sigma_3$), compressive stresses counted positive. We ignore the curve for twisted solid cylinders since the stresses are not uniform. The stresses are, however, nearly uniform in the twisted thin-walled hollow cylinders, and we can legitimately compare the results those from compression and extension tests on solid cylinders. We note that the failure curves are not the same for different states of stress. We also note the typical increases of strength and ductility with mean pressure as the curves become non-linear. The three Mohr envelopes are not the same either, of course, though at room temperature the differences are not large.

In compression, failure is by shear fracturing or faulting below the brittle-ductile transition at 2.7 kb, and by "plastic" flow (intracrystalline slip) above this transition. To mean

249

pressures of the order of 3 kb, the failure mechanism in both extension and torsion is tensile fracturing, and the tensile strength of about 0.15 kb is essentially constant and independent of mean pressure. Between 3 kb and the brittle-ductile transitions of 4.0 kb in torsion and 5.4 kb in extension, failure is due to shear fracturing. Above these transitions uniform flow again occurs, and all three curves tend to approach about the same constant value of octahedral shear stress.

Figure 3 shows how the stress state, the temperature, and the strain rate affect the brittle-ductile transition. The transition confining pressure is highest in extension ($\sigma_3 < \sigma_1 = \sigma_2$) and lowest in compression ($\sigma_1 > \sigma_2 = \sigma_3$). It lies about midway in the torsion range where the relative magnitude of σ_2 is midway between the extremes, $\sigma_2 = \sigma_3$ and $\sigma_2 = \sigma_1$. In all three types of test, lowering the strain rate and raising the temperature reduce the transition pressures. The state of stress associated with an explosion in a spherical underground cavity is probably analogous to that of the compression test, since the radial compressive stress is greatest (σ_1), and the equal tangential principal stress are least ($\sigma_2 = \sigma_3$).

Our discussion of the difficulties of rock mechanics problems is not meant to imply that we should not try to obtain meaningful solutions. Indeed we must try. And whereas we can now solve very few problems of natural rock deformation because we know too little about the tectonic forces, the boundary conditions, and the proper equation of state, solutions of the coupling problem are far from hopeless.

In the transitional region between the hydrodynamic and elastic zones associated with a nuclear explosion, the temperatures and mean pressures are relatively low and the strain rates are intermediate (about 1 to 100 per second). Under these conditions we can expect the constituents of many earth materials to be in the brittle state and failure to be predominantly by shear fracture, faulting, or cataclastic (triboplastic) flow. For most crystalline igneous and metamorphic rocks, dolomite, sandstone, and well indurated shale, we can probably use the Coulomb-Mohr criterion of internal friction with an uncertainty that is small relative to the other simplifying assumptions necessarily introduced into a typical problem, especially the assumptions of homogeneity and isotropy. Unconsolidated materials like alluvium possess internal friction, but of course no cohesive strength.

On the other extreme, when the rock is fully ductile, we can use the Mises criterion of ideal plasticity as figure 2 suggests. The uncertainty is larger because we have ignored the strain hardening of real rocks and because yield stresses have not yet been measured at the appropriate strain rates. Salt, limestone, soft argillaceous shale and kerogenous shale will probably be ductile at mean pressures of the order of a kilobar, but their brittle-ductile transitions remain to be determined at the relevant strain rates.

At Texas A&M we are preparing to investigate the effects of strain rate in the spectrum of 10^{-2} to 10^2 per second on rocks under confining pressures to 8 kb. Also of concern are the effects of stress differences of a few kilobars acting for a few milliseconds. The input to the

seismic coupling problem is the more or less steady pressure acting on the wall of the cavity after the initial reverberation; the spike is ignored (figure 4). This is legitimate because the earth is an efficient low-pass filter, and the high frequencies are not observed in the teleseismic signal. However, we do not know whether or not the transient peak stress of a few milliseconds duration modifies the mechanical properties of the rock. This we will try to determine in high-speed triaxial compression tests.

With regard to the seismic coupling problem, then, our knowledge of the properties of intact rocks is adequate, or soon will be. Our most pressing need in this or any other problem in rock mechanics is the better understanding of the influence of defects on the behavior of large masses of rock. In particular, jointing is nearly ubiquitous in the shallow crust. Natural fractures affect compressibility and may represent discontinuities in the displacement field.

Essentially all our knowledge of rock deformation comes from laboratory experiments and a few prototype tests, and it is almost wholly empirical. Our understanding of the physics of flow and fracture is now woefully inadequate. Thus extrapolations to untested conditions must still be fashioned with caution.

REFERENCES

1. J. Handin, H. C. Heard and J. N. Magouirk, "Effects of the Intermediate Principal Stress on the Failure of Limestone, Dolomite, and Glass at Different Temperatures and Strain Rates," J. Geophys. Res., Vol. 72, 1967, pp. 611-640.

2. A. L. Latter, E. A. Martinelli, J. Mathews and W. G. McMillan, "The Effect of Plasticity on Decoupling of Underground Explosions," J. Geophys. Res., Vol. 66, 1966, pp. 2929-2936.

BIBLIOGRAPHY

Clark, S. P., Jr., ed., Handbook of Physical Constants, Revised Edition, Geol. Soc. America Mem. 97, New York, 1966.

Griggs, D. and J. Handin, eds., Rock Deformation, Geol. Soc. America Mem. 79, New York, 1960.

Judd, W. R., ed., International Conference on State of Stress in Earth's Crust, Elsevier, New York, 1964.

Riecker, R. E., ed., NSF Advanced Science Seminar in Rock Mechanics, Special Rept., Air Force Cambridge Research Lab., Bedford, Mass., 1968.
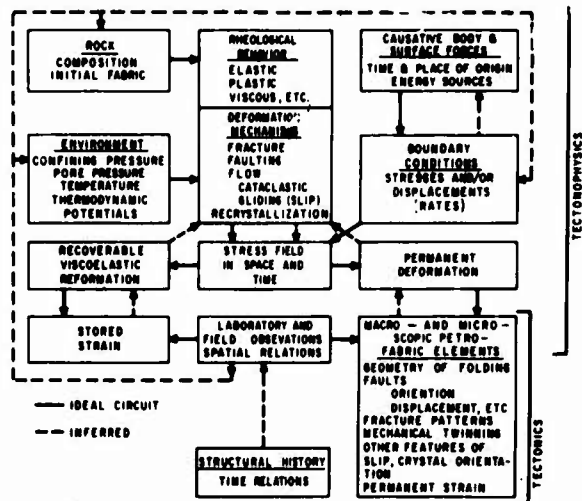
FIGURE 1.
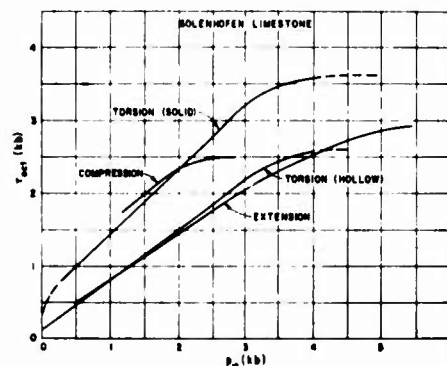
FIGURE 2. OCTAHEDRAL SHEAR
STRESS — MEAN PRESSURE RE-
LATIONS FOR FAILURE OF SOLEN-
HOFEN LIMESTONE IN COMPRES-
SION, EXTENSION, AND TORSION
AT 25°C AND STRAIN OF 10^{-4} PER
SECOND (AFTER HANDIN, ET AL., [1],
FIGURE 15)
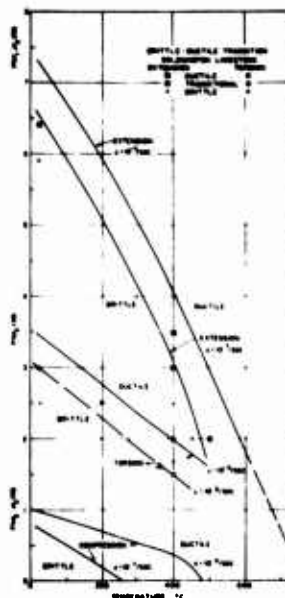
FIGURE 3. CONFINING
PRESSURE VERSUS TEM-
PERATURE OF THE
BRITTLE-DUCTILE TRAN-
SITION OF SOLENHOFEN
LIMESTONE IN COMPRES-
SION, EXTENSION, AND
TORSION AT DIFFERENT
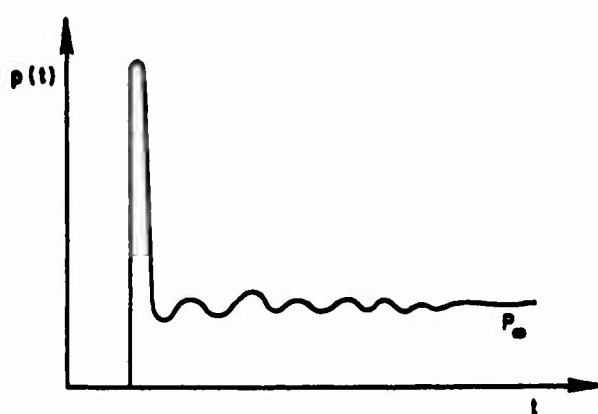STRAIN RATES (AFTER
HANDIN, ET AL., [1],
FIGURE 20)

FIGURE 4. PRESSURE VERSUS TIME ON
WALL OF CAVITY CONTAINING A NUCLEAR
EXPLOSION (AFTER LATTER, ET AL., [2],
FIGURE 5)

12
STRESS WAVE CALCULATIONS AND ROCK MECHANICS RESEARCH AT LRL[*]

J. T. Cherry
Lawrence Radiation Laboratory
University of California
Livermore, California

ABSTRACT

In this paper we present the current status of rock mechanics research at LRL, how this effort influences the equation of state of a medium and how this equation of state effects the decoupling process.

The rock mechanics effort has been directed primarily towards obtaining the medium compressibility and strength. There is some indication that the Hugoniot Elastic Limit obtained from shock wave data may also be obtained from static strength measurements.

The hydrostatic compressibility data, both loading and unloading, are used for the pressure-volume relation below 40 kb. Above 40 kb Hugoniot measurements are used to complete the P-V portion of the equation of state. Failure data obtained from three types of static strength tests have led to a failure criteria that combines both "shear" and "tension" failure into a single invariant expression. In functional form the failure surface is given by

$$Y = F(P_m)$$

where Pm is the mean stress and

$$Y = \frac{3}{4}\left[(3 I_{2D})^{\frac{1}{2}} + \frac{I_3}{|I_3|}\left(\frac{|I_{3D}|}{2}\right)^{1/3}\right]$$

The functional relation is established from laboratory strength tests.

Calculations are presented which show the effect of strength and compressibility on decoupling.

ROCK MECHANICS RESEARCH AND CODE CALCULATIONS AT L.R.L.

J. T. Cherry
Lawrence Radiation Laboratory
University of California
Livermore, California

INTRODUCTION

A minimum requirement needed to calculate the extent of fracturing produced by an explosive source is the "strength" of the medium as a function of the state of stress. In this paper we present a failure law in terms of stress invariants that seems to adequately predict the onset of failure in a number of brittle materials. We then use this failure criteria to calculate the extent of cracking from the HARDHAT (5 kt, 290 m deep, granite), HANDCAR (12 kt, 402 m deep, dolomite) and SALMON (5.3 kt, 837 m deep, salt) events.

FAILURE OF A BRITTLE MATERIAL

In a recent paper, Handin, Heard and Magourik [1] discussed the results of various destructive tests (compression, extension and hollow torsion) on glass, dolomite and limestone. They demonstrated that the second invariant of the stress deviator plotted versus mean stress did not give a constant failure surface when the test type changed.

In figures 1 through 6 we show the results of their tests on samples at room temperature subjected to strain rates of 10^{-4} per sec. In figures 1, 2 and 3 the octahedral shear stress (τ_{0c}) is plotted versus mean stress (P_m) for the above three materials.

$$P_m = -\frac{1}{3}I_1 \tag{1}$$

and

$$\tau_{0c} = \left(\frac{2}{3}I_{2D}\right)^{1/2} \tag{2}$$

where I_1 is the first invariant of the stress tensor at failure and I_{2D} is the second invariant of the stress deviator at failure. As Handin, Heard and Magourik [1] noted, I_{2D} does not give a consistent description of material failure.

We have found that a consistent failure surface results if we define a function Y as follows:

$$Y = \frac{3}{4}\left[(3I_{2D})^{1/2} + \frac{I_3}{|I_3|}\left(\frac{|I_{3D}|}{2}\right)^{1/3}\right] \tag{3}$$

256

In equation 3 the stress invariants I_{2D}, I_3 and I_{3D} are determined by the existing stress field at failure. In terms of principal stresses T_{11}, T_{22}, T_{33} (positive for tension) we have

$$I_1 = T_{11} + T_{22} + T_{33} \tag{4}$$

$$\left.\begin{aligned} T_1 &= P_m + T_{11} \\ T_2 &= P_m + T_{22} \\ T_3 &= P_m + T_{33} \end{aligned}\right\} \quad \text{Stress deviators}$$

$$I_{2D} = \frac{1}{2}\left(T_1^2 + T_2^2 + T_3^2\right) = \frac{1}{6}\left[(T_{11} - T_{22})^2 + (T_{11} - T_{33})^2 + (T_{22} - T_{33})^2\right]$$

$$I_3 = T_{11} T_{22} T_{33}$$

$$I_{3D} = T_1 T_2 T_3$$

In figures 4, 5 and 6 the failure data of Handin, Heard and Magourik [1] are used to plot Y against mean stress (P_m). The agreement between the various tests regarding the failure of glass and dolomite is now quite good (figures 4 and 5). The scatter for limestone (figure 6) is large. However, the torsion and extension data for limestone now bracket the data from the compression tests at mean stresses greater than 1.5 kb, and also permit an extension of the failure curve back to zero mean stress. This extension was not possible when only I_{2D} was used to determine failure (figure 3).

Whether the scatter in the limestone data results from material variation, tests procedure, or inadequacy of equation 3 to represent material failure is not known. However, the ability of the $Y - P_m$ relation to predict the failure of glass and dolomite, relatively brittle and uniform materials, and to extend the limestone failure data to zero mean stress represents a significant success.

The form of equation 3 was obtained by making assumptions concerning the failure relation in compression and extension. In compression,

$$T_{11} < T_{22} = T_{33} < 0$$

and the assumed relation for Y was

$$Y_c = \frac{|T_{11}| - |T_{22}|}{2} \tag{5}$$

In extension, two cases occur:

$$T_{33} = T_{22} < T_{11} < 0 \qquad \text{(Case 1)}$$

and

$$T_{33} \quad T_{22} \quad 0 \quad T_{11} \qquad \text{(Case 2)}$$

The assumed relation for Y for Case 1 was

257

$$Y_{E1} = \frac{|T_{22}| - |T_{11}|}{2} \tag{6}$$

For Case 2 we assumed

$$Y_{E2} = \frac{3}{2}(P_m + T_{11}) \tag{7}$$

Also, if a test could be devised in which

$$T_{11} < 0 < T_{22} = T_{33}$$

then we wanted Y to have the same form as (7) except with T_{11} replaced by T_{22}, i.e.,

$$Y_{E3} = \frac{3}{2}(P_m + T_{22}) \tag{8}$$

We show in the Appendix that, depending on the test, equation 3 reduces to equations 5, 6, 7 or 8.

The form of equation 7 was obtained by considering the stress components from a spherically symmetric stress field (T_{RR}, $T_{\theta\theta} = T_{\phi\phi}$). We can write

$$\begin{bmatrix} T_{RR} & 0 & 0 \\ 0 & T_{\theta\theta} & 0 \\ 0 & 0 & T_{\phi\phi} \end{bmatrix} = \begin{bmatrix} -P_m & 0 & 0 \\ 0 & -P_m & 0 \\ 0 & 0 & -P_m \end{bmatrix} + \begin{bmatrix} -\frac{4}{3}K & 0 & 0 \\ 0 & +\frac{2}{3}K & 0 \\ 0 & 0 & +\frac{2}{3}K \end{bmatrix} \tag{9}$$

If we assume that $P_m > 0$ and $K > 0$ then K equals Y (see Appendix), T_{RR} is negative, and $T_{\theta\theta}$ may be positive or negative. If $T_{\theta\theta}$ is positive and failure occurs because the "tensile strength" of the material is exceeded, then we must have

$$K = Y = \frac{3}{2}(P_m + T_{\theta\theta}) \tag{10}$$

This equation led to the assumption concerning the form of Y in extension (equations 7 and 8). No assumptions concerning the failure expression were made for torsion. When an expression involving stress invariants was found that satisfied equations 5, 6, 7 and 8 (equation 3) the torsion data were used to check the model.

An interesting consequence of equation 3 is that the "tensile strength" of a material depends on the test type. In order to have the same value of Y at a given mean stress, we find that

$$\frac{\sqrt{3}}{2} TS_T = TS_E + P_m \left(1 - \frac{\sqrt{3}}{2}\right) \tag{11}$$

where TS_T is the "tensile strength" in torsion (twist plus confining pressure) and TS_E is the "tensile strength" in extension. Obviously, $TS_T > TS_E$ for $P_m > 0$.

258

CALCULATION OF FRACTURE RADIUS FROM CONTAINED NUCLEAR EXPLOSIONS

We have used the strength properties of granite, dolomite and salt to calculate the extent of cracking from the HARDHAT (5 kt, 290 m deep, granite), HANDCAR (12 kt, 402 m deep, dolomite) and SALMON (5.3 kt, 837 m deep, salt) events. The post-shot investigations of these experiments are discussed by Boardman [2], Boardman, et al. [3] and Rawson, et al. [4].

Figure 7 gives the Y-P_m curves for the three materials. Hugoniot elastic-limit measurements were used to obtain the limiting values of Y (14 kb for granite, 7 kb for dolomite). No dynamic elastic-limit measurements were available for salt. However, the triaxial data gave 0.7 kb for the limiting value of Y. Figure 8 shows the hydrostatic compressibility data and Poisson's ratio for each material.

The strength, compressibility, and Hugoniot data and Poisson's ratio, along with the source description, form the basic input into SOC (Cherry, [5]) a one-dimensional, Lagrangian, stress-wave code. The results of the SOC calculations on HARDHAT and HANDCAR are shown in figure 9. It is interesting that the calculated extent of cracking for both HARDHAT and HANDCAR agrees with the observed chimney height to within 14%. The calculated and measured cavity radii are in excellent agreement for both experiments. If the strength of the material and the shock-induced cracking control chimney formation, then it is no longer surprising that a 12-kt source in dolomite produces a smaller chimney than a 5-kt source in granite.

Figure 10 shows the results of the SOC calculations for SALMON. We obtained the uncracked 25-m buffer zone between the cavity and the cracked material by allowing a brittle-ductile transition to take place at 68-bars mean stress. This value of mean stress in the Y-P plane corresponds to the unconfined compressive strength of the SALMON salt.

The calculated interface between the cracked and plastically deformed sa   nds on the location of the brittle-ductile transition in the Y-P plane. For a transition .00 bars mean stress, the buffer zone is reduced to 18 m and for a transition at 300 bars, the zone is reduced to 4 m. Since the SALMON event did not produce a chimney, a significant layer of coherent salt must surround the cavity.

The location of the brittle-ductile transition, along with the level of the entire failure surface, must be both stress-rate and temperature dependent. These parameters will be included in the code when the magnitude of their effects has been measured.

CONCLUSIONS

A failure model has been presented which combines both "shear" and "tensile" failure into a single invariant expression. The usefulness of the expression lies in its ability to consistently describe material failure produced by the compression, extension and hollow torsion laboratory tests. A correct extension of the failure surface back to zero mean stress is now possible.

We have used the failure law to calculate the extent of cracking from three nuclear experiments. A preliminary observation suggests that the chimney height is related to the crack radius.

ACKNOWLEDGEMENTS

APPENDIX

1. Compression $T_1 < T_{22} = T_{33} < 0$

   From equation (4) we find

   $$\frac{I_3}{|I_3|} = -1, \quad I_{2D} = \frac{1}{3}(|T_{11}| - |T_{22}|)^2, \quad |I_{3D}| = \frac{2}{27}(|T_{11}| - |T_{22}|)^3$$

   Equation (3) gives

   $$Y = \frac{|T_{11}| - |T_{22}|}{2}$$

2. Extension

   Case 1. $T_{33} = T_{22} < T_{11} < 0$

   $$\frac{I_3}{|I_3|} = -1, \quad I_{2D} = \frac{1}{3}(|T_{22}| - |T_{11}|)^2, \quad |I_{3D}| = \frac{2}{27}(|T_{22}| - |T_{11}|)^3$$

   Therefore

   $$Y = \frac{|T_{22}| - |T_{11}|}{2}$$

   Case 2. $T_{33} = T_{22} < 0 < T_{11}$

   $$\frac{I_3}{|I_3|} = +1, \quad I_{2D} = \frac{1}{3}\left(\frac{3}{2}\right)^2 (T_{11} + P_m)^2, \quad |I_{3D}| = \left(\frac{1}{2}\right)^2 (P_m + T_{11})^3$$

   Therefore,

   $$Y = \frac{3}{2}(T_{11} + P_m)$$

   Case 3. $T_{11} < 0 < T_{22} = T_{33}$

   $$\frac{I_3}{|I_3|} = -1, \quad I_{2D} = 3(P_m + T_{22})^2, \quad |I_{3D}| = 2(P_m + T_{22})^3$$

   Therefore,

   $$Y = \frac{3}{2}(T_{22} + P_m)$$

261

3. Spherically Symmetric Stress field, $P_m > 0$, $K > 0$

$$\frac{I_3}{|I_3|} = -1, \quad I_{2D} = \frac{12}{9}K^2, \quad |I_{3D}| = \frac{16}{27}K^3$$

Therefore,

$$Y = K$$

REFERENCES

1. J. Handin, H. C. Heard and J. N. Magouirk, "Effects of the Intermediate Principal Stress on the Failure of Limestone, Dolomite and Glass at Different Temperatures and Strain Rates," J. Geophys. Res., Vol. 72, 1967, pp. 611-640.

2. C. R. Boardman, Some Characteristics of the HARDHAT Chimney and Surrounding Wall Rock, Rept. UCRL-50177, Lawrence Rad. Lab., Univ. of Calif., Livermore, Calif., 1966.

3. C. R. Boardman, G. L. Meyer and D. D. Rabb, Macrodeformation Resulting from the HANDCAR Event, Rept. UCRL-50149, Lawrence Rad. Lab., Univ. of Calif., Livermore, Calif., 1966.

4. D. Rawson, P. Randolph, C. Boardman and V. Wheeler, "Post-Shot Environment Resulting from the SALMON Event," J. Geophys. Res., Vol. 71, 1966, pp. 3507-3521.

5. J. T. Cherry, "Computer Calculations of Explosion-Produced Craters," Intern. J. Rock Mechanics and Mineral Sci., Vol. 4, 1967, pp. 1-22.
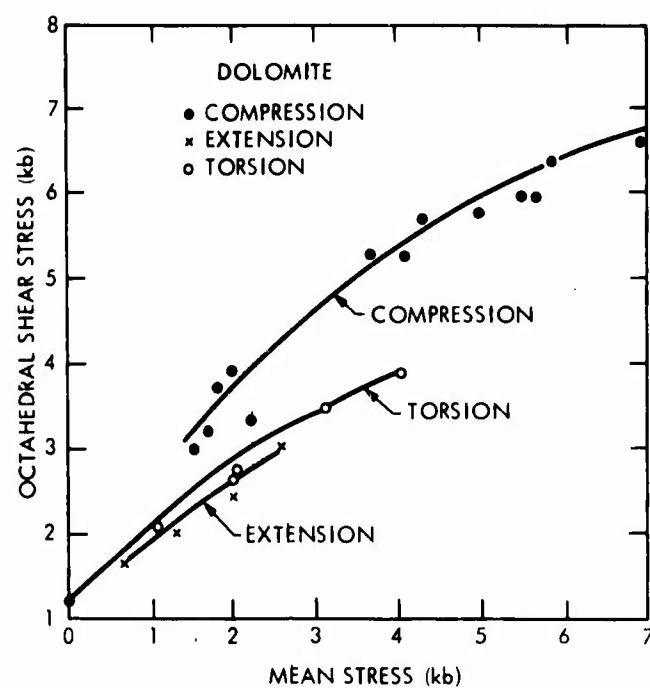
FIGURE 1. OCTAHEDRAL SHEAR STRESS vs. MEAN STRESS FOR GLASS
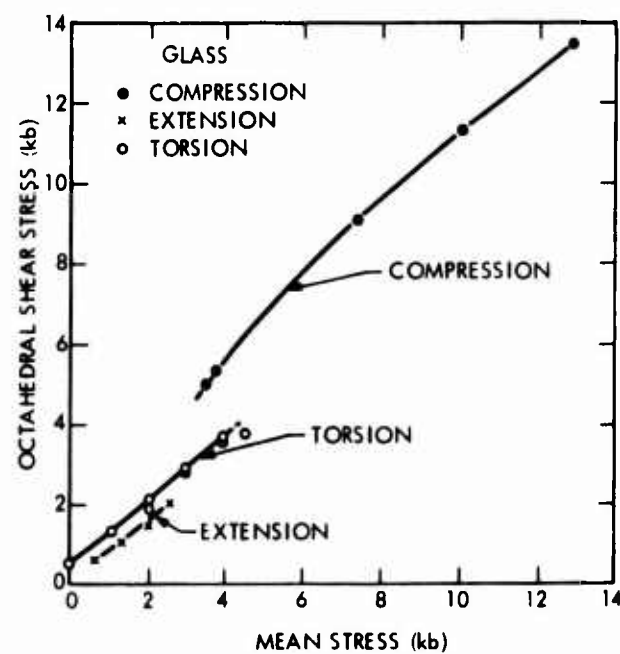
FIGURE 2. OCTAHEDRAL SHEAR STRESS vs. MEAN STRESS FOR DOLOMITE
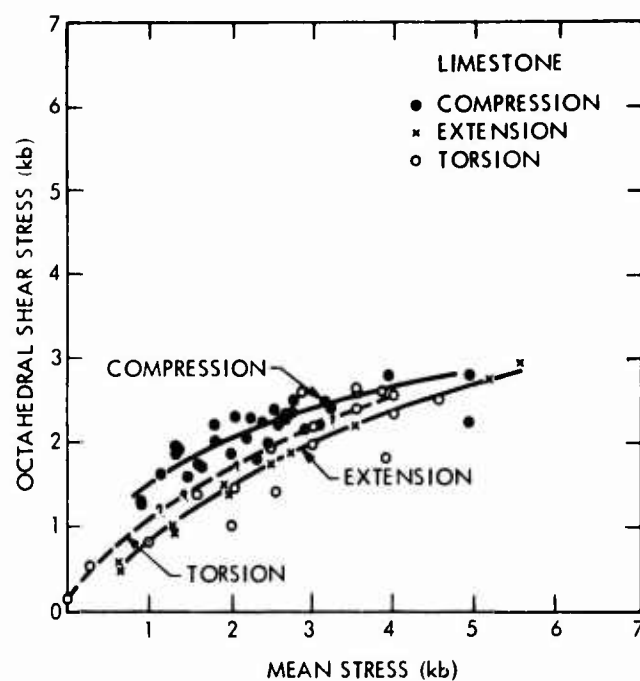
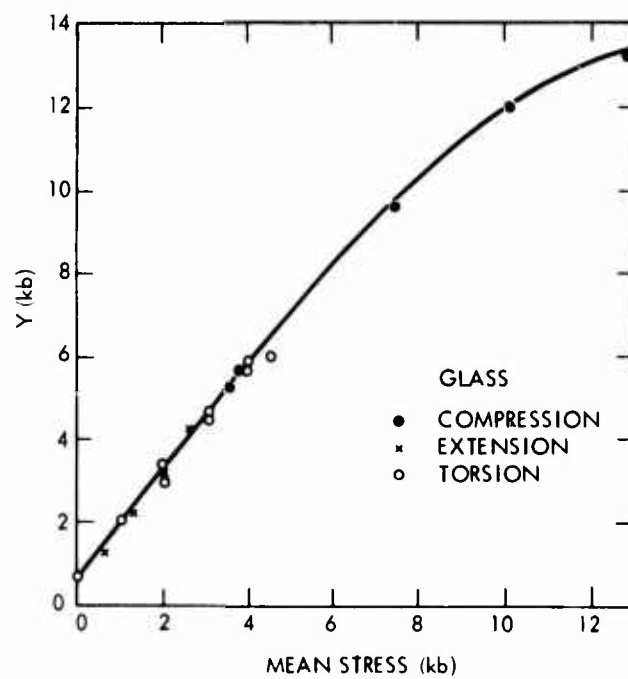FIGURE 3. OCTAHEDRAL SHEAR STRESS vs. MEAN STRESS FOR LIMESTONE
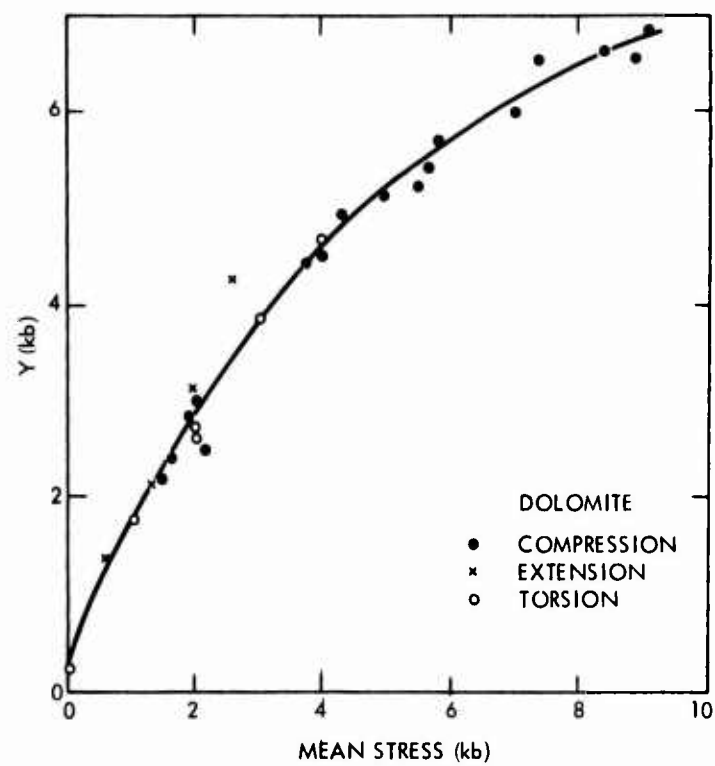

FIGURE 4. Y vs. MEAN STRESS FOR GLASS
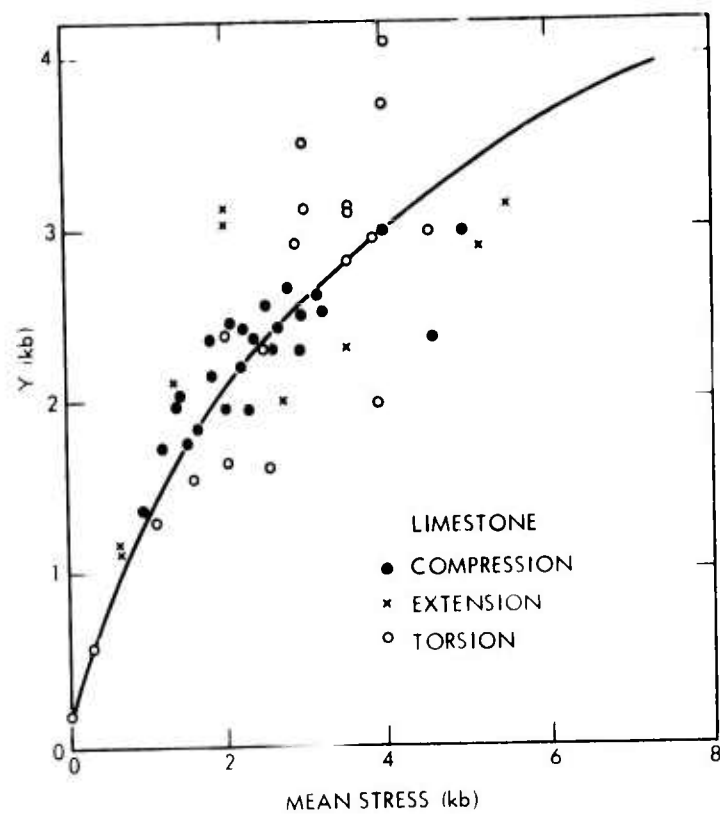
265

FIGURE 5. Y vs. MEAN STRESS FOR DOLOMITE
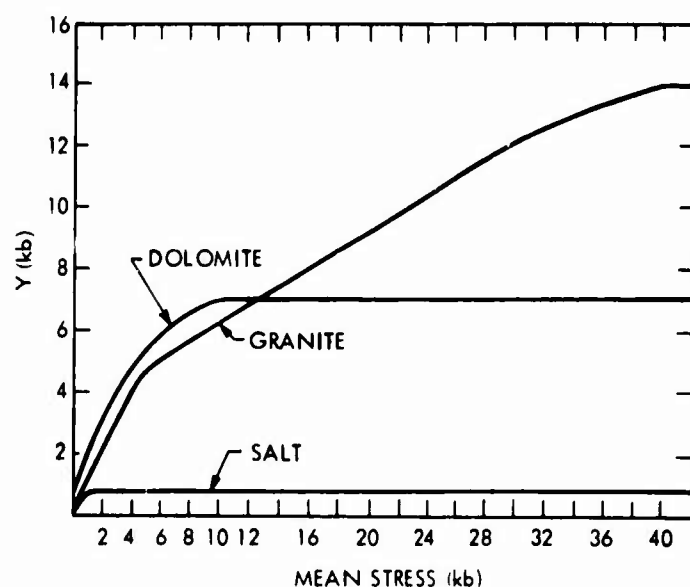
266

FIGURE 6. Y vs. MEAN STRESS FOR LIMESTONE
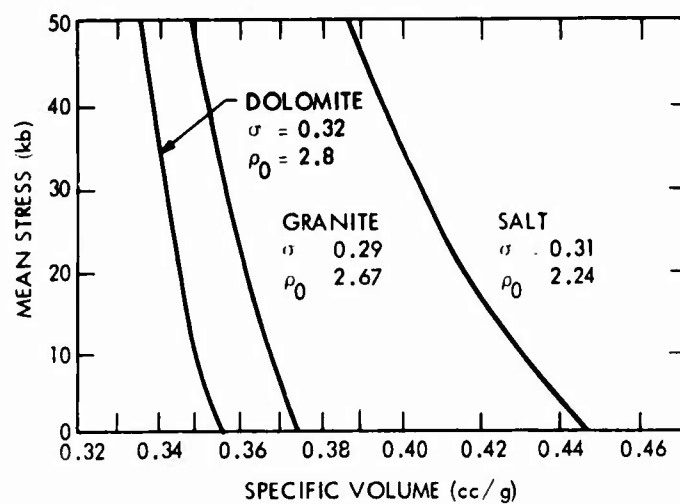
FIGURE 7. Y vs. MEAN STRESS FOR DOLOMITE, GRANITE AND SALT

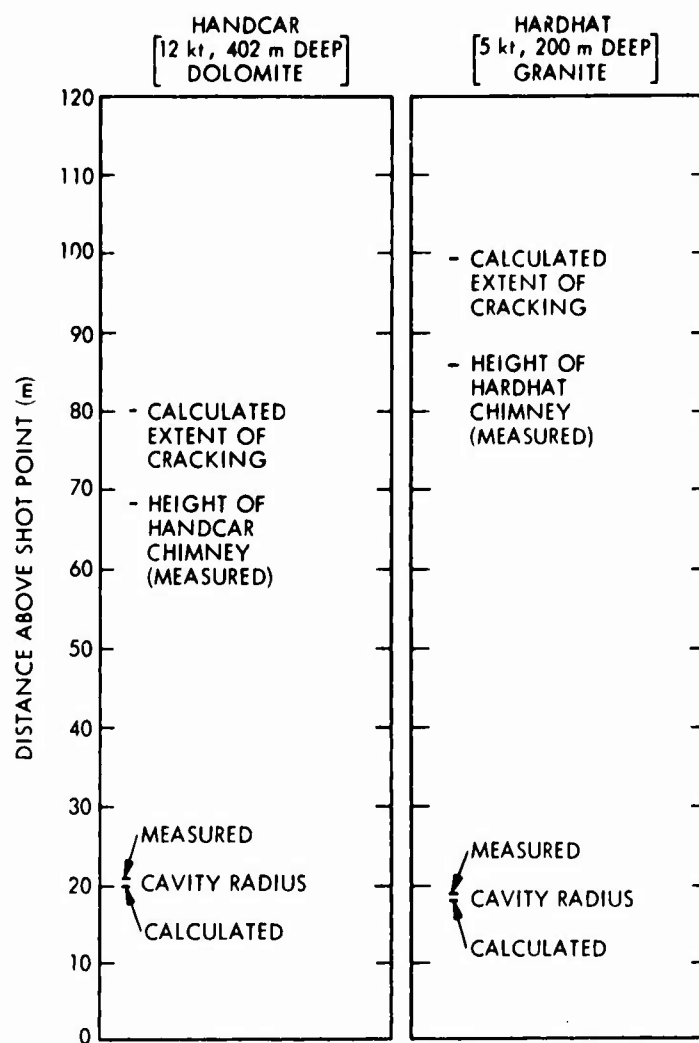FIGURE 8. HYDROSTATIC COMPRESSIBILITY OF SALT, GRANITE AND DOLOMITE
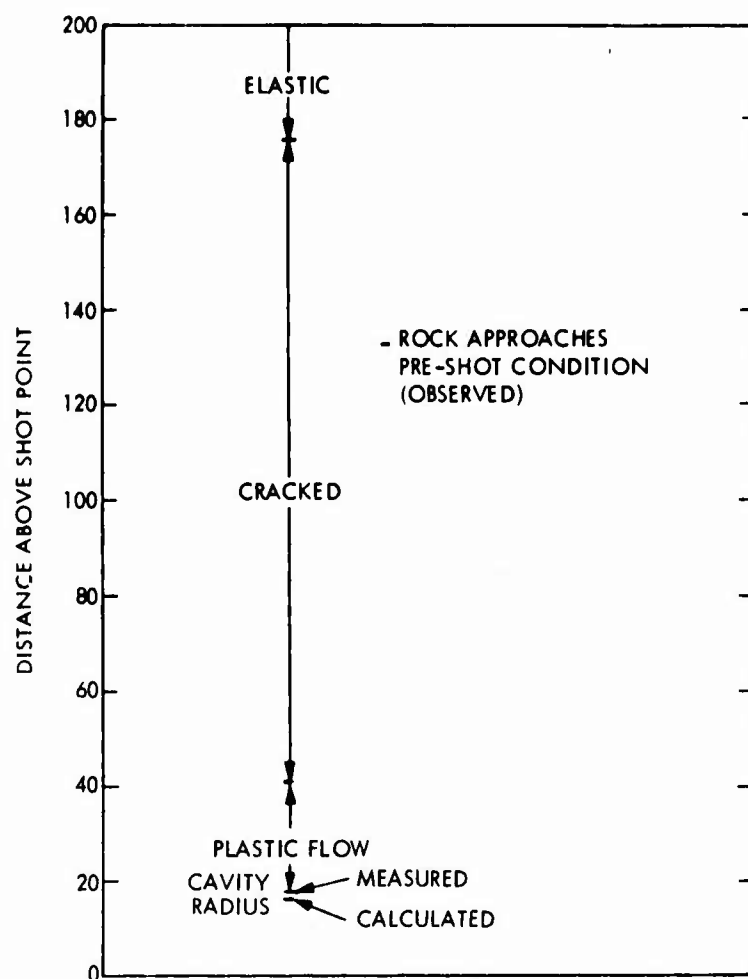
FIGURE 9. HARDHAT AND HANDCAR CALCULATIONS

269

FIGURE 10. SALMON CALCULATION

13
QUENCHING NUCLEAR EXPLOSIONS

A. L. Latter, E. A. Martinelli and J. E. Whitener
The RAND Corporation
Santa Monica, California

ABSTRACT

A technique for quenching nuclear explosions is proposed, in which appropriate heat-sink materials are distributed throughout a small underground cavity in a definite geometric arrangement. With plausible, conservative assumptions it is shown that the energy is absorbed and the cavity pressure drops in a small fraction of a second. If the technique is experimentally verified, decoupling of nuclear explosions could be achieved in smaller cavities located nearer the surface of the earth.

EXPERIMENTS AND CALCULATIONS OF COUPLING PHENOMENA

C. S. Godfrey
Physics International Company
San Leandro, California

INTRODUCTION

When nuclear explosion is detonated in an underground environment, the response of the surrounding earth medium to the outgoing spherical wave system can be considered in three regions. In the first or hydrodynamic region, the stresses are large enough so that the material's constitutive relations play an insignificant role and can be logically ignored. The third region can be called the seismic region in which the stress waves can be considered to be largely elastic. In between is the region of non-elastic, non-linear response in which the numerous constitutive properties of the material affect its response in ways that cannot be ignored.

It is this latter region which probably represents, at present, the weakest link in attempts to predict by calculations the far seismic signal to be expected for various explosives set off in various size cavities in various media. The range of peak stress usually assumed for this region extends from several hundred kilobars down to some lower limit which is not well defined at this time. Within this region shear strength, dislocation dynamics, strain hardening, crack formation, stress relaxation, viscosity, irreversible compaction, etc. may play undefined roles. It has been shown (ref. 1), for example, that the yield model assumed for the material plays an important role in the attenuation of the stress. It becomes highly desirable, therefore, to be able to determine experimentally the response of earth media to spherically divergent shocks and to be able to develop calculational models to predict this response.

Physics International has been engaged in an effort which lends itself well to the above problem. The experimental technique consists of detonating a spherical charge of high explosive which has been asymmetrically embedded in a large (typically 1 ft^3) block of the test material, and monitoring the resulting stress-time profiles at each of the sample faces with manganin piezoresistive transducers. Inasmuch as each face is at a different distance from the explosive charge, a wide range of stresses can be covered in a single experiment. This approach is unique in that spherically symmetric waves are studied instead of the traditional plane waves, and comparatively large test samples are used so that the results will generally be characteristic of the bulk properties of the materials, rather than being dominated by small-scale inhomogeneities. The theoretical work has consisted of a series of spherically symmetric, one-dimensional (POD) computer code calculations, which are ultimately intended to determine the most consistent and reasonable model for the experimental data.

Data have been obtained on Raymond granite and Westerly granite. During the remainder of the program similar data will be measured on tuff from G tunnel, Area 12, of the Nevada Test Site. Both saturated and dry samples will be tested.

EXPERIMENTAL PROGRAM (TAMPED)

The basic experimental geometry for the Westerly granite experiments is shown in figure 1. A sphere of high explosive is placed in a block of granite so that each of the five faces of the granite is at a different radius from the center of the sphere. The hole through which the high explosive is introduced is plugged with a type of aluminum that has the same impedance characteristics as the granite. The detonator leads are brought out through a hole in the center of this plug. Stress gauges are placed on the other five faces of the granite block. By varying the size of the block and the position of the high-explosive sphere, data is obtained for radial stress as a function of radial position over a wide range of stresses.

The stress gauge used in these experiments is shown in figure 2. It consists of two active elements in the same current loop. One element is a manganin wire, which is used as a piezoresistive pressure transducer, while the other is a copper-nickel wire that has almost the same resistivity as the manganin but a negligible piezoresistive coefficient. Because of the divergence of the stress wave in spherical geometry, part of the change in resistance of the manganin wire is due to stretching. This part of the signal can be eliminated by subtracting the response of the copper-nickel wire. When this is done the remaining part of the manganin signal is directly proportional to the magnitude of the stress acting on the wire. This gauge is embedded in an epoxy layer between the granite block and a granite backing piece, as shown in figure 1. The epoxy is a strengthless material whose pressure equilibrates to the radial stress in the granite after a few reflections.

The high explosive used is LX04-01. The equation of state of this high explosive is well documented (ref. 2), and the Chapman-Jouget pressure has been measured at 360 kbar.

By varying the size of the granite blocks and the location of the high explosive charge, experiments have given sufficient data to cover the range from just below 135 kbar down to 13 kbar. These experiments used a 1-inch-radius high explosive sphere. To investigate time-dependent effects, several experiments were performed using charges with 2-inch radius.

A typical trace in the high stress region is reproduced in figure 3. This shows the uncorrected manganin gauge response and the corresponding copper-nickel gauge response. The corrected stress profile is obtained by subtraction. At lower stress levels where the ratio of radial displacement to circumference becomes small, the correction becomes almost negligible.

Corrected traces from several shots are shown in figures 4 and 5, representing data from 1-inch and 2-inch-radius explosive spheres, respectively. A precursor is seen to emerge whose amplitude decays as a function of radius. Both this wave and the accompanying second wave show dispersion as a function of radius. The attenuation of the peak stress and the

274

broadening of the stress pulse are readily observable. The precursor amplitude and peak stress amplitude for all shots are plotted in figure 6 as a function of scaled radius. The peak stress for both 1-inch and 2-inch sources seems to be scalable. The precursor amplitudes for both 1-inch and 2-inch spheres appear to fall off as $1/R$. They are displaced substantially from each other, however, at corresponding scaled radii. This would suggest that stress relaxation effects are present.

Future shots will employ a deviatoric gauge to measure the yield stress behind the shock as a function of stress and time. An exploded view of the deviatoric stress gauge is snown in figure 7. It consists of a manganin wire ABC embedded in two separate layers of epoxy. Segment AB is embedded in an epoxy layer oriented perpendicular to the direction of shock propagation; the pressure of the epoxy layer equilibrates to σ_x, where x is in the direction of shock propagation. Segment BC is embedded in an epoxy layer oriented parallel to the x direction; this layer equilibrates to σ_y. Therefore, by observing the voltage across voltage taps A' and B' we can measure σ_x and likewise the vol age across B' and C' is proportional to σ_y. In plane geometry $\sigma_x - \sigma_y$ is equal to the yield stress Y, so by subtracting the two responses we have a dynamic measurement of Y. This can be expressed as a function of hydrostatic stress, 1 3 $(\sigma_x + 2\sigma_y)$, to give an expression for the yield surface. These relationships between Y and the principal stresses also exist in spherical geometry making this gauge useful on the spherical granite shots.

CALCULATIONS

At this time, the reduction of data to a suitable calculational model has just begun.

The basic theoretical tool being used is a one-dimensional elastic-plastic computer code known as POD. This code solves, in finite difference form, the equations of motion for an elastic-plastic solid in spherical geometry. By adjusting material properties parameters in an iterative manner, the results of the computer calculations are made to fit the data for both the decay of radial stress as a function of distance and the stress-time profiles obtained from the stress gauges.

There is some analytical work which is helpful to this effort. Hopkins has shown that for a Von Mises plastic solid in spherical geometry subjected to an internal source expanding at a constant velocity the solution of the equation of motion for the displacement potential contains a term corresponding to a plane wave attenuating as r^{-1} combined with a term corresponding to dispersion of the wave front (ref. 3). An extension of Hopkins' method of analysis to a Coulomb plastic solid, as used in our model of granite, shows that the solutions for large r approach a plane wave attenuating as $r^{-\alpha}$ (where α depends upon the slope of the yield surface and α goes to 1 as the Von Mises condition is approached) combined with a similar dispersive term. This dispersive term is also a function of the yield stress so that the dispersion of the wave front as well as the rate of attenuation give an estimate of the equation of the yield surface to be put into the computer code. Neither of these models, however, would predict

275

dispersion of the precursor. Other measurements, such as velocity of propagation as a function of stress level and stress level of precursors help to define the material properties parameters.

Figure 8 shows the Hugoniot data to which our model is fitted. Since the region from approximately 60 kbar to 360 kbar appears to represent a phase change, and since the phase change of quartz (one of the constituents of granite) does not appear to be reversible within observable time scales during relaxation, one model employs unloading paths as indicated in figure 9.

To fit the attenuation of peak stress amplitude observed in nuclear explosions in granite we have customarily used a Coulomb model having a rather strong dependence of yield stress on pressure. The yield stress increases to approximately 25 kbar at the 50-kbar Hugoniot point and then remains constant. This basic model can be made to fit the peak attenuation of our data reasonably well, but fails to match the pulse width. Figure 10 shows typical computed and observed profiles at high and low stress levels. The computed profile matches reasonably at the high stress level but is much too narrow at low stress levels. Momentum considerations would indicate that our yield stress is too high. Further evidence for this comes from a recent shot in Westerly granite to measure the deviatoric stresses in granite behind a shock wave of approximately 100 kbars. Preliminary data indicate that the yield stress is at most a few kilobars. It is apparent that further work is needed, but that the technique offers a powerful way of deriving and testing calculational models. The use of the deviatoric gauge in future shots should simplify the task.

SIMULATION OF A DECOUPLED EXPLOSION

The results of the above experiments are encouraging enough to consider how the technique might be expanded to simulate a decoupled explosion. The characteristic loading on the walls of an underground cavity in which a nuclear weapon is detonated can probably be simulated by some combination of a small explosive sphere suspended in the center of the cavity and perhaps a detonable gas filling the cavity. The main problem in achieving such a geometry in a large block of earth material seemed to be the perturbation caused by attempting to plug up a h le in the manner shown in figure 1. The presence of a plug having a radius equal to the cavity radius would probably introduce unacceptable perturbations to spherical symmetry. With this in mind we investigated ways to drill or shape a reasonably large spherical hole in blocks of earth material such that a relatively small plug need be used.

The study resulted in the design shown in figure 11. A small hole is first drilled by conventional techniques. The drill shown is then inserted. As the drill assembly rotates about the axis of this hole, an external hydraulic control forces a diamond-edged cutter to pivot about a point corresponding to the center of the cavity. Both cutting and inspection can be performed by the same apparatus.

276

By using gauging techniques on the outside of the block, data similar to that shown in figures 4 and 5 can be obtained. These data will be a valuable starting point for deriving a knowledge of the coupled energy, the cavity response and the wave profiles leading to a seismic signal.

REFERENCES

1. H. W. Lewis and S. B. Treiman, Seismic Signals from Nuclear Explosions in Overdriven Cavities, IDA. HQ 65-3890, Institute for Defense Analysis, Arlington, Va., 1965.

2. M. L. Wilkins, B. Squier and B. Halperin, The Equation of State for the Detonation Products of PBX 9404 and LX04-01, Rept. UCRL 7797, Lawrence Rad. Lab., Univ. of Calif., Livermore, Calif., 1964.

3. H. G. Hopkins, Progress in Solid Mechanics, Vol. I, Ch. III, I. N. Sneddon and R. Hill, eds., North Holland Publishing Company, Amsterdam, Holland, 1960, pp. 83-164.

278
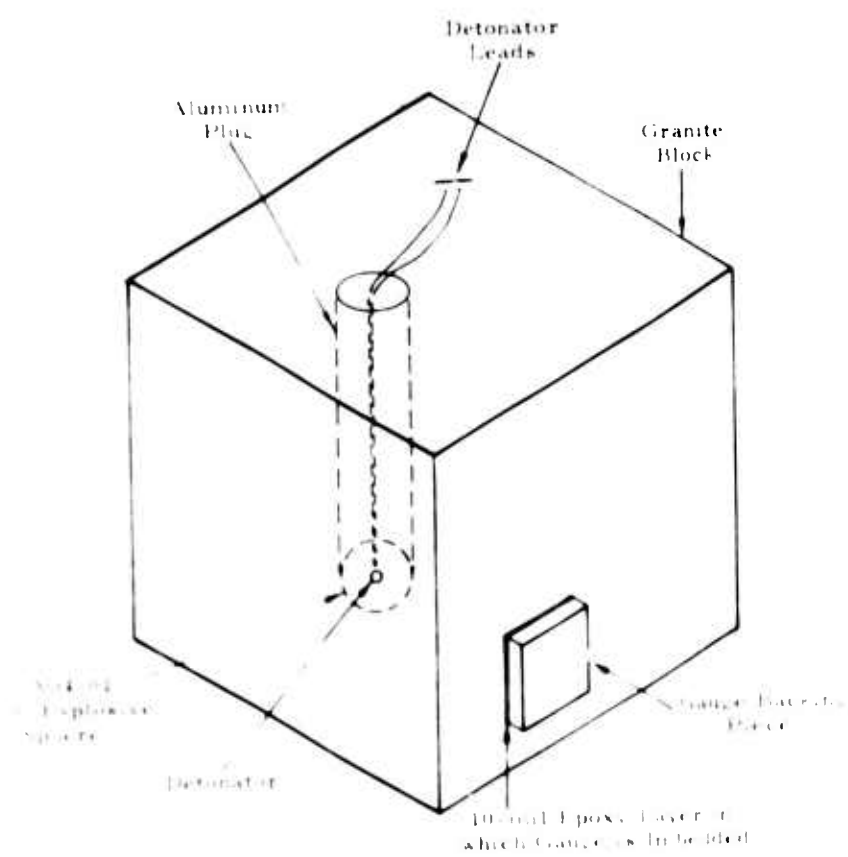
FIGURE 1. BASIC EXPERIMENTAL CONFIGURATION

Granite Block

Manganin Wire
0.003-inch Diameter

Copper-Nickel Wire
0.003-inch Diameter

Granite Backing Piece
1-inch Thick

Copper Foil Leads
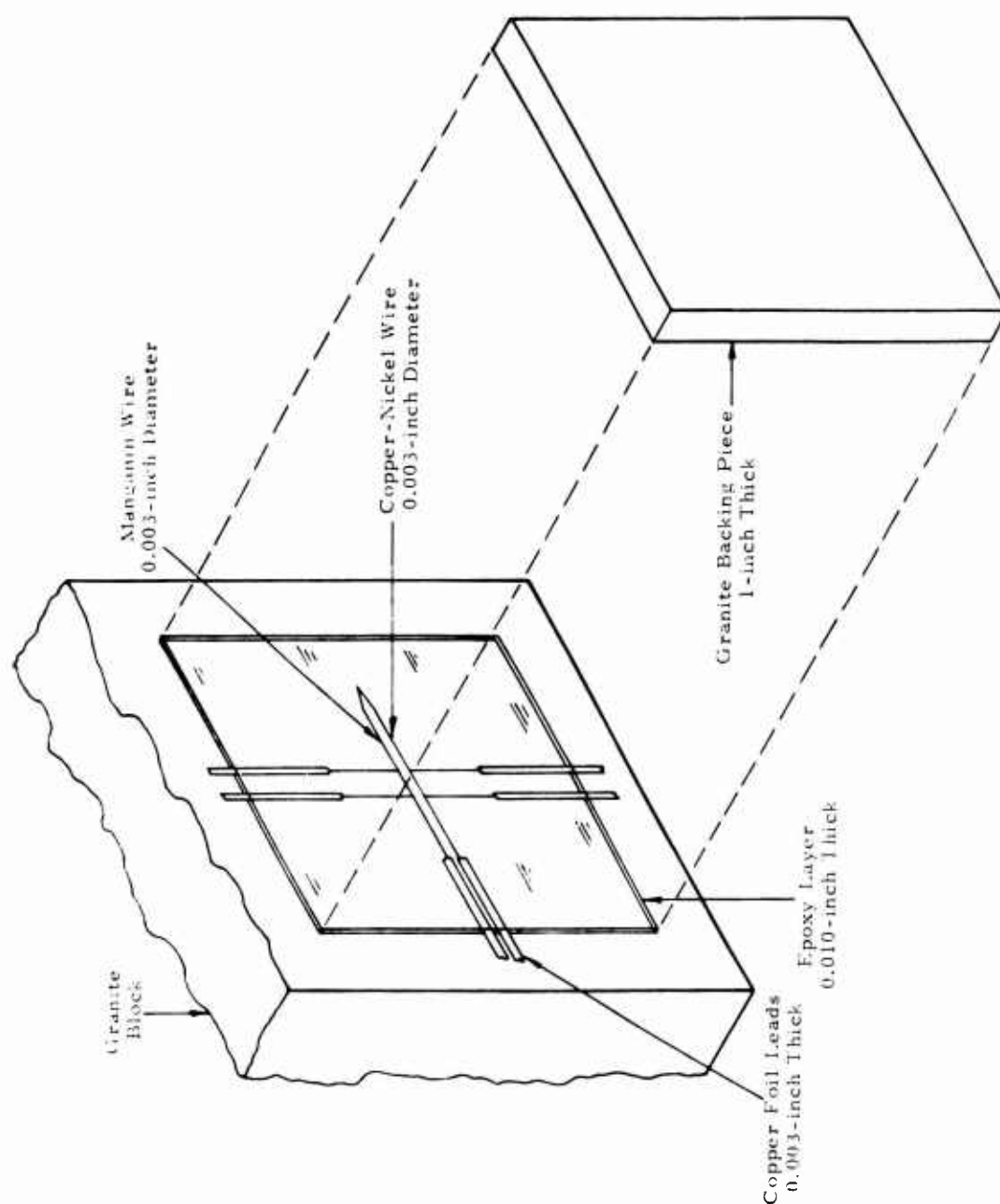0.003-inch Thick

Epoxy Layer
0.010-inch Thick

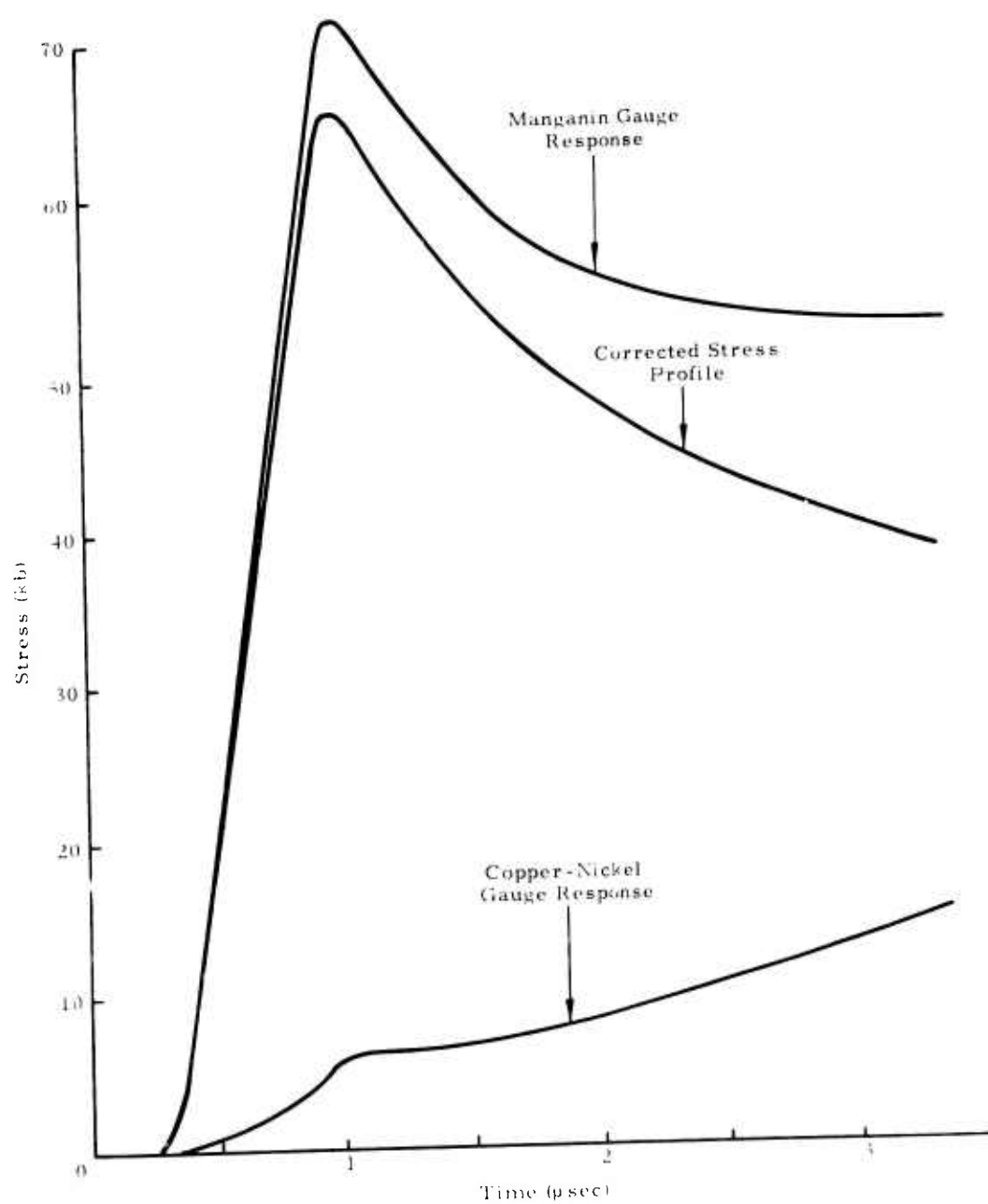FIGURE 2. DETAIL OF GAUGE CONSTRUCTION

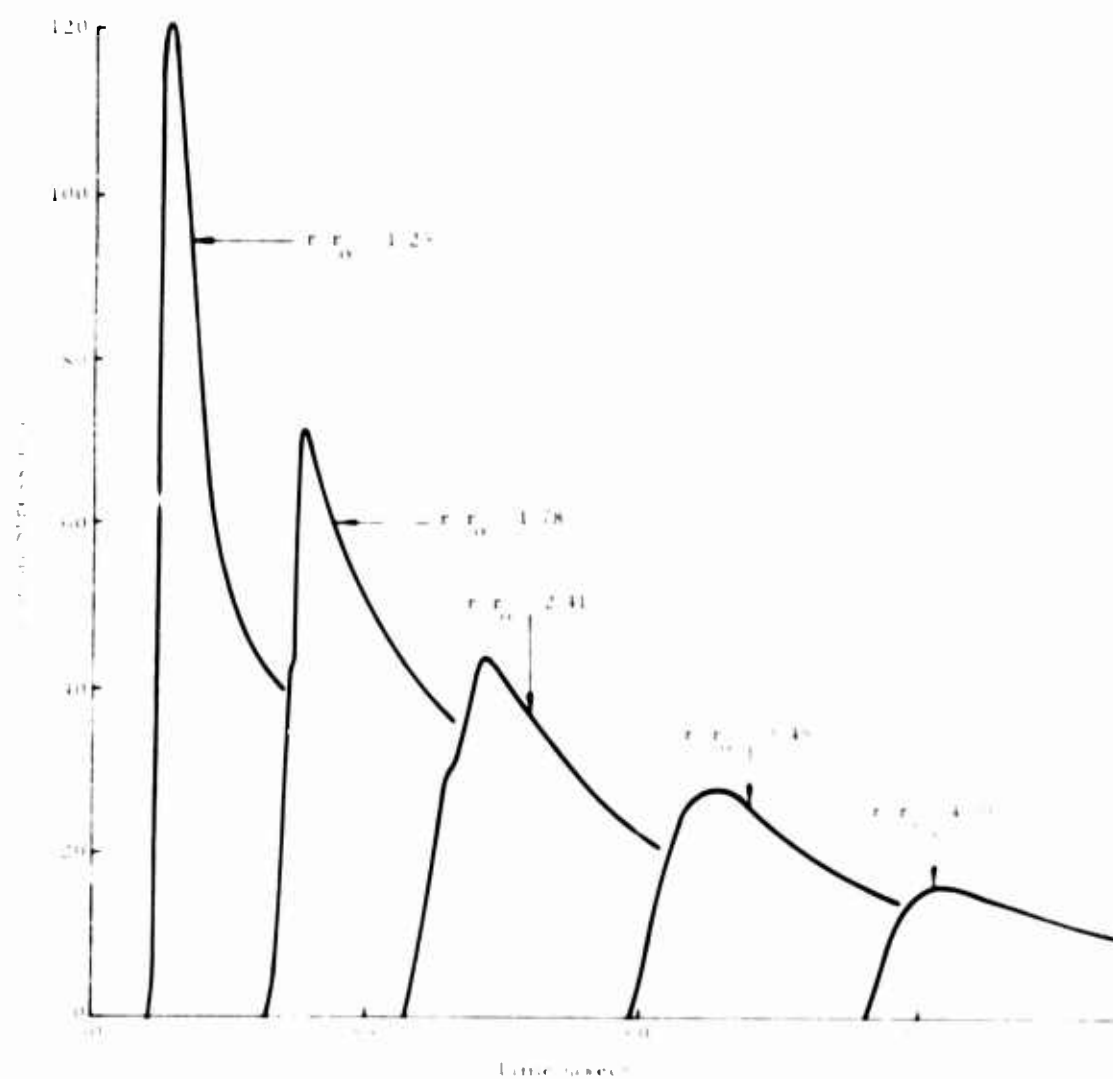FIGURE 3. CORRECTION OF STRESS PROFILE FOR STRETCHING
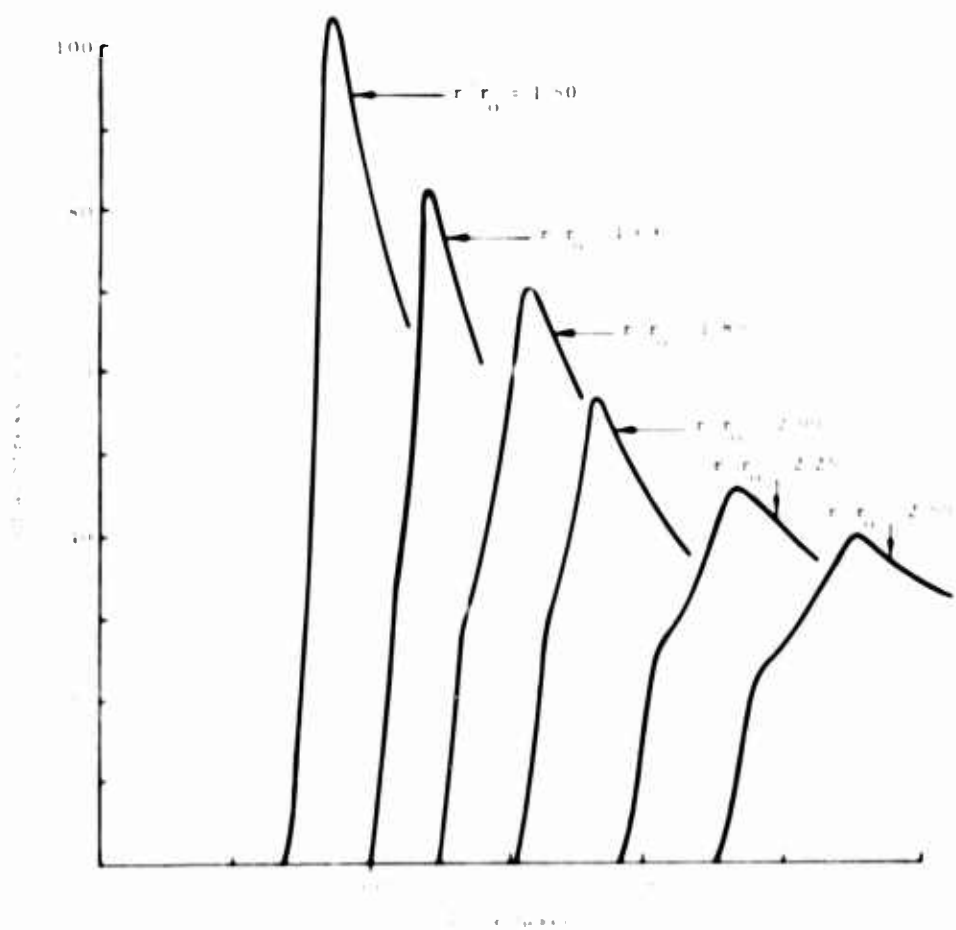
FIGURE 4. STRESS-TIME PROFILES FOR 1-INCH CAVITY RADIUS

262

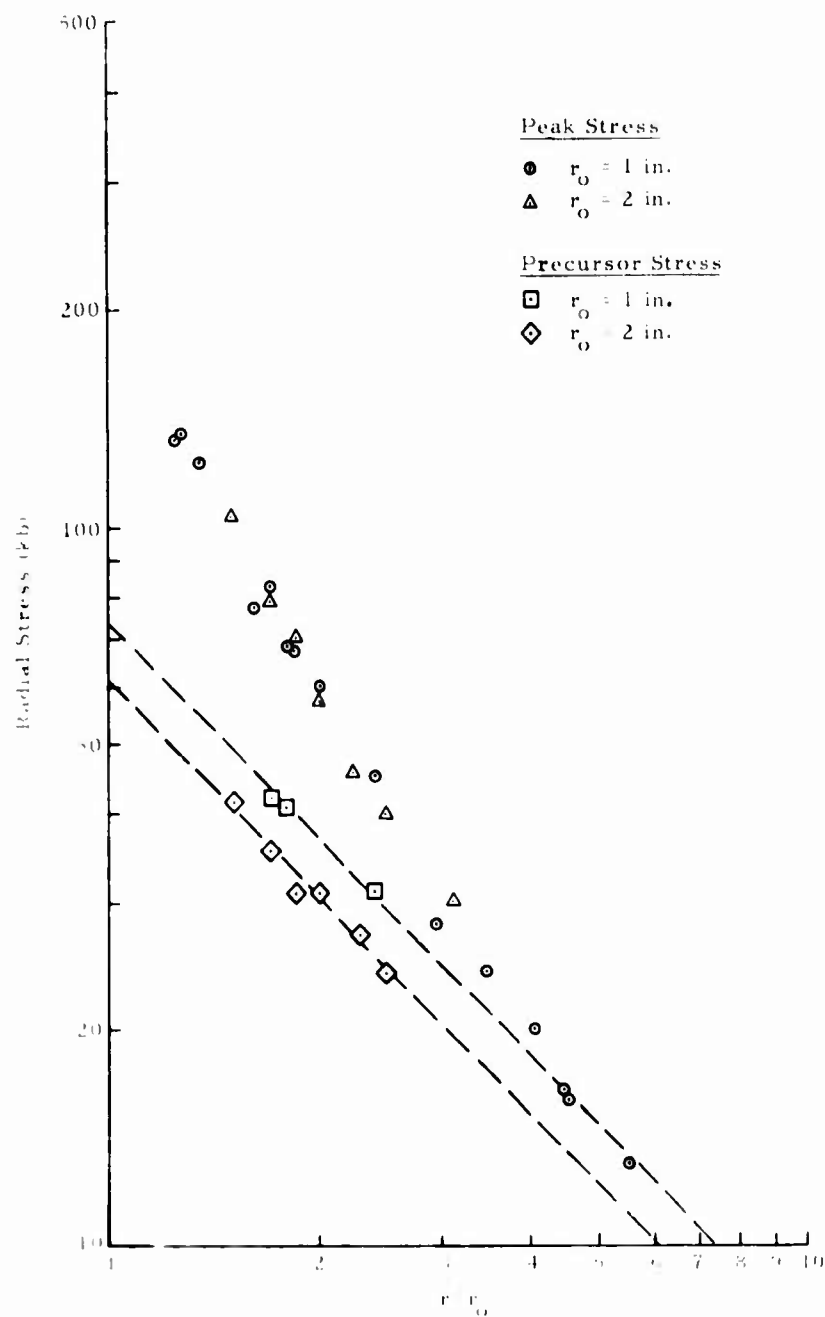FIGURE 5. STRESS-TIME PROFILES FOR 2-INCH CAVITY RADIUS

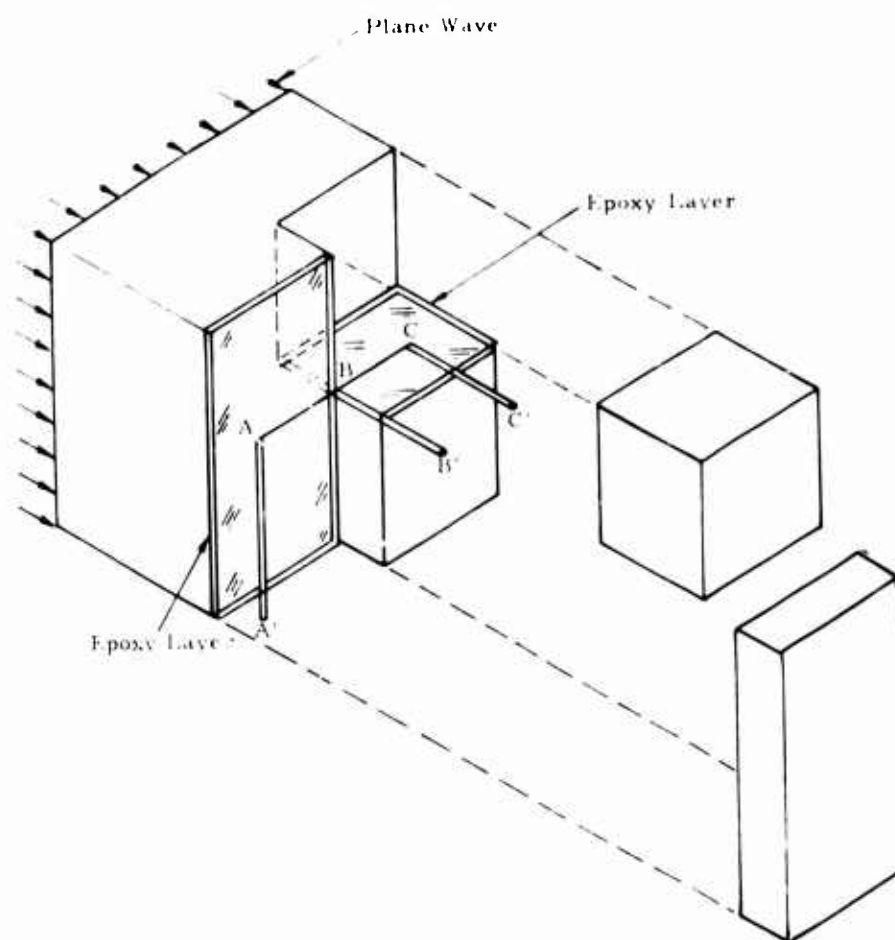FIGURE 6. STRESS ATTENUATION AS A FUNCTION OF SCALED
RADIUS

284

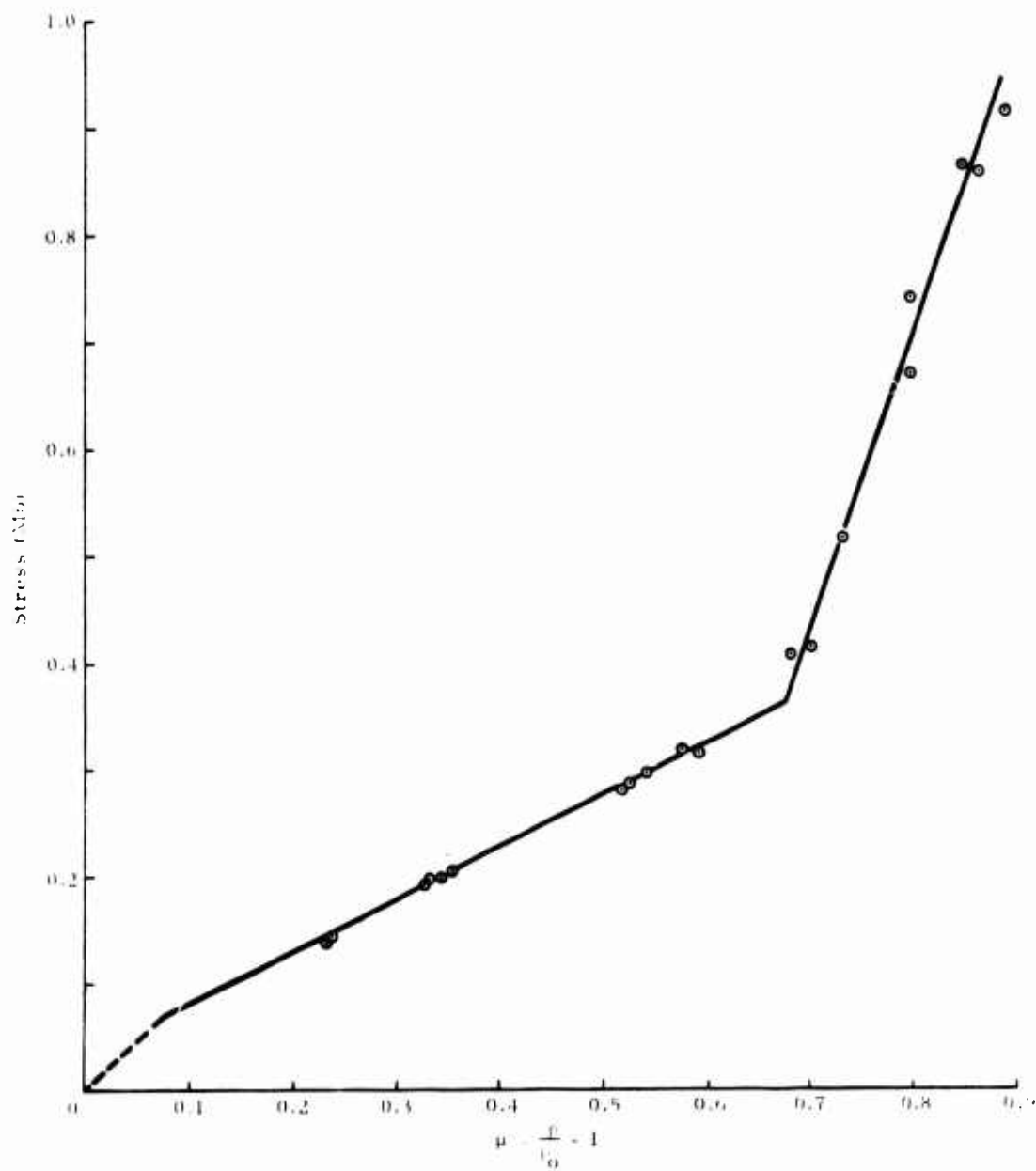FIGURE 7. EXPLODED VIEW OF DEVIATORIC STRESS GAUGE

285

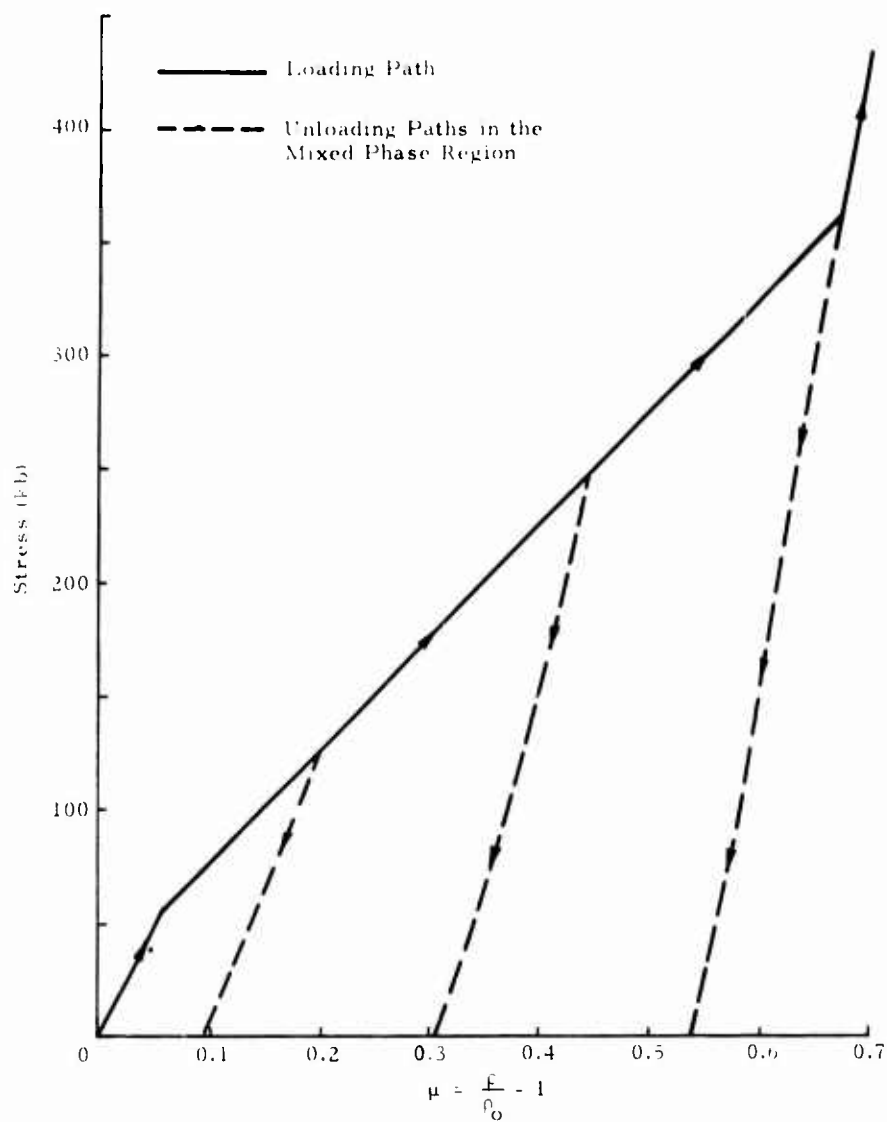FIGURE 8. WESTERLY GRANITE HUGONIOT DATA (McQueen,
Marsh, Fritz - 1967)

286

FIGURE 9. IRREVERSIBLE PHASE TRANSITION MODEL

287
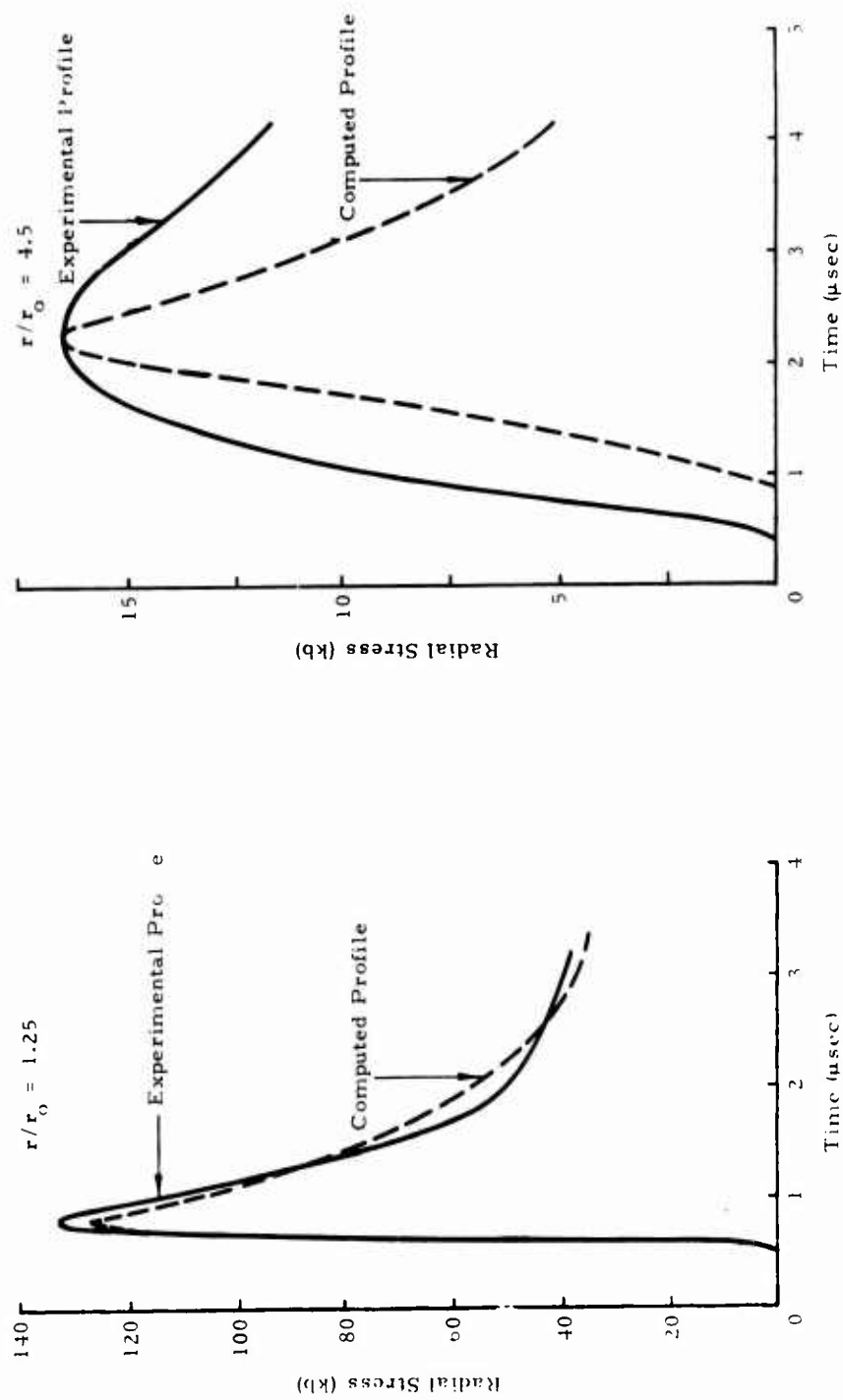
FIGURE 10. COMPARISON OF THE EXPERIMENTAL AND THEORETICAL STRESS PROFILES

288

FIGURE 11. 8-INCH-DIAMETER SPHERICAL CUTTER SYSTEM

289

15
SOURCE MECHANISM STUDIES AND THEIR APPLICATION TO DETECTION AND IDENTIFICATION PROBLEMS

J. F. Evernden
Air Force Technical Applications Center
Washington, D. C.

ABSTRACT

The nature of the detection and identification problems as now understood are reviewed. Several lines of investigation for source mechanism studies are reported which would contribute to solution of these problems.

16

RECENT STUDIES OF SHORT-PERIOD DISCRIMINANTS*

E. J. Kelly
Massachusetts Institute of Technology
Cambridge, Massachusetts

ABSTRACT

This paper is the result of a large-population study of discrimination between earthquakes and explosions, using only short-period data from a single station. The data was obtained from the Large Aperture Seismic Array and the two discriminants studied were waveform complexity and special ratio. Procedures for multivariate discrimination are developed and results are given in terms of earthquake identification percentages using these discriminants singly, and in combination with each other and with magnitude. The results are quite encouraging, complete separation being found for explosions and shallow earthquakes using spectral ratio and magnitude together.

1. INTRODUCTION

The problem of discriminating between earthquakes and explosions by seismic means has progressed to the point where positive separation is clearly possible for large events. Barring unforeseen anomalies in the behavior of explosive sources, detonated in untried, aseismic regions, this separation can be provided by comparing the relative excitation of long-period surface waves to that of short-period P-waves [1, 2] and the threshold of effective discrimination by this means appears at present to be at a body-wave magnitude somewhere in the range 4.3-4 to 5. These results are based upon data from world-wide networks of stations, but very similar results have been reported for Central and Eastern Asian events recorded at a single station, the large aperture Montana LASA [3] array, by Capon, et al., [4] who quote a conservative discrimination threshold of 4.9 (body-wave magnitude). The problem that remains is to lower the threshold of discrimination to a value closer to the threshold of detection of P-waves for a given network or array station. The surface wave — P wave method is presently limited by the difficulty of detecting the long-period waves from weak events, and many people are now concentrating their efforts on improving this detectability.

Recently, however, it has been found by Briscoe [5] that very good separation can be obtained at a single station from short-period data alone, by plotting the spectral ratio versus P-wave magnitude (spectral ratio is the ratio of received P-wave energy in the 1.4 to 1.9 Hz

---

band to that in the 0.4 - 0.8 Hz band). This has caused a revival of interest in short-period discriminants, and the present investigation was undertaken in order to collect a population of Sino-Soviet earthquakes, using LASA data, and to study spectral ratio, as well as the older discriminant, complexity, with three objectives:

(1) To obtain single-station performance estimates of these discriminants, used singly and in combination, on a large population of Sino-Soviet events,

(2) To determine the magnitude threshold at which effective discrimination can be achieved using single-station short-period data alone, and

(3) To learn what, if any, advantages there are in the use of a large short-period array for discrimination purposes, other than its obvious ability to enhance signal-to-noise ratio.

A summary of our conclusions, not exactly unequivocal, will be found in section VI.

II. THE DATA BASE

In order to collect data from events in the Soviet Union and China, arrangements were made with the Data Center in Billings to send us routinely recordings of all events for which epicenters in this region were obtained by the usual triangulation procedures. After about two months, only recordings of events showing no evidence of the existence of pP on the raw data were sent. In this way a library of over 200 events was formed and further processing initiated. Data continues to be collected, of course, for future extension of the study.

The recordings forming the raw data base were subjected to a sequence of measurements, beginning with a redetermination of epicenter by beamsplitting. An initial pattern of beams was formed from the 21 subarray straight sums. The pattern had a spacing of about 2° and was centered on the preliminary epicenter reported in the LASA bulletin (sometimes a starting epicenter was redetermined by triangulation). The coordinates of the best beam were taken as a revised epicenter. If this epicenter was near the edge of the pattern, a new pattern was formed centered on the revised epicenter and, in most cases, a finer pattern was formed (with 1° and sometimes 0.5° spacing) to obtain a final result. Events too weak to permit epicenter determination in this way were removed from the data base. Events were retained if their epicenters were within a few degrees of the Soviet Union, China or Eastern Europe, including Greece and Turkey. About 100 earthquakes remained at this point. Figure 1 shows a rough map of this area, together with the earthquake and explosion epicenters.

Once an epicenter was determined, a new beam was formed, as follows. Steered subarray beams were first formed, using only the 4, 7, and 8 rings, a total of nine elements, from each subarray. These subarray beams were then combined, with appropriate steering delays and the best available station corrections, to form the final beam. Dead or excessively noisy channels were automatically deleted from the beam. The output of this beam, both raw and bandpass filtered (with a 0.6 to 2.0 Hz pass band) was played out on a chart recorder, along

294

with the individual steered subarray beams, each delayed by the amount used in forming the beam. If the revised epicenter was still in error, or if the station corrections used were inadequate, then the failure of subarray alignment would be observed and corrected, using hand-picked corrections to guarantee alignment.

As a result of the processing up to this point, playouts were available of the filtered and unfiltered beam waveforms, representing some 15 to 18 db of signal-to-noise ratio gain in the signal band, relative to the individual raw recorded seismograms [6]. P-phase amplitudes and dominant periods were manually read from these waveforms, permitting a measurement of body-wave magnitude, and a search was made for pP. Any secondary P-phase within two minutes of P and not associated with the expected arrival time of PcP was considered a possible pP. If the amplitude of such a phase exceeded either that of P itself or 1.5 mμ (on the normalized beam), and if the phase delay after P exceeded four seconds, then the phase was called pP and the event was considered "deep." Events not showing this evidence of depth were retained as "shallow." We realize, of course, that single-station pP determination is risky, and that in practice one would rely heavily on the P-arrival times at a world-wide network of stations. However, only about half of the earthquakes in our population were identified by the U. S. Coast and Geodetic Survey (USCGS), and many of these were located at the non-committal 33 km depth (USCGS depths, when reported, agreed well with our determinations). Hence, we relied on our own measurements in order to screen out "deep" events as earthquakes. About half the initial population was considered deep by this test, but the subsequent discrimination analyses were done on both the screened ("shallow") population and the original total population for comparison.

In figure 2 we show the magnitude distribution for the initial population of 93 earthquakes for which a final beam was formed. The data is presented here in the form of a cumulative seismicity curve, in which the logarithm of the number of events in the population having a magnitude greater than some value is plotted against that magnitude value. Thus the curve rises for smaller magnitudes until the logarithm of the total number of events is reached. In all the remaining histograms in this report, we plot the percentage of the population, on a linear scale, having a parameter value less than or equal to a given number versus that number. Figure 3 is such a histogram of epicentral distance for the same events used in figure 2. Events more than 95° from LASA have been removed from the population and not subjected to further processing, in order not to prejudice the study by data beyond the normal range at which a station would be expected to provide useful information.

We have tried not to screen our population in any way which would affect its suitability as a typical sample for the discrimination analysis. The magnitude distribution looks quite reasonable, and the leveling off at small magnitude in figure 2 is indicative of our threshold for detection and location. Figure 3 describes a broad and fairly uniform distribution of distances, although natural seismicity has concentrated much of the data in the Kurile-Kamchatka region. The depth screening done at the site during part of the experiment may unbalance the population

slightly, but we found phases identified as probable pP on beam outputs at about the same rate after as before the beginning of this screening period.

A list of the earthquakes used in this study may be found in the Appendix.

Nineteen events of possible or confirmed explosive origin (hereafter referred to collectively as "explosions") were used in the study, five of which occurred during the data collection period itself. The others are older recordings, altogether representing four source points (1) Amchitka, the epicenter of the Longshot event; (2) Novaya Zemlya, the source of a large Soviet shot; (3) Semipalatinsk, the source of a large number of possible Soviet explosions, and (4) Southern Algeria, the site of two possible French explosions.

A serious deficiency in our present population of events is the disparity in the magnitudes of the earthquakes and the explosions. All of the explosions exceed magnitude 4.9, while the initial population of earthquakes had an average magnitude of 4.7. Magnitude histograms of these two populations are given in a composite plot in figure 4.

In order not to present only results which might be seriously biased by the magnitude differences between earthquakes and explosions, we have used both the total earthquake population and the smaller number of earthquakes having magnitudes not less than 4.8. We previously mentioned that we were using both the total population and the apparently shallow events, hence the discrimination performance results given below in section V are quoted for four earthquake populations as shown in table I.

Table I

All earthquakes*	85 events
Large earthquakes**	32 events
Shallow earthquakes†	48 events
Large, shallow earthquakes	12 events

III. THE DISCRIMINANTS

For the purposes of this study, the short-period discriminants considered were depth (pP detection), waveform complexity, and spectral ratio. The depth determination and pP detection criterion were described in section II. The remaining two are described in detail here. Of course, location is a primary discriminant, but this study began with a population of events which were just from the area that would presumably be monitored (Eastern Europe, the U. S. S. R. and China). Moreover, location is best determined by a network of stations, and

---

*All events, at distances not greater than 95°, for which a final beam was formed and all discriminant measurements were made.

**Measured magnitude equal to or greater than 4.8.

†pP phase not identified on beam output.

one of our purposes was to assess the contribution of a single array station to the discrimination operation by means of its ability to measure waveform discriminants on processed (i.e., high signal-to-noise ratio) traces.

It has often been observed that explosion seismograms, at teleseismic distances, are impulsive and relatively simple. Nearly all the energy that is ultimately received arrives in the first several seconds. While some earthquakes share this property, a great many are more complex, with P phases lasting from many seconds to minutes. Moreover, the simplest earthquake waveforms are usually associated with very deep events which would easily be removed from consideration at an early stage of the screening process. In order to get a quantitative measure of waveform complexity, the British seismic discrimination group (at UKAWRE) has suggested [7] a particular functional of the waveform, namely the inverse ratio of the energy received in the first five seconds of the P phase to that received in the subsequent 30 seconds. The durations of the two time intervals represent arbitrary, but reasonable, choices. However, the results can be expected to depend upon several details such as (1) the processing which went into the formation of the trace in question, (2) the procedure used to determine the start of the first interval, and (3) the manner in which the energy is defined. Moreover, the British definition was always applied to the cross-correlation function between two steered beams, formed from different portions of the total array. We have adopted what we consider to be the essential feature of their definition so as to apply it to a single beam output. In this study the complexity measurements were made on the bandpass filtered (0.6 to 2.0 Hz) beam waveform, and the starting point for computer processing was determined manually (using a light pen on a scope display).

The energy was defined in two ways, as the integral of the square of the signal (quadratic complexity) and as the integral of the absolute value of the signal (linear complexity). The use of the less physical linear measure was motivated originally by dynamic range problems in a fixed-point computer. Taking a time origin at the start of processing, and letting $x(t)$ represent the seismic waveform as a function of time in seconds, then the two definitions are as follows

Quadratic Complexity

$$C_Q = \int_5^{35} |x(t)|^2\, dt \Big/ \int_0^5 |x(t)|^2\, dt,$$

Linear Complexity

$$C_L = \int_5^{35} |x(t)|\, dt \Big/ \int_0^5 |x(t)|\, dt.$$

In practice, of course, the "integrals" are actually sums over the data samples, in our case, 20 samples per second. If $x(t)$ were a constant, either definition would yield complexity of 6, the ratio of interval lengths. We may expect that for pure seismic noise, values like 6 will be

observed. We find that for complex and emergent earthquakes, much larger values are attained, while simple events attain values less than unity on both definitions. Figure 5 is an example of a filtered beam seismogram showing the complexity measurement intervals and results. Histograms of the two complexities, as measured on 85 earthquakes, are shown in figures 6 and 7.

We also expect an intimate relation between the two definitions. On dimensional considerations alone, we may expect a relation of the form

$$\frac{1}{T}\int_0^T |x(t)|^2 \, dt \; = \; K \left\{ \frac{1}{T}\int_0^T |x(t)| \, dt \right\}^2$$

to hold in some average sense. The above relation is true literally for a constant $x(t)$, and true as a relation between expectation values for a random noise model of $x(t)$. Since the constant K drops out in the ratio of complexities, we can expect, roughly, a relation of the form

$$C_Q \; = \; (C_L)^2/6.$$

In figure 8 we give a scatter diagram of C_Q vs. C_L measurements for the same 85 earthquakes used in figures 6 and 7, with the simple relation derived above plotted as the solid curve. It appears that the relation between the two complexities is sufficiently deterministic to permit us to dispense with one of them, and we have chosen to retain the linear definition, mainly to facilitate comparison with earlier measurements made on LASA data. The two definitions have also been compared in terms of their discrimination capability with the same result, that they are equally effective.

In figure 9 we present a composite plot of four histograms of the linear complexity. One curve is for the total earthquake population, another for the earthquake population with the deep events removed and a third in which the Kurile-Kamchatka earthquakes are also removed. The fourth curve is for the explosion data. The fact that shallow earthquakes yield a smaller value of complexity is due to the fact that for most of the deep events, the phase identified as pP falls inside the second time interval used in the measurement, hence increasing the measured complexity value. Events deep enough so that pP does not interfere with the measurement usually have low complexities. The further shift towards small complexity values for continental earthquakes may be significant, but the population involved (shallow, non-Kurile-Kamchatka events) is small and heterogeneous, and may not represent a good sample of continental Sino-Soviet events (part of that area is beyond 95^0 from LASA).

The curve showing the smallest average complexity is the histogram for our population of 19 explosions. The average value is very close to unity, and actually only four explosions exceeded that value. The really anomalous event was the Novaya Zemlya shot of 27 October 1966 with a measured complexity of 2.7. Other studies of this event show that the relatively long P coda consists of energy arriving from the same location as the source. The next largest value was attained by Longshot, at 1.2. The separation of these populations for discrimination purposes is discussed in section V.

Background studies of the spectral character of seismic signals and the motivation for the particular choice of definition of spectral ratio used here are given in reference 5. The measurement procedure used in this study begins with the unfiltered beam waveform, which is passed through a parallel bank of fifty 0.1 Hz wide digital bandpass filters. These filters have a [sin x/x]-type frequency response, and the absolute values of their outputs are smoothed and sampled once per second and used to form a sonogram on a scope display. This is a display which shows the variation of spectral density with time. Frequency is the ordinate, time is the abscissa and spectral density (the filter output) is represented by the intensity of the display. An example is shown in figure 10. Using a light pen, an operator chooses a start time as close as possible to the onset of P, and a stop time defining an interval of 30 - 35 seconds avoiding, if possible, pP or other phases or data errors. The filter output samples falling inside the processing interval chosen by the operator are summed to provide a spectrum of the chosen portion of the waveform. The five spectral values corresponding to the frequencies 1.5 Hz through 1.9 Hz are then summed to form the numerator, and the values corresponding to the frequencies 0.4 Hz through 0.8 Hz are summed to form the denominator of the output spectral ratio. In figure 10 the start and stop times are shown by cursor lines, and the spectrum obtained from this time base is shown as the dotted curve above the sonogram.

Separate studies have shown that the measured value of spectral ratio is not critically sensitive to the time interval used in the measurement, but the intervals used were standardized as much as possible. In one relatively bad test case, the spectral ratio decreased by 10% as the length of the measurement interval increased from 25 to 45 seconds.

Measurements of the spectral ratio of pure seismic noise gave an average value of 0.158 (with a range from 0.057 to 0.317), while earthquakes yield a broad distribution, as shown in the histograms of figure 11.

The four populations used in figure 11 are the same as were used in figure 9. This time the explosions have high values, relative to the earthquakes, and a more distinct regional dependence for earthquakes is apparent. It is interesting that the removal of the deep events from the total earthquake population simply removes the tail of the distribution at high values of spectral ratio, without changing the shape of the remaining part. The details of the population separation by means of spectral ratio are given in section V.

A much less sensitive characterization of the spectral content of an event waveform is provided by the dominant period. We measured these periods, in the traditional way (time between peaks), on the bandpass-filtered beam waveforms and compared the results with the corresponding measurements of spectral ratio. Figure 12 is a scatter diagram of dominant period versus spectral ratio for our full earthquake and explosion populations. The correlation is rather poor, except that the value of period seems to set an upper bound to the spectral ratio. Very similar results are obtained when only the shallow earthquakes are used. We have also noticed a poor correlation between dominant period and the peak frequency of the corresponding spectral density, altho numerical data are not now available.

299

Two spectra, one from an earthquake, one from an explosion are shown in more detail in figure 13. The similarity of the spectra at frequencies above the peak frequency is typical of the two populations. The main difference seems to be the sharp drop in signal energy at the low end for explosions, compared to earthquakes. It is perhaps useful to think of the spectral ratio as an inverse measure of low frequency content, normalized by the relatively stable high frequency portion. In a similar way, the complexity is a measure of the highly variable coda content, normalized by the primary energy in the initial part of the P phase.

It is clear that reliable measurements of complexity and spectral ratio require a certain minimum signal-to-noise ratio. The complexity is likely to be too high for weak, simple events because the coda is weaker than the noise, while the spectral ratio is affected by the non-uniform noise spectrum, especially by the usual low frequency peak. It is difficult to give accurate values to these limits, in magnitude units, but for the earthquakes studied in this work it appears that complexity and spectral ratio are being reliably measured on the signal component of the seismogram only for magnitudes greater than 4.3 for our present methods of processing. Reliable measurements are obtained for all the explosions in our data base because they are all large. One of the most interesting questions to be resolved when we obtain data from weaker explosions is the analogous magnitude threshold for reliable measurement of the short period discriminants.

IV. DISCRIMINATION PROCEDURES

There exists a considerable literature devoted to the study of statistical techniques for multivariate discrimination between two or more populations. However, a common feature of nearly all this work is a statistical model governing the behavior of the variables used for discrimination under different hypotheses. In our case we have no basis for making such statistical assumptions and the measurements made so far (on rather small populations) do not suggest any simple joint probability densities among the discriminants used here. Instead we have adopted a simple principle of exclusive regions, which is best viewed geometrically in the following way.

Suppose that a set of M measurements (such as body-wave magnitude, surface wave magnitude, spectral ratio, etc.) is made on each event of two large populations, one consisting of earthquakes and the other consisting of explosions. We can think of each set of measurements as a point in an M-dimensional space, so that the earthquakes constitute one swarm of points and the explosions another. In many similar problems such swarms for different populations would overlap significantly so that separation can only be accomplished at the cost of occasionally mistaking each population for the other. However, it usually turns out when explosions and earthquakes are compared that there is a limited region of population overlap, a sizeable region containing only earthquakes and, in some cases, a region containing only explosions. In general, the earthquakes represent a large family of waveforms compared to explosions, and, with respect to some parameters, the explosion population is completely contained within that of the earthquakes.

300

Based on this observation, our procedure is to define a region, R_X, in the M-space which is just large enough to contain all the explosion points, and another, R_Q, which is just large enough to contain all the earthquakes. These regions can be defined in various ways, one convenient definition being the smallest convex body bounded by hyperplanar surfaces which includes the points. We now divide the entire space into four regions, as follows:

$$R_1 = R_X - R_Q \qquad \text{(points in } R_X \text{ but not in } R_Q\text{)},$$
$$R_2 = R_Q - R_X \qquad \text{(points in } R_Q \text{ but not in } R_X\text{)},$$
$$R_3 = R_X R_Q \qquad \text{(points in both } R_X \text{ and } R_Q\text{)},$$
$$R_4 = M - R_3 \qquad \text{(points in neither } R_X \text{ nor } R_Q\text{)}.$$

We envision using these regions to classify a new measurement by saying that if the corresponding point falls in R_1 that "explosions are known to look like that, but no earthquake in our experience does," and a converse statement if the point falls in R_2. In the case of R_3 or R_4 we are non-committal, in the former case because such measurements have been observed for both types, and in the latter because we have no observations in that part of the space at all. If a measurement falls in region R_1 or R_2, it is tempting to make a quantitative statement of confidence in the decision made. However, in the absence of assigned probability measures, any numerical assignment of confidence would be highly arbitrary. Even so, if one makes a measurement and the corresponding point lies in the earthquake-only region (R_2) and is very far from the nearest boundary of R_X (i.e., far from any explosion point), one feels more confident of his decision than if the measurement lies near R_X. We shall not pursue the point further in this report.

The procedure described above in somewhat mathematical terms should, of course, be used only as a guide, but some sort of rough separation with exclusive regions should be attempted. In particular, we are interested in regions R_1 and R_2, since an event falling in either is then positively identified. Of course, the entire separation procedure should be preceded by such binary screening operations as tests for epicenter (in or out of the region being monitored) and depth (any reliable seismic evidence of depth puts the event out of the explosion category).

This procedure may be used as a way of combining several measurements, each of which can meaningfully be used separately as a single-variable discriminant. However, in the multidimensional case, measurements can be included which have no discrimination significance by themselves, such as magnitude. In this case it is the nature of the dependence of one or more discriminants on magnitude which is diagnostic of the source.

In the one-dimensional case, i.e., discrimination based on the value of a single quantity, the regions described above reduce to simple intervals. Thus, taking complexity as an example, both explosions and earthquakes attain values near zero, but the largest value for explosions is 2.7. Hence, to use this measurement alone, we would classify an event with complexity

greater than 2.7 as an earthquake. To be more conservative, one would probably increase this threshold a little, and be non-committal regarding any value greater than 10.0 (region R_4). In this case there is no region R_1 because explosions attain no values not also attained by earthquakes.

Having established these regions for one pair of reference populations, one would like to test them on a second pair. Given only the reference population itself, we can only establish the four regions and see how many earthquakes fall in R_2 and how many explosions fall in R_1. The corresponding percentages can then be interpreted as estimated performance characteristics. In other words we can only say, on the basis of regions established on one pair of populations, that a certain percentage of the earthquakes and another percentage of the explosions of a second very similar pair of populations would be correctly identified. It is in this sense that the discriminants are evaluated, singly and in combination, in the next section.

It would be desirable to have a definition of what constitutes satisfactory discrimination performance. Since perfect separation is clearly desirable, one is really asking how useful imperfect separation is, and this in turn depends upon the political ground rules. If one fails to identify an explosion, then the entire system has simply failed to function. If this happens only rarely, then such an error may be tolerable, since one can still gauge the level of testing activity of the countries being monitored. However, in most discussions it is assumed that this error is unacceptable, and that all events are explosions until proven to be earthquakes. The error of failure to identify an earthquake as such may now lead to an inspection and the permissible rate of falsely triggered inspections, while no doubt very small, is totally dependent on the terms of a treaty. It is therefore, beyond the scope of this report to give a numerical definition of satisfactory discriminant performance and we shall let the reader judge the results for himself. It must be kept in mind that our performance percentages refer to various discriminant combinations as applied at a single station. We do not suggest that discrimination be performed, in actual operation, using data from one station if it is at all possible to obtain measurements at other stations of a network.

V. DISCRIMINATION PERFORMANCE

We have already described, as an example in section IV, how complexity would be used alone as a discriminant. A threshold complexity is chosen, slightly higher than that of the most complex explosion, and events having larger values are classed as earthquakes, i.e., as being in the R_2 region. There is no classification of events as explosions (no R_1 region), since there is no evidence that explosions attain values lower than those ever attained by earthquakes. Identification percentages, based on our populations themselves, are given in table II.

The use of spectral ratio alone as a discrimination procedure is closely analogous, except that now high values are associated with explosions. A threshold near 0.425 (the lowest spectral ratio observed for explosions) is chosen to form the boundary of the R_2 region, and events with smaller values are classed as earthquakes. Again, no really unique values are attained

302

by explosions, except when compared only with our screened population of apparently shallow events, in which case nearly all the explosions have higher values than any earthquake. Although spectral ratio shows promise of providing positive identification of explosions as such, we would rather not quote performance figures of this type based on our present data, since they would depend heavily on our single-station screening for depth based on pP. Earthquake identification percentages are given in table II.

When we plot complexity against body-wave magnitude, we find a much better separation than when complexity is used alone. Figures 14 and 15 show such scatter diagrams for two populations: all earthquakes and shallow earthquakes, respectively. The inadequacy of our data with respect to overlap in magnitude is clearly evident in figure 15. According to this plot, we could easily establish an earthquake-free region which also contains nearly all the explosions (type R_1 region), but it is clear that we would merely be discriminating on the basis of magnitude! However, R_2 regions can be defined which seem not to be entirely functions of magnitude, and they are shown on figure 14 and 15 as the regions to the left of the dashed curves. The behavior of these curves below magnitude 4.9 is rather arbitrary, in view of our lack of explosion data, and we have drawn them in a way which is perhaps unjustifiably favorable to the performance of complexity as a discriminant. The performance figures in table II are just the percentages of the various earthquake populations lying within these R_2 regions.

When spectral ratio is plotted versus magnitude, a real separation begins to appear. Figures 16 and 17 are analogous to 14 and 15 with respect to populations. Again we refrain from defining an R_1-type region and the associated explosion identification percentage, although the data is very encouraging that such a region exists. R_2-type regions are again outlined by dashed curves, and earthquake identification percentages are given in table II. Note that the separation is perfect when our shallow population is used. Using the total population, four earthquakes cannot be distinguished from explosions. However, all four of these were reported

Table II
EARTHQUAKE IDENTIFICATION PERCENTAGES

Conditions Defining Earthquake Population	All Data	Magnitude ≥ 4.8	Shallow Events	Shallow and Magnitude ≥ 4.8
Size of Earthquake Population	85	32	48	12
Earthquake Identification Percentages Using:				
Complexity Alone	36.5%	43.4%	22.9%	16.7%
Spectral Ratio Alone	57.6%	65.6%	62.5%	66.7%
Complexity vs. Magnitude	84.7%	59.4%	87.5%	50.0%
Spectral Ratio vs. Magnitude	95.2%	90.6%	100.0%	100.0%
Spectral Ratio vs. Complexity vs. Magnitude	98.8%	96.9%	100.0%	100.0%

by USCGS and assigned depths in excess of 50 km. Events of this kind would probably have been screened out as deep by a network of stations on the basis of P-arrival times alone, and these four events in particular were judged to be deep from our single-station data on the basis of pP identification.

We have also plotted dominant period versus magnitude in order to assess the discrimination potential of this simple discriminant. Figure 18 is such a plot for the shallow earthquakes. A fairly good separation is shown here, but we are reluctant to claim performance figures because of the coarse quantization of the data (0.1 second increments) and the subjectivity of the measurement process itself. A very favorable interpretation of figure 18 would credit this display with correctly identifying 41 of the 48 earthquakes, i.e., 85.4%, while the corresponding percentage for the total earthquake population (not shown) is about 70%.

With our population of shallow events, there is no point in considering three dimensional discrimination, based on plotting spectral ratio versus complexity versus magnitude, since perfect separation is found in two dimensions. Since the separation is imperfect on the total population (because of the presence of deep events), it makes sense to try the three-dimensional plot in this case. The simplest way to use the three-dimensional data is to see if an event is identified as an earthquake by either the complexity versus magnitude or the spectral ratio versus magnitude criterion. Geometrically, this corresponds to extending both of the two-dimensional R_2 regions into the corresponding third dimension and then taking the union of the resulting three-dimensional regions. In general one could do better than this in three dimensions, but with our data base it is unnecessary, since three of the four earthquakes which are ambiguous on the spectral ratio versus magnitude criterion are clearly rejected on the complexity versus magnitude criterion, and the fourth is hopelessly embedded in the explosion swarm of points. The reason these three events are rejected by complexity is that they all have a phase (picked as pP) in the second time window used for the complexity measurement, thus raising the value of that parameter. The fourth event is from Rumania, reported by USCGS at a depth of 158 km. Its pP phase is visible on our data at 38 seconds after P, just too late to influence the complexity. The three-dimensional discrimination percentages given in the first two columns of table II represent identification of all but this one earthquake.

It is interesting to note that a set of five earthquakes, lying roughly on a line parallel to the dashed curve on our spectral ratio versus magnitude plot (figure 16) and very close to that line, are all rejected by the complexity versus magnitude criterion. All had pP phases on our data, and three were reported by USCGS at depths 26, 28 and 33 (R) km. One needs to be wary of the effect of PcP on complexity, but it appears that complexity of P waveform may be a useful adjunct to spectral ratio, even if it is only responding to pP.

We have not tried to derive a quantitative regional dependence of discrimination performance because the only well-defined region in our data is the Kurile-Kamchatka group of earthquakes and only Longshot represents an explosion in a similar kind of region. The non-

304

Kurile-Kamchatka earthquakes are all continental in origin, but are very widely distributed in location. However, we have seen from the histograms that these continental earthquakes have lowe₁ spectral ratios, as a group, and this is reflected in an even wider separation of the earthquake and explosion populations on a spectral ratio — magnitude plot. The elimination of Kurile-Kamchatka events has little effect on the performance of complexity, decreasing the 87.5% figure (for shallow events using a complexity — magnitude plot) to about 70%.

VI. CONCLUSIONS

We summarize our conclusions here in terms of the objectives outlined in the Introduction. We hesitate to draw any really firm conclusions from a study based upon such limited, unbalanced populations as is this one, but we feel that the following statements are justified by the facts.

A. General Effectiveness of the Short-Period Discriminants

Waveform complexity appears to be a discriminant of rather limited usefulness. Used alone it is probably not a satisfactory discriminant, in the sense discussed in section IV. The results of the present study on this point are in remarkable agreement with earlier published results of ours, [8] on a different population, where an identification percentage of 15.8% was found. The complexity was defined differently in this earlier study, being an average value of the complexities measured on individual single-sensor waveforms from a number of subarrays. In that report, undue attention was perhaps drawn to the performance that would result (87%) if we ignored the Novaya Zemlya event. The analogous figure for our present population of shallow events is 62.5%. Since Novaya Zemlya is probably not the only source of complex explosions, it does not seem prudent to treat this event as an anomaly and forget it. Complexity looks much better when displayed as a function of magnitude, but our data is severely limited by the magnitude disparity and the scatter diagrams (figures 14 and 15) do not suggest that separation would be as good as the table II values for a population including larger earthquakes and smaller explosions.

Spectral ratio, used alone, would not provide really useful separation by a single station, but when plotted against magnitude the results are most encouraging. The separation found here is complete, after screening for depth, and very nearly so for the total population. Moreover, the scatter diagrams (figures 16 and 17) suggest that the separation will persist with larger earthquakes and smaller explosions. Regional effects, if real, seem to work in our favor, by increasing the separation. We plan to pursue the study of this discriminant, extending the populations and varying the type of preprocessing used. We also plan to try variations and simplifications in the definition of spectral ratio.

B. Magnitude Thresholds for Short-Period Discriminants

In section III we quoted the magnitude 4.3 as a threshold for reliable measurement of either of the short-period discriminants studied here. This is a strictly qualitative number, based on studying the waveforms and spectra of all the marginal events in our data base, and making

305

a judgment on the degree to which the measure. :i seemed to be affected by the noise. Since the measurement quality is hardly determined by magnitude alone and is in any case very difficult to measure quantitatively, we feel that 4.5 is a reasonable threshold magnitude for discriminant measurement on Sino-Soviet earthquakes by LASA. It has been conservatively estimated [4] that surface waves are reliably detected at and above magnitude 4.9 for shallow Sino-Soviet earthquakes by LASA, hence we conclude that short-period discrimination by means of spectral ratio is potentially a very valuable supplement to the established long-period technique. The average distance for earthquakes used in this study was 68°, while nearly all the explosions were at 83°. A station with the sensitivity of the Montana LASA at an average distance of 30° from its sources of events would have nearly a half-magnitude advantage in signal strength, and hence could push the measurement threshold down near 4.0. However, we do not know what to expect for the spectral ratios of explosions of that size, since this represents an extrapolation of our present data by a whole magnitude unit.

C. The Contribution of the Large Array to Short-Period Discrimination

In this study the large array was used only to form a preprocessed waveform of enhanced signal-to-noise ratio on which the discriminant measurements were made. The fact that we also used the resolving power of the array to provide epicenters is irrelevant to the evaluation of the array as an element in a world-wide network, since location (and to some extent depth) is determined by the network as a whole. Other ways of using the array in the discriminant-measuring process, such as measuring complexity and spectral ratio on subarray outputs and combining these, have not been considered here. Thus the discussion reduces to the characteristics of the single waveform produced by the array.

This waveform differs from the waveform produced by a single sensor or small array (such as a LASA subarray) in two ways. First, the signal-to-noise ratio is higher, by the equivalent of about three-quarters of a magnitude unit, on the array output due to the noise reduction resulting from the averaging of subarray waveforms. Second, the signal component of the waveform is the average of the time-aligned signal waveforms from individual subarrays, and is therefore representative of that part of the signal waveform which is common to all these subarrays.

From the point of view of signal-to-noise ratio alone, the array can be thought of as a means of providing a single output trace of unusually low noise level. While preserving the signal level of a typical LASA single sensor, which is comparable to or slightly higher than other western U. S. stations (in one study, [6] LASA magnitudes averaged 0.2 units higher than USCGS magnitudes), the LASA beam output has a noise level of about[6] 0.2 to 0.3 mμ (r.m.s. value in the 0.6 to 2.0 Hz band). It is natural to compare the array to other techniques for obtaining high signal-to-noise ratios, such as the development of especially remote, quiet sites, deep holes or vertical arrays. It is important to compare the LASA to other such stations on the basis of signal-to-noise ratio, not signal or noise levels alone, after which it becomes a matter of how much signal-to-noise gain is obtained as a function of station cost, a comparison which is equally relevant to the detection problem, as well as the discrimination problem.

The second factor, however, relates specifically to the large geometrical aperture of the array. It is well known that event waveforms vary greatly from subarray to subarray within LASA, presumably since each waveform is influenced by different parts of the earth's crust and upper mantle under the array. We would like to think that the beam waveform is closer to that portion of the source waveform that survives the long propagation path through the earth than is a single-sensor or subarray waveform. If this is so, then the beam waveform should be a more reliable one on which to measure discriminants than a waveform of comparable signal-to-noise ratio obtained from a single site. This conjecture can be tested only by carrying out the implied experiment, of which the present study represents one half. It would be very interesting to see the results of the other half, a large population study of short-period discriminant performance on single-station waveforms of comparable signal-to-noise ratio.

ACKNOWLEDGEMENT

REFERENCES

1. J. N. Brune, A. Espinosa and J. Oliver, "Relative Excitation of Surface Waves by Earthquakes and Underground Explosions in the California-Nevada Region," J. Geophys. Res., Vol. 68, 1963.

2. R. C. Liebermann, et al., "Excitation of Surface Waves by the Underground Nuclear Explosion LONGSHOT," J. Geophys. Res., Vol. 71, 1966.

3. P. E. Green, R. A. Frosch and C. F. Romney, "Principles of an Experimental Large Aperture Seismic Array (LASA)," Proc. IEEE, Vol. 53, 1965.

4. J. Capon, R. J. Greenfield and R. T. Lacoss, Long-Period Signal Processing Results for Large Aperture Seismic Array, Tech. Note 1967-50, Lincoln Labs., M.I.T., Lexington, Mass., 1967.

5. Staff, Seismic Discrimination, Semiannual Tech. Summ. Rept., Lincoln Labs., M.I.T., Lexington, Mass., 1967, p. 5.

6. E. J. Kelly, LASA On-Line Detection, Location and Signal-to-Noise Enhancement, Tech. Note 1965-36, Lincoln Labs., M.I.T., Lexington, Mass., 1965.

7. E. W. Carpenter, Teleseismic Methods for the Detection, Identification and Location of Underground Explosions, VESIAC Rept. 4410-67-X, VESIAC, Willow Run Labs., Univ. of Michigan, Ann Arbor, Mich., 1964.

8. Staff, Seismic Discrimination, Semiannual Tech. Summ. Rept., Lincoln Labs., M.I.T., Lexington, Mass., 1966, p. 7.
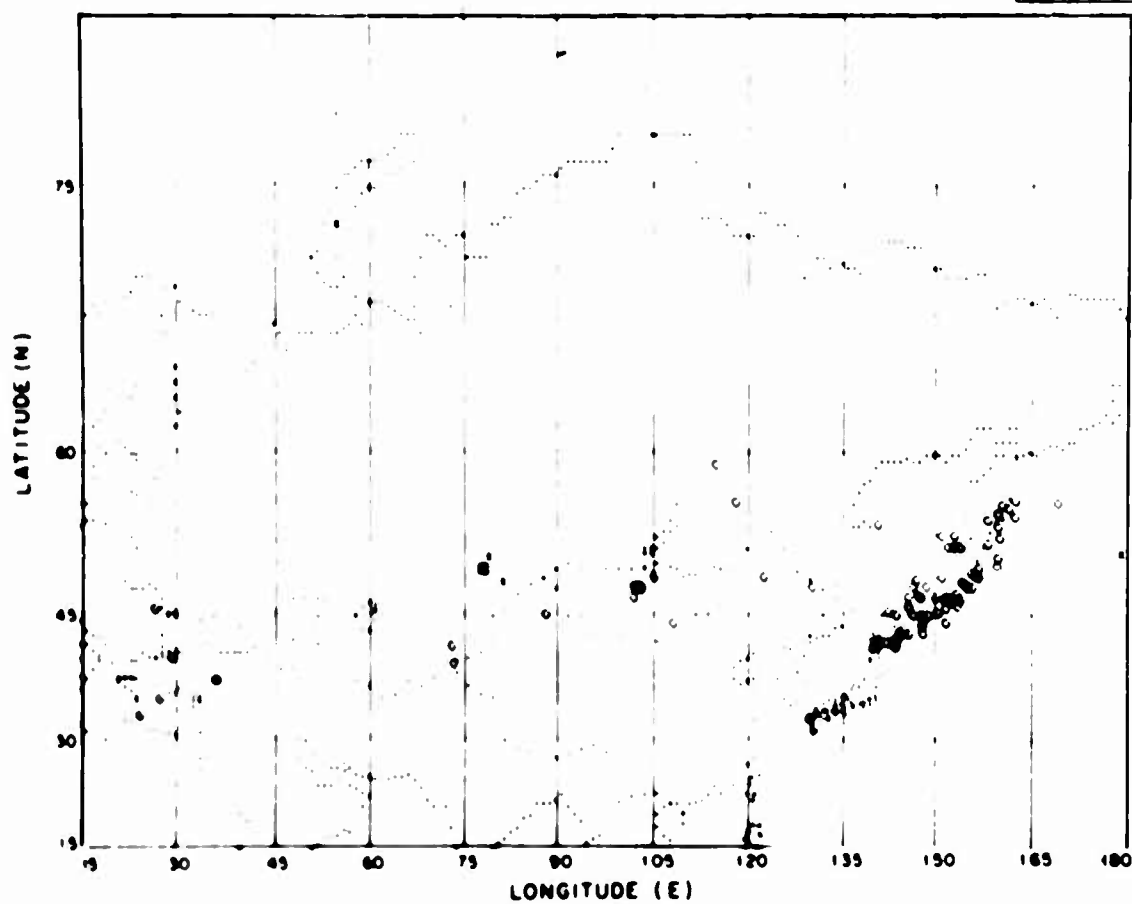
Fig. 1. Geographical distribution of earthquakes (O) and explosions (X).
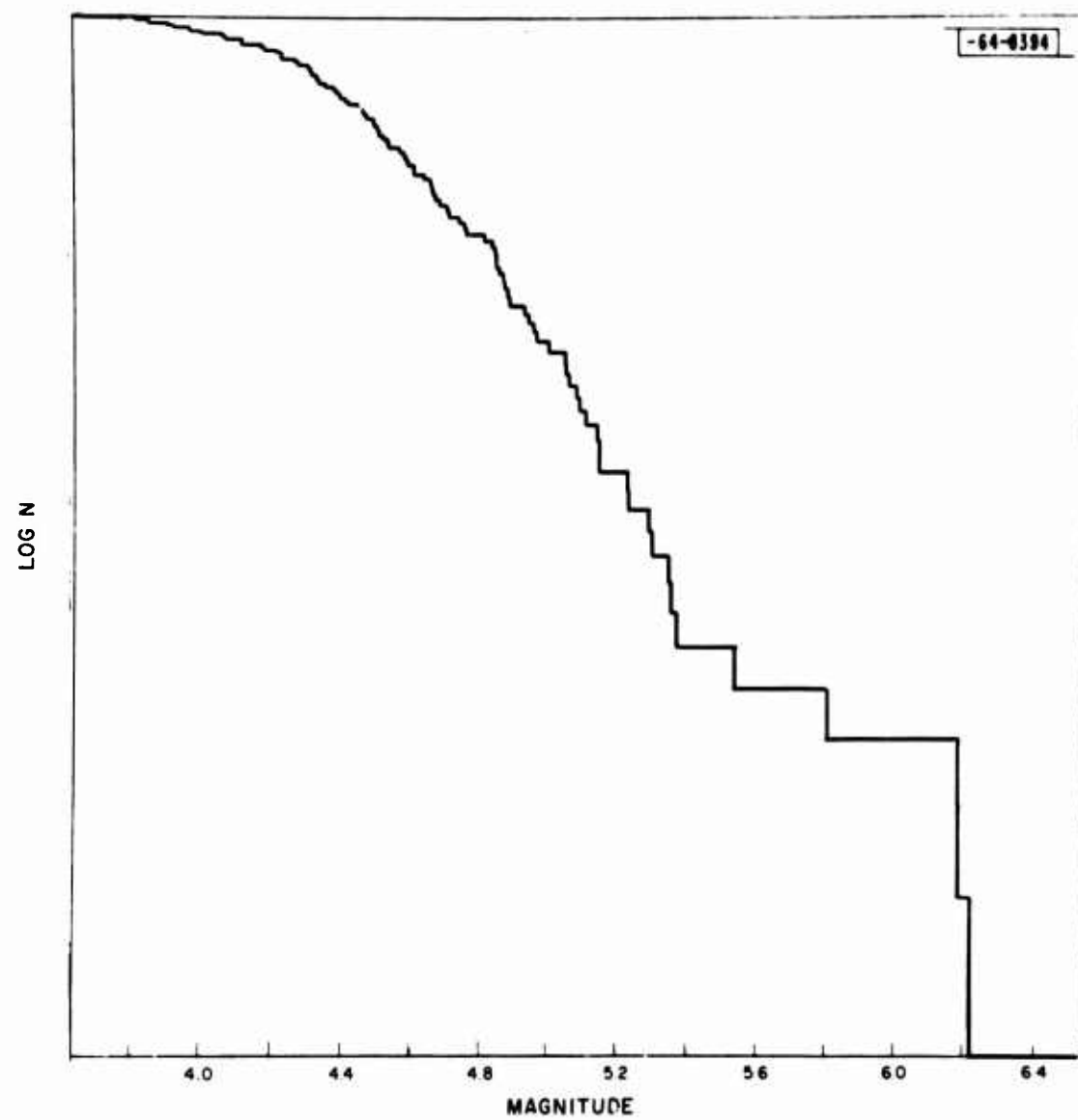
Fig. 2. Cumulative seismicity curve for the earthquake population. (Logarithm of the number of earthquakes exceeding a given magnitude vs magnitude.)
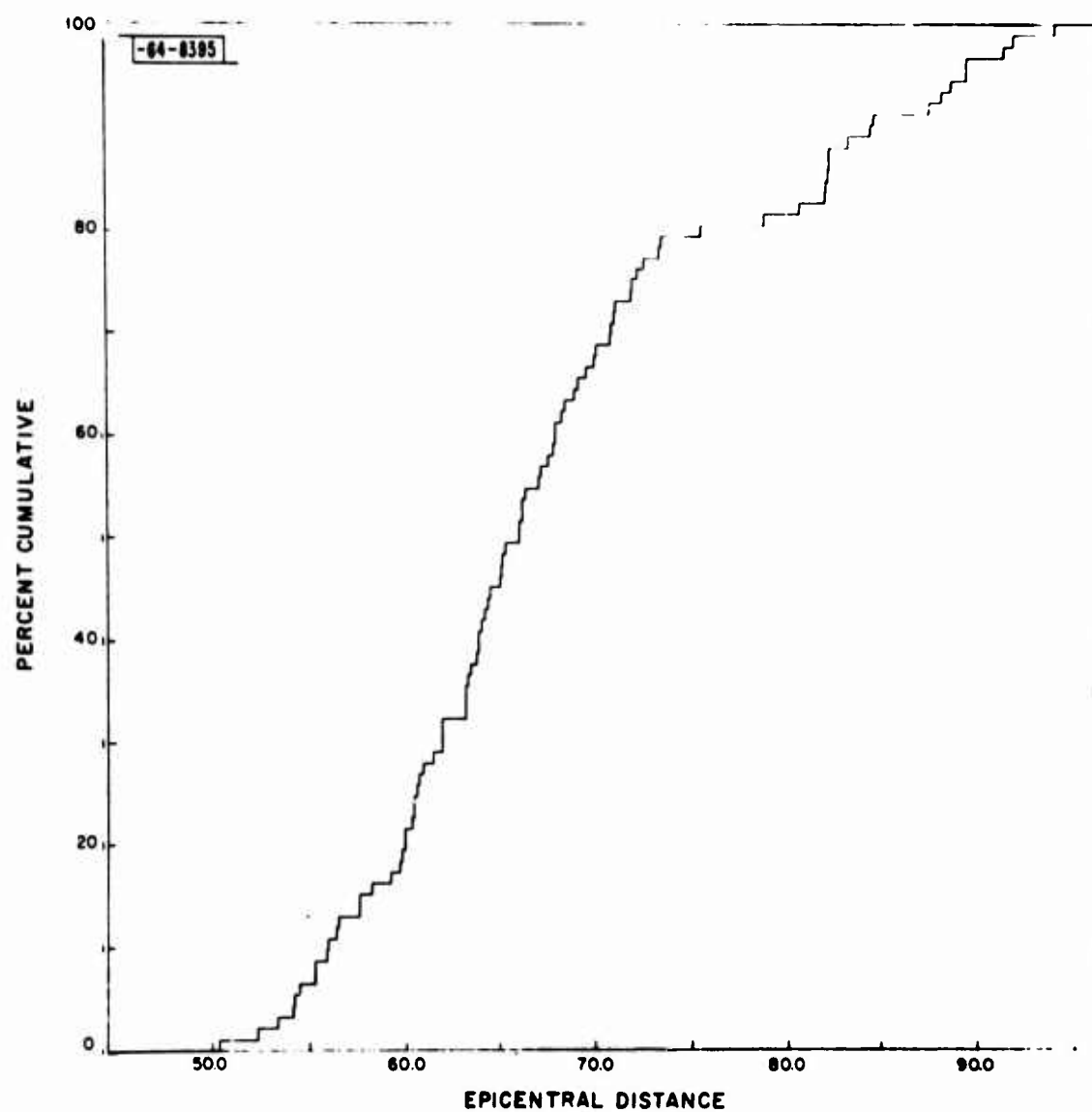
311

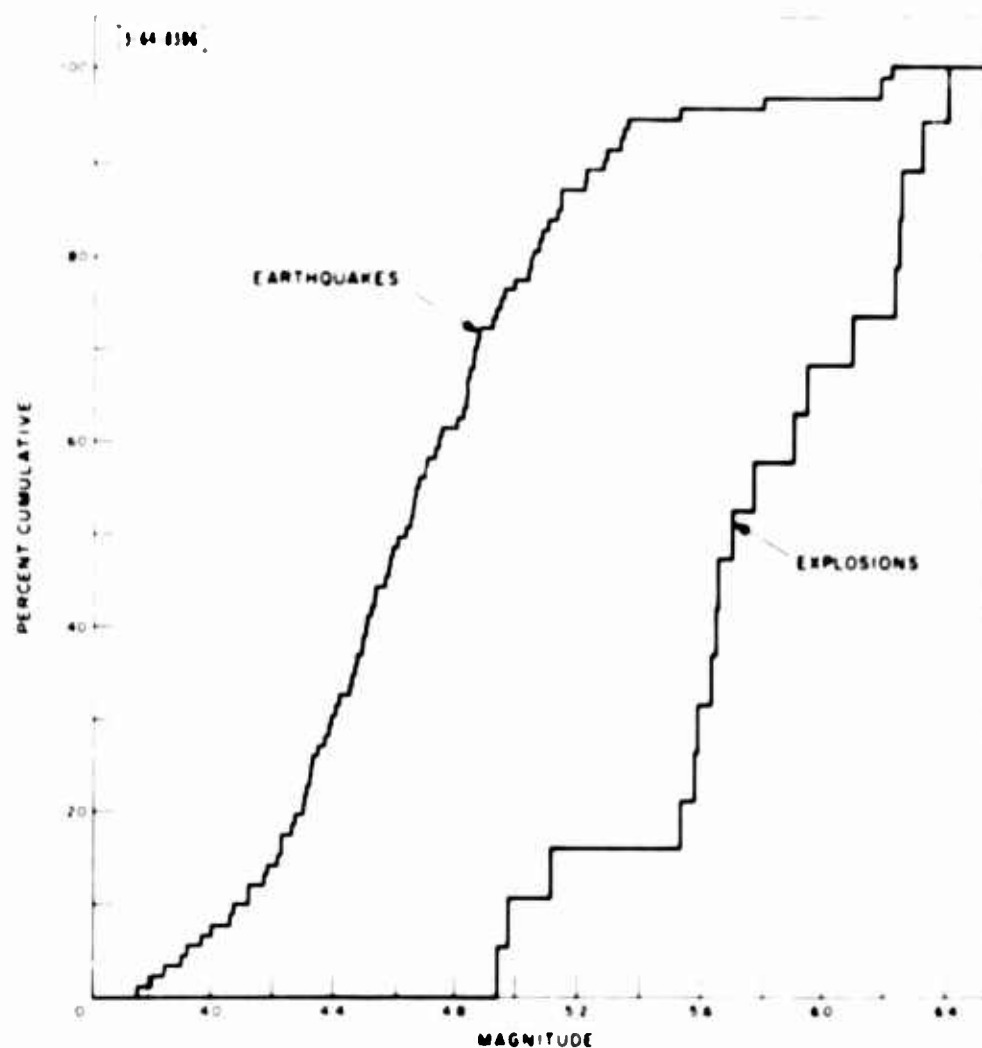Fig. 3. Cumulative histogram of epicentral distance for earthquakes.

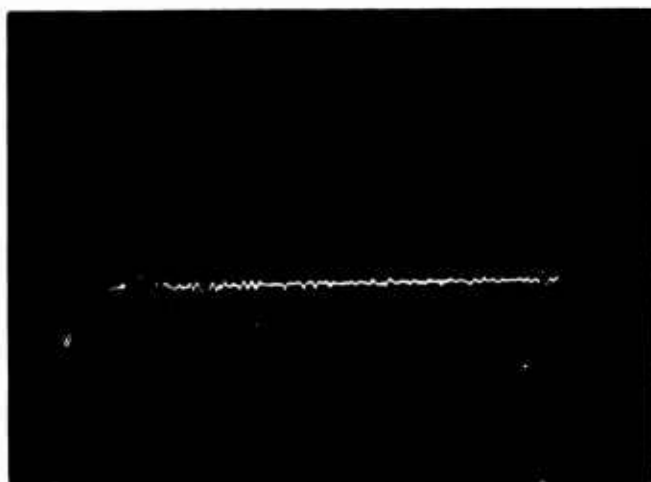Fig. 4. Cumulative histograms of measured magnitude for earthquakes and explosions.

Fig. 5.   Example of a waveform illustrating
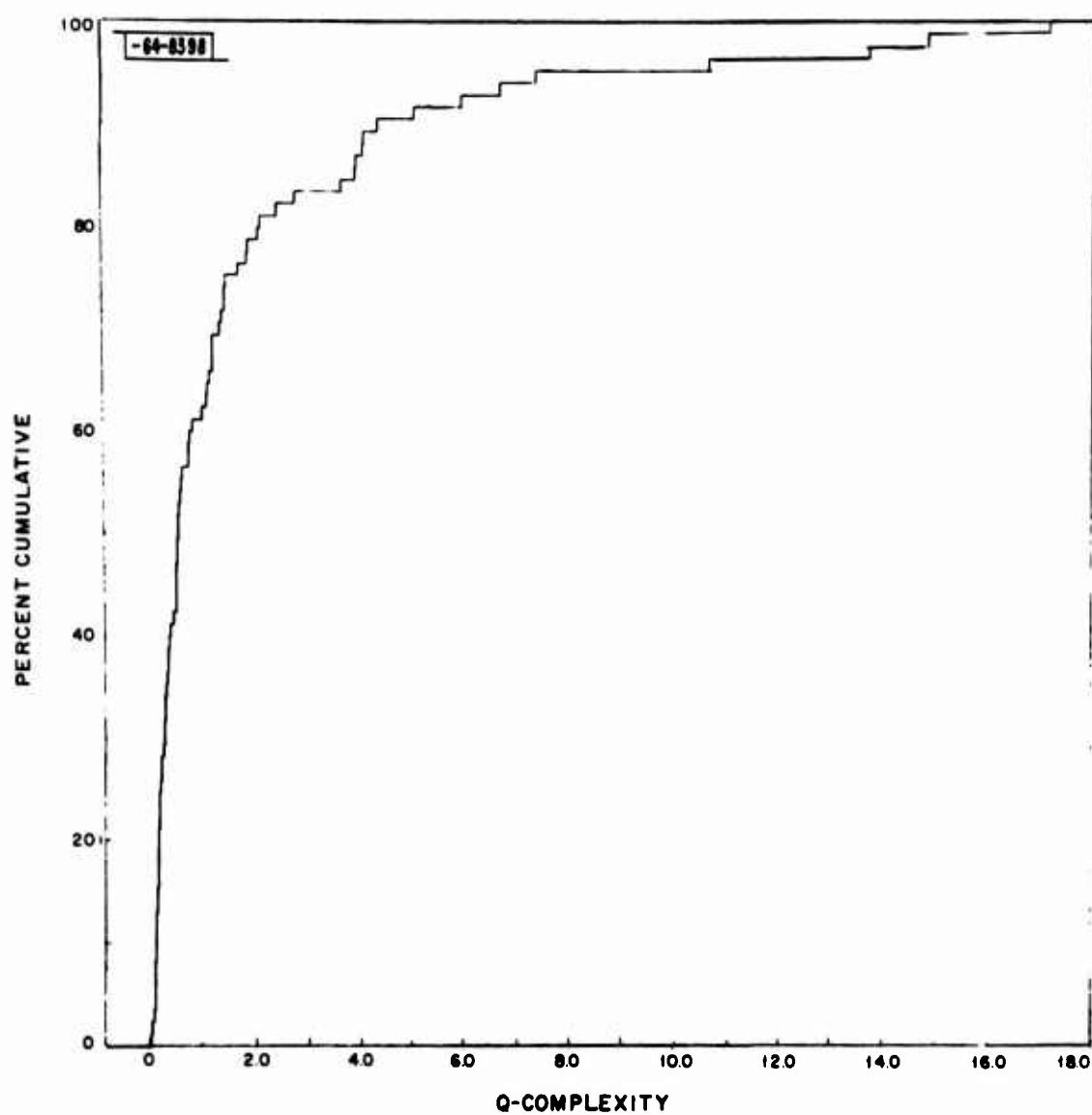the complexity measurement.

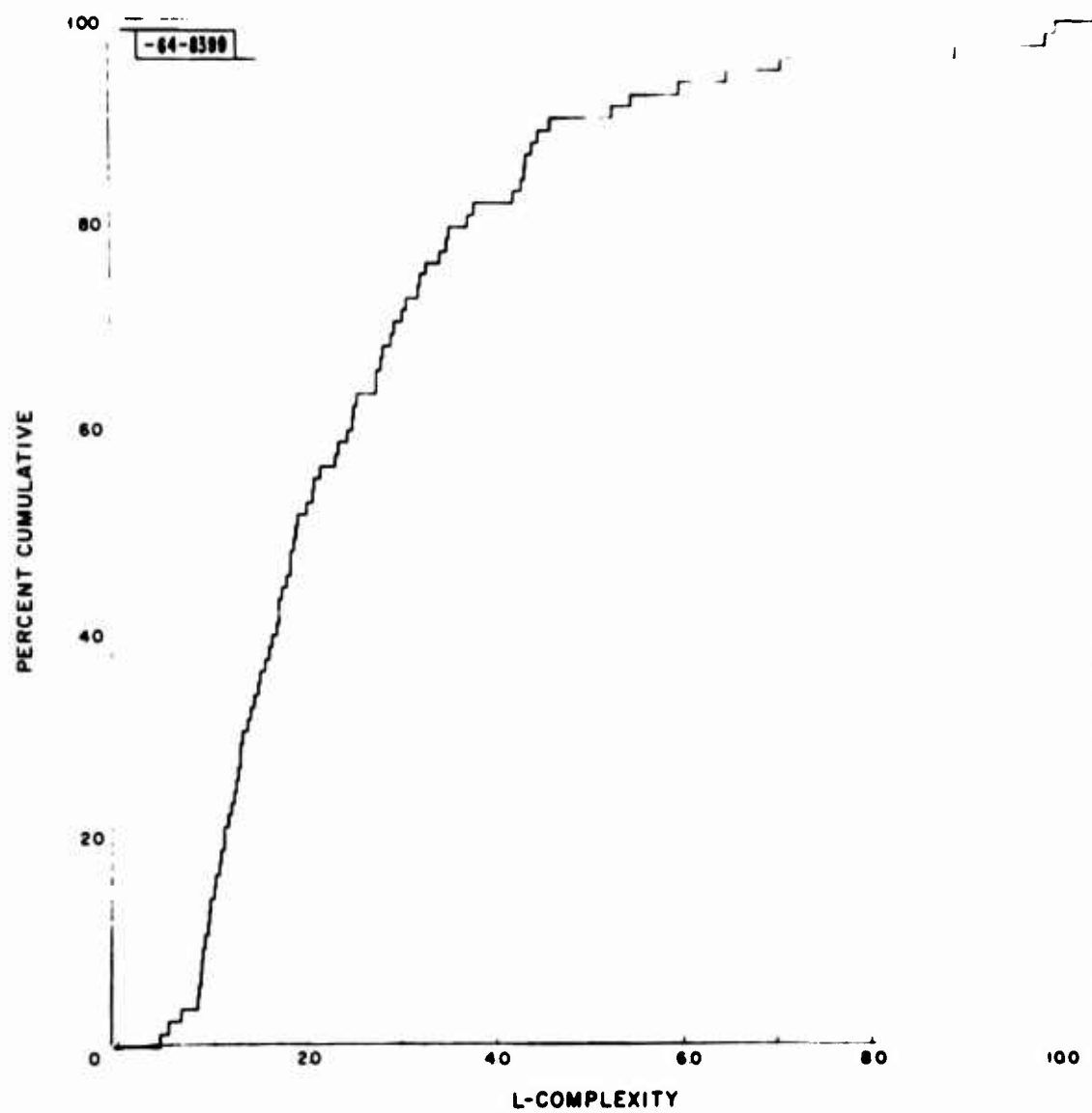Fig. 6. Cumulative histogram of quadratic complexity for earthquakes.

315

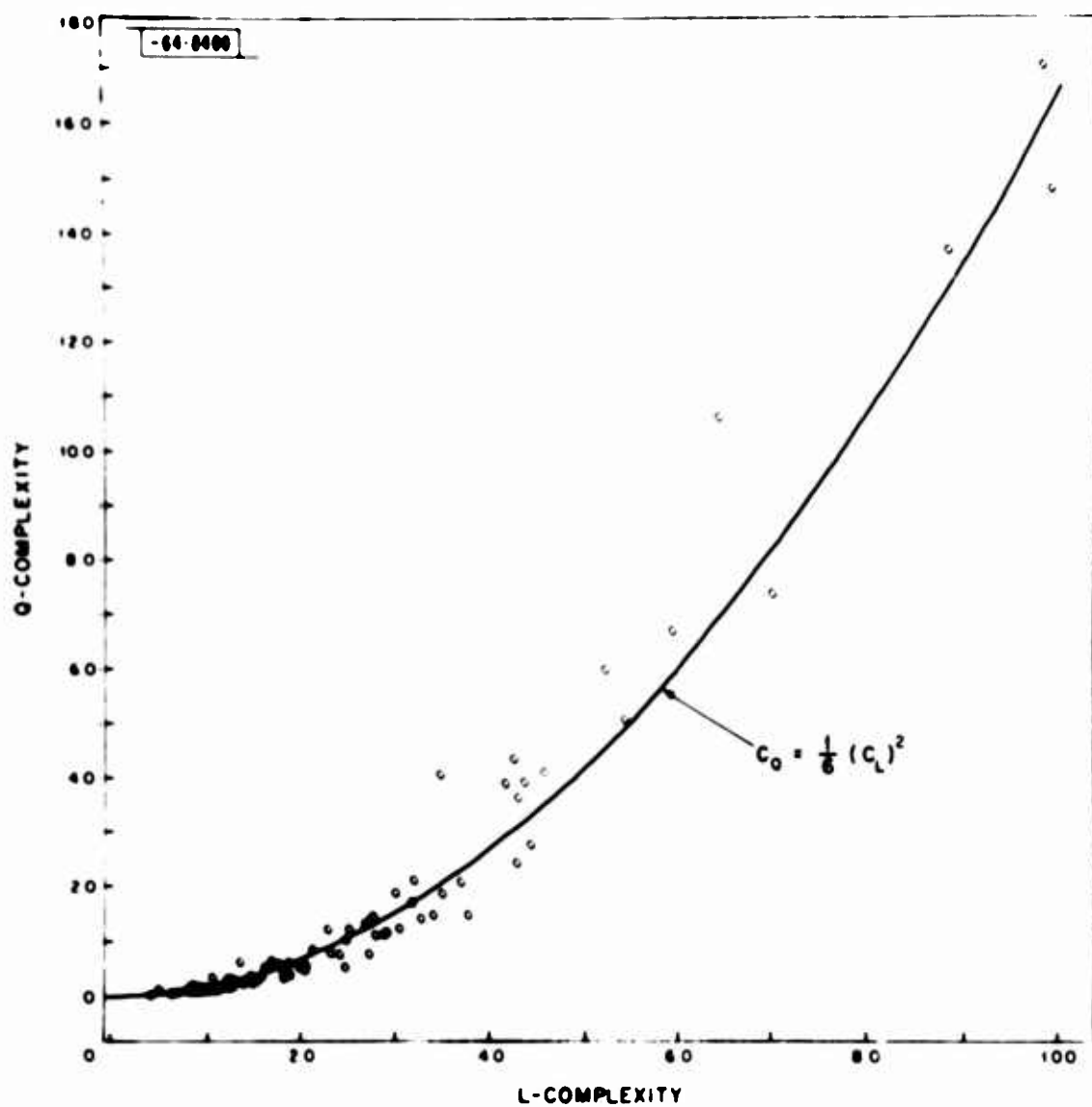Fig. 7. Cumulative histogram of linear complexity for earthquakes.

Fig. 8. Quadratic complexity $\underline{vs}$ linear complexity for earthquakes (O) and explosions (X).
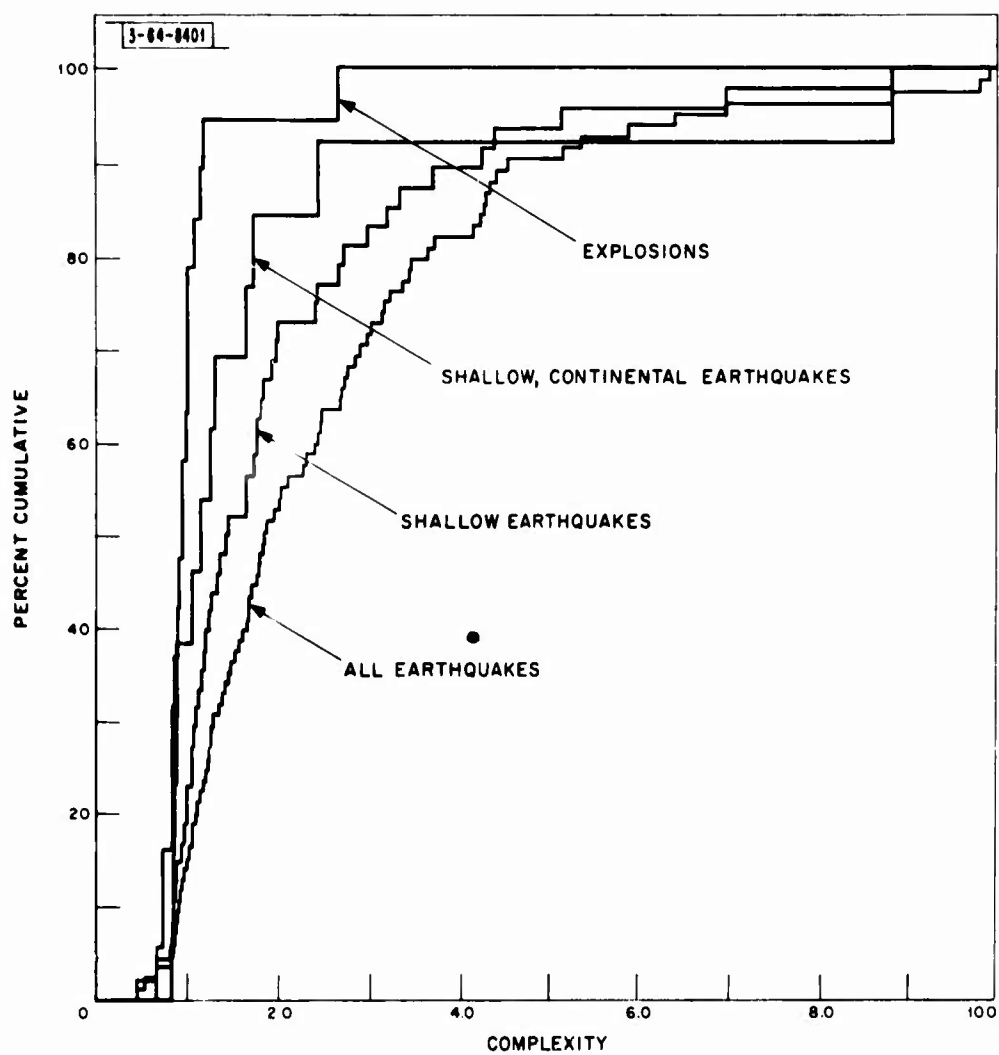
Fig. 9. Cumulative histograms of complexity for explosions and three earthquake populations.
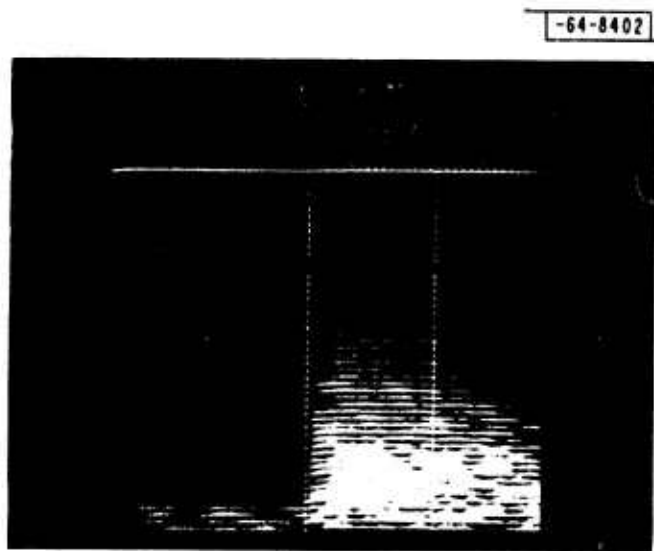
Fig. 10. Example of a sonogram illustrating
the spectral ratio measurement.
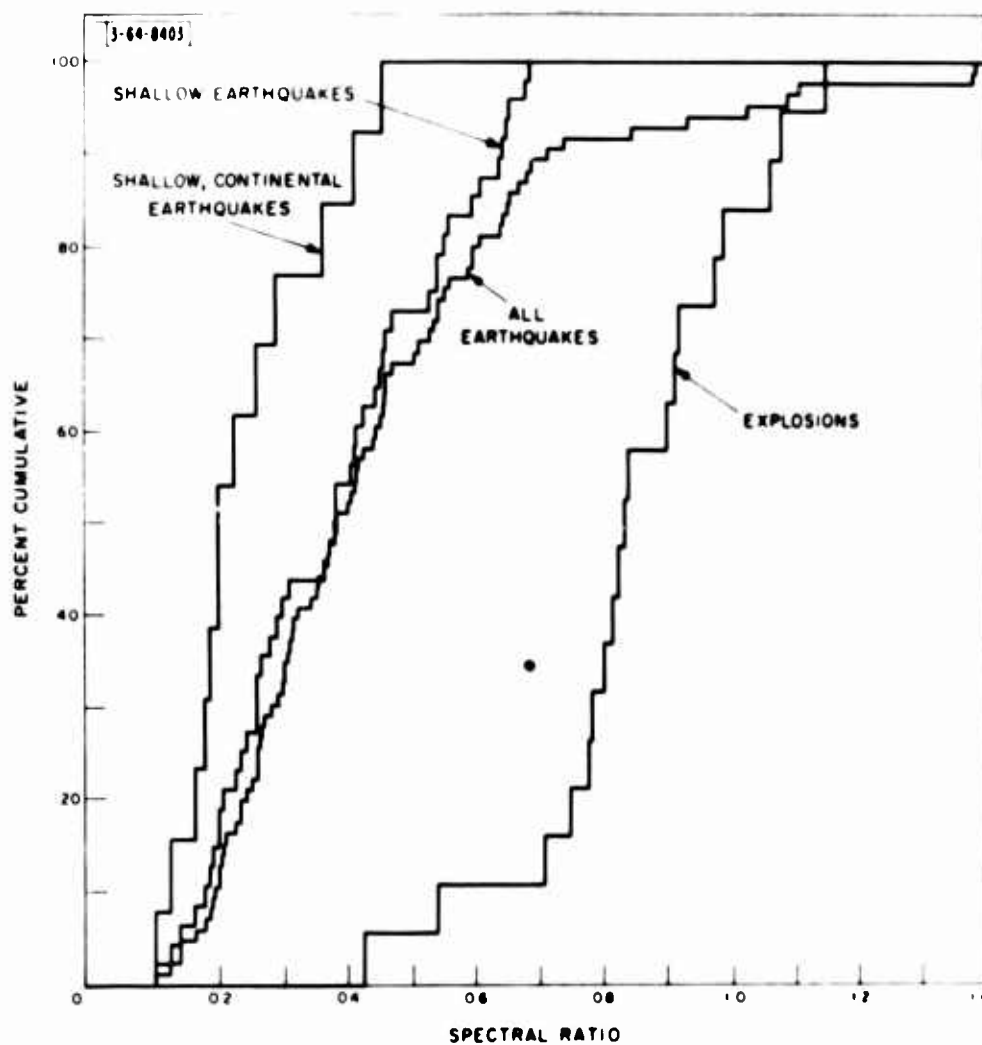
Fig. 11. Cumulative histograms of spectral ratio for explosions and three earthquake populations.
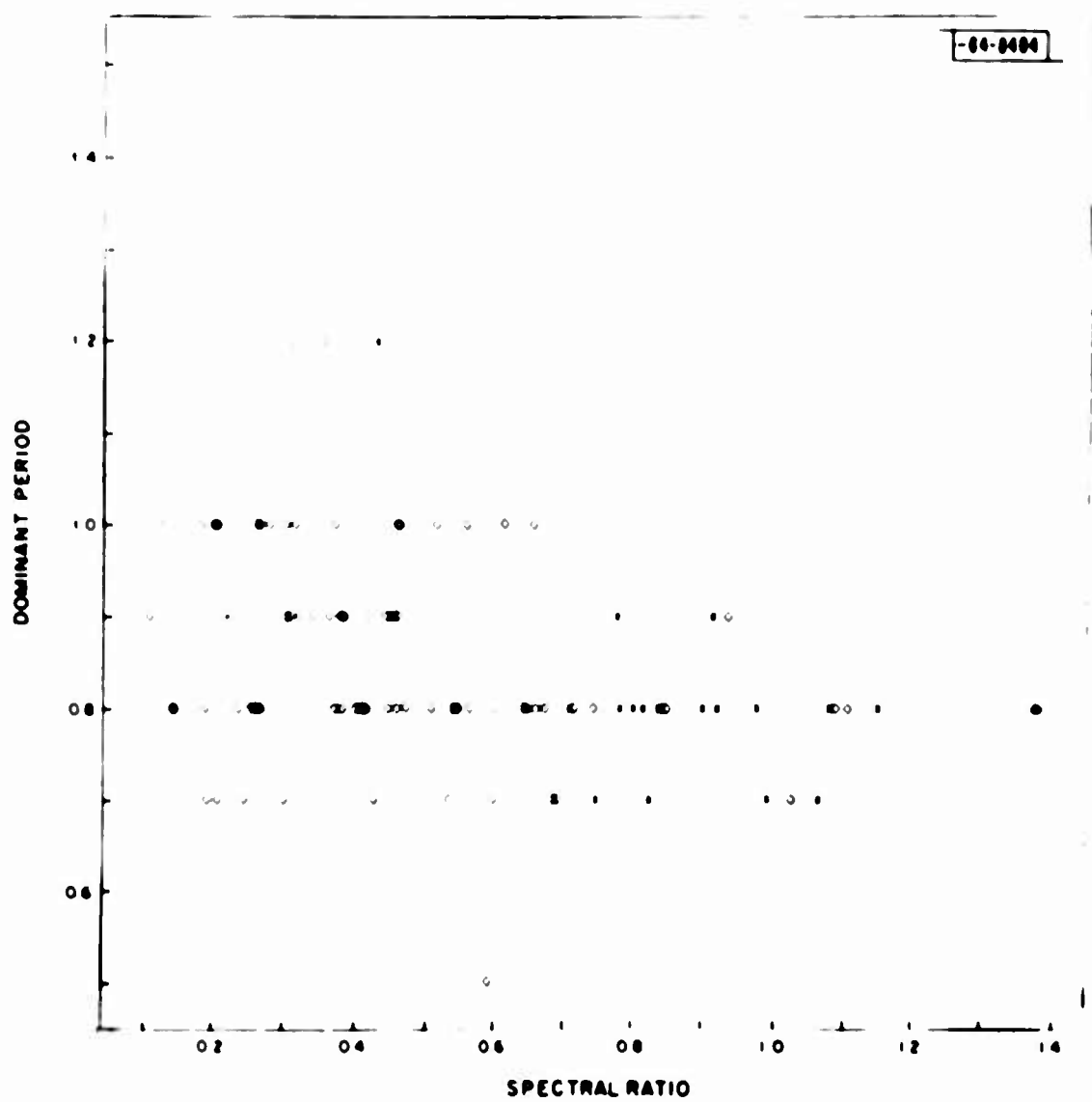
Fig. 12. Dominant period vs spectral ratio for 85 earthquakes (O)
and 19 explosions (X).

321
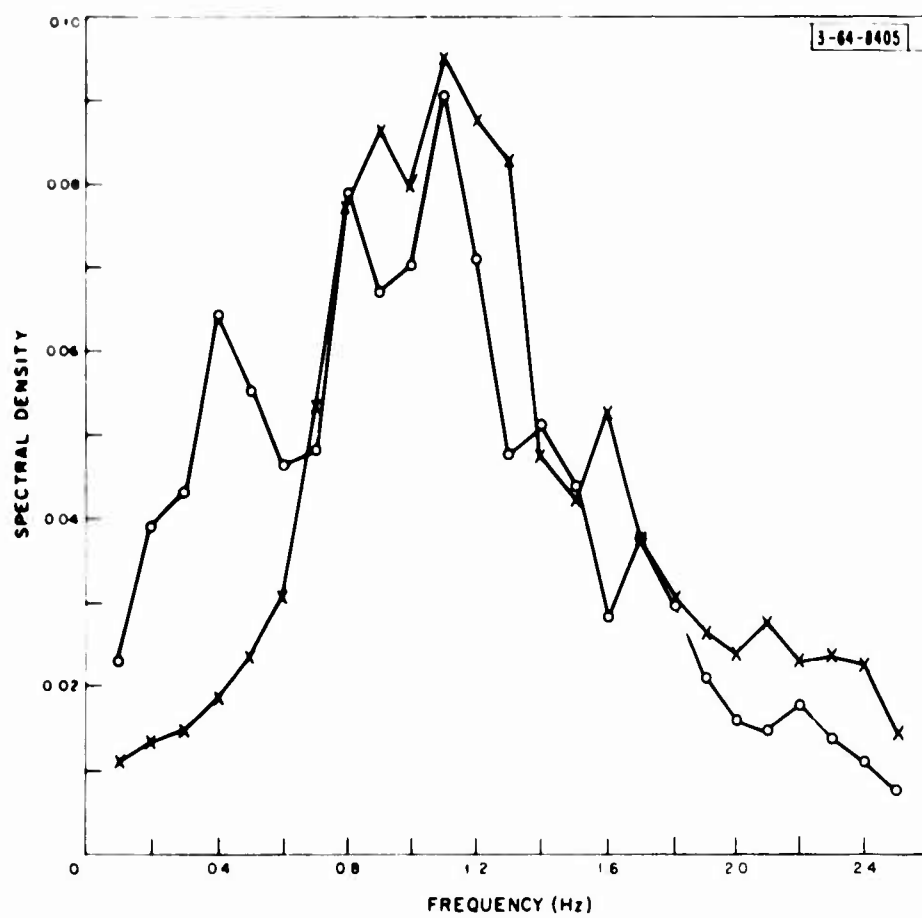
Fig. 13. Typical spectral densities for an earthquake (O) and an explosion (X). (Arbitrary vertical scale.)
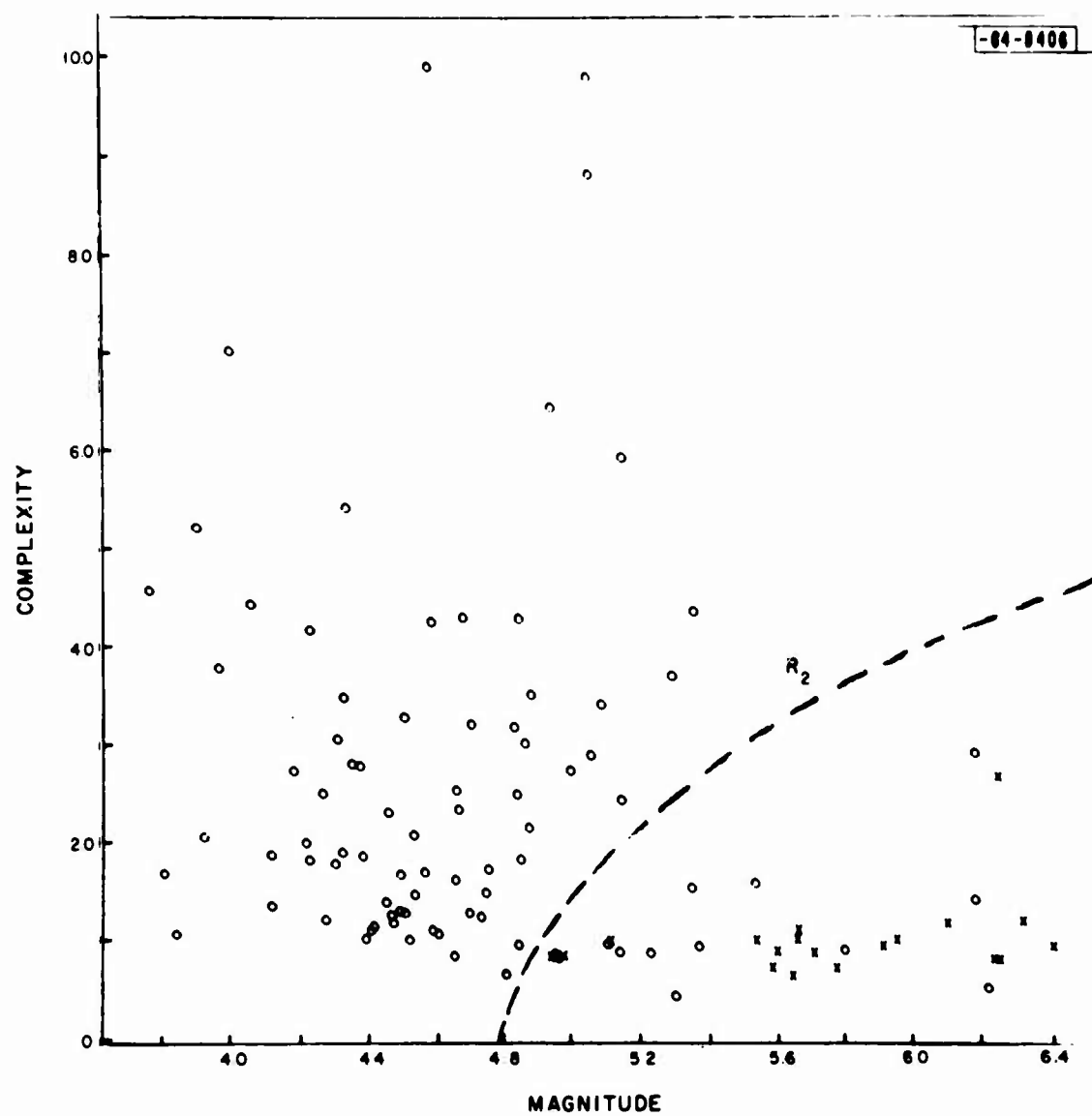
Fig. 14. Complexity vs magnitude for 85 earthquakes (O) and 19 explosions (X).
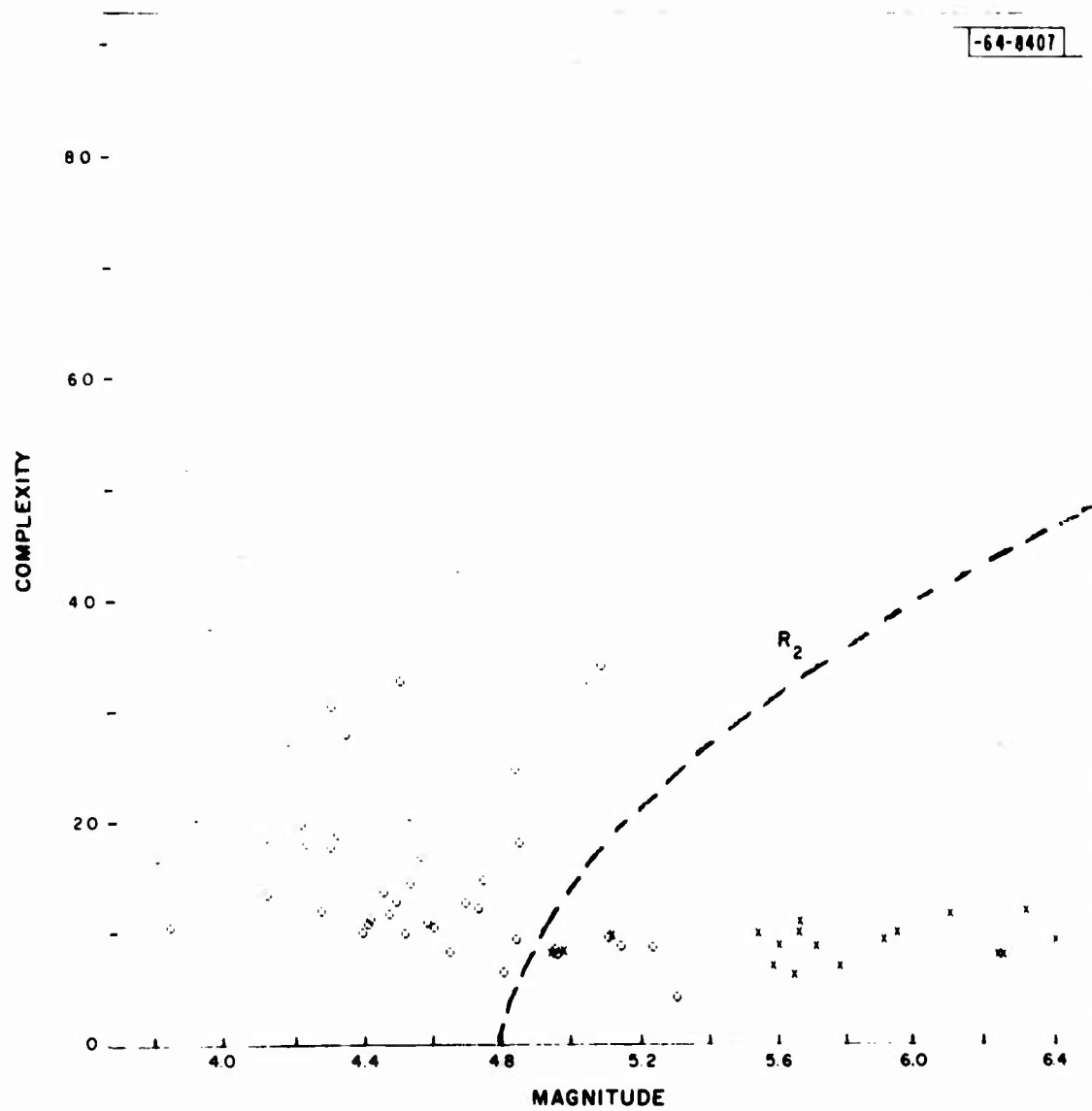
Fig. 15. Complexity vs magnitude for 48 shallow earthquakes (O) and 19 explosions (X).
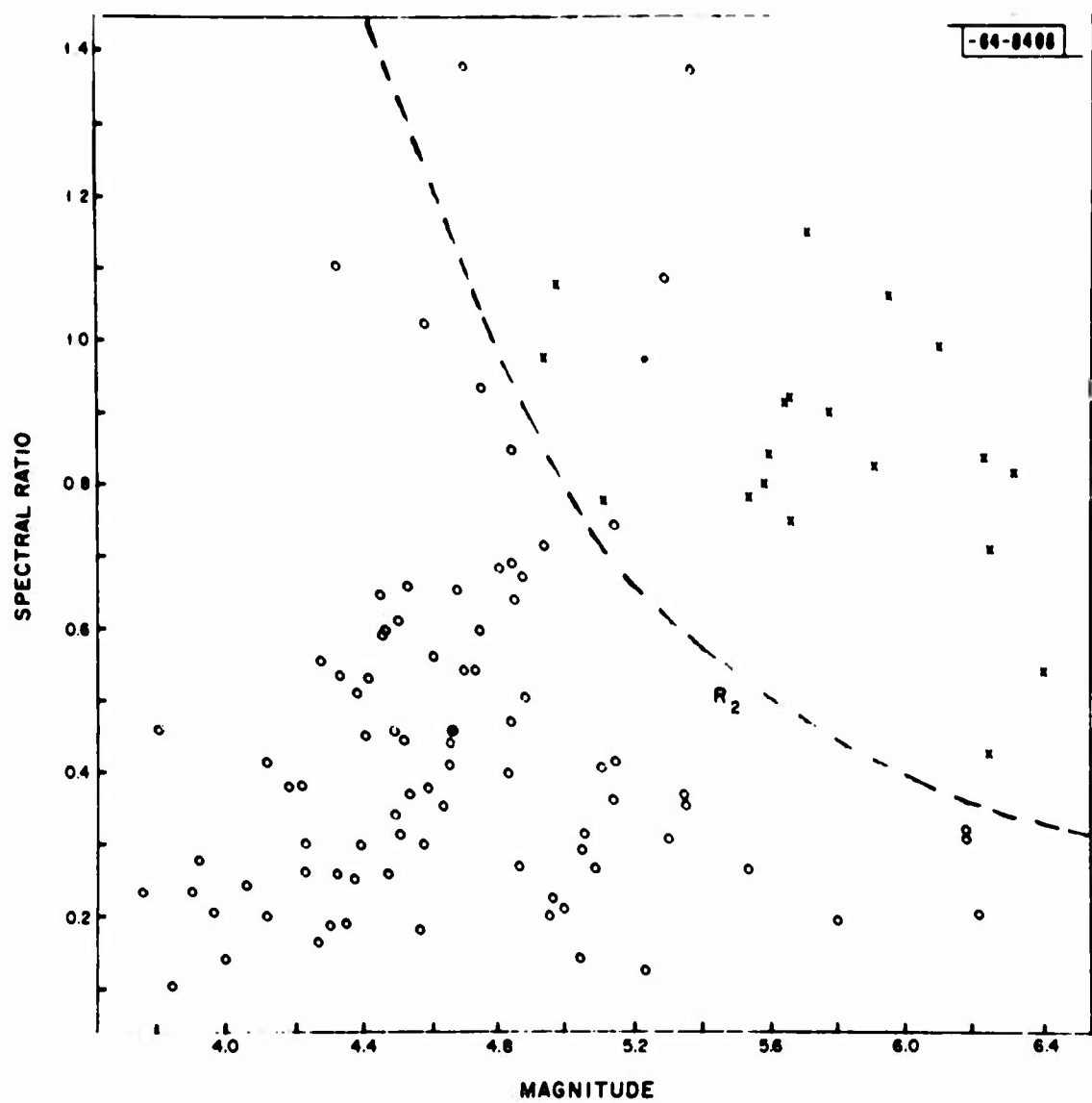
Fig. 16. Spectral ratio <u>vs</u> magnitude for 85 earthquakes (O) and 19 explosions (X).
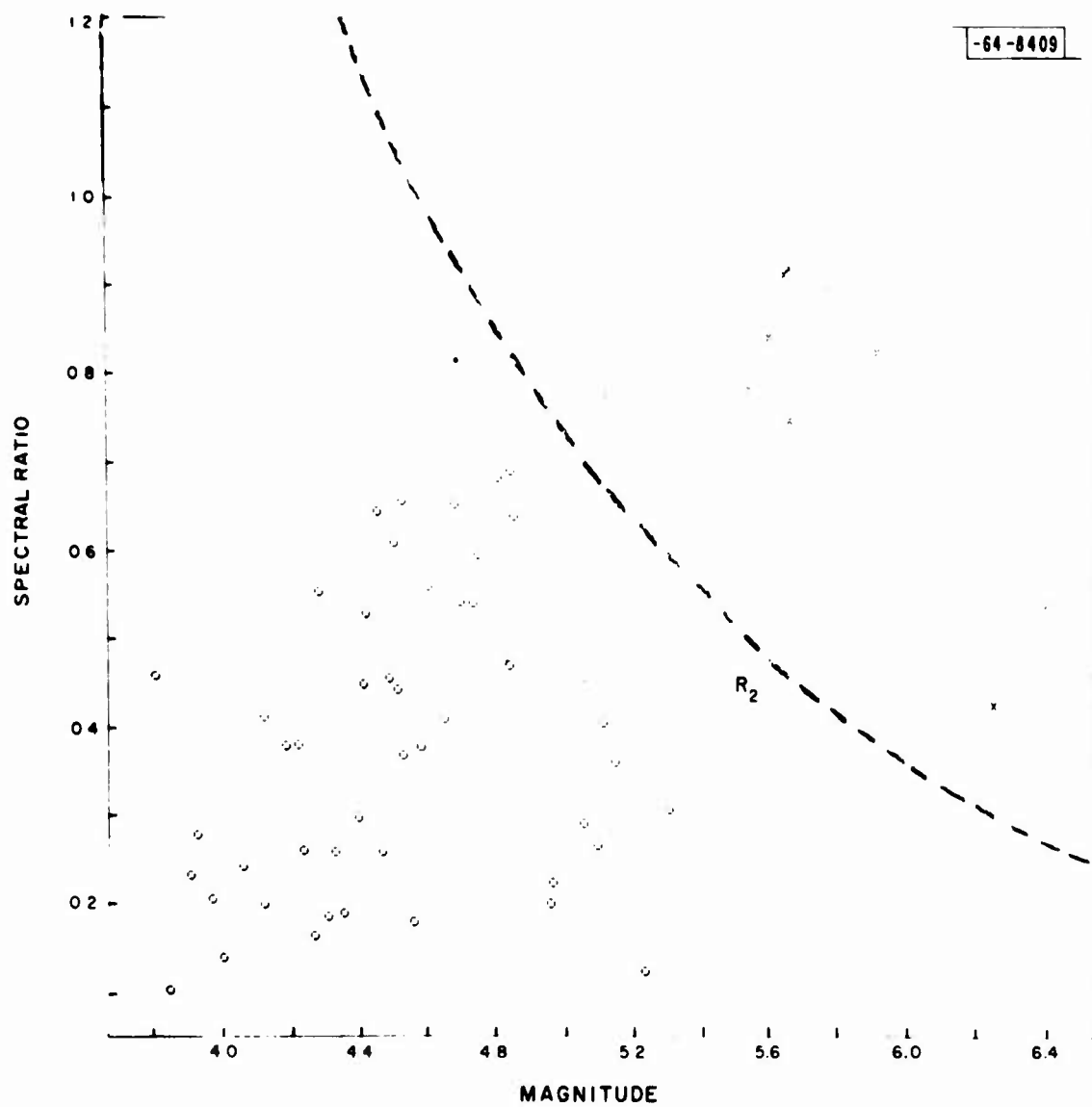
Fig. 17. Spectral ratio vs magnitude for 48 shallow earthquakes (O)
and 19 explosions (X).
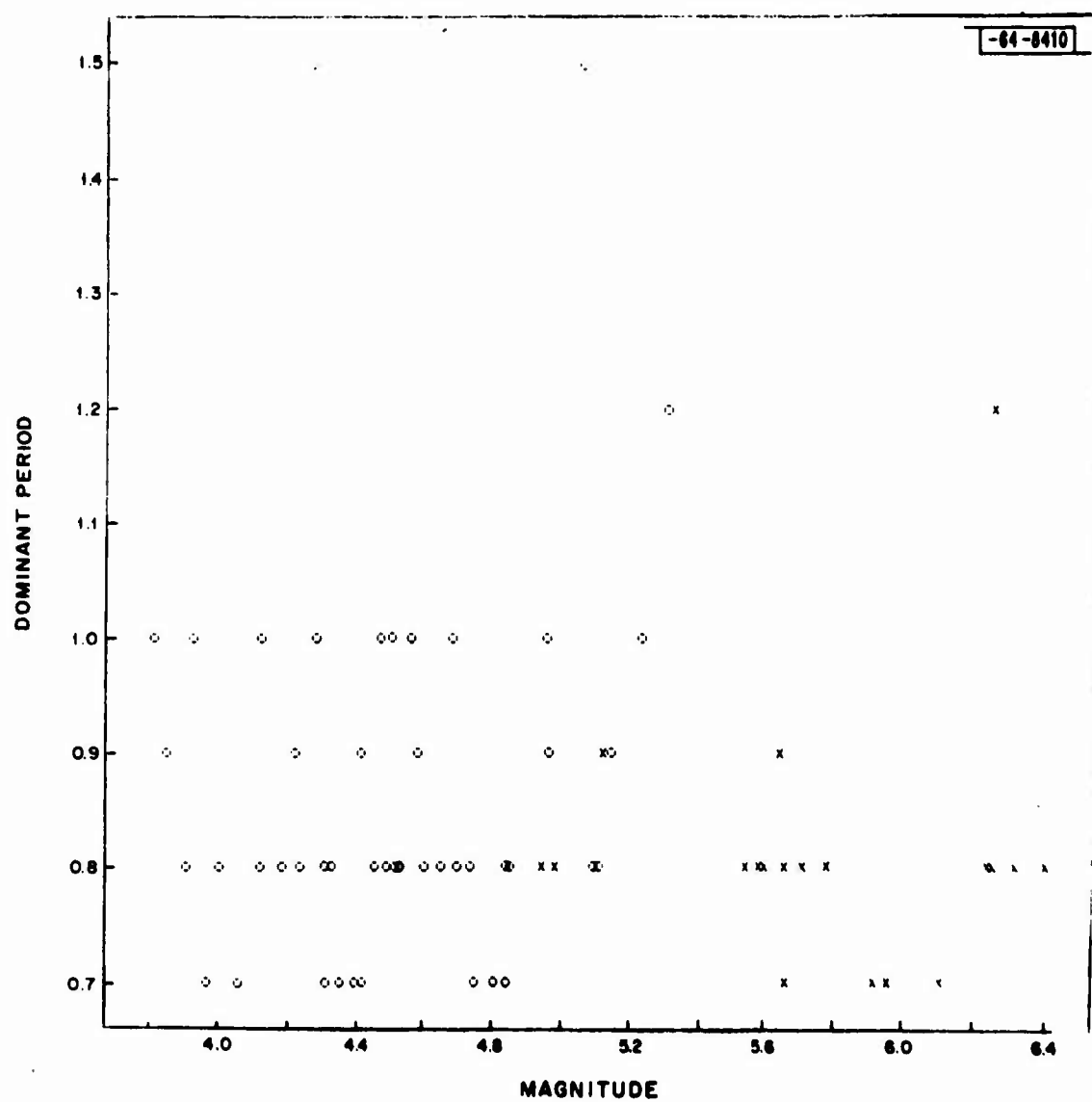
Fig. 18. Dominant period vs magnitude for 48 shallow earthquakes (O) and 19 explosions (X).

327

APPENDIX

The following is a list of the earthquakes used in this study. If a PDE number is given, then all data is taken from the PDE card (card 80/43 refers to the forty-third event on card 80 of the year in question). Otherwise the data is obtained from the LASA recording, as described in the text.

Date	Origin (GMT)	Lat. (N)	Long. (E)	Depth (km)	Mag.	PDE
1966						
12 Nov	12 49 43.6	41.7	144.1	33 (R)	5.8	80/43
12 Nov	13 28 23*	41.5	143.8	54	4.1	88/2
16 Nov	14 57 18.1	56.0	169.0	106	4.3	
17 Nov	19 27 05*	46.1	153.6	33 (R)	4.4	81/34
18 Nov	08 46 11.7	50.0	157.0	33	4.0	
19 Nov	02 02 52.9	48.1	148.7	33	4.6	
19 Nov	13 19 30.6	49.2	156.5	33	4.3	
21 Nov	12 19 27.3	46.7	152.5	40 (P.)	5.6	88/6
22 Nov	06 29 53.5	48.1	146.7	453 (R)	5.6	82/40
24 Nov	02 56 36.6	42.9	146.0	33	3.9	
25 Nov	19 32 34.9	45.9	146.0	33	4.8	
25 Nov	20 31 36*	41.5	72.6	33 (R)	5.1	88/10
26 Nov	17 05 08*	42.6	144.5	54	3.9	89/10
27 Nov	00 20 18.6	52.0	153.0	33	4.6	
27 Nov	11 01 10*	49.5	155.8	40	4.9	85/41
27 Nov	12 48 02*	48.1	155.0	28	4.5	84/42
27 Nov	18 00 55.8	45.0	144.0	33	4.7	
29 Nov	08 09 39.9	55.0	160.0	33	4.4	
29 Nov	14 08 13.8	42.1	143.4	33	4.1	86/54
30 Nov	00 04 36*	46.9	152.7	33 (R)	4.4	88/11
30 Nov	08 49 57.5	46.8	154.1	33	4.1	
1 Dec	11 38 43.8	47.1	147.5	33	4.2	
2 Dec	01 39 49.2	54.4	158.2	33	3.9	
3 Dec	05 21 05.9	43.8	148.0	33	4.2	
4 Dec	11 06 17.7	55.5	161.7	33	4.3	
5 Dec	05 13 31.4	45.4	142.6	33	4.4	
6 Dec	07 18 40*	50.1	159.8	27	5.4	85/56
6 Dec	10 45 02.0	41.8	141.1	127	4.3	85/57
7 Dec	04 15 22*	46.8	153.6	49	4.5	92/17
7 Dec	15 12 44.5	49.0	157.0	33	4.7	
7 Dec	17 17 42.0	44.2	151.7	26	5.8	85/59
8 Dec	05 51 18.1	45.0	148.0	33	4.1	
8 Dec	13 02 46.0	43.0	148.2	33	4.0	
9 Dec	05 56 33.0	52.0	154.0	33	4.8	
11 Dec	19 47 34.2	42.9	144.5	57	4.8	87/43
12 Dec	10 35 57.1	47.0	151.8	33	4.5	
14 Dec	14 49 59.8	45.6	26.3	158	4.8	87/46
18 Dec	07 42 18.8	35.1	27.1	33 (R)	4.7	90/32
21 Dec	02 30 11.4	47.0	148.0	33	4.5	

328

Date	Origin (GMT)	Lat. (N)	Long. (E)	Depth (km)	Mag.	PDE
21 Dec	11 41 50.1	33.0	24.0	33	4.3	
22 Dec	12 10 06*	52.3	158.5	61	4.4	93/14
22 Dec	17 26 32*	48.8	147.2	38	4.5	93/15
22 Dec	19 24 06.5	48.6	154.3	77 (R)	5.2	90/41
23 Dec	14 05 54.3	47.0	150.0	33	4.7	90/41
23 Dec	23 37 39.5	53.8	160.0	26	4.4	
23 Dec	23 49 27*	54.7	162.5	28	4.9	91/33
30 Dec	01 57 09.7	40.0	29.0	33	4.3	
30 Dec	04 40 07*	52.8	160.3	33 (R)	4.8	96/24
31 Dec	00 29 14.0	48.0	130.0	31	4.5	
31 Dec	00 30 08.6	56.0	118.0	33	4.6	
31 Dec	04 53 56.6	49.0	122.4	33	4.5	
31 Dec	06 51 25.5	51.0	160.0	33	4.3	
1967						
5 Jan	02 10 00.4	49.0	105.0	33	3.8	
5 Jan	04 54 22.4	44.0	108.0	13	4.5	
5 Jan	10 07 58.3	39.4	72.9	11	5.3	1/11
7 Jan	10 49 16.7	59.0	115.0	33	4.7	
8 Jan	18 31 59.7	56.2	162.7	24	4.9	3/18
11 Jan	06 56 42.4	46.9	101.8	33	4.1	
18 Jan	06 21 27.0	45.3	150.6	33 (R)	4.3	7/31
18 Jan	08 29 03.4	42.0	142.4	65	4.8	4/31
18 Jan	11 17 44.7	48.0	156.0	33	4.8	
20 Jan	03 27 13.9	48.0	103.0	33 (R)	5.0	7/36
20 Jan	06 23 16.3	47.8	103.1	33 (R)	5.0	6/17
22 Jan	12 01 49.0	48.0	102.1	33 (R)	5.1	6/21
22 Jan	12 16 02*	48.0	102.8	33 (R)	5.0	7/43
27 Jan	06 22 29.5	52.0	154.0	65	4.5	
1 Feb	09 18 50.5	55.8	160.7	140 (R)	4.4	10/47
22 Feb	14 50 33.1	48.3	154.7	45	4.7	12/57
24 Feb	04 32 21.6	53.0	151.0	20	4.5	
5 Mar	09 55 15*	46.8	152.7	33 (R)	4.4	16/36
10 Mar	09 02 20.5	45.0	146.7	33	4.5	
19 Mar	03 36 49.8	45.0	149.0	47	4.2	
29 Mar	10 01 10*	44.4	148.4	26	4.4	26/22
30 Mar	15 32 24.8	45.9	146.0	33	5.1	
1 Apr	14 00 33.8	45.8	151.7	23	5.4	21/60
5 Apr	08 08 49.5	52.0	152.0	33	4.5	
7 Apr	17 07 16.2	37.4	36.1	49	4.8	27/23
7 Apr	17 39 47.7	37.4	36.1	33	4.5	
7 Apr	19 39 13*	47.0	146.0	296	5.0	28/22
8 Apr	08 55 40*	47.3	153.4	60 (R)	4.6	31/6
22 Apr	05 18 53.8	45.0	88.0	17	4.6	
22 Apr	23 00 32*	46.8	151.6	73	4.4	31/26
26 Apr	16 47 06.1	53.0	153.0	33	4.4	
28 Apr	03 07 20.2	49.0	151.0	33	3.8	
28 Apr	08 56 41.1	54.0	141.0	33	4.4	

17
IMPLICATIONS OF SOURCE PARAMETERS ON
SEISMIC SYSTEM STUDIES

Joseph T. Beardwood, III
General Atronics Corporation
1200 East Mermaid Lane
Philadelphia, Pa. 19118

ABSTRACT

Seismic system studies have been concerned with the ability of networks of stations to detect, locate, and identify seismic events. The emphasis in our studies to date has been on the detection problem. The source and propagation models used to formulate this problem are discussed, and the relation between detection sensitivity and source spectrum is considered. Assuming a source spectrum corresponding to detonation in tuff, it is tentatively concluded that changes with yield in the source spectrum are not important (in the context of the complete detection system) for yields less than 50 kt. This result is a consequence of the increasing severe attenuation of the propagation medium with increasing frequency and the limited frequency response of the seismometer. Similar results are expected for different source media. Finally, the implications of source parameters on the discrimination problem are briefly discussed.

In attempting to evaluate the detection sensitivity and identification capability of a hypothetical network of seismic stations it is necessary to make several assumptions concerning the characteristics of the seismic source, the propagation path, the seismometer, and the signal processing to be performed on the outputs of the seismometers. In this paper we are concerned with indicating what properties of the source are and are not important in the context of seismic system studies. To do this we shall have to briefly consider the other components of the problem, principally the attenuation associated with propagation. It will be concluded that only a very limited region of the source spectrum is relevant to this problem.

The seismic networks under consideration typically consist of a collection of stations distributed around the world. Geographical and political considerations make it quite unlikely that any of the stations can be located very close to potential test sites. For this reason, we shall assume that all stations are at teleseismic ranges from the epicenters of interest. As will be illustrated below, this assumption will assure sufficient attenuation at higher frequencies that only a relatively narrow frequency region of the source spectrum influences the received signal at the network station.

The frequency bands of interest are those immediately on either side of the principal microseismic noise band, 0.025 - 0.05 Hz and 0.4 - 4.0 Hz. The lower frequency band is useful

primarily for discriminating between earthquakes and underground nuclear explosions. This discrimination is based on the general tendency for earthquakes to couple relatively more energy into surface waves than explosions. The upper frequency band provides a superior means of detecting and locating seismic events as well as some additional discriminants. In the remainder of this paper we shall be concerned primarily with the detection problem and, therefore with the upper band.

In considering the detection problem it is normally assumed that the detector is an energy detector with an integration interval of 1-1.5 sec, and only direct P-wave arrivals are considered. More sophisticated detectors (e.g., matched filters) are excluded because multipath propagation in the crust in the vicinity of both receiver and source, and other factors, make it impossible to predict completely the received waveform. In addition, these factors prevent reliable estimates of signal level after 1-1.5 sec, and reduce the correlations of this portion of the signals across distances as small as 10 km sufficiently to hinder any useful array processing for signal-to-noise ratio enhancement.

In summary, we are interested in predicting the energy in the output of a short-period seismometer as a function of the range and yield of the event. To do this we shall consider the properties of the source and the propagation medium and illustrate these in the frequency domain.

FREE FIELD SOURCE FUNCTION

According to Latter, et al. [1] "it is easily shown that the Fourier transform of the displacement at a distance r is, in general

$$\hat{\xi}(\omega) = \frac{\hat{p}a}{8\pi\mu} \frac{1}{r^2} + \frac{i\omega}{rc} \frac{c^2}{\omega_o^2 + i\omega_o\omega - \frac{\lambda + 2\mu}{4\mu}\omega^2} \tag{1}$$

where a is the (unknown) radius at which the medium begins to behave elastically, $\hat{p}$ is the (unknown) Fourier transform of the pressure that acts at a, and where $\omega_o = c/a \ldots$"

Based on the Ranier explosion (1.7 kt) Latter, et al., observe that ω_o scales to

$$\omega_o = 25(1.7/W_{kt})^{1/3}\sec^{-1} \tag{2}$$

Following Latter, et al.'s formulation for concealing an underground shot, we assume a step-function pressure proportional to the yield divided by the cavity volume,

$$\hat{p} \sim \frac{W}{a^3 i\omega} \tag{3}$$

The frequency dependence implied by Eq. 3 appears to be consistent with the Ranier data presented by Werth and Herbst [2]. It will turn out that moderate changes in the frequency dependence of Eq. 3 will not significantly affect the results of this paper. For this reason we shall not here consider alternate assumptions for $\hat{p}$.

PROPAGATION CHARACTERISTICS

Equations 1-3 can be combined to yield the Fourier transform for the displacement at a distance. These equations, however, neglect the frequency dependent attenuation of the earth as a propagation medium. Following Knopoff and MacDonald [3], we have assumed a "constant Q" attenuation characteristic.

$$A(r, \omega) = \exp\left[-\frac{\pi r}{\lambda Q}\right] = \exp\left[-\frac{|\omega| r}{2Qc}\right] \tag{4}$$

The path has been approximated by two segments, two passes through the crust (each with distance D and Q of Q_0), and one through the mantle (distance r and Q of Q_1). These assumptions are, of course, only a rough approximation to reality. The Q of the crust varies greatly with geographic position, and the thickness of the crust is highly variable. The partitioning of energy into the various multipath signals and reverberations within the crust is also difficult to account for quantitatively. This partitioning clearly depends on both the absolute and relative locations of source and receiver. One consequence of this partitioning is that an arbitrary gain factor must be determined for each station, either by measurement on actual data from that station, or by assumption.

FREQUENCY DOMAIN ILLUSTRATIONS

Equations 1-4 can be combined to give the Fourier transform of the displacement at teleseismic range

$$\left(\frac{i\omega}{rc} + \frac{1}{r^2}\right)\frac{KW}{i\omega}\underbrace{\frac{1}{1 + i\frac{\omega}{\omega_0} - \frac{\lambda + 2\mu}{4\mu}\left(\frac{\omega}{\omega_0}\right)^2}}_{\text{source}}\underbrace{\exp\left[-\frac{|\omega|}{2c}\left(\frac{2D}{Q_0} + \frac{r}{Q_1}\right)\right]}_{\text{attenuation}} \tag{5}$$

where $\omega_0 = 25(1.7W_{kt})^{1/3}$

For the ranges of interest we can neglect the $1/r^2$ term compared to the $1/r$ term in the first factor.

We assume the following parameter values

$$c = 8 \text{ km/sec} \qquad Q_0 = 200$$
$$\lambda = \mu$$
$$D = 50 \text{ km} \qquad Q_1 = 2000$$

and plot the resulting magnitude-squared of the Fourier transform (the energy density spectrum).

Figure 1 shows the energy density spectrum for the source function for several values of yield. These and all subsequent curves are normalized to the same peak value in plotting.

333

From the figure it is apparent that the shape of the spectrum is highly dependent on the yield: the smaller the yield, the higher in frequency will be the peak of the spectrum. Within 0.5 Hz of 1.0 Hz, the dominant frequency of teleseismic signals, the spectrum level does not vary more than a few dB. This appears to be independent of the medium in which the shot is detonated [2].

Figure 2 illustrates the magnitude-squared of the attenuation factor for each of four ranges. The increasingly severe attenuation with increasing range and frequency is apparent in this figure. The energy density spectrum of the combined expression is plotted in Figure 3 for a range of 20° and in Figure 4 for a range of 90°. Figure 3 indicates that the change in spectral shape with yield can be observed at a range of 20°. Figure 4 shows that it is negligible at 90° since, at this range, the attenuation term completely dominates the shape of the spectrum.

The multipath signals due to reverberations at the receiver were mentioned earlier when we confined our attention to the first 1-1.5 sec of the P-wave in order to avoid the multipath contribution. An additional multipath contribution that cannot be avoided is that due to the surface reflection near the source, which corresponds to the pP phase for earthquakes. The addition of this reflected signal (which has the opposite polarity of the original signal) produces a marked effect on the spectrum. Specifically, zeros are introduced (assuming unity gain in the reflection) at zero frequency and at frequencies which are integer multiples of the reciprocal time delay between the direct and reflected signals. This effect is illustrated in Figure 5 for explosions with yields from 1 to 100 kt. In calculating these energy density spectra, it was assumed that the depth was 2000 feet. As before, the spectra are about identical in shape; however, they now peak between 0.5 - 1.0 Hz which is consistent with observed seismic data.

SUMMARY AND CONCLUSIONS

For the discussion above, we have used a very simplified model of the seismic source function of an underground explosion, and an approximate model for the propagation path from the explosion to receivers at teleseismic ranges. It is apparent that only a very limited portion of the spectrum of the explosion signal is of interest, and this would be the case even with a more refined model. This spectral region lies roughly between 0.5 and 2.5 Hz. Furthermore, only the first 1-1.5 sec of the signal are of interest in the network problem. Clearly much more remains to be known concerning the pressure function at the beginning of elastic propagation, and the propagation models could certainly be refined. In pursuing this effort, however, it is appropriate to bear in mind the limited region of time and frequency that is relevant to the system problem.

334

REFERENCES

1. A. L. Latter, R. E. LeLevier, E. A. Martinelli, and W. G. McMillan, A Method of Concealing Underground Nuclear Explosions, J. Geophys. Research, 66, 943, 1961.

2. G. C. Werth and R. F. Herbst, Comparison of Amplitudes of Seismic Waves from Nuclear Explosions in Four Mediums, J. Geophys. Research, 68, 1453, 1963.

3. L. Knopoff and G. J. F. MacDonald, Attenuation of Small Amplitude Stress Waves in Solids, Revs. Modern Phys., 30, 1178, 1958.
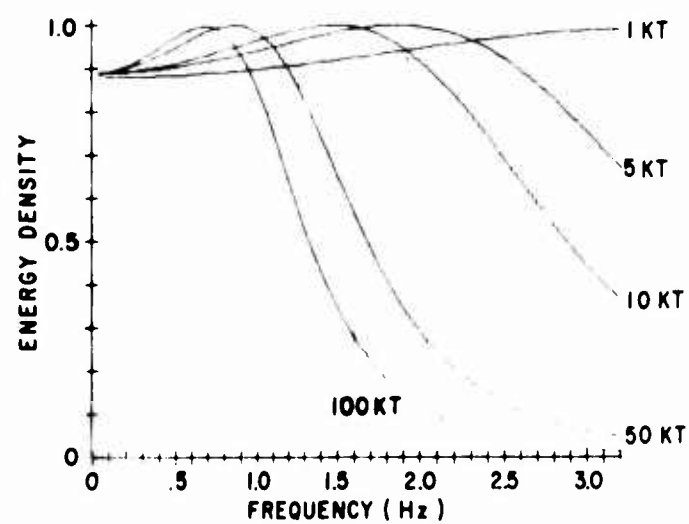
335

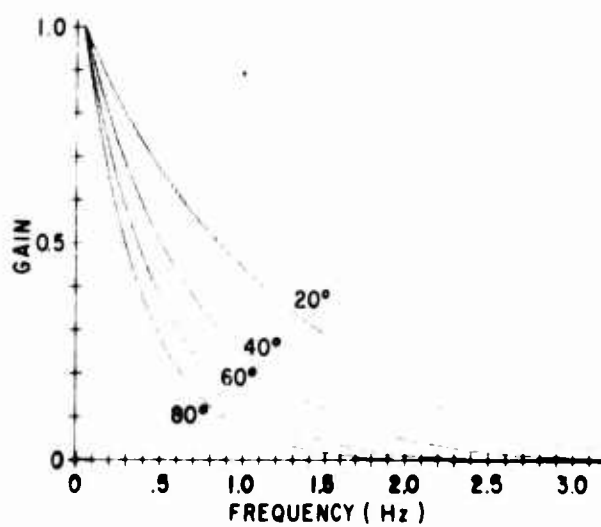FIGURE 1
SOURCE SPECTRA
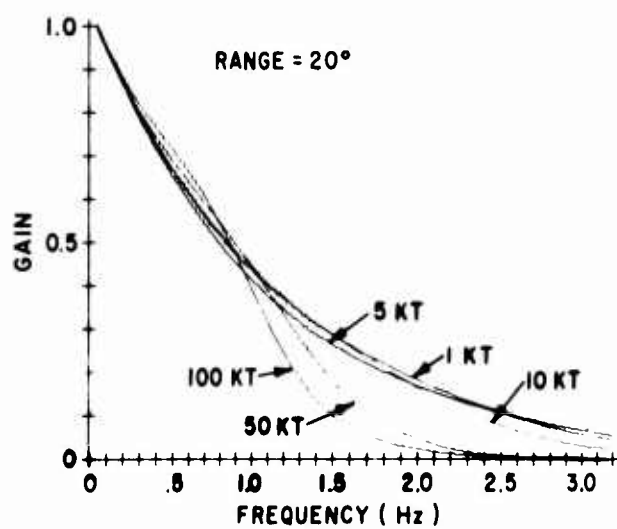
336

FIGURE 2

ATTENUATION VS FREQUENCY AND RANGE
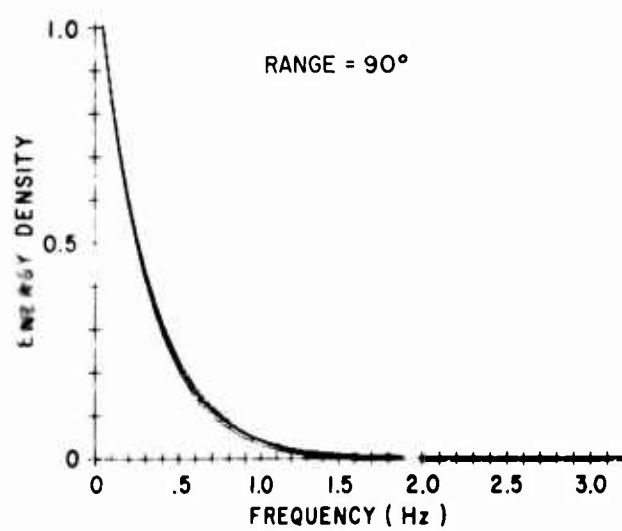
FIGURE 3
FREE FIELD TELESEISMIC SPECTRA

FIGURE 4
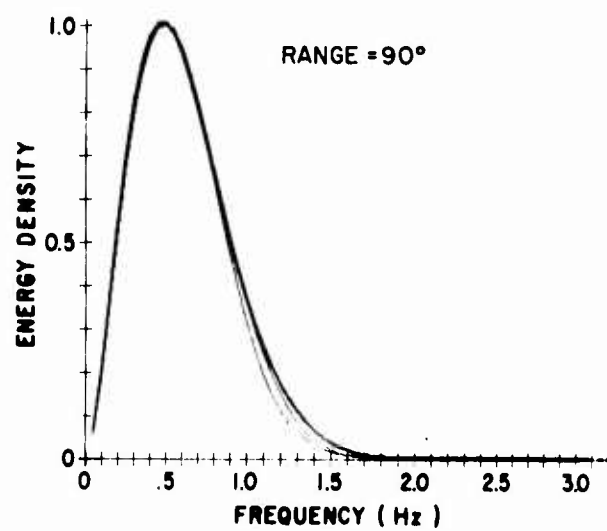FREE FIELD TELESEISMIC SPECTRA

FIGURE 5

TELESEISMIC SPECTRA (INCLUDING pP)

18
A BIBLIOGRAPHY ON DECOUPLING

J. B. Walsh and W. F. Brace
Department of Geology and Geophysics
Massachusetts Institute of Technology
Cambridge, Massachusetts

To be published at a later date.

19
THE PRESENT STATUS OF SEISMIC COUPLING

G. Simmons
Massachusetts Inst. of Technology
Cambridge, Massachusetts

and

E. Herrin
Southern Methodist University
Dallas, Texas

Our ability to detect, identify, and locate underground nuclear explosions has been improved considerably during the last five years. From the seismic signal, location, and rough knowledge of the attenuation of the earth, we are able also to obtain estimates of the seismic magnitude of the event. The accurate determination of nuclear yield from seismic magnitude is by no means perfected. In fact, the weakest link in the underground nuclear detection program, at present, is the determination of nuclear yields from observed seismic signals. For well-observed events in the magnitude range 5 to 6, the scatter of magnitude estimates among the stations is often as great as 1 magnitude unit. For explosions in tuff below 10 KT, magnitude and the logarithm of the yield are, to a first approximation, linearly related. Thus a scatter of 1 magnitude unit implies an uncertainty of an order of magnitude in yield. Above 10 KT, because magnitude is more closely proportional to log yield to the 2/3 power, the scatter in the yield estimates is even greater. Thus we must consider two sources of error in yield determinations from seismic data: (1) uncertainties in the estimate of seismic magnitude and (2) uncertainties in the yield - magnitude relation (scaling law) for various media. In this conference we have concentrated on the second source of error.

The basic problem in relating yield to magnitude is our lack of understanding of the phenomena that occur in materials under shock conditions in the pressure range 0 - 300 kb. Specifically, we need not only better data on physical properties in this pressure range, but also an improved understanding of the physics of the phenomena in this pressure region due to dynamic loading. The weakest link in the CODE calculations is the statement of physical properties (i.e., the stress and strain and strain rate) in the zone corresponding to this pressure range. In this short discussion, it is our purpose to point out some of the areas of research in which our needs are greatest and in which additional work can be expected to contribute towards the solution of the present problem of estimating nuclear yields.

The presence of cracks in ι   gic media affects the physical properties. The behavior of "cracked media" under the c   .amic loading imposed by shock waves, seems anomalous.

Relatively little is known about the physics of materials containing cracks. Handin, (Paper 11, this symposium) in a slightly different way, points out the need to select the best criteria of yielding for the various geologic media that best fits the observational data on nuclear explosions.

The changes of properties with pressure, anisotropic loading, and, especially, the changes with pressure that occur under the conditions of dynamic loading that obtain in the plastic-elastic region of a nuclear explosion must be understood in order to predict the behavior of the materials in this region. An understanding of the behavior of materials under these conditions, and in this zone is absolutely necessary for the estimation of the nuclear yield of an event with a given seismic magnitude. The present state of our knowledge of the strength of materials at pressures of only a few tens of kilobars is inadequate. As Anderson and Linde (Paper 3, this symposium) and Ahrens (Paper 4, this symposium) show, the finite strength of some materials that persist at pressures near, or even exceeding, the Hugoniot elastic limit (HEL) can cause significant departures from the normal Hugoniot relations. Thus, in some materials it would seem necessary to take into account the added factor of this strength.

Most materials of geophysical interest that have been studied with shock wave techniques exhibit phase transitions in the pressure range 0 - 300 kb. At pressures above that of the first phase transition, the experimental data obtained with shock waves fit very well the equations of state obtained from fairly simple theory. There is a general consensus that the equations of state of matter under shock conditions, on the high pressure side of these first phase transitions, are quite satisfactory (McQueen, Paper 5, Cherry, Paper 12, Ahrens, Paper 4, all this symposium). Indeed, the fit between experimental data at very high pressure and the various theoretical equations of state is extraordinary. Furthermore, as McQueen shows, our ability to predict the equation of state for new materials, above the transition point, based on the presently available results for a number of oxides, seems to be adequate. Our predictive techniques fail completely though in the low pressure region from zero to a few hundred kilobars.

Observational data obtained from underground nuclear explosions, as well as indications from CODE calculations, clearly show changes in wave form with both distance and time. The energy spectrum near the cavity contains considerable high frequency energy; however, in the far-field practically all of the energy is contained in the spectral window of 0.3 to 3 cps. The material of the earth, as a transmission medium, rapidly attenuates energy of higher frequencies. These observations imply to us that the properties of materials at frequencies around 1 cps are the factors that most affect the seismic signatures of events obtained at stations at distances greater than a few hundred kilometers from the source, yet practically all of the data on the dynamic properties of rocks are obtained at much higher strain rates. The only signals that are available for analysis by seismic means in underground nuclear detection are those in the spectral window of about 0.3 to 3 cps. These signals have been shaped by a filter with properties that correspond to a relatively slow strain rate. It seems to us particularly

important at the present time to investigate the physical properties of materials at strain rates that correspond to the seismic frequencies. It is also desirable to extend the CODE calculations to distances and times sufficient for the displacements to become infinitesimal. It is especially important that the CODE calculations provide good estimates of the energy spectra at these distances.

The chief use in the surveillance of underground nuclear explosions, of the CODE calculations, as well as an understanding of the basic physics of the behavior of matter at high pressures and temperatures under shock conditions, is the enhancement of our predictive abilities. It seems to us impractical, though perhaps not impossible, to obtain calibration data for every possible area, and every geologic medium, potentially available on earth. Clearly, it is possible to obtain the equations of state for all materials of possible interest to the Vela Program, including porous and cracked materials. However, the task is not small and the development of our ability to predict accurately the equations of state for materials not yet measured experimentally, and especially for porous materials, is desirable at the present time in the VELA UNIFORM PROGRAM.

Trulio discusses the results obtained on the behavior of granite in the SHOAL, HARDHAT, and PILE DRIVER experiments, and notes that the calculated and measured displacements in the near-field differ by an order of magnitude. Cherry (Paper 12, this symposium) notes the same discrepancy for granite. The large differences are attributed to a difference in the physical properties that existed in situ and the values of the properties that were measured in the laboratory. The present data indicate clearly that the propagation of waves in media with cracks is very poorly understood.

G. D. Anderson and R. K. Linde (Paper 3, this symposium) report work on foams with shock waves. The experimental data obey a very different equation of state of the matrix material. Their results indicate a real need for additional work on fluid-filled porous media.

The results of the symposium may be summarized in the following way. Our present ability to detect, identify, and locate underground nuclear explosions far exceeds our ability to estimate reliably the nuclear yield of the device. The improvement of our ability to estimate reliably the nuclear yield, will require that a considerable effort be expended to gather data, develop concepts, and understand the basic behavior of geologic materials under shock conditions at pressures to 200 or 300 kb so that the yield-magnitude relationship can be established for a variety of media and to find more accurate methods for estimating the seismic magnitude of underground explosions.